# *Multiscale Modelling to Develop and Understand Future Photovoltaics*

CAI WILLIAMS

# Multiscale Modelling to Develop and Understand Future Photovoltaics

Cai Williams

A Thesis presented for the degree of
Doctor of Philosophy


Advanced Materials and Electronic Devices
Department of Engineering
University of Durham
England

December 2023

*Uchelgaer uwch y weilgi – gyr y byd*
*Ei gerbydau drosti,*
*Chwithau, holl longau y lli,*
*Ewch o dan ei chadwyni*

*- Dewi Wyn o Eifion*

# Multiscale Modelling to Develop and Understand Future Photovoltaics

**Cai Williams**

*Submitted for the degree of Doctor of Philosophy*
*December 2023*

## Abstract

In this thesis, multiscale modelling from the device to energy systems is used to identify and examine applications for emerging photovoltaics within our future climate and energy markets.

The concept of photovoltaics of enhanced capacity factors are introduced, and their benefits are demonstrated through a combination of plant dispatch modelling utilising experimental characteristics from collaborators. It is shown that possessing an increasing efficiency with reducing irradiance enables better alignment between demand and solar generation, increasing capacity factors. At most saving more than 3.5 times the greenhouse gas emissions than silicon photovoltaics.

A atmospheric composition model combining a radiative transfer model and single diode model is used to examine the effects wildfires, dust storms and pollution upon photovoltaics. Showing spectrally calculated losses of more than $100\text{Wm}^{-2}$ can be accrued due to local effects. Paying further attention to spectral losses different photovoltaics are tested showing the benefits of broad and narrow absorption spectra.

Finally, genetic algorithms are used to design and optimise organic photovoltaics. Optimising for power conversion efficiency (PCE); PCE per unit cost, and levelised cost of energy. Resulting in different devices per objective function. Considering the cost of the active layer to be a variable the maximally acceptable commercial cost for the active layer material is shown to be £10 for P3HT:PCBM, and £100 for PM6:Y6.

# Declaration

The work in this thesis is based on research carried out at the Advanced Materials and Electronic Materials Node, the Department of Engineering, Durham University, England. No part of this thesis has been submitted elsewhere for any other degree or qualification, and it is all my own work unless referenced to the contrary in the text.

# Acknowledgements

Firstly, I would like to thank my supervisors: Chris Groves; Natasha Shirsova, and Roderick Mackenzie. Your support and guidance as supervisors has been impeccable throughout my PhD. I will forever be grateful for your patience with me as I continued to learn.

To all the non-academic staff and technicians of the Department of Engineering, thank you. Without you, I am sure this thesis would have come to a sudden halt. In particular, I would like to thank the coffee bar for providing me with perhaps at times a bit too much coffee.

My friends, your support during my PhD has been invaluable, thank you. For those in Durham, conversations over coffee and ~~cake~~ biscuits were often the highlights of my week. To those away from Durham, the evenings of escapism I continued to share with you, I could not have done without.

I fy deulu diolch am rhoi fynnu gyda i tra roeddwn yn tynnu gwallt fyn mhen, ag yn poeni am pethau dibwys. Heb lleisiau cyfarwydd dwi'n siŵr mi fysa i dal yn poeni. i pawb sydd wedi cyfieithu hwn, ychydig dros ben llestri na.

*Diolch o gwelod fy galon!*

*Thank you from the bottom of my heart!*

# Contents

# List of Figures

# List of Tables

# List of Publications

[1] C. Williams *et al.*, "Decarbonising electrical grids using photovoltaics with enhanced capacity factors," *Energy & Environmental Science*, vol. 16, no. 10, pp. 4650–4659, 2023.

# List of Conferences

[1] C. Williams, R. MacKenzie, N. Shirshova, and C. Groves, "Machine learning to enable the full range of organic pv performance to be realised," in *Next-Generation V+ PV Materials*, 2022.

[2] C. Williams *et al.*, "Optimising grid connection utilisation through device design," in *Proceedings of International Conference on Hybrid and Organic Photovoltaics (HOPV23)*, 2023.

# List of Publications in Preperation

[1] C. Williams, N. Shirshova, R. C. MacKenzie, and C. Groves, "Decarbonising electrical grids using photovoltaics with enhanced capacity factors," 2024.

# Acronyms

| | |
|---|---|
| **AM1.5G** | Air Mass 1.5 Global tilt Refrence Specra. |
| **AOD** | Aerosol Optical Depth. |
| **API** | Application Programming Interface. |
| **BEIS** | Department of Business, Energy & Industrial Strategy. |
| **BHJ** | Bulk Heterojunction. |
| **BMRS** | Balancing Mechanism Reporting Service. |
| **CAISO** | California Independent Systems Operator. |
| **CAMS** | Copernicus Atmosphere Modelling Serivce. |
| **CF** | Capacity Factor. |
| **CFPV** | Capacity Factor Photovoltaics. |
| **$CO_2e$** | Carbon Dioxide Equivilent. |
| **DC** | Dispatch Class. |
| **DD** | Drift-Diffusion. |
| **DSSC** | Dye Sensetised Solar Cell. |
| **DUKES** | Digest of UK Energy Statistics. |
| **ECMWF** | European Center for Medium-Range Weather Forcasts. |
| **ENTSO-E** | European Network of Transmission System Operators for Electricity. |
| **EQE** | External Quantum Efficency. |
| **ESO** | Electricity Systems Operator. |
| **FF** | Fill Factor. |

| | |
|---|---|
| **FFDI** | Forest Fire Danger Index. |
| **GA** | Genetic Algorithum. |
| **HOMO** | Highest Ocupied Molecular Orbital. |
| **IEA** | International Energy Agency. |
| **ITO** | Indium Tin Oxide. |
| **$J_{SC}$** | Short Circuit Current. |
| **JSON** | Java Script Object Notation. |
| **JV** | Current-Voltage. |
| **LCOE** | Levelised Cost of Energy. |
| **LUMO** | Lowest Unocupied Molecular Orbital. |
| **MPP** | Maximum Power Point. |
| **MPPT** | Maximum Power Point Tracking. |
| **NPV** | Net Present Value. |
| **NREL** | National Renewable Energy Laboratory. |
| **NSW** | New South Wales. |
| **OPV** | Organic Photovoltaic. |
| **PCE** | Power Conversion Efficiency. |
| **PD** | Plant Dispatch. |
| **PERC** | Passivated Emitter and Rear Contact. |
| **PM** | Particulate Matter. |
| **ppm** | parts per million. |
| **PSH** | Peak Sun Hours. |
| **PV** | Photovoltaic. |
| **PVGIS** | Photovoltaic Geographical Information Systems. |
| **SA** | Southern Australia. |
| **SMARTS** | Simple Model of the Atmospheric Radiative Transfer of Sunshine. |

| | |
|---|---|
| **SOC** | State of Charge. |
| **SRH** | Shockley-Reed-Hall. |
| **TCO** | Transparent Conducting Oxide. |
| **$V_{OC}$** | Open Circiut Voltage. |
| **VIC** | Victoria. |
| **WASG** | Wide Area Synchronous Grid. |

# Chapter 1

# Introduction



## 1.1 Chapter Overview

Emerging photovoltaics hold the promise of enabling an acceleration towards net-zero, due to their potential for low-costs and high efficiencies. However, with challenges both in their development, and from existing technologies, these promises have yet to come to fruition. Multiscale modelling, offers the ability to enable the consideration of factors from across length scales within device development. Coupling emerging photovoltaics with multiscale modelling may reveal new opportunities and paradigms in solar photovoltaics that emerging photovoltaics can address.

In this chapter, both emerging photovoltaics and multiscale modelling are introduced, as well as the context providing motivation for this work. Additionally, the structure of the thesis exploring this hypothesis is presented.

## 1.2 Context

Since the industrial revolution, the concentration of carbon dioxide found in the atmosphere has grown from 280 to 417ppm [1]. This rise in concentration driven by anthropogenic pollution has seen global temperature anomalies rise, as is shown in figure 1.1. Maintaining current green house gas emissions, global surface temperature is predicted to rise by 3.3 to 5.7°$C$ by 2100 compared to the turn of the millennium [2]; leading to a highly variable climate; an increase in sea level [3]; further drought and the expansion of arid environments [4], and the loss of food security [5].

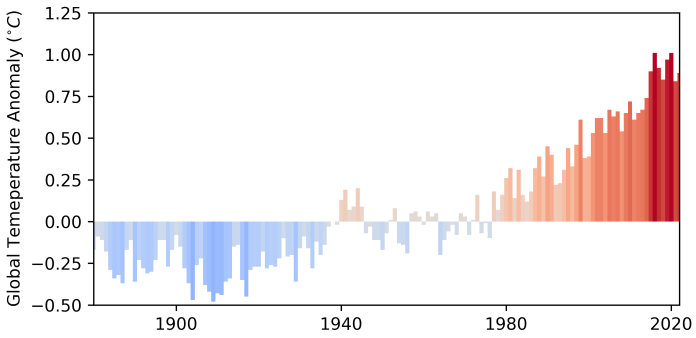


Figure 1.1: Global temperature anomalies from 1880 to 2022 [6]. The change in temperature compared to an average from 1951 to 1980.

Nations are committed to limiting this rise within The Paris Agreement [7]. Signatories face legal pressure if they do not seek to limit the rise in global surface temperature to 2°$C$ by 2100. States are declaring they will reach net-zero emissions by at latest 2050 [8]. To reach net-zero, electricity generation must transition to low carbon energy sources, and photovoltaics are likely to be an important generation source in within this transition.

Already, the global installed capacity of photovoltaics has risen within the past decade, from 97 to 1185 GW [9, 10]. This has been driven by the exponential reduction in cost of silicon based photovoltaics, which over the same period have seen their price reduce by a factor of 5 [11]. This has seen silicon photovoltaics make up 95% of that installed [11]. Whilst the sum of energy generated by silicon may be the highest of commercial

technologies [11], challenges are present that may be addressed by emerging photovoltaics, some of which will be tackled in this thesis.

## 1.3 Emerging Photovoltaics

Emerging photovoltaics, the third generation of photovoltaics [12], are comprised of technologies including, but not limited to, dye-sensitised solar cells (DSSCs); organic photovoltaics (OPVs), and perovskite solar cells (PSCs). All have shown promise of achieving high efficiencies with low costs [13, 14, 15]. Spurring wide efforts to see them to fruition. However, these efforts have yet to see the wide scale adoption of these technologies, but the early stages of commercialisation can be seen [16, 17].

Today, these emerging photovoltaics in experimental laboratory research achieve efficiencies ever nearing that achieved by silicon based cells of 28.6% [18]. With DSSCs, OPVs, and PSCs reaching champion efficiencies of 13%, 19.2%, and 26.1% respectively [19, 20, 21], both OPVs and PSCs have shown large increases in efficiencies within the last decade [18].

The promis of low costs is due to both low-cost materials and manufacturing techniques [13, 14, 15]. Organic materials are already synthesised in industrial quantities [22], and DSSCs and PSCs are capable of avoiding critical raw materials [23, 24]. OPVs, DSSCs and PSCs have all been demonstrated to be manufacturable through the roll-to-roll process [25, 26, 27]. Enabling the near continuous manufacture of photovoltaics at high throughputs, thereby reducing costs [26, 27]. Unfortunately these promises of low costs have yet to be seen, challenges, such as degradation and lifetime [28, 29, 30], stop these emerging devices reaching commercialisation. Despite efforts to address these challenges [31, 32], much of active research does consider these factors as holistically as needed for commercialisation, instead concentrating upon singular factors, such as power conversion efficiency [33].

Whilst this holistic development may be achieved experimentally, the expense of such studies may prove prohibitive, through the use of models

of emerging photovoltaics both new opportunities and new approaches to design in order to compete with silicon may be explored.

## 1.4 Multiscale Modelling

Multiscale modelling, the interlinking of models at various scales, enables the examination of factors from across these scales against each other, and simulation of the system modelled as a whole. This technique has been applied in many fields such as for the simulation of composites [34], proteins [35], and previously emerging photovoltaics [36, 37, 38]. However, previous works upon multiscale modelling have only explored from molecules to devices.

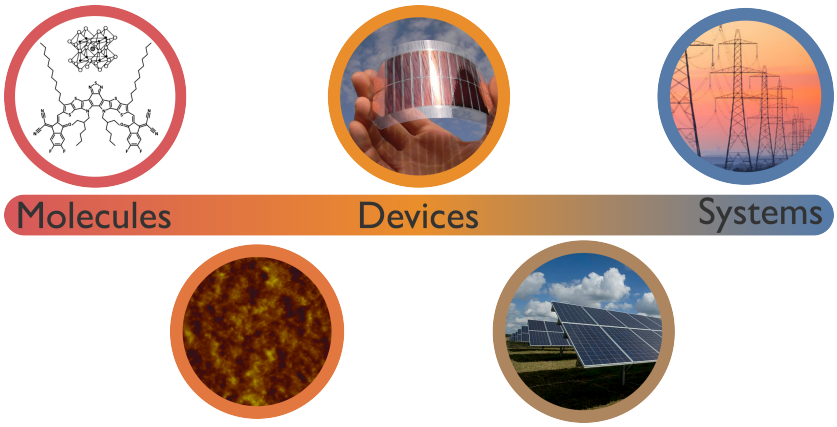


Figure 1.2: Length scales of consideration for emerging photovoltaics.

Towards systems, as shown in figure 1.2, models of photovoltaics have been developed considering: the energy yield expected from devices [39]; the cost of this energy [40]; and its usefulness for anthropogenic demands [41]. Despite their development, the direct feedback from models of these scales to device development can not be widely found. For example, by the examination of a device characteristics influence upon energy systems a device may be optimised, or challenges faced at the system level may highlight new opportunities for devices.

Integrating these models of emerging photovoltaics covering the range of scales presented in figure 1.2 may enable for a more holistic development of emerging photovoltaics. Enabling the consideration of the interconnected

factors from the smallest to largest scale, and the development of emerging photovoltaics designed for new applications or following new approaches. Potentially leading to photovoltaics explicitly designed for the low carbon energy future.

## 1.5 Research Hypothesis

In order to enable emerging photovoltaics to realise their potential in application that both compete with or complement silicon photovotlaics, their development must consider the interconnected factors found beyond the device itself. This may be realised through the development of a multiscale model spanning from molecules, devices, to systems. Particular attention should be paid to: the usefulness of the energy generated in meeting anthropogenic demands; their tolerance to our increasingly variable climate, and the viability of the materials which are developed upon. Through placing attention to these areas the development and understanding of future photovoltaics maybe furthered.

## 1.6 Thesis Structre

**Chapter 2** shows background information about photovoltaics, the wide area synchronous grid they operate upon, and the irradiance which drives their generation. Further information is given about the emerging photovoltaic technologies of OPVs and DSSCs.

**Chapter 3** introduces the concept of multiscale modelling, before providing detail as to the models utilised throughout this thesis and their development. This includes: plant dispatch modelling; genetic algorithm optimisation; drift-diffusion modelling; atmospheric composition modelling and levelised cost of energy modelling.

**Chapter 4** is the first results chapter and explores the benefits of designing photovoltaics for enhanced capacity factors. Through the use of the plant dispatch model, experimental DSSCs are placed upon the wide area synchronous grid of the mainland UK and the influence of their design upon their achieved capacity factor, saved carbon equivalent emissions, and potential revenue are reported. This work was published in Energy and Environmental Science.

**Chapter 5** utilises satellite atmospheric composition data and the atmospheric composition model to report the losses in power yield seen by photovoltaics themselves, due to their exposure to both long term and short term changes to the composition of the atmosphere including wildfires and dust storms.

**Chapter 6** optimises the architecture of OPV systems of P3HT:PCBM and PM6:Y6 for several objective functions. Firstly, optimising for power conversion efficiency, before exploring how changes to the active material blend cost influences the optimal design for power conversion efficiency per unit cost and levelised cost of energy.

**Chapter 7** outlines the main conclusions of this thesis, and suggests several possible directions for future research.

# Bibliography

[1] "Climate Change: Atmospheric Carbon Dioxide | NOAA Climate.gov." [Online]. Available: http://www.climate.gov/news-features/understanding-climate/climate-change-atmospheric-carbon-dioxide

[2] P. Arias *et al.*, "Climate change 2021: the physical science basis. contribution of working group i to the sixth assessment report of the intergovernmental panel on climate change; technical summary," 2021.

[3] S. Solomon, G.-K. Plattner, R. Knutti, and P. Friedlingstein, "Irreversible climate change due to carbon dioxide emissions," *Proceedings of the national academy of sciences*, vol. 106, no. 6, pp. 1704–1709, 2009.

[4] A. Dai, "Increasing drought under global warming in observations and models," *Nature climate change*, vol. 3, no. 1, pp. 52–58, 2013.

[5] H. C. J. Godfray *et al.*, "Food security: the challenge of feeding 9 billion people," *science*, vol. 327, no. 5967, pp. 812–818, 2010.

[6] N. J. Lenssen *et al.*, "Improvements in the gistemp uncertainty model," *Journal of Geophysical Research: Atmospheres*, vol. 124, no. 12, pp. 6307–6326, 2019.

[7] C. A. Horowitz, "Paris agreement," *International Legal Materials*, vol. 55, no. 4, pp. 740–755, 2016.

[8] "Climate Change Act 2008," Nov. 2008. [Online]. Available: https://www.legislation.gov.uk/ukpga/2008/27/pdfs/ukpga_20080027_en.pdf

[9] "Snapshot of Global PV Markets - 2023," IEA, Tech. Rep., 2023.

[10] "Snapshot of Global PV Markets - 2012," IEA, Tech. Rep., 2012. [Online]. Available: https://iea-pvps.org/wp-content/uploads/2020/01/PVPS_report_-_A_Snapshot_of_Global_PV_-_1992-2012_-_FINAL_4.pdf

[11] F. I. for Solar Energy Systems, "Photovoltaics report," *Fraunhofer ISE*, p. 53, 2023.

[12] G. Conibeer, "Third-generation photovoltaics," *Materials today*, vol. 10, no. 11, pp. 42–50, 2007.

[13] B. O'regan and M. Grätzel, "A low-cost, high-efficiency solar cell based on dye-sensitized colloidal tio2 films," *nature*, vol. 353, no. 6346, pp. 737–740, 1991.

[14] C. J. Brabec, "Organic photovoltaics: technology and market," *Solar energy materials and solar cells*, vol. 83, no. 2-3, pp. 273–292, 2004.

[15] H. J. Snaith, "Perovskites: the emergence of a new era for low-cost, high-efficiency solar cells," *The journal of physical chemistry letters*, vol. 4, no. 21, pp. 3623–3630, 2013.

[16] M. Nielsen, "Combining Perovskite with Silicon, Solar Cells Convert More Energy from Sun," Aug. 2021. [Online]. Available: https://publishing.aip.org/publications/latest-content/combining-perovskite-with-silicon-solar-cells-convert-more-energy-from-sun/

[17] "Heliatek - Independent. Green. Future." [Online]. Available: https://www.heliatek.com/de/

[18] N. T. Energy, "Best research-cell efficiency chart," 2023.

[19] G. Di Carlo, A. O. Biroli, F. Tessore, S. Caramori, and M. Pizzotti, "$\beta$-substituted znii porphyrins as dyes for dssc: a possible approach to photovoltaic windows," *Coordination Chemistry Reviews*, vol. 358, pp. 153–177, 2018.

[20] L. Zhu *et al.*, "Single-junction organic solar cells with over 19% efficiency enabled by a refined double-fibril network morphology," *Nature Materials*, vol. 21, no. 6, pp. 656–663, 2022.

[21] J. Wang *et al.*, "Advancing vapor-deposited perovskite solar cells via machine learning," *Journal of Materials Chemistry A*, 2023.

[22] C. J. Brabec *et al.*, "Material strategies to accelerate opv technology toward a gw technology," *Advanced energy materials*, vol. 10, no. 43, p. 2001864, 2020.

[23] D. Sebastián *et al.*, "Dye-sensitized solar cells based on critical raw material-free fe–n–c counter electrodes," *Materials for Renewable and Sustainable Energy*, pp. 1–10, 2023.

[24] L. Wagner *et al.*, "The resource demand of terawatt-scale perovskite tandem photovoltaics," *arXiv preprint arXiv:2306.13375*, 2023.

[25] J. Gong, K. Sumathy, Q. Qiao, and Z. Zhou, "Review on dye-sensitized solar cells (dsscs): Advanced techniques and research trends," *Renewable and Sustainable Energy Reviews*, vol. 68, pp. 234–246, 2017.

[26] F. C. Krebs, J. Fyenbo, and M. Jørgensen, "Product integration of compact roll-to-roll processed polymer solar cell modules: methods and manufacture using flexographic printing, slot-die coating and rotary screen printing," *Journal of Materials Chemistry*, vol. 20, no. 41, pp. 8994–9001, 2010.

[27] D. Beynon *et al.*, "All-printed roll-to-roll perovskite photovoltaics enabled by solution-processed carbon electrode," *Advanced Materials*, vol. 35, no. 16, p. 2208561, 2023.

[28] C. Wöpke *et al.*, "Traps and transport resistance are the next frontiers for stable non-fullerene acceptor solar cells," *Nature communications*, vol. 13, no. 1, p. 3786, 2022.

[29] S. Chen *et al.*, "Stabilizing perovskite-substrate interfaces for high-performance perovskite modules," *Science*, vol. 373, no. 6557, pp. 902–907, 2021.

[30] Y.-H. Wang and D. S.-H. Wong, "Modelling accelerated degradation test and shelf-life prediction of dye-sensitized solar cells with different types of solvents," *Solar Energy*, vol. 118, pp. 600–610, 2015.

[31] M. O. Reese *et al.*, "Consensus stability testing protocols for organic photovoltaic materials and devices," *Solar Energy Materials and Solar Cells*, vol. 95, no. 5, pp. 1253–1267, 2011.

[32] M. V. Khenkin *et al.*, "Consensus statement for stability assessment and reporting for perovskite photovoltaics based on isos procedures," *Nature Energy*, vol. 5, no. 1, pp. 35–49, 2020.

[33] M. Moser, A. Wadsworth, N. Gasparini, and I. McCulloch, "Challenges to the success of commercial organic photovoltaic products," *Advanced Energy Materials*, vol. 11, no. 18, p. 2100056, 2021.

[34] K. Lin and Z. Wang, "Multiscale mechanics and molecular dynamics simulations of the durability of fiber-reinforced polymer composites," *Communications Materials*, vol. 4, no. 1, p. 66, 2023.

[35] B. R. Jagger, S. E. Kochanek, S. Haldar, R. E. Amaro, and A. J. Mulholland, "Multiscale simulation approaches to modeling drug–protein binding," *Current opinion in structural biology*, vol. 61, pp. 213–221, 2020.

[36] J. Nelson, J. J. Kwiatkowski, J. Kirkpatrick, and J. M. Frost, "Modeling charge transport in organic photovoltaic materials," *Accounts of Chemical Research*, vol. 42, no. 11, pp. 1768–1778, 2009.

[37] C. G. Bischak *et al.*, "Origin of reversible photoinduced phase separation in hybrid perovskites," *Nano letters*, vol. 17, no. 2, pp. 1028–1033, 2017.

[38] R. C. MacKenzie, C. G. Shuttle, M. L. Chabinyc, and J. Nelson, "Extracting microscopic device parameters from transient photocurrent measurements of p3ht: Pcbm solar cells," *Advanced Energy Materials*, vol. 2, no. 6, pp. 662–669, 2012.

[39] T. Huld, R. Müller, and A. Gambardella, "A new solar radiation database for estimating pv performance in europe and africa," *Solar Energy*, vol. 86, no. 6, pp. 1803–1815, 2012.

[40] B. A. Nieto-Díaz, A. F. Crossland, and C. Groves, "A levelized cost of energy approach to select and optimise emerging pv technologies: The relative impact of degradation, cost and initial efficiency," *Applied Energy*, vol. 299, p. 117302, 2021.

[41] A. Crossland, K. Scoles, A. Wang, C. Groves, and S. Sun, "Assessment of Electricity Decarbonization Scenarios for New Zealand and Great Britain using a Plant Dispatch and Electrical Energy Storage Modelling Framework," *Energies*, vol. 13, no. 11, p. 2799, Jan. 2020, number: 11 Publisher: Multidisciplinary Digital Publishing Institute. [Online]. Available: https://www.mdpi.com/1996-1073/13/11/2799

# Chapter 2

# Background



## 2.1 Overview

This chapter introduces the array of technologies and systems discussed in this thesis in order to explore the future of photovoltaics. From the photovoltaics themselves, the electrical grid they operate upon, and the light that hits them. Following an introduction as to how these systems interact is important to both the future of photovoltaics, and the world, an explanation of the relevant features of these technologies or systems is given, placing them in a wider context when appropriate. To begin, photovoltaics are discussed generally in their journey from curiosity to main stream technology, how they may further develop, and the conditions they are tested under. As this thesis

is particularly interested in the commercial application of photovoltaics; an overview of solar farms is given; how solar farms interacts with the grid and how this may be modelled, and finally challenges that introducing increasing amounts of renewable generation to the grid may face. Further in this thesis both organic photovoltaics and dye sensitised solar cells are explored at length, therefore their history, operation, and possibilities for commercialisation are discussed. Away from the laboratory, photovoltaics experience a wide arrange of conditions, concentrating on the incident spectrum, the variables effecting this spectrum are explored.

## 2.2 Introduction

Unless carbon emissions are curtailed dramatically the global average temperature will rise [1]. By some accounts a rise in the global average temperature is now near inevitable [2], and irreversible change to the worlds' climate will occur [3]. To diminish this potential rise in global average temperatures to $1.5°C$, carbon equivalent emissions must be cut to net-zero by 2050 [4]. In 2015 the Paris Agreement was signed, legally binding 194 states and the European Union [5]. Limiting the rise in temperature this century to a maximum of $2°C$ [5]. Many states confirmed this commitment with their own legal systems [6, 7].

Within this thesis, net-zero is that defined by the Committee on Climate Change [8] and later amended into the climate change act of 2008 [9]. Namely, net-zero is the reduction of carbon dioxide and other targeted greenhouse gasses, such as methane, nitrous oxide, hydrofluorocarbons, and any other gasses designated a targeted greenhouse gas, to a 100% of that recorded in a baseline year [9]. In the case of the United Kingdom, the baseline year of 1990, and a target of 2050, was chosen. It is worth noting that the detailed definition put forward explicitly states that the goal should be met excluding carbon credits, a method of international carbon offsetting, and including emissions from international aviation and shipping.

Action must be taken for the target to be met. Some reduction in greenhouse gasses may be achieved through societal changes, such as a shift away from high carbon activities or shift in dietary habits [8]. Additional reductions may be achieved through carbon capture and storage [8], however, these technologies are unproven and controversial [10]. Whilst these efforts may reduce net greenhouse gas emissions by 2050, our electricity demands are predicted to double [8]. Not only due to greater use of electricity, but due to the electrification of transport and heating [8]. With this increase in electricity demand, a great deal of the reduction of carbon emissions will therefore come from the move to low carbon energy sources [8].

Whilst these plans are well intended, the actions undertaken are insufficient to meet the goal set out by the Paris Agreement. As can be seen in figure 2.1, the policies and actions of governments worldwide are predicted to see rises in global average temperature of 2.6 to 2.9°$C$ this century.

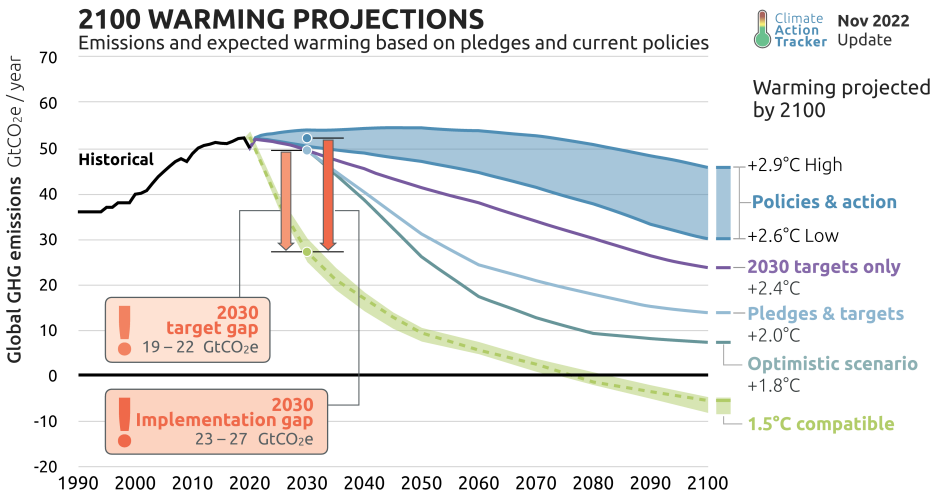


Figure 2.1: Predictions for global average temperature with current policies and actions, compared to that promised by governments [11].

Therefore, more must be done to ensure that we are able to stay as close as possible to our temperature goals. This may be done through a great acceleration in the deployment of low-carbon generation, such as photovoltaics. However, current photovoltaic technologies may not perform ideally to the demands that we place upon them and may suffer in the changing climate we are likely to see. Therefore, we look to future photovoltaic technologies to

better meet our demands and enable better performance under our variable global conditions.

## 2.3 Photovoltaics

Despite their relatively recent widespread adoption, photovoltaics are not a new concept. The photovoltaic effect was first described by Becquerel in 1839, where platinum electrodes submerged in a silver chloride solution when exposed to light generated a voltage and current [12]. However, it was not until 1954 when the first "practical" solar cell was demonstrated. This cell, from Bell labs, utilised silicon, and upon testing reported an efficiency of 6% [13]. Four years later in 1958 the first solar cells entered orbit, powering the Vanguard 1 satellite with a reported efficiency of 10% [14].

### 2.3.1 Solar Cell Operation

Photovoltaics, or solar cells, are devices which upon exposure to light generate both a current and voltage, as described by Becquerel [12]. The photovoltaic will act as a current source, generating a current proportional to the energy of the incident photons, and a voltage will be generated which will drive this current output. However, there is a limit to the voltage a device may generate and an ideal point of current and voltage exist where the power generated is at its maximum. These points may be found through characterisation of the device.

This can be achieved through examining a single characterisation technique known as the Current-Voltage (JV) curve. To perform a JV sweep the device is illuminated, typically by a solar simulator, and an increasing bias voltage is applied to the two terminals of the device under test and the current produced is recorded. As can be seen in figure 2.2. Starting from short circuit conditions until open circuit conditions are achieved.

Firstly, this curve tells us the Short Circuit Current ($J_{SC}$) of the cell, the current that is produced when the cell is effectively shorted, 0V bias between

the two terminals of the device. The $J_{SC}$ is proportional to the number of electron-hole pairs collected from those generated by incident photons, accounting for those lost due to recombination [15]. By increasing the bias voltage, the measured voltage will reach the Maximum Power Point (MPP) of the device, at this point the cell produces its maximum power, and it is where ideally commercial solar cells operate using MPP trackers [15]. Increasing the bias voltage further, the device will reach open circuit conditions and Open Circiut Voltage ($V_{OC}$) will be found. The ideal $V_{OC}$ will match that produced by the effective band gap of the device, however due to losses such as recombination, the found $V_{OC}$ will be lower and reveal the electronic losses found in the device. With these parameters found, the Fill Factor (FF) of the device may be found ratio between the product of the voltage ($V_{MPP}$) and current ($J_{MPP}$) found at the maximum power point, and the product of $V_{OC}$ and $J_{SC}$ of the device showing the influence of both shunt and series resistance upon the cell.

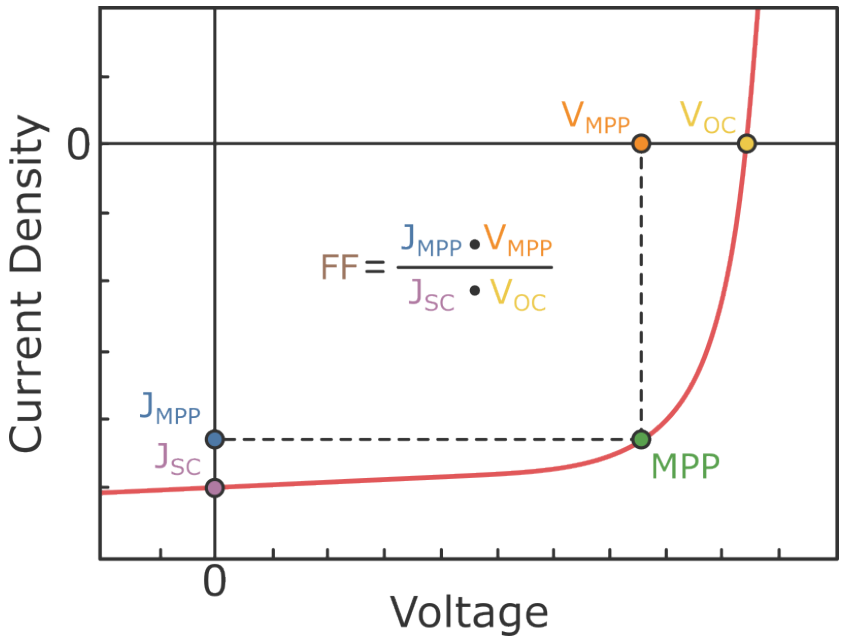


Figure 2.2: Illustration of a JV curve, with $J_{SC}$, $V_{OC}$, FF, and MPP noted.

From these points found by performing the JV curve the Power Conversion Efficiency (PCE) of the device may be found, as can be seen in equation 2.3.1, comparing the power output of the device with that incident upon it,

$P_{in}$.

$$PCE = \frac{P_{max}}{P_{in}} = \frac{J_{MPP} \cdot V_{MPP}}{P_{in}} = FF\frac{J_{sc} \cdot V_{oc}}{P_{in}} \tag{2.3.1}$$

In addition to the JV curve, another useful characterisation which may be undertaken is External Quantum Efficency (EQE), revealing the efficiency of collected charge to incident photons as a function of wavelength ($\lambda$).

### Standard Test Conditions

To ensure the fair comparison of one research cell to another, testing under standard conditions has become a standard throughout all Photovoltaics (PVs) research. When calculating the PCE of the devices, the temperature, spectra, and integrated power are standardised [16]. The current standard, ISO 9845-1, from 1992, describes that the cell must be at a temperature of $25°C$ and exposed to an integrated power of $1000\text{Wm}^{-2}$ using a light source closely matching that described by Air Mass 1.5 Global tilt Refrence Specra (AM1.5G). The AM1.5G spectrum was not derived from measurement, instead it was derived from calculation utilising a radiative transfer model known as Simple Model of the Atmospheric Radiative Transfer of Sunshine (SMARTS) [17]. Working from extraterrestrial irradiance ($AM0$), and the atmospheric composition as described by the US standard atmosphere of 1976 the spectra seen in figure 2.3 were calculated [18]. Points as how the incident spectrum may change away than that represented by AM1.5G will be discussed later in section 2.7.

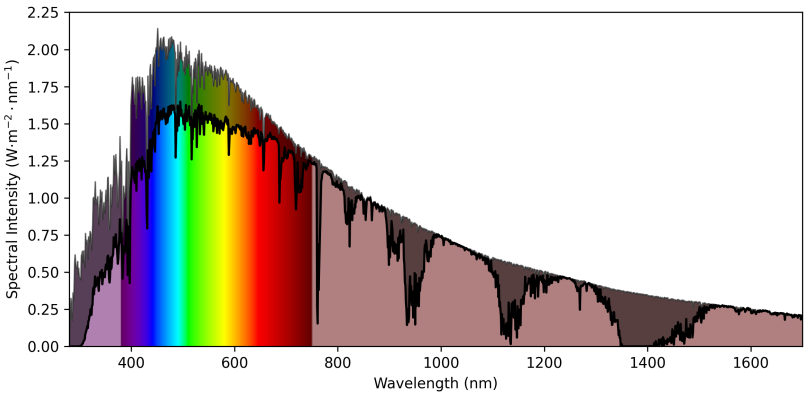


Figure 2.3: AM1.5 and AM0 reference spectra [16]. Where AM0 is shown by the shaded spectra, and AM1.5 is the saturated subsection of AM0.

### 2.3.2 Generations

The development of PVs in research may be split into three "generations". Whilst these generations do not show the distinct changes in the development of the same "family" of devices, generally they show the introduction of new technologies of interest in research. Driven by either the promise of higher efficiencies, or lower costs, as can be seen in figure 2.4 [19]. These generations may be classified in to three areas: thick film, thin film, and emerging PVs. Each of these generations will now be discussed in greater detail.

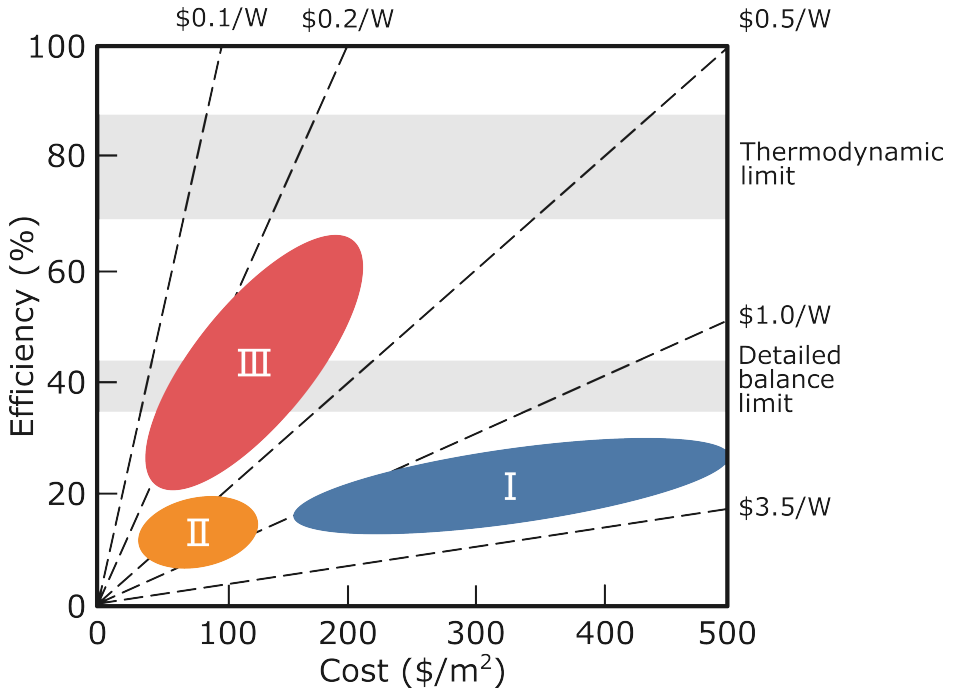


Figure 2.4: Predictions for cost and efficiency as to the PV generations. I: Thick Film, II: Thin film, III: Emerging [19]. It is of note the costs projected here have now been shown to be overestimates for first generation PVs [20].

### $1^{st}$ Generation

The first generation of PV devices, here known as thick film, are those based upon monocrystalline silicon. Despite other devices being previously demonstrated, silicon PVs were the first to be demonstrated as workable for commercial applications. Here, these thick film devices have been named so due to their comparatively thick nature compared to both following generations. Devices of this generation today can be found to have a wafer thickness approximately 280 $\mu m$ [21], compared to the several hundred nanometres of successive generations, both in part due to the manufacturing and properties of silicon. With manufacturing techniques limiting the minimum thickness of the wafer [22], and indirect band gap and low absorption requiring a thick bulk of material [23]. Initial technologies of this generation were monocrystalline silicon, where a single crystal of silicon is grown, through methods such as the Czochralski process [24]. Later polycrystalline silicon cells were demonstrated, in part due to their potential for lower cost, but at the cost

of efficiency [25].

The current champion device of this generation of PVs devices developed by LONGi achieves a PCE of 28.6%, approaching the theoretical limit for silicon of approximately 33% [26]. Architectures like that seen in this champion are complicated and require additional cost to manufacture [27]. Due to this, they are not seen in widespread commercial use, which is predominantly the passivated emitter and rear cell (PERC) architecture, crystalline silicon accounts for 95% of commercial solar cells [21, 20]. The key advantage of this architecture is that both surfaces of the device have been passivated, through the deposition of an oxide layer, reducing the surface recombination of carriers in the cell. This advantage saw the first reported PERC device reach an efficiency of 22.8% an efficiency that is now surpassed by commercially available panels. Commercial panels can now be found with efficiencies of as high as 23.2% [20].

The original motivation for beginning to look at second generation PVs are derived from the key disadvantage of silicon, its indirect band gap, requiring a thick bulk of material [28]. Coupled with the high energy cost of silicon, and its status as a critical raw material means that both the sustainability and availability of silicon PV may be increasingly difficult in future [20, 28]. Allowing for materials with direct band gaps, which are not cheaper thatn silicon on a per gram basis to be explored. Due to the siginifcantly reduced active layer thickness required, cheaper panels may be produced.

It is worth noting that from the 1970s an exponential decline in the cost of first generation PVs has been seen, with average prices of monocrystalline photovoltaics installations declining from 3629 to 725 €/kWp in the past eleven years [20]. This dramatic reduction in cost has seen this generation remain the most deployed PVs across the globe.

### $2^{nd}$ Generation

The second generation of PVs name, thin film PVs, is derived from their comparatively thin nature to the first generation PVs with only several hun-

dred nanometres to single micrometres of bulk is need for the second generation [29, 30, 31]. Unlike the first generation of PV these material systems possess a direct band gap.

The first technology to note are III-V semiconductor PVs, where in which a group III and group V element are both used to form a singular crystalline material. A notable example of which is gallium arsenide (GaAs), which even in the 1970s was demonstrated to achieve efficiencies of 22.2% [32], and with continued development reached a current single junction efficiency of 30.8% [33]. However, due to the high manufacturing cost associated with this technology use of GaAs cells outside specialised applications have not been seen [34].

To overcome this high manufacturing cost, several technologies in this generation have sought to utilised polycrystalline materials, such as copper indium gallium selenide (CIGS) cells, and cadmium telluride (CdTe) cells. Abandoning a crystalline structure entirely amorphous silicon (a-Si), where due to deposition through glow discharge, silicon becomes amorphous [35]. Of these technologies, only CdTe has seen widespread utility scale application [36] with 30 $GW_p$ deployed.

These technologies all have their failings. Amorphous silicon is inherently unstable [37], CIGS cells manufacturing is difficult and therefore high cost [38], CdTe' s use of Cadmium, requires their manufactures to offer extensive recycling programs raising the cost of the devices, beyond their materials and manufacturing [36].

### $3^{rd}$ Generation

The third generation of PVs, were denoted emerging PVs, as at the time of their designation they were emerging fields of research, however, as time goes on this name becomes more of a misnomer as they become more established fields of research [19]. As previously mentioned, the motivation behind this generation is not inherently different to the second, seeking higher efficiencies and at the low costs of the previous generation. The technologies of this

generation which are of interest to this thesis, but are not limited to, Organic Photovoltaics (OPVs), Dye-Sensitised Solar Cells (DSSCs), and hybrid metal-organic halide perovskites solar cells (PSCs).

Of these technologies, the current highest efficiencies among them are reported by PSCs, with the current champion efficiency of 26.1% [39], rising quickly from their first reported efficiency of 14.1% by Park in 2013 [40]. PSCs are a set of materials which share a common crystal structure of $ABX_3$. Where in both A and B are cations of dissimilar sizes, where A's are typically organic cations and B's are usually lead. X in the case of PSCs are halogen anions. The perovskite crystal structure used by the champion device, for example, is formamidinium lead iodide ($FAPb_3I_3$) [41], and another is Methyl Ammonium lead iodide ($CH_3NH_3I_3$) [42]. An initial issue with perovskites is their stability, coupled with the inclusion of lead in their structure, and worries regarding the leaching of toxic lead were raised. This has led to efforts of improving the stability of perovskites [43], which have been seen to be successful in increasing their stability [44], but concerns are still present [45]. Current state of the art perovskite device have been shown to possess T80 lifetimes are in the order of hundreds of hours when exposed to light, an increase of two orders of magnitude from that seen in 2015. [46]. However, when compared to the tens of thousands of hours of Organic Photovoltaic (OPV) this may present a barrier to commercialisation [47]. Additionally efforts to produce lead-free PSCs have been made, the highest efficiencies of these have been achieved by Tin based PSCs at 13.24% which is far from that achieved by the current champion PSC device [48]. Despite these issues commercialisation of lead-based PSC is ongoing with Oxford PV and others, producing tandem PSC-Si devices [49].

DSSCs are the oldest of the emerging categories discussed here [50]. Utilising a photosensitised anode within an electrolyte together with a counter electrode to form a solar cell [50]. From their modern form as reported by Grätzel in 1991, with a 7.1% efficiency [50], the current champion DSSCs achieves an efficiency of 13% [51]. This lower than idea efficiency has seen

the concentration of research upon DSSCs towards novel use cases, such as indoors [52]. DSSCs will be discussed further in section 2.6.

Today OPVs utilise a blend of organic molecules within their active layer to generate bound electron hole pairs, such as the now model system of PM6:Y6 [53]. The current champion OPV device reaches an efficiency of 19.2% [54], rising significantly in the last decade due to the move of the field towards named Non-Fullerene Acceptors (NFAs) rising from 7.4% before their invention [55]. The benefits of OPVs rises from their organic nature, allowing for low-cost synthesis of the molecules themselves [56], and low-cost fabrication due to solution processing [56]. However, they have yet to seen widespread commercialisation, in part due to their lower module efficiency and low lifetimes which require more frequent replacement [57]. OPVs will be discussed in more detail in section 2.5.

The maximal efficiency that is achievable by single junction photovoltaics is defined by the detail balance limit [26]. This limit dependent upon band gap for the AM1.5 spectrum can be seen in figure 2.5. Several device architectures seek to relax the constraints upon devices, to exceed the efficiency defined by the detail balance limit for a single junction. To understand these devices, it is important to understand what energy a photovoltaic may absorb and what energy is lost. Within low band gap devices, if the energy of a photon is higher than the bandgap it may be absorbed, but the excess energy will be lost by thermalisation. However, within high band gap devices, these photons may not be absorbed at all. This boundary between what may be considered a low or high band gap material is dependent upon the incident spectrum, here are the AM1.5 spectrum is considered, Balancing these losses results in the highest efficiency of 33% at a band gap of 1.34eV. As alternative spectra may possess a different distribution of energy within their spectrum a different optimum bandgap may be found. A scenario where this can be seen is in doors due to the mixture of both natural and artificial light seen resulting in an optimal band gap of 1.95eV and maximal efficiency of 45% [58]. However, through considering alternative architectures, coupling

a high and low band gap material together a greater proportion of photons maybe absorbed.

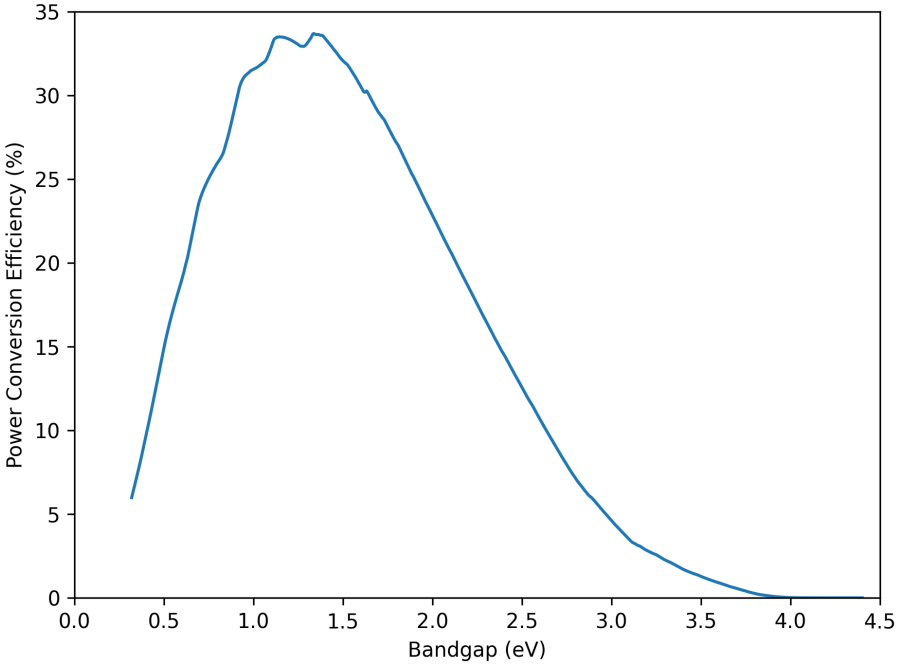


Figure 2.5: Detail Balance Limit for the AM1.5 Spectrum.

Devices which can exceed the detail balance limit are, tandem devices, concentrator, and hot carrier devices. Hot carrier devices attempt to capture the energy lost, when photon energy exceeds the bandgap of the devices, which would usually lead to thermalisation. Investigations into capturing this energy have not progressed beyond demonstration through novel systems utilising metamaterials [59]. Concentrator photovoltaics, utilise optics to concentrate light to a small area where an efficient solar cell may be placed [60]. These may exceed the detail balance limit for AM1.5 as it is dependent upon the intensity of light as well as its source [26]. These cells see continued development in research, however, due to their concentrating nature, challenges arise from temperature management [61]. Lastly is tandem, or multijunction, devices, these employ several active layers of sequential band gaps, each absorbing subsequent wavelengths of the incoming spectrum. Multijunction devices have been explored for decades, although not widely commercialised due to the high cost of their manufacturing, they have seen application in

space. However, with the advent of both OPVs and PSCs, renewed interest has been seen due to their controllable bandgaps [62, 63]. As previously mentioned, tandem PSC-Si devices are sought to be commercialised by Oxford PV as well as others [49].

## 2.4 The Grid

Wide Area Synchronous Grids (WASGs) are critical for modern life in many nations within populous environments, ensuring electrical power is available near continuously [64]. Two parties can act upon WASGs, users, those demanding power from the grid, and suppliers, those generating the supplied power. Ensuring that a balance between the generation and demand is critical for maintaining both the frequency and the voltage of the power. Failure to maintain these may result in blackouts and damage to the property of users and generators [64]. With wide efforts to decarbonise electrical grids, this section will concentrate upon utility scale solar applications and the grid.

### 2.4.1 Solar Farms

From 2012 to 2022 the capacity of solar connected to the British WASGs has grown from 1,474MW to 14,651MW a greater than eight times increase [65, 66]. As silicon solar panels dominate produced capacity, solar farms found within the United Kingdom are likely to be comprised of silicon solar panels [20]. As discussed previously, due to their comparatively low cost and high efficiencies, they are the preferred technology [20]. Additionally, commercial silicon solar panels are guaranteed to effectively maintain at least 80% of their efficiency for a period of 25 years [67].

Other than the panels that are utilised, the key determining factor of the energy yield of a solar farm is the location. Through conducting studies based upon the satellite irradiance measurements, estimations for the solar resources of an area may be calculated [68]. The solar resource of an area may be estimated through averaging the cumulative irradiance that has been

seen over several years. Or in a more complicated fashion by estimating the average yield for each kW of peak installed capacity (kWh/kW$_p$). As can be seen in figure 2.6. Examining databases of commercial solar farms within the United Kingdom, the location of farms was found to preferentially be in areas of high solar resource [69].

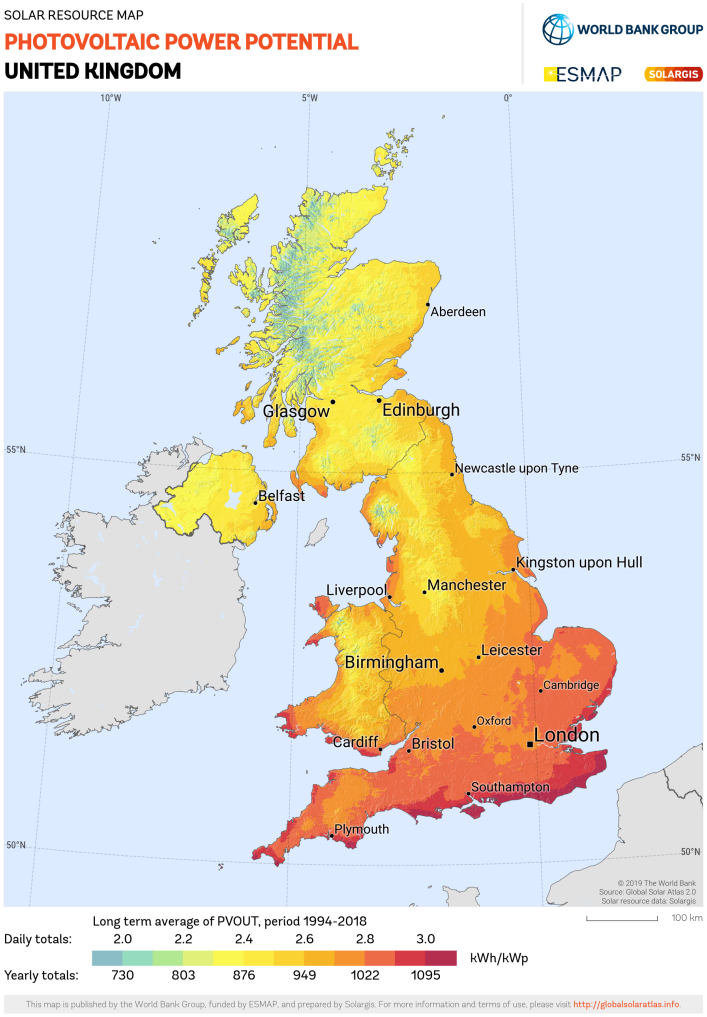


Figure 2.6: Estimations of energy yield for a silicon based solar farm through the United Kingdom, estimated by Global Solar Atlas [70].

However, the chosen location of a solar farm may limit its capacity through factors beyond the technology, capacity, and irradiance of the farm. An additional challenge to solar farms, within the UK, is obtaining a connection to the WASG, due to a lack of infrastructure and information [71]. However, the inverter system may be undersized in comparison to their peak generation

capacity, resulting in the outputted power from the farm being clipped [72]. Therfore, enabling a farm to provide their inverter capacity for a longer period of the day.

Assuming clear sky conditions typically the peak generation of a solar farm, typically noon, may not align with demand which is seen in the morning and afternoon [73]. This mismatch of generation and demand, means that not all power from solar farms is maximally useful. The dependability of the power generated, may be measured by capacity factor, as can be seen in equation 2.4.2.

The capacity factor of an asset may be affected by many factors, such as how easily dispatched the assets is, and variability in generation. Assets which require a long time to be maximally dispatched, such as nuclear, may be utilised continuously providing a base of generation, and hence possess a high capacity factor [74]. Whilst assets which only require a short time to be dispatched maximally, such as hydro, may be used to meet rapid increases in demand and hence a low capacity factor [74]. Serving different purposes within the grid, both important. Within renewable assets, the capacity factor may additionally be affected by the variation in their environmental conditions of interest. Such as wind speed and irradiance in wind and solar assets, respectively. Hence, the capacity factor may serve as a measure of ideality of generation of the asset to demand.

$$Capacity\ Factor = \frac{Measured\ Generation\ (MWh)}{Maximum\ Theoretical\ Generation\ (MWh)} \tag{2.4.2}$$

Within the United Kingdom, solar generation as a whole is found to possess a capacity factor of 11.3% [75]. It is worth noting that the maximum theoretical generation, even for solar generation, assumes continual generation at peak capacity over the entire period examined, leading to lower capacity factors for solar generation. Despite this, the contrasting capacity factors of solar generation in the United Kingdom and California, 11.3% to 24.8% shows that solar generation in the United Kingdom is significantly less useful [75, 76].

### 2.4.2 Wide Area Synchronous Grids

Apart from ensuring the safe transmission of electricity to a wide area, the challenge of WASGs is ensuring the power generation meets the demand placed upon them. This balancing requires significant coordination and planning, and is achieved ultimately by the balancing mechanism.

The balancing mechanism of the mainland UK splits a day in to forty-eight thirty-minute-long windows, called settlement periods. Initially, electricity suppliers may estimate their demand and seek generators to fulfil their predicted demand for each settlement period [77]. This fulfilment may take place years ahead of time, up until an hour prior to the settlement period [77]. In this market, both generators and suppliers are expected to deliver or use the exact amount of energy they contracted, if not penalties are applied [77]. If a supplier failed to meet their demands, or generators were unable to meet theirs. Management through the balancing mechanism is required. During each settlement period, suppliers, or generators my either, offer to increase generation or reduce demand, or bid to reduce generation or increase demand respectively. Suppliers may be able to reduce demand if the needs of their customers are flexible [77]. The Electricity System Operator (ESO) may then accept these bids or offers, depending on what the imbalance of the WASG requirements.

After each settlement periods, meter readings are collected from suppliers and generators, and compared to their contracted volumes. If the meter reading does not match the contracted volume, then energy must either be bought or sold to the grid to match the contracted volumes. In addition to this system, short term operating reserve and interconnects may be used [77]. Interconnects are often used, representing 7.4% of generation in 2022, due to the separate energy markets of the UK and EU price differentials may occur resulting in import becoming more cost-effective [74].

This effort to ensure the continuous operation of the grid has resulted in many models which seek to improve this stability. This may either be through studies as to how demand side management may be implemented

[78, 79] through simulating the power seen by the grid when these methods are implemented, or through examining how the energy of the grid be made less carbon intensive by examine the grid as a numerical balance, by plant dispatch modelling [41]. Plant dispatch modelling will be discussed further in section 3.3.

### 2.4.3 Renewable Generation Sources

With the target for net-zero by 2050 ever approaching, the need to replace generation with low carbon renewable generation sources is ever-growing if we are to meet our goal on time.

To reach net-zero, it is predicted that the penetration of solar generation within the European Union must reach 21% [80]. Globally, predictions see the penetration of solar generation reaching 25% [80]. With these penetrations of highly variable generation sources, it is to be expected that a great increase in energy storage may be needed [80]. Therefore, with today's inherently variable photovoltaics, the additional expense of storage, to counteract their variable nature, is needed. According to the UK's "Smart Systems and Flexibility Plan 2021" states that the UK will need 30GW of low carbon flexible assets by 2050 [81]. Where flexible assets include storage, demand side management, to maintain cost-effective low carbon generation [81]. Of this future capacity, there is expected to be 60GWh of energy that may be stored for at most 4 hours, generating at most 15GW [81]. Flexibility in the energy system is proposed to be driven by storage provided by electric cars, and the consumer becoming more flexible in the way they use energy [81]. The flexibility and storage needed may be able to be reduced through designing renewable generation sources to be less variable as applied to wind turbines [82].

## 2.5 Organic Photovoltaics

OPVs first appear in the ubiquitous National Renewable Energy Laboratory (NREL) Best Research Efficiencies chart in 2001 with a reported efficiency of 2.8% [83]. Through changes in both material systems and architecture, the champion efficiency has today increased to 19.2% [83]. This section will cover the operating principle, development, and state of the art of OPVs, ending with a reflection of the challenges that still face OPVs.

### 2.5.1 Operating Principle

Key to the operation of OPVs are conjugated polymers and small molecules [84, 53]. These conjugated systems formed of alternating single and double bonds cause the delocalisation of electrons from the double bonds, which possess a higher energy than other electrons within the molecule [15]. The existence of these states is equivalent of the conduction and valance band found in the inorganic semiconductors [85]. However, within organic semiconductors these are known as the Lowest Unocupied Molecular Orbital (LUMO) and, Highest Ocupied Molecular Orbital (HOMO) respectively, additionally these states are usually localised [85]. The degree of conjugation within the polymers controls the difference in energy between the HOMO and LUMO, the band gap [85].

Due to the low dielectric constant of organic materials [86], a bound electron-hole pair is formed when a photon of higher energy than the bad gap is incident [84]. This bound electron-hole pair is known as an exciton, and for charges to be extracted the bound pair must be dissociated. To achieve this, dissociation is achieved by utilising two materials with differing electron affinities, where the exciton may dissociate at their interface. The offset must but be greater than the exciton binding energy [84], as depicted in figure 2.7 for dissociation to occur.

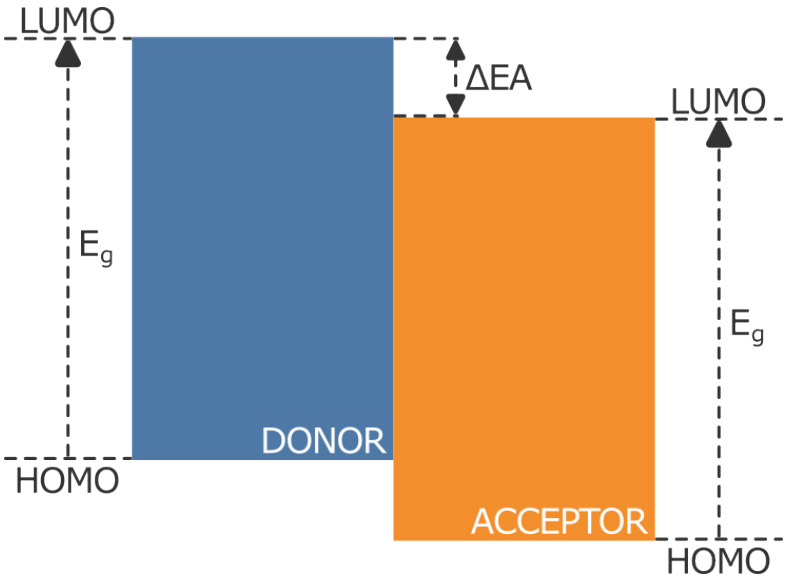


Figure 2.7: Energy diagram of a OPV, where Eg is the Band gap of each respective material, and $\Delta EA$ describes the difference in electron affinity (energetic offset) between the donor and acceptor to overcome the binding energy of the exciton.

These materials are classified as either donor or acceptors, as labelled in figure 2.7, The donor refers to the material which has the highest electron affinity, and the acceptor the lowest electron affinity. When photoexcitation does occur, as illustrated in figure 2.8, excitons must diffuse to the interface between donor and acceptor materials prior to the exciton decaying to the ground state in a process known as exciton recombination. If the excitons do reach the donor acceptor interface, then charge transfer may occur where the exciton becomes an electron and hole.

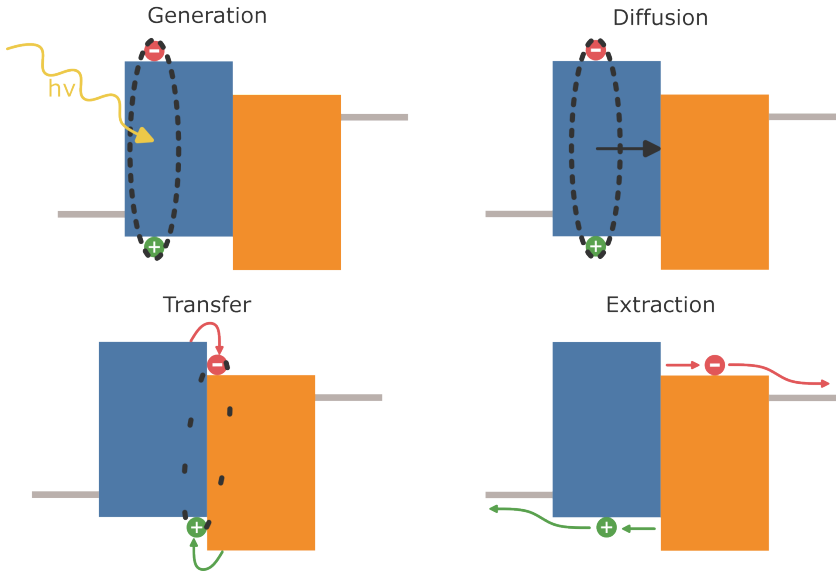


Figure 2.8: Operating principle of organic photovoltaics, from exciton generation, exciton diffusion, charge transfer and carrier extraction.

These free electrons and holes may then drift to their respective electrodes, but not all carriers will be extracted, some carriers will be lost due to geminate or non-geminate recombination. Two forms of non-geminate are of great concern within OPVs, bimolecular and trap assisted recombination. Bimolecular recombination is also known as band-to-band recombination, and it is when charges decay from their free state directly to the ground state [86]. Trap assisted recombination occurs due to the presence of defects within the device, causing an energy state within the band gap of the material, from this state either the carrier may escape the trap or decay back to the ground state. The models which may be used to describe the recombination within OPVs are discussed in more detail in section 3.5 in the context of Drift-Diffusion (DD) modelling.

### 2.5.2 Bilayer to Bulk

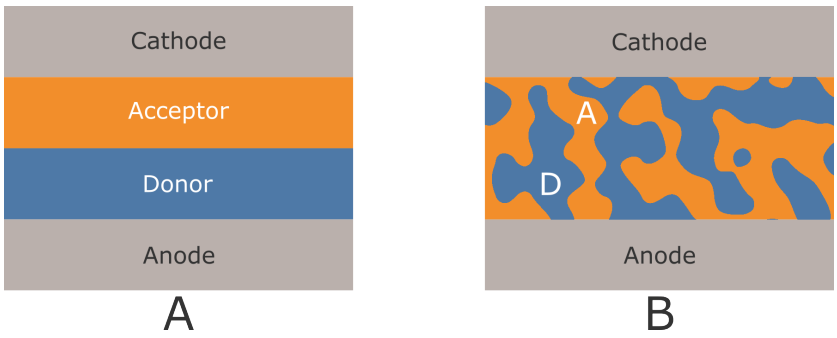


Figure 2.9: A) Bilayer OPV device structure, B) Bulk Heterojunction OPV device structure.

In 1986 Tang suggested the bilayer architecture for OPVs, achieving a PCE of 1% [87]. A great increase from the previously reported single layer OPVs which have been reported [88]. The generated excitons were difficult to split due to the exciton binding energy of 0.1 to 0.5 eV [84]. With the introduction of a secondary material, acceptors, OPVs had arrived at the operating principle as was previously discussed with the bilayer device structure as seen in figure 2.9. However, due to the exciton diffusion length being shorter than the absorption length, excitons would recombine before reaching an interface. With a donor layer thickness of at least 100nm required, due to the short exciton diffusion length only approximately 10nm near the interface was effective at generating free charges [84].

To reduce the exciton recombination, Halls et at. proposed the Bulk Heterojunction (BHJ) [89]. In contrast to the bilayer devices, rather than depositing both the donor and acceptor materials as two distinct layers, both donor and acceptor are blended to form a single bulk layer as is depicted in figure 2.9. When blended separate domains of donor and acceptor materials form, however these domains are found to be in the order of several nanometres [89]. This decrease in domain size from the bilayer device greatly increases the proportion of the total active material where excitons may reach an interface within their lifetimes [84] greatly reducing losses due to exciton recombination. This is the best performing structure that is used in current

state of the art OPV devices [54].

### 2.5.3 Fullerene Acceptors

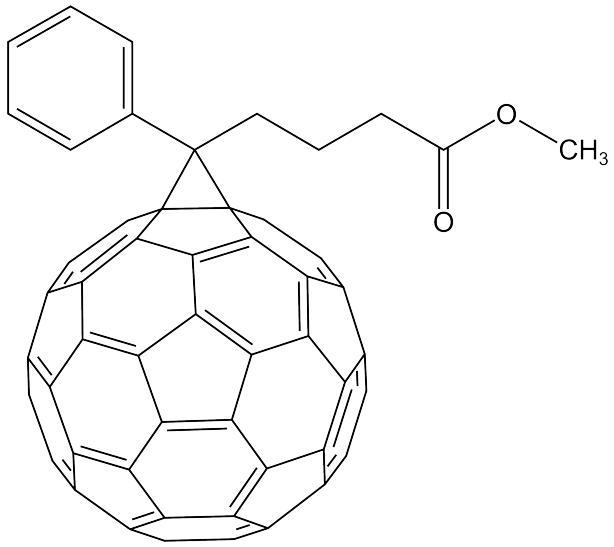


Figure 2.10: Chemical structure of [6,6]-phenyl-$C_{61}$-butyric acid methyl ester (PCBM)

Buckminsterfullerene and its derivatives have seen use in BHJ OPVs since their first demonstration [90]. The eponymous molecule was and is used within photovoltaics, although now it is more widely used as an electron transport layer within perovskites [91, 92]. Fullerene was favoured within OPVs due to its band gap alignment and high electron affinity [90]. For solution processing the derivative of fullerene seen in figure 2.10, [6,6]-phenyl-$C_{61}$-butyric acid methyl ester (PCBM), as was demonstrated in by Yu et al. [90]. The peak efficiency demonstrated by a fullerene acceptor device of 10.8 % was achieved by Liu et al. in 2014 utilising $PC_{71}BM$, which due to its nonspherical shape achieves better absorption [93].

Despite its initially attractive properties, problems were found with fullerene derivatives. Namely, the low PCE achieved by devices in comparison to commercialised technologies such as silicon, who's record efficiency at the time was more than double that achieved by Liu et al. [93, 20]. Additionally, the structure of PCBM, does not lend itself to chemical modification, mean-

ing the band gap of the acceptor could not be easily tuned [94]. Lastly, PCBM based devices were found to be inherently unstable [95], regardless of photo-oxidation [96], and degradation when exposed to water [95], even with perfect encapsulation aggregation was found to occur [95]. Due to this challenge, researchers explored alternatives.

### 2.5.4 Non-Fullerene Acceptors

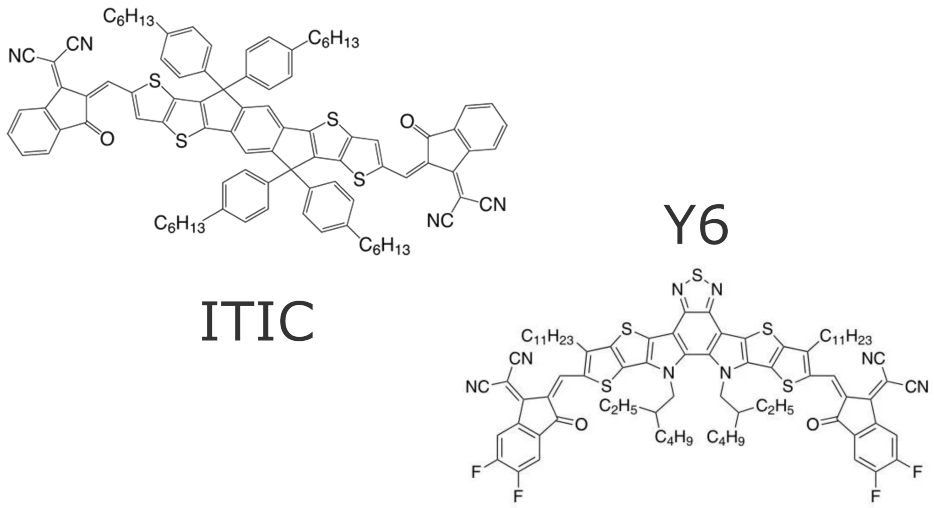


Figure 2.11: Chemical structure of Non-Fullerene Acceptors ITIC and Y6

Generally, molecules utilised for acceptor materials within OPVs that are not fullerene derivatives are known as Non-Fullerene Acceptors (NFAs). These molecules may be more usefully split into categories based upon either the common derivative or motif of the molecules. These may be categories such as Perylene diimide (PDI), Diketopyrrolopyrrole (DPP), or A-D-A-type [97]. In this section and thesis, concentration is upon A-D-A-type NFAs as they currently demonstrate the state-of-the-art efficiencies [54].

A-D-A-type acceptors are constructed of a core of high electron affinity, and two terminal groups of lower electron affinity creating a concentrated backbone within the molecule, or a donor core with two acceptors as terminal groups, this concentrated backbone results in better absorption and higher $J_{SC}$ [97]. This allows for both component molecules to be modified individual,

allowing for the band gap to be finely tuned, as well as other properties [15]. The first molecule which followed this motif were molecules based upon ITIC, and its many derivatives [97], seen in figure 2.11. These molecules were first demonstrated with an efficiency of 6.8% in a PTB7-TH:ITIC blend [98]. From this, various base molecules have been suggested and explored [97]. An advantage of the A-D-A-type acceptors the ease of synthesis of modifications of existing molecules has led to many more molecules than could be discussed within this thesis [97]. One of these which is of note is Y6 seen in figure 2.11, which is often found coupled with PM6 as a donor material [53] and first demonstrated to achieve an efficiency of 14.9% [99]. This has seen a rapid rise in efficiency from first reporting, where a derivative of Y6, L8-BO, currently holds the record efficiency for an OPV with a certified efficiency of 19.2% [54]. This efficiency is achieved due to the morphology that is achieved, which is achievable due to the tuneable nature of the acceptor molecule [54].

Despite these advantages over fullerene, as we see greater PCEs, this has been coupled with a rise in the synthetic complexity of these molecules [100]. The more steps that are required in the synthesis of a material, the more complex it is and the more costly it becomes as the yield reduces [101].

### 2.5.5 Commercialisation

OPVs have yet to see wide commercialisation as seen in silicon-based devices. With lower efficiencies and predicted lifetimes more often measured in hours as opposed to years [102], however, by utilising the inherent advantages of OPVs over silicon based PVs, applications for OPVs may be found which may be commercialised.

Due to their light weight and ability to be placed upon flexible substrates [103], OPVs may be suited to building integrated or building attached applications. Such a product is currently being commercialised by Heliatek [104].

To see utility scale solar farms based upon OPVs the achievable Levelised Cost of Energy (LCOE) of these devices, must be comparable or lower than

that achieved by silicon PV. Studies examining the LCOE of OPVs find that the initial efficiency of devices in not a good indication as to the commercial viability of devices and shows that the then champion OPVs achieves a higher LCOE than silicon PV [57]. Additionally, with the rise in synthetic complexity of the acceptor molecules uncertainty exist about the future cost of OPV materials [56].

## 2.6 Dye-Sensitised Solar Cells

From the first paper by O'Regan and Grätzel discussing modern high efficiency Dye Sensetised Solar Cells (DSSCs) the possibility of DSSCs low cost and easily manufacturable nature has led to many applications to be explored [50]. Through utilising a high surface area sensitised electrode, a certified efficiency of 6.3% was achieved [50]. Additionally, achieving an efficiency of 12% under diffuse daylight [50], due to better alignment of their absorption and diffuse daylight. Today the champion efficiencies have risen slowly since 1991 reaching a certified efficiency of 13% [105].

### 2.6.1 Operating Principle

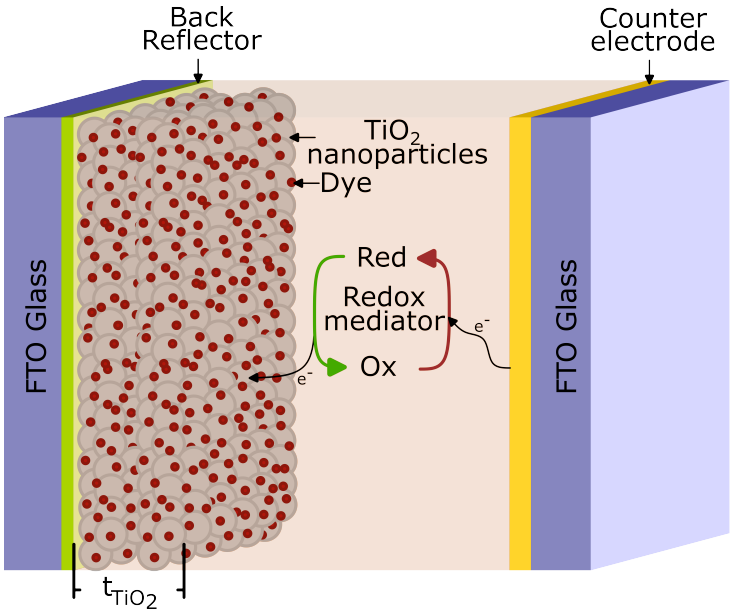


Figure 2.12: Architecture and operating principle of a DSSC.

Presented in figure 2.12 is the architecture of the device later utilised in chapter 4, typical for DSSCs [106]. Sandwiched between two layers of Transparent Conducting Oxide (TCO) coated glass, FTO (Fluorine doped tin-oxide) in the presented architecture, the device is encapsulated [106]. From left to right, first is the back reflector, comprised of a compacted $TiO_2$ enables the reflection and scattering of light to enhance the photoactivation of dye molecules found in the next layer [107]. The following layer is also formed of $TiO_2$, but of a different morphology, here nanoparticles of $TiO_2$ are utilised to form a mesoporous morphology [106].

This mesoporous morphology is utilised to increase the number of photoactive dye molecules which may be absorbed to the layer, this is achieved due to the high surface area of mesoporous morphologies [50]. These dye molecules, generate the charges produced by the device. When photoexcitation does occur, an electron is excited, this electron may then move into the conduction band of the $TiO_2$ electrode leaving behind an oxidised dye molecule.

For this dye molecule to be able to absorb another photon and produce further charges, it must be reduced, to facilitate this reduction an electrolyte is found between the working and counter electrode. This electrolyte in many high efficiency devices is found to be iodide/triiodide [108]. Where iodide reduces the oxidised dye molecules giving up an electron, and forms triiodide.

To be reduced back to iodide the triiodide molecules must diffuse to the counter electrode. At the counter electrode, formed of either sputtered metal such as gold or organic conductive layer such as PEDOT [106], the triiodide may be reduced back to iodide and the cycle of charge generation may repeat.

### 2.6.2 Applications

The better alignment to the spectrum under diffuse sunlight has seen interest in the application of DSSCs where diffuse conditions are expected. Some of these are, in integration into the fabric of a building, thorough building integration [109]. Indoors applications, where the lower light intensity sees high efficiencies reported [110], this can be used to further extend the lifetime of low power wireless sensors. Additionally, the dyes utilised may be tailored to indoor applications [106].

## 2.7 Incident Irradiance

As discussed through this chapter, the light that is incident upon the devices is a critical factor to determining the power they many generate. Efforts to standardise the spectrum used to test solar cell, whilst critical for the development of further efficient solar cells, does not lead directly to devices which can perform well under real world conditions. In this section, the parameters effecting the incident irradiance experienced by a solar cell are explored, as well as how these might change in future.

### 2.7.1 Diurnal

Perhaps obviously, the maximal incident irradiance which may be experienced at a location on earth is determined by the rotation of the earth, both as the earth spins about its axis and as it orbits the sun [111].

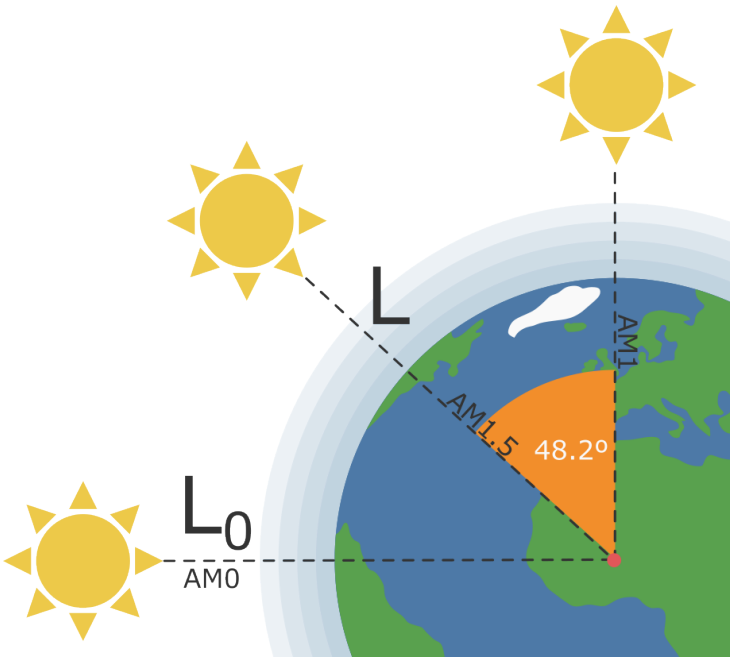


Figure 2.13: Illustration of both L and $L_0$, being the current length of the path to the sun, and the length when the sun is normal to the surface to the earth. AM1.5 is shown to occur when the zenith angle of the sun is approximately 48.2°.

As shown by figure 2.13 and defined by equation 2.7.3 the air mass value of the incident irradiance is the ratio of the path length to the sun in its current position, L, and when normal to the earth, $L_0$. Critically, the higher the Air Mass (AM) value the greater amount of atmosphere the incident light must travel through, and therefore it will experience greater attenuation.

$$AM = \frac{L}{L_0} \tag{2.7.3}$$

Additionally, on an annual basis, due to the tilt of the earth the distance of each hemisphere of the earth gets either closer or further from the sun depending on the time of year [111]. This variation in distance varies the position of the sun in the sky and consequently the angle of the sun in the

sky, and AM values achieved. In each hemisphere respective winter, higher AM values are seen than in summer, leading to reduced irradiance in winter. Shown by figure 2.14 is an illustration of this effect. It is worth nothing that the commonly used AM1.5 is therefore only exactly experienced during a short period of the day.

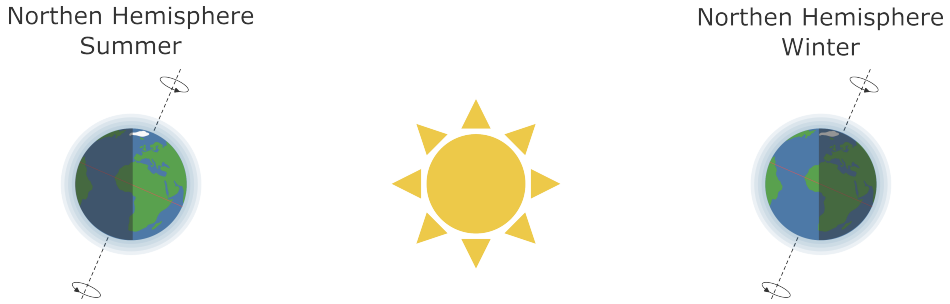


Figure 2.14: Effect of the earths tilt and orbit about the sun upon distance to the sun in at Northern Hemisphere winter and summer.

### 2.7.2 Weather

Whilst the standard test spectrum for solar cells assumes clear sky conditions, may location rarely experience these conditions [112], for example Edinburgh, United Kingdom, only experiences on average of 1427 sunshine hours. Whilst Seville, Spain, experiences 3279 sunshine hours [113]. It is therefore clear the weather must significantly affect the incident irradiance a locality experiences over a year. As global average temperatures are set to rise over the next century [11]. It is expected that extreme weather events are to increase in frequency [114]. These extreme weather events may in some location seen an increase in the experienced sunshine hours, others may see decreases. The application of clear sky conditions therefore becomes more unrepresentative of current real-world conditions. With the significant variation in the conditions a PV device may experience, there is the need to be able to optimise devices for these varied conditions to ensure the maximal performance

### 2.7.3 Pollution

The current standard test spectrum was derived by calculation [18] from data from the US standard atmosphere of 1976 [115]. Since both periods, the atmospheric concentration of gasses has changed due to human influence [116]. Whilst these gasses may be trace gasses within the atmosphere with limited effect to the spectrum [115]. The increase in global average temperature seen due the introduction of these gasses may result in greater periods of localised high pollutant concentrations. These localised events, such as smog, wildfires, and mineral dust storms [117, 118, 119] have been shown to increase the concentration of Particulate Matter (PM) and attenuate incident irradiance [120, 121, 122] driving losses in photovoltaics by studying their effect upon integrated irradiance. However, there is the need for the examination of these effects accounting for the change in spectra seen, allowing for devices to both be modelled and designed for these conditions.

## 2.8 Conclusion

Through examining the literature it has been show that collectively we will miss our targets for limiting the global average temperature rise this century to 2 $°C$ [5] with rises of about 2.6 to 2.9 $°C$ expected with our current policies and actions expected by the end of the century [11]. It is clear that more must be done to meet our targets.

A well explored avenue within renewable energy are photovoltaics, which since their advent have seen many technologies developed [83]. Of particular note are silicon photovoltaics have seen continual development since their advent in the 1950s, and today commercial device reach excellent efficiencies [20]. Despite this very mature technology, there is interest in emerging photovoltaic technologies such as perovskites, organics, and dye sensitised solar cells. Of these technologies, the highest efficiencies are achieved by perovskite solar cells, achieving a record efficiency of 28.6% [39]. However, due to inclusion of lead in their structure, and issues with stability, they are

not explored within this thesis [44, 46]. Instead, concentrating on OPVs and dssc.

Organic photovoltaics have seen a great increase in efficiency in the last ten years, now reaching an record efficiency of 19.2% from 7.4% [83, 55], due to the advent of various non-fullerene acceptors. Wide commercialisation has however not been seen, due to their lower efficiency and lifetime and uncertainty cost [102, 56]. Dye-Sensitised Solar Cells have also seen an increase in efficiency, just to 13% resulting in commercialisation not being pursued widely [105]. Both OPVs and DSSCs have differentiating factors from silicon photovoltaics which could be used to create their own market for commercialisation. Such as the tuneable lightweight nature of opv [15, 103], and the excellent diffuse light performance of DSSCs [50].

The deployment of solar generation within the UK within the last 10 years has seen a great increase from 1,474MW to 14,651MW [65, 66]. This increase is in spite of the poor capacity factor of just 11.3% compared to 24.8% achieved in California [75, 76]. This is due to the misalignment of the generation of the solar assets to electrical demand. Despite this increase more is required in order to decarbonize the electrical network, but in order to achieve this the use of expensive energy storage will be required due to the poor alignment and variability in generation [81]. Lastly, due to our changing climate, and atmosphere, we are likely to see more variation in the light incident upon solar generation assets due to weather or continued pollution [114, 116]. From examining the literature, it can be seen that there are many ways in which emerging photovoltaics may be used in future, as well as questions as to their future which may be explored through the use of multiscale modelling.

# Bibliography

[1] S. Boehm *et al.*, "State of Climate Action 2022," *World Resources Institute*, Oct. 2022. [Online]. Available: https://www.wri.org/research/state-climate-action-2022

[2] M. Allen *et al.*, "Special report: Global warming of 1.5 c," *Intergovernmental Panel on Climate Change (IPCC)*, 2018.

[3] S. Solomon, G.-K. Plattner, R. Knutti, and P. Friedlingstein, "Irreversible climate change due to carbon dioxide emissions," *Proceedings of the national academy of sciences*, vol. 106, no. 6, pp. 1704–1709, 2009.

[4] IEA, "Net Zero by 2050 - A Roadmap for the Global Energy Sector," Paris, Tech. Rep., 2021.

[5] C. A. Horowitz, "Paris agreement," *International Legal Materials*, vol. 55, no. 4, pp. 740–755, 2016.

[6] G. Erbach, "European climate law," *Regulation (EU)*, vol. 1119, 2021.

[7] Joseph R Biden, "Catalyzing Clean Energy Industries and Jobs Through Federal Sustainability," Dec. 2021. [Online]. Available: https://www.govinfo.gov/content/pkg/FR-2021-12-13/pdf/2021-27114.pdf

[8] C. Stark *et al.*, "Net zero: The uk's contribution to stopping global warming," 2019.

[9] "Climate Change Act 2008," Nov. 2008. [Online]. Available: https://www.legislation.gov.uk/ukpga/2008/27/pdfs/ukpga_20080027_en.pdf

[10] V. Scott, S. Gilfillan, N. Markusson, H. Chalmers, and R. S. Haszeldine, "Last chance for carbon capture and storage," *Nature Climate Change*, vol. 3, no. 2, pp. 105–111, 2013.

[11] C. A. Tracker, "Warming projections global update november 2022," 2022.

[12] E. Becquerel, "On electric effects under the influence of solar radiation," *Compt. Rend.*, vol. 9, p. 561, 1839.

[13] D. M. Chapin, C. S. Fuller, and G. L. Pearson, "A new silicon p-n junction photocell for converting solar radiation into electrical power," *Journal of applied physics*, vol. 25, no. 5, pp. 676–677, 1954.

[14] R. L. Easton and M. J. Votaw, "Vanguard I IGY Satellite (1958 Beta)," *Review of Scientific Instruments*, vol. 30, no. 2, pp. 70–75, Feb. 1959. [Online]. Available: https://pubs.aip.org/rsi/article/30/2/70/464408/Vanguard-I-IGY-Satellite-1958-Beta

[15] "Organic Photovoltaic (OPV) Cells | How Organic Solar Cells Work." [Online]. Available: https://www.ossila.com/en-eu/pages/organic-photovoltaics-introduction

[16] R. R. D. Center, "Reference solar spectral irradiance: Astm g-173," *National Renewable Energy Laboratory, Golden, CO, accessed July*, vol. 21, p. 2018, 2009.

[17] F. S. E. Center and C. Gueymard, "Smarts2, a simple model of the atmospheric radiative transfer of sunshine," 1995.

[18] C. A. Gueymard, D. Myers, and K. Emery, "Proposed reference irradiance spectra for solar energy systems testing," *Solar energy*, vol. 73, no. 6, pp. 443–467, 2002.

[19] G. Conibeer, "Third-generation photovoltaics," *Materials today*, vol. 10, no. 11, pp. 42–50, 2007.

[20] F. I. for Solar Energy Systems, "Photovoltaics report," *Fraunhofer ISE*, p. 53, 2023.

[21] A. W. Blakers, A. Wang, A. M. Milne, J. Zhao, and M. A. Green, "22.8% efficient silicon solar cell," *Applied Physics Letters*, vol. 55, no. 13, pp. 1363–1365, 1989.

[22] C. Chen, "Minimum silicon wafer thickness for id wafering," *Journal of The Electrochemical Society*, vol. 129, no. 12, p. 2835, 1982.

[23] K. R. McIntosh, M. J. Cudzinovic, D. D. Smith, W. P. Mulligan, and R. M. Swanson, "The choice of silicon wafer for the production of low-cost rear-contact solar cells," in *3rd World Conference onPhotovoltaic Energy Conversion, 2003. Proceedings of*, vol. 1. IEEE, 2003, pp. 971–974.

[24] R. Uecker, "The historical development of the czochralski method," *Journal of Crystal Growth*, vol. 401, pp. 7–24, 2014.

[25] Y. Yang *et al.*, "Development of high-performance multicrystalline silicon for photovoltaic industry," *Progress in Photovoltaics: Research and Applications*, vol. 23, no. 3, pp. 340–351, 2015.

[26] W. Shockley and H. Queisser, "Detailed balance limit of efficiency of p–n junction solar cells," in *Renewable Energy*. Routledge, 2018, pp. Vol2_35–Vol2_54.

[27] Y. Liu *et al.*, "High-efficiency silicon heterojunction solar cells: materials, devices and applications," *Materials Science and Engineering: R: Reports*, vol. 142, p. 100579, 2020.

[28] "COMMUNICATION FROM THE COMMISSION TO THE EUROPEAN PARLIAMENT, THE COUNCIL, THE EUROPEAN ECONOMIC AND SOCIAL COMMITTEE AND THE COMMITTEE OF THE REGIONS Critical Raw Materials Resilience: Charting a Path towards greater Security and Sustainability," 2020. [Online]. Available: https://eur-lex.europa.eu/legal-content/EN/TXT/?uri=CELEX:52020DC0474

[29] R. C. Knechtli, R. Y. Loo, and G. S. Kamath, "High-efficiency gaas solar cells," *IEEE Transactions on electron devices*, vol. 31, no. 5, pp. 577–588, 1984.

[30] A. Salavei, I. Rimmaudo, F. Piccinelli, and A. Romeo, "Influence of cdte thickness on structural and electrical properties of cdte/cds solar cells," *Thin Solid Films*, vol. 535, pp. 257–260, 2013.

[31] H. Movla, "Optimization of the cigs based thin film solar cells: Numerical simulation and analysis," *Optik*, vol. 125, no. 1, pp. 67–70, 2014.

[32] J. Woodall and H. Hovel, "An isothermal etchback-regrowth method for high-efficiency ga1- x al x as-gaas solar cells," *Applied Physics Letters*, vol. 30, no. 9, pp. 492–493, 1977.

[33] M. A. Green *et al.*, "Solar cell efficiency tables (version 62)," *Progress in Photovoltaics: Research and Applications*, vol. 31, no. 7, pp. 651–663, 2023. [Online]. Available: https://onlinelibrary.wiley.com/doi/abs/10.1002/pip.3726

[34] B. Lee, D. Fan, and S. R. Forrest, "A high throughput, linear molecular beam epitaxy system for reduced cost manufacturing of gaas photovoltaic cells: will gaas ever be inexpensive enough?" *Sustainable Energy & Fuels*, vol. 4, no. 4, pp. 2035–2042, 2020.

[35] D. E. Carlson and C. R. Wronski, "Amorphous silicon solar cell," *Applied Physics Letters*, vol. 28, no. 11, pp. 671–673, 1976.

[36] M. A. Scarpulla *et al.*, "Cdte-based thin film photovoltaics: Recent advances, current challenges and future prospects," *Solar Energy Materials and Solar Cells*, vol. 255, p. 112289, 2023.

[37] D. L. Staebler and C. Wronski, "Reversible conductivity changes in discharge-produced amorphous si," *Applied physics letters*, vol. 31, no. 4, pp. 292–294, 1977.

[38] T. Feurer *et al.*, "Progress in thin film cigs photovoltaics–research and development, manufacturing, and applications," *Progress in Photovoltaics: Research and Applications*, vol. 25, no. 7, pp. 645–667, 2017.

[39] J. Wang *et al.*, "Advancing vapor-deposited perovskite solar cells via machine learning," *Journal of Materials Chemistry A*, 2023.

[40] N.-G. Park, "Organometal perovskite light absorbers toward a 20% efficiency low-cost solid-state mesoscopic solar cell," *The Journal of Physical Chemistry Letters*, vol. 4, no. 15, pp. 2423–2429, 2013.

[41] Y. Tang *et al.*, "Fapbi3 perovskite solar cells: From film morphology regulation to device optimization," *Solar RRL*, vol. 6, no. 6, p. 2200120, 2022.

[42] W. Tress, "Perovskite solar cells on the way to their radiative efficiency limit–insights into a success story of high open-circuit voltage and low recombination," *Advanced Energy Materials*, vol. 7, no. 14, p. 1602358, 2017.

[43] M. V. Khenkin *et al.*, "Consensus statement for stability assessment and reporting for perovskite photovoltaics based on isos procedures," *Nature Energy*, vol. 5, no. 1, pp. 35–49, 2020.

[44] F. A. Roghabadi *et al.*, "Stability progress of perovskite solar cells dependent on the crystalline structure: From 3d abx 3 to 2d ruddlesden–popper perovskite absorbers," *Journal of Materials Chemistry A*, vol. 7, no. 11, pp. 5898–5933, 2019.

[45] J. Dou, Y. Bai, and Q. Chen, "Challenges of lead leakage in perovskite solar cells," *Materials Chemistry Frontiers*, vol. 6, no. 19, pp. 2779–2789, 2022.

[46] H. Zhu *et al.*, "Long-term operating stability in perovskite photovoltaics," *Nature Reviews Materials*, vol. 8, no. 9, pp. 569–586, 2023.

[47] J. Luke, E. J. Yang, C. Labanti, S. Y. Park, and J.-S. Kim, "Key molecular perspectives for high stability in organic photovoltaics," *Nature Reviews Materials*, vol. 8, no. 12, pp. 839–852, 2023.

[48] M. A. Kamarudin *et al.*, "Suppression of charge carrier recombination in lead-free tin halide perovskite via lewis base post-treatment," *The journal of physical chemistry letters*, vol. 10, no. 17, pp. 5277–5283, 2019.

[49] M. Nielsen, "Combining Perovskite with Silicon, Solar Cells Convert More Energy from Sun," Aug. 2021. [Online]. Available: https://publishing.aip.org/publications/latest-content/combining-perovskite-with-silicon-solar-cells-convert-more-energy-from-sun/

[50] B. O'regan and M. Grätzel, "A low-cost, high-efficiency solar cell based on dye-sensitized colloidal tio2 films," *nature*, vol. 353, no. 6346, pp. 737–740, 1991.

[51] D. Zhang *et al.*, "A molecular photosensitizer achieves a v oc of 1.24 v enabling highly efficient and stable dye-sensitized solar cells with copper (ii/i)-based electrolyte," *Nature communications*, vol. 12, no. 1, p. 1777, 2021.

[52] M. Freitag *et al.*, "Dye-sensitized solar cells for efficient power generation under ambient lighting," *Nature Photonics*, vol. 11, no. 6, pp. 372–378, 2017.

[53] S. Shoaee *et al.*, "What we have learnt from pm6: Y6," *Advanced Materials*, p. 2302005, 2023.

[54] L. Zhu *et al.*, "Single-junction organic solar cells with over 19% efficiency enabled by a refined double-fibril network morphology," *Nature Materials*, vol. 21, no. 6, pp. 656–663, 2022.

[55] Y. Liang *et al.*, "For the bright future—bulk heterojunction polymer solar cells with power conversion efficiency of 7.4%," *Advanced materials*, vol. 22, no. 20, pp. E135–E138, 2010.

[56] A. Gambhir, P. Sandwell, and J. Nelson, "The future costs of opv–a bottom-up model of material and manufacturing costs with uncertainty analysis," *Solar Energy Materials and Solar Cells*, vol. 156, pp. 49–58, 2016.

[57] B. A. Nieto-Díaz, A. F. Crossland, and C. Groves, "A levelized cost of energy approach to select and optimise emerging pv technologies: The relative impact of degradation, cost and initial efficiency," *Applied Energy*, vol. 299, p. 117302, 2021.

[58] M. Freunek, M. Freunek, and L. M. Reindl, "Maximum efficiencies of indoor photovoltaic devices," *IEEE Journal of Photovoltaics*, vol. 3, no. 1, pp. 59–64, 2012.

[59] K. K. Paul, J.-H. Kim, and Y. H. Lee, "Hot carrier photovoltaics in van der waals heterostructures," *Nature Reviews Physics*, vol. 3, no. 3, pp. 178–192, 2021.

[60] M. Wiesenfarth, I. Anton, and A. Bett, "Challenges in the design of concentrator photovoltaic (cpv) modules to achieve highest efficiencies," *Applied Physics Reviews*, vol. 5, no. 4, 2018.

[61] N. Gilmore, V. Timchenko, and C. Menictas, "Microchannel cooling of concentrator photovoltaics: A review," *Renewable and Sustainable Energy Reviews*, vol. 90, pp. 1041–1059, 2018.

[62] X. Li *et al.*, "Medium band-gap non-fullerene acceptors based on a benzothiophene donor moiety enabling high-performance indoor organic photovoltaics," *Energy & Environmental Science*, vol. 14, no. 8, pp. 4555–4563, 2021.

[63] D. B. Straus and R. J. Cava, "Tuning the band gap in the halide perovskite cspbbr3 through sr substitution," *ACS Applied Materials & Interfaces*, vol. 14, no. 30, pp. 34 884–34 890, 2022.

[64] National Grid ESO, "National Electricity Transmission System Performance Report," Tech. Rep., 2022. [Online]. Available: https://www.nationalgrideso.com/document/267701/download

[65] Iain MacLeay, Kevin Harris, and Anwar Annut, "Digest of United Kingdom Energy Statistics," Department of Energy & Climate Change, London, Tech. Rep., 2014. [Online]. Available: https://assets.publishing.service.gov.uk/media/5a7eca94e5274a2e87db1eea/DUKES_2014_printed.pdf

[66] Kevin Harris *et al.*, "Digest of United Kingdom Energy Statistics," Department for Energy Security & Net Zero, London, Tech. Rep., Jul. 2023. [Online]. Available: https://assets.publishing.service.gov.uk/government/uploads/system/uploads/attachment_data/file/1182229/DUKES_2023_Chapters_1-7.pdf

[67] J. Kettle *et al.*, "Review of technology specific degradation in crystalline silicon, cadmium telluride, copper indium gallium selenide, dye sensitised, organic and perovskite solar cells in photovoltaic modules: Understanding how reliability improvements in mature technologies can enhance emerging technologies," *Progress in Photovoltaics: Research and Applications*, vol. 30, no. 12, pp. 1365–1392, 2022.

[68] T. Huld, R. Müller, and A. Gambardella, "A new solar radiation database for estimating pv performance in europe and africa," *Solar energy*, vol. 86, no. 6, pp. 1803–1815, 2012.

[69] "Solar photovoltaics deployment," Department for Energy Security & Net Zero, London, Tech. Rep., Oct. 2023. [Online]. Available: https://www.gov.uk/government/statistics/solar-photovoltaics-deployment

[70] G. S. Atlas, "The world bank group," 2023.

[71] Felicia Rankl, "Planning for solar farms," House of Commons Library, London, Tech. Rep., Aug. 2023. [Online]. Available: https://researchbriefings.files.parliament.uk/documents/CBP-7434/CBP-7434.pdf

[72] J. Fiorelli and M. Zuercher-Martinson, "How oversizing your array-to-inverter ratio can improve solar-power system performance," *Solar Power World*, vol. 7, no. 7, pp. 42–48, 2013.

[73] D. Tong *et al.*, "Geophysical constraints on the reliability of solar and wind power worldwide," *Nature communications*, vol. 12, no. 1, p. 6146, 2021.

[74] D. of Energy Security and D. o. B. E. . I. S. Net Zero, "Digest of UK Energy Statistics (DUKES)," Aug. 2022. [Online]. Available: https://www.gov.uk/government/collections/digest-of-uk-energy-statistics-dukes

[75] Kevin Harris *et al.*, "Energy Trends," Department for Energy Security & Net Zero, London, Tech. Rep., Sep. 2023.

[76] M. Bolinger and J. Seel, "Utility-Scale Solar: Empirical Trends in Project Technology, Cost, Performance, and PPA Pricing in the United States – 2018 Edition," Tech. Rep. 1477381, Sep. 2018. [Online]. Available: http://www.osti.gov/servlets/purl/1477381/

[77] "The Electricity Trading Arrangements A Beginner's Guide," ELEXON, Tech. Rep., Feb. 2019.

[78] D. Li, W.-Y. Chiu, H. Sun, and H. V. Poor, "Multiobjective optimization for demand side management program in smart grid," *IEEE Transactions on Industrial Informatics*, vol. 14, no. 4, pp. 1482–1490, 2017.

[79] H. Thomas, H. Sun, and B. Kazemtabrizi, "Calculating the maximum penetration of electric vehicles in distribution networks with renewable energy and v2g," in *2023 IEEE PES Conference on Innovative Smart Grid Technologies-Middle East (ISGT Middle East)*. IEEE, 2023, pp. 1–5.

[80] IRENA, "Future of Solar Photovoltaics: Deployment, investment, technology, grid intergration and socio-economic aspects," International Renewable Energy Agency, Abu Dhabi, Tech. Rep., 2019. [Online]. Available: https://www.irena.org/-/media/Files/IRENA/Agency/Publication/2019/Nov/IRENA_Future_of_Solar_PV_2019.pdf

[81] "Transitioning to a net zero energy system: Smart Systems and Flexibility Plan 2021," 2021.

[82] M. Trenkel-Lopez and P. Matthews, "Method for designing a high capacity factor wide area virtual wind farm," *IET Renewable Power Generation*, vol. 12, no. 3, pp. 351–358, 2018.

[83] N. T. Energy, "Best research-cell efficiency chart," 2023.

[84] C. J. Brabec *et al.*, "Polymer–fullerene bulk-heterojunction solar cells," *Advanced Materials*, vol. 22, no. 34, pp. 3839–3856, 2010.

[85] B. Kippelen and J.-L. Brédas, "Organic photovoltaics," *Energy & Environmental Science*, vol. 2, no. 3, pp. 251–261, 2009.

[86] K. M. Pelzer and S. B. Darling, "Charge generation in organic photovoltaics: a review of theory and computation," *Molecular Systems Design & Engineering*, vol. 1, no. 1, pp. 10–24, 2016.

[87] C. W. Tang, "Two-layer organic photovoltaic cell," *Applied physics letters*, vol. 48, no. 2, pp. 183–185, 1986.

[88] R. Marks, J. Halls, D. Bradley, R. Friend, and A. Holmes, "The photovoltaic response in poly (p-phenylene vinylene) thin-film devices," *Journal of Physics: Condensed Matter*, vol. 6, no. 7, p. 1379, 1994.

[89] J. Halls *et al.*, "Efficient photodiodes from interpenetrating polymer networks," *Nature*, vol. 376, no. 6540, pp. 498–500, 1995.

[90] G. Yu, J. Gao, J. C. Hummelen, F. Wudl, and A. J. Heeger, "Polymer photovoltaic cells: enhanced efficiencies via a network of internal donor-acceptor heterojunctions," *Science*, vol. 270, no. 5243, pp. 1789–1791, 1995.

[91] K. Wojciechowski *et al.*, "C60 as an efficient n-type compact layer in perovskite solar cells," *The journal of physical chemistry letters*, vol. 6, no. 12, pp. 2399–2405, 2015.

[92] D. Liu *et al.*, "Impact of ultrathin c60 on perovskite photovoltaic devices," *ACS nano*, vol. 12, no. 1, pp. 876–883, 2018.

[93] Y. Liu *et al.*, "Aggregation and morphology control enables multiple cases of high-efficiency polymer solar cells," *Nature communications*, vol. 5, no. 1, p. 5293, 2014.

[94] Y. Lin and X. Zhan, "Non-fullerene acceptors for organic photovoltaics: an emerging horizon," *Materials Horizons*, vol. 1, no. 5, pp. 470–488, 2014.

[95] W. R. Mateker and M. D. McGehee, "Progress in understanding degradation mechanisms and improving stability in organic photovoltaics," *Advanced materials*, vol. 29, no. 10, p. 1603940, 2017.

[96] H. K. H. Lee *et al.*, "The role of fullerenes in the environmental stability of polymer: fullerene solar cells," *Energy & Environmental Science*, vol. 11, no. 2, pp. 417–428, 2018.

[97] Q. He, P. Kafourou, X. Hu, and M. Heeney, "Development of non-fullerene electron acceptors for efficient organic photovoltaics," *SN Applied Sciences*, vol. 4, no. 9, p. 247, 2022.

[98] Y. Lin *et al.*, "An electron acceptor challenging fullerenes for efficient polymer solar cells," *Advanced materials*, vol. 27, no. 7, pp. 1170–1174, 2015.

[99] J. Yuan *et al.*, "Single-junction organic solar cell with over 15% efficiency using fused-ring acceptor with electron-deficient core," *Joule*, vol. 3, no. 4, pp. 1140–1151, 2019.

[100] M. Moser, A. Wadsworth, N. Gasparini, and I. McCulloch, "Challenges to the success of commercial organic photovoltaic products," *Advanced Energy Materials*, vol. 11, no. 18, p. 2100056, 2021.

[101] R. Po, G. Bianchi, C. Carbonera, and A. Pellegrino, ""all that glisters is not gold": an analysis of the synthetic complexity of efficient polymer donors for polymer solar cells," *Macromolecules*, vol. 48, no. 3, pp. 453–461, 2015.

[102] C. J. Brabec *et al.*, "Material strategies to accelerate opv technology toward a gw technology," *Advanced energy materials*, vol. 10, no. 43, p. 2001864, 2020.

[103] L. J. Sutherland, H. C. Weerasinghe, and G. P. Simon, "A review on emerging barrier materials and encapsulation strategies for flexible perovskite and organic photovoltaics," *Advanced Energy Materials*, vol. 11, no. 34, p. 2101383, 2021.

[104] "Heliatek - Independent. Green. Future." [Online]. Available: https://www.heliatek.com/de/

[105] S. Mathew *et al.*, "Dye-sensitized solar cells with 13% efficiency achieved through the molecular engineering of porphyrin sensitizers," *Nature chemistry*, vol. 6, no. 3, pp. 242–247, 2014.

[106] H. Michaels *et al.*, "Dye-sensitized solar cells under ambient light powering machine learning: towards autonomous smart sensors for the

internet of things," *Chemical Science*, vol. 11, no. 11, pp. 2895–2906, 2020.

[107] M. N. Mustafa and Y. Sulaiman, "Review on the effect of compact layers and light scattering layers on the enhancement of dye-sensitized solar cells," *Solar Energy*, vol. 215, pp. 26–43, 2021.

[108] O. I. Francis and A. Ikenna, "Review of dye-sensitized solar cell (dsscs) development," *Natural Science*, vol. 13, no. 12, pp. 496–509, 2021.

[109] G. Di Carlo, A. O. Biroli, F. Tessore, S. Caramori, and M. Pizzotti, "$\beta$-substituted znii porphyrins as dyes for dssc: a possible approach to photovoltaic windows," *Coordination Chemistry Reviews*, vol. 358, pp. 153–177, 2018.

[110] K.-W. Chen, L.-S. Chen, and C.-M. Chen, "Post-treatment of nb 2 o 5 compact layer in dye-sensitized solar cells for low-level lighting applications," *Journal of Materials Science: Materials in Electronics*, vol. 30, pp. 15 105–15 115, 2019.

[111] I. Reda and A. Andreas, "Solar Position Algorithm for Solar Radiation Applications (Revised)," Tech. Rep. NREL/TP-560-34302, 15003974, Jan. 2008. [Online]. Available: http://www.osti.gov/servlets/purl/15003974/

[112] "UK climate averages." [Online]. Available: https://www.metoffice.gov.uk/research/climate/maps-and-data/uk-climate-averages

[113] "NOAA Archive Data." [Online]. Available: https://www.nodc.noaa.gov/archive/arc0216/0253808/1.1/data/0-data/Region-6-WMO-Normals-9120/Spain/CSV/

[114] P. Stott, "How climate change affects extreme weather events," *Science*, vol. 352, no. 6293, pp. 1517–1518, 2016.

[115] U. S. Atmosphere, *US standard atmosphere*. National Oceanic and Atmospheric Administration, 1976.

[116] K. Tørseth *et al.*, "Introduction to the european monitoring and evaluation programme (emep) and observed atmospheric composition change during 1972–2009," *Atmospheric Chemistry and Physics*, vol. 12, no. 12, pp. 5447–5481, 2012.

[117] L. J. Mickley, "A future short of breath? possible effects of climate change on smog," *Environment: Science and Policy for Sustainable Development*, vol. 49, no. 6, pp. 32–43, 2007.

[118] U. N. Environment, "Spreading like Wildfire: The Rising Threat of Extraordinary Landscape Fires," Feb. 2022, section: publications. [Online]. Available: http://www.unep.org/resources/report/spreading-wildfire-rising-threat-extraordinary-landscape-fires

[119] J. F. Kok *et al.*, "Mineral dust aerosol impacts on global climate and climate change," *Nature Reviews Earth & Environment*, vol. 4, no. 2, pp. 71–86, Feb. 2023, number: 2 Publisher: Nature Publishing Group. [Online]. Available: https://www.nature.com/articles/s43017-022-00379-5

[120] A. Masoom *et al.*, "Investigation of the effects of the greek extreme wildfires of august 2021 on air quality and spectral solar irradiance," *Atmospheric Chemistry and Physics*, vol. 23, no. 14, pp. 8487–8514, 2023.

[121] R. Dickerson *et al.*, "The impact of aerosols on solar ultraviolet radiation and photochemical smog," *science*, vol. 278, no. 5339, pp. 827–830, 1997.

[122] P. G. Kosmopoulos *et al.*, "Dust impact on surface solar irradiance assessed with model simulations, satellite observations and ground-based measurements," *Atmospheric Measurement Techniques*, vol. 10, no. 7, pp. 2435–2453, 2017.

# Chapter 3

# Modelling Methods



## 3.1 Introduction

This chapter covers the development of models later used to explore across multiple scales the performance of future photovoltaics. Each model is placed in context of existing literature, highlighting their novelty. From this, a discussion of the operation of each model with outputs of the model briefly outlined.

## 3.2 Multiscale Modelling

The use of a device model to inform Photovoltaic (PV) device development has been widely used in combination with characterisation techniques such as those discussed in section 2.3 [1, 2, 3]. Whilst this illuminates a devices performance under experimental conditions, if commercialised, the degree to which these conditions may be controlled is reduced. No longer are PV operating in isolation, they are under the influence of various systems interacting at various length scales. From the local climate they experience, to the demands placed upon them by electrical grids.

From the perspective of the PV device, as seen in figure 3.1, different length scales both can be explored inwardly to further understand mechanisms of device performance, and outwardly showing how the device interacts with its respective electrical grid and local climate.

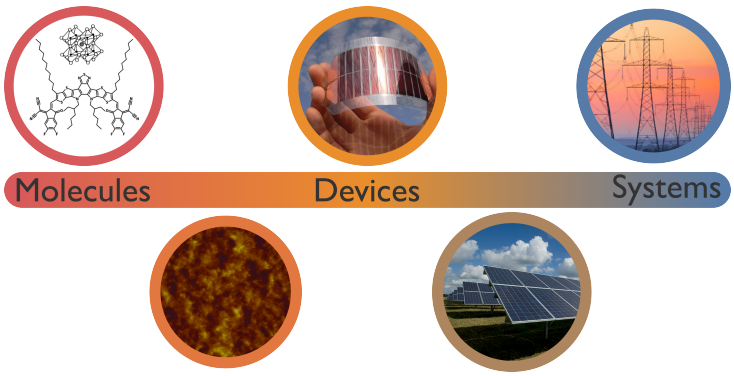


Figure 3.1: The inward and outward looking scales, which may be related to each other using multiscale modelling, from molecules to devices and systems.

Inwardly, the material properties and morphology of the complete device, may be examined [4], further insight of the charge generation and loss processes may be considered [5]. Looking outward, following the path of the energy generated, the implementations of cells with solar farms [6] can be considered, accounting for the local environment [7, 8], yielding both insight to their generation and cost or Levelised Cost of Energy (LCOE). Following the power further, farms of devices may be attached to a Wide Area Synchronous Grid (WASG) where the interaction between energy demands and

the power generated may be studied.

multiscale modelling, the usage of multiple interlinked models at different length scales provides an avenue for a greater level of understanding about the modelled systems to be gathered. Whilst the use of modelling at a single length scale may be a powerful tool for examining a system or device its learnings are limited to the scale of the model, however, with multiscale modelling the effects seen at a small scale may be projected on to a larger scale and vice versa. Therefore to develop and examine how emerging photovoltaics may be applicable in our future multiscale model is required and applied in this work. Allowing for an understanding to be gained for how these systems, both inwardly and outwardly, are coupled, so that future PV may be developed with these systems in mind. Enabling emerging photovoltaics to be developed for factors beyond its own performance, and instead to further enable the performance of the system it finds itself operating in. Previously within emerging photovoltaics, the concentration of multiscale modelling has been upon materials, rather than devices, with devices utilising multiscale modelling to examine charge mobility and recombination [9, 10]. Whilst contributions have been made at the individual length scales of the models, it is important to note the interconnection of these models is also a contribution. Some of the component models of for example the atmospheric composition model, have been interconnected, spectrally for the first time to my knowledge.

## 3.3 Plant Dispatch

Large scale commercial PV developments, solar farms, are attached to WASGs, as discussed in section 2.4. To predict how future PV devices may affect the energy dispatched in these grids, a Plant Dispatch (PD) model was developed. This model underpins the results in chapter 4.

Code for this model is available at: github.com/CaiWilliams/Ryfeddod

### 3.3.1 Introduction

Moving forward, Carbon Dioxide Equivilent ($CO_2e$) emissions emitted to the atmosphere must be curtailed to a net-zero state by 2050, to reduce the expected rise in global average temperatures, to a maximum of $2°C$ this century [11]. One method for reducing the $CO_2e$ emissions is to change our electricity away from non-renewable sources such as coal and gas to renewable sources such as wind and solar. Suggestions for how the global electrical mix may look in future expect the global penetration of PV to reach at least 25% with the International Energy Agency (IEA) predicting increases of up to 36% in their presented scenarios [12, 13]. To enable this increase in penetration, storage is expected to be installed alongside the PVs in conjunction with demand side management, to deal with the inherent intermittency of PVs [12]. However, the costs of such storage systems and demand side management may become prohibitive to further solar penetration [14, 15].

In chapter 4, an alternative approach to the sole reliance upon energy storage and demand side management is presented. Modelling how these PVs perform when they are introduced to their respective WASGs, linking device characteristics to benefits observed at grid level.

To determine the effects of the introduction of such devices to country's WASG we may seek to "replay" historic scenarios. Modified for different generation scenarios using a plant dispatch model replacing the control and balancing mechanisms on an aggregated scale to determine behaviours at a national scale.

Using PD models, multiple alternative scenarios based upon historical aggregated assets may be evaluated. Scenarios may include the removal of existing or introduction of new generation assets, this allowing for the assessment of changes in generation to be assessed in terms of changes to the generation mix, and reduction in annual $CO_2e$. Additionally, the Capacity Factor (CF) may be calculated which is, the ratio between the calculated generation through the PD model against the maximum generation which may have been theoretically achieved.

National electrical energy budgeting tools, which work on the same principles as PD models by balancing the generation and demand, have been developed [16, 17, 18]. However, these models do not capture the temporal variation of energy needs examining annual demand, higher temporal resolutions have been utilising allowing the effect of seasonal variation to be resolved [19, 20, 21]. Others have explored the impact of changes of capacity of assets to examine the effect upon $CO_2e$ reduction [22]. Crossland et al. explored how increased capacity of solar and wind may interact with storage assets with an increase in the penetration of renewable assets in Great Britain and New Zealand [23]. However, these works have not allowed for the introduction of a new class of assets at high temporal resolution, allowing for dinaural variation to be resolved improving estimates of generation. Utilising a multiscale modelling approach, new classes of assets may be introduced whilst accounting for dinaural variation as is shown within this chapter.

Presented here is the development of a PD model, which has been modified from the work of Crossland et al. [23]. The Crossland et al. model has been has been translated into python from excel to allow for quicker and programmatic operation. The model has also been expanded to allow for the integration of novel PV devices in to a WASG through their irradiance-efficiency characteristics, allowing for the integration of new generation assets rather than the reduction or increase of existing assets. This has been achieved through the integration of the Photovoltaic Geographical Information Systems (PVGIS) API. Further, the scope of the model was expanded

from the United Kingdom and New Zealand to the entirety of Europe.

### 3.3.2 Model Operation

The developed PD model splits generation assets found within a WASG into various Dispatch Classs (DCs). In order of carbon intensity and curtailability.

| **Asset Type** | **Capacity** ($MW$) | **Carbon Intensity** ($gCO_2e \cdot kWh^{-1}$) | **Dispatch Class** |
|---|---|---|---|
| Nuclear | 8,981 | 12 | 1 |
| Solar | 11,970 | 48 | 2 |
| Wind Onshore | 8,562 | 11 | 2 |
| Wind Offshore | 5,011 | 12 | 2 |
| Hydro Run-of River and Poundage | 1,540 | 24 | 2 |
| Hydro Pumped Storage | 2,744 | 24 | 3 |
| Fossil Gas | 25,702 | 490 | 4 |
| Fossil Hard Coal | 14,889 | 820 | 4 |

Table 3.1: Asset types, Capacities and Carbon Intensities and assigned Dispatch Classes used to model the WASG of Great Britain in 2016. [24, 25]

Classes are be dispatched from 1 to 4, and intra-DC assets will be dispatched in ascending order of carbon intensity. Each asset within the classes will be dispatched up to the minimum of the remaining demand or the capacity of the asset type at each settlement period. If curtailment or over generation does occur, and storage assets are not at capacity, storage assets will be charged. However, much work is required prior to the operation of the model.

Firstly, data of the chosen countries WASG was gathered. As much of the latter presented results is related to Mainland Great Britain, Balancing Mechanism Reporting Service (BMRS) was utilised for generation data. [26]. Within the European Union, generation data may be gathered from European Network of Transmission System Operators for Electricity (ENTSO-E) transparency platform [27, 28]. Code has been written to parse data from both these respective Application Programming Interfaces (APIs) to common data formats.

The generation of each aggregated asset must be determined. Unfortu-

nately, both BMRS and ENTSO-E have a minimum peak capacity (1 MW), an asset must possess to be counted towards the aggregated generation for the asset type [29]. As the generation capacity of newer technologies may be lower due to perceived risk, leading to smaller capacity investments, the generation reported for these technologies especially PV is underestimated. To resolve this underestimation of generation, data for PV generation for Great Britain was gathered from PV Live, which has no minimum capacity of assets considered. [25]. With these sources, aggregated generation data for each asset type was gathered.

The available generation capacity of each asset type is gathered again from both BMRS and ENTSO-E. Where the generation capacity is the peak generation which could be achieved by the aggregated installations of an asset type. However, to ensure small PV farms were included, a separate source was applied for PV assets. For the capacity of PVs within Great Britain, the Department of Business, Energy & Industrial Strategy (BEIS) Digest of UK Energy Statistics (DUKES) were used [24]. DUKES reports a capacity of 11,970MW, whilst PV live reports marginally slight less at 11,714MW in 2016 [24, 25]. The capacities of the assets used for simulation of 2016 can be seen in table 3.1.

With data on the aggregated generation and capacity of each asset type, these assets are placed in respective DCs. Each DC consists of generation assets, of similar ability to be curtailed and carbon intensity. Carbon intensity values are gathered from the IPCC as shown in table 3.1 [30].

The capacity of the aggregated storage assets found in Great Britain is not available, however the generation capacity of these assets can be found through BMRS. Assuming these assets to be of equal charging and discharge rate, we limit storage assets by its generation capacity at each time step rather than its storage capacity. As in to limit the maximum amount of energy that may be stored and discharged. The storage asset is controlled through equation 3.3.1 and 3.3.2. With equation 3.3.1 controlling the State of Charge (SOC), $SOC(t)$, the net energy. Equation 3.3.2 controllers the

energy discharged from storage assets, $Dis(t)$.

$$SOC(t) = min\left(\left(SOC(t-1) + Curt(t) \times RTE - \frac{Dis(t)}{RTE}\right), Generation\,Capacity\right) \quad (3.3.1)$$

$$Dis(t) = min\left(D(t), \left(SOC(t-1) \times RTE\right), Generation\,Capacity\right) \quad (3.3.2)$$

Both equation 3.3.1 and 3.3.2 measure their respective outputs in MW, and limiting the net flow of energy and the amount which may be discharged respectively to the minimum of their considered terms.

In equation 3.3.1, the SOC at each time step the $SOC(t)$ is set to the minimum of either the maximum generation allowable from the storage assets, or net result of the balance remaining from the previous time step, the energy that was curtailed from the current time step, and that dispatched from storage accounting for round trip efficiency. Equation 3.3.2, sets the discharge of the storage system, $Dis(t)$, to a minimum of the maximum allowable generation capacity, the demand, $D(t)$, seen by the grid, and the continued storage of energy. A flow chart of the dispatch and storage mechanisms can be seen in figure 3.2.

The description of the models' operation has this followed the work of Crossland et al. [23]. However, the model has been expanded to allow for the introduction of novel PV devices to the WASG.

Here, the developed PD model is used as a tool to understand how new PV devices may contribute to national energy mix. To PV devices for which Power Conversion Efficiency (PCE) reduces with irradiance [31], as shown [32, 33]. Whilst PV devices PCE will vary dependent on several environmental conditions, in the first order, the performance of PVs will vary with the incident irradiance experienced. For this purpose, the resolved irradiance was gathered through PVGIS [34]. Where half-hourly values were derived by the midpoint of hourly values, achieving the same time windows

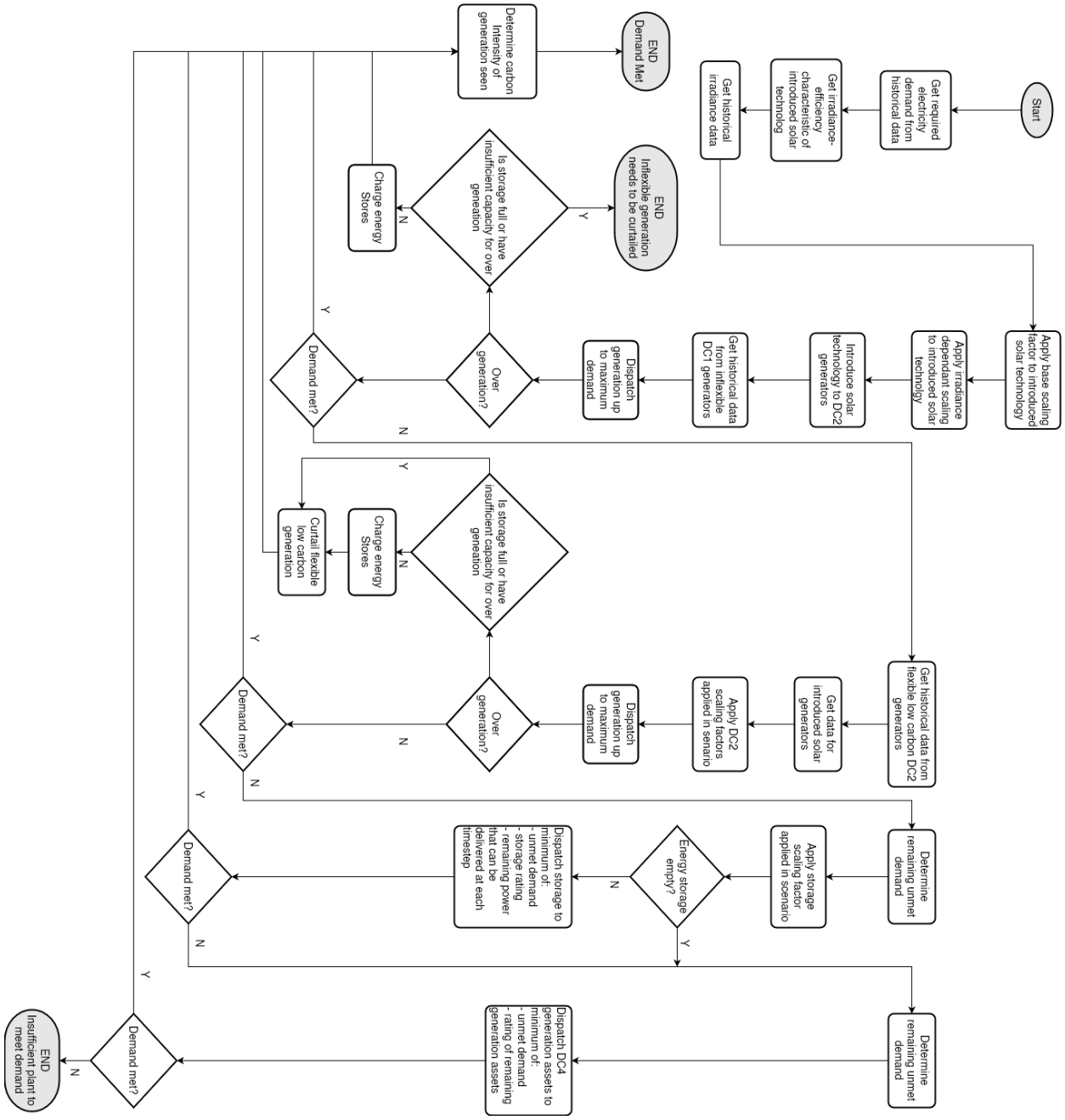


Figure 3.2: Flow chart of the developed PD model.

as BMRS.

With experimental irradiance-PCE characteristics from a representative device, the change in the device performance, or enhancement, may be applied to the PVs installed on the grid in the relevant period. As experimental characteristics are not continuous, linear interpolation is used between experimentally derived values. Thus, the enhancement for each time step may be calculated and applied to the assets peak capacity, as can be seen in equations 3.3.3 and 3.3.4.

$$E(I) = \frac{PCE(I)}{PCE(1000)} \tag{3.3.3}$$

$$C(t) = C_p \times E(I(t)) \tag{3.3.4}$$

Where $E(I)$ is the enhancement of the PCE under irradiance of $I$ relative to is PCE under $1000W^{-2}$. $E(I(t))$ may then be applied to the defined peak capacity ($C_p$) to calculate the capacity at time step $t$ ($C(t)$).

As the PD model utilised aggregated generation, in the ideal case the enhancement would be calculated at each location of each PV farm and then aggregated. However, this is not possible as not all locations are known. Therefore, within the model, the irradiance values used relate to a single location. This is a simplification, as an aggregated asset this may not fully show how devices distributed across the chosen country may perform. A test was carried out, utilising randomly chosen locations assumed to be more representative of actual PV locations than one site, as can be seen in figure 3.3. With the time resolved capacity calculated at each location, the mean of the novel devices at each may be introduced into a dispatch class and performance measures may be calculated. Though it is of note that a random distribution will not match that of solar farms within the UK, as their distribution is expected to be weighted towards areas of high solar resource. From 1 site to 1000, small variation in the performance can be seen, with the greatest change in energy generated from 1 to 2 locations being approxi-

mately 6%. Thus, due to the small variation seen and slight underestimation, a single location was used. This location was latitude: 53.13359 and longitude: -1.746826 a location at the south of the Peak District National Park, as it is about the mean irradiance experienced in the United Kingdom [35].

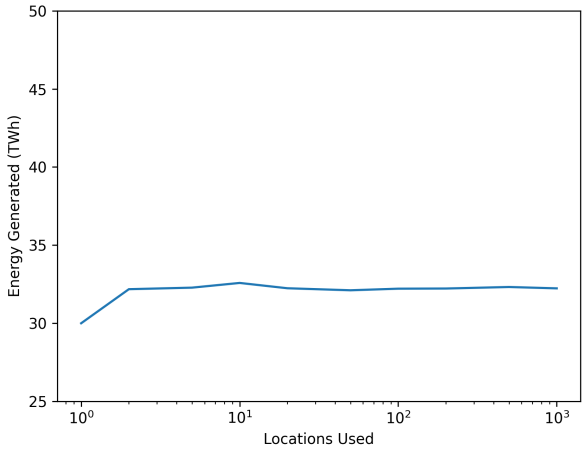


Figure 3.3: Energy generated by introduced solar assets when varying the number of locations used to calculate enhancement data. Locations when greater than 1 were randomly chosen from the land area of Britain and the average enhancement of said locations is used calculated and applied to the model.

The performance measures, which may be calculated from the PD model are CF, $CO_2e$ savings. Further descriptions of these performance measures were given in chapter 2. From these measures, the performance of future PV may be assessed when deployed to a grid. Capacity factor may be calculated by comparing the maximum theoretical generation of a novel class of assets over a 24-hour period, this mean continual maximal generation over a 24-hour period, and comparing it to the generation that was dispatched to the grid by that asset. $CO_2e$ savings may be calculated by multiplying the generation seen by each asset with its respective carbon intensity when novel devices are introduced, and comparing the value calculated to a scenario where traditional solar of equal capacity have been introduced. The difference in carbon emission between these scenarios will result $CO_2e$ in savings due to the introduction of these novel devices. From these measures, the performance of

future PV may be assessed when deployed to a grid.

## 3.4 Genetic Algorithms

Optimisation of multidimensional problems present a complicated problem to solve which though a grid search would take a very long time to find a solution. These multidimensional problems present themselves in studies of PV devices, through optimisation of devices, be it for purposes of PCE, cost, or LCOE. A method of solving these multidimensional problems faster than a grid search is Genetic Algorithums (GAs). To this end, a GA was developed, and used within chapter 6.

Code for this model is available at: github.com/CaiWilliams/GA

### 3.4.1 Introduction

The use of algorithms which use analogies for the operation from the biological processes are not a new phenomenon, Genetic Algorithums (GAs) have been discussed and developed since the advent of modern computing [36, 37]. As computers have become more capable, as have the scope of problems where GAs have been applied [38, 39, 40].

To provide additional context to the algorithm, an illustration of the algorithm can be seen in figure 3.4

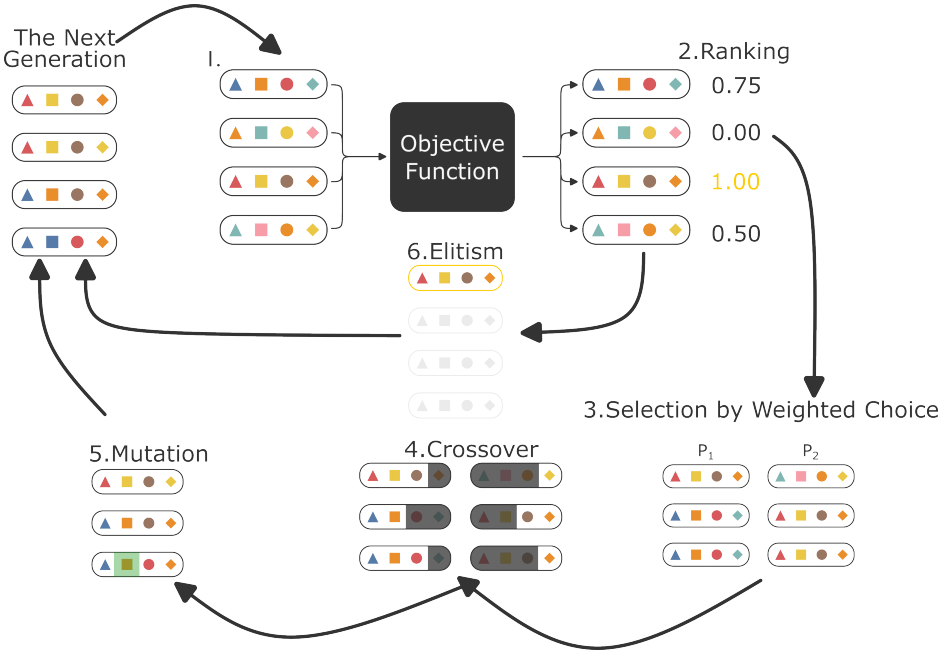


Figure 3.4: Illustrative explanation of the operation of Genetic Algorithum (GA)

GA solves optimisation problems through generating a population, where members hold chromosomes representative of parameters of the optimisation problem. These chromosomes, initially randomly set, are optimised through generations by selecting the highest scoring members. Members are scored by how well they achieve the objective function, which may be to minimise or maximise a parameter controlled by the chromosomes. At each generation, the best are selected to swap and pass on these chromosomes to the next generation. Over generations, the value of these chromosomes is subject to mutation, where their value may be replaced by a new random value, decreasing the likelihood of converging upon a local minimum/maximum. When change to the achieved score of the best member at each generation stagnates, the problem is assumed to be optimised. In the context of PVs, the optimisation problem may represent the PCE and the chromosomes may represent the architecture of the device, the objective function in this case may be a device model from which PCE may be derived. This brings an important point to light, the optimisation found is only a good as the device model applied.

In this presented work, we apply GAs to the multidimensional optimisation of PV design. PVs presents many optimisation problems and GAs have been applied to many of these problems. At the solar farm scale, GA have been applied to optimise the sizing of components, scheduling, and the optimisation of off-grid systems [41, 42, 43], as well as within Maximum Power Point Tracking (MPPT) algorithms [44, 45]. From the laboratory, GAs have been used in material discovery, particularly for Organic Photovoltaics (OPVs), both for both donor and acceptor materials for BHJ devices [46, 47]. However, to our knowledge, GAs have not been applied to the optimisation of Organic Photovoltaics (OPVs) with respect to cost and LCOE. This will be the focus here.

Furthermore, for OPVs, uncertainty exists as to the future cost of OPV materials due to their synthetic complexity, used analogously for cost [48]. When cost is directly estimated it is dependent upon the scale of the industry chosen within the study [49]. Using the developed GA, the effects of material costs have upon the optimal OPV device were explored.

Here the development and operation of the developed GA is presented. The developed GA is a standard GA and is not unique in its operation. However, it is applied for the first time in conjunction with a drift-diffusion model and levelised cost of energy model, for the objective function of PCE, PCE per unit cost, and levelised cost of energy. This results form this can bee seen in chapter 6.

### 3.4.2 Model Operation

Here, the objective function is PCE, and this is to be optimised by device architecture.

Firstly, at point one in figure 3.4, an initial population is generated. Each population member represents an architecture. Each of the member's chromosomes represents the thickness of a layer within the device. The size of the population is required to be large enough to enable a rich set of possible solutions to exist. The size of the population need is dependent upon the

problem, a representative sample is needed within the first generation [50]. At the first generation the chromosomes may be randomly set between appropriate bounds for the optimisation problem.

With the initial population defined, the members may be tested against the chosen objective function. The objective function is a measure of fitness, the algorithm seeks to maximise the chosen objective function. Within the chosen problem, the aim of the algorithm is to improve the architecture of the devices to achieve the maximum fitness, maximum PCE.

Once the objective function has been applied to each member, the population is ranked according to numeric fitness, as shown in point two in figure 3.4. In the chosen problem, this means the devices are ranked by PCE. From this ranking, parents are selected for the next generation based on their fitness. The parents are selected through performing a weighted random choice. The probability of selection decays linearly with the members ordered fitness. This weighted random choice is performed twice, generating two distinct lists of parents. As the selection of parents is random, they are paired by their respective index values. This can be seen in step three in figure 3.4.

To generate the new population members from the respective parents, both crossover and mutation must be performed. Crossover, $C$, defines which chromosomes of one parent takes place of the others. This point is specified by random selection of a chromosome. In context of the chosen problem, this would be taking the top half of layer thicknesses from one device and the bottom half of layer thicknesses from the other. With crossover performed, mutation may now occur, as seen in figure 3.4 at point four. Mutation is not applied to those selected for the next generation through elitism. For each newly generated member of the new population, a random float between zero and one is generated, if the value is below the set mutation rate, $M$, mutation will occur. When mutation occurs, a further random integer is generated between 0 and the number of chromosomes which determines the mutated chromosome, and the selected chromosome is then randomly generated between its respective bounds. This can be seen at point five in

figure 3.4, and in the chosen problem, mutation may result in the thickness of a layer being changed to a random value between the layer's upper and lower bounds.

The number of members selected to be parents may not be equal to the population size. In addition to selecting population members by crossover and mutation, elitism may be applied. Allowing for the best performing, highest fitness, members of the current population to be passed directly to the next generation. As shown in point six in figure 3.4. Elitism ensures that the fitness of the best member of the population will not decrease from one generation to another. In the same vein, the worst performing members may be removed from the population prior to the selection of parents. The number of members subject to each respective operation was simply set as either the top, $P_{best}$, or bottom, $P_{worst}$, percent.

With the newly generated next generation, the described process of the genetic algorithm may be repeated as is seen in figure 3.4 until the exit condition is achieved. The exit condition used for the developed GA is if no improvement is seen in the achieved fitness for the last 10 generations, the optimisation is assumed to be completed. The number of generations may vary depending on the number of chromosomes and objective function. While a minimum may be achieved, it may not be the global minimum, the GA may become stuck within local minima or maxima.

Through the described algorithm, PV devices may be optimised for various objective functions, such as PCE, LCOE, or total device cost, potentially informing how future PVs may be developed.

## 3.5 Drift-Diffusion Modelling

Drift-Diffusion (DD) modelling is a powerful tool for understating the electronic processes within PV devices. Here the DD model used in this work (OghmaNano) is discussed. In chapter 6, the DD model (OghmaNano) is used extensively as an objective function for the calculation of PCE in described GA in section 3.4.

The model is available at: oghma-nano.com

### 3.5.1 Introduction

These models have long since been applied within the field of ordered semiconductors, such as with the works of van Roosbroeck [51], as well as Scharfetter and Gummel [52]. However, with the rise in interest in semiconductor devices based upon disordered materials such as organic polymers, the needs for tools capable of modelling these devices has grown. A key difference between the ordered and disordered materials is the greater number of trap states present within these materials [53].

Methods have been developed to allow for the replication of the recombination rates seen under characterisation experiments. Such as Langevin recombination [54], reliant upon a recombination strength proportional to the mobility of electrons and holes, without explicitly accounting for the presence of traps. Dynamic Shockley-Reed-Hall (SRH) recombination however does, [55, 56] and is thus capable of simulating the device beyond the steady state [57].

Dynamic SRH has been implemented in the DD model used in this work, OghmaNano [58, 59] (previously known as GPVDM) developed by R. MacKenzie and has been widely applied in several publications [60, 61, 62, 63, 64, 65]. In this work, OghmaNano is used in combination with other models to describe the operation of devices of interest.

Here the theory of operation of the drift-diffusion utilised, OghmaNano, is presented, and later the operation of the developed programmatic inter-

face for OghmaNano is presented. The typical operation of OghmaNano is through its graphical user interface. However, for optimisation algorithms such as GA, where many thousands of device simulations are required, using the user interface is impractical. Therefore a programmatic interface was developed, allowing for the properties of the devices and experimental conditions to be modified programmatically. This is used to a great extent in chapter 6.

### 3.5.2 Theory of Operation

The method of solving the drift and diffusion equation is often shown as an iterative process [66], as seen in figure 3.5. The discretisation of the equations will not be presented, in OghmaNano the iterative scheme is not utilised. OghmaNano solves these equations simultaneously, guaranteeing convergence. However, the iterative scheme presents a useful method for understanding the operation of a DD model.

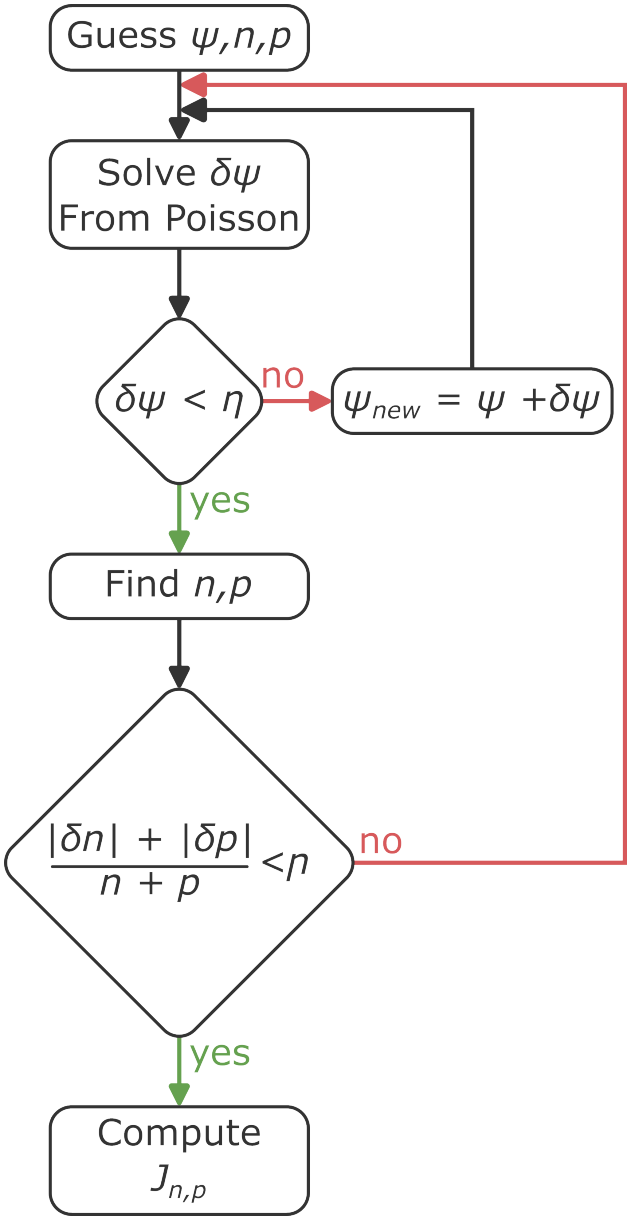


Figure 3.5: Flow diagram of the iterative scheme for the solving of drift-diffusion equations [66].

Before the equations can be solved, each layer of the PV devices and the properties of the material or blend of materials must be defined. whilst the DD model may be applied to the entire device, here it is only applied to the active layer of the device. Within OPVs a blended acceptor and donor material is used within a Bulk Heterojunction (BHJ) as discussed in chapter 2. As the DD model is one dimensional, these two materials are represented through an effective medium, as a singular material. This is achieved through

considering the Lowest Unocupied Molecular Orbital (LUMO) of the effective medium to be the LUMO of the donor, and the Highest Ocupied Molecular Orbital (HOMO) of the effective medium is the HOMO of the acceptor. The difference between these energies leads to the band gap of the effective medium, $Eg$. Within OghmaNano the HOMO and LUMO of the effective medium are defined by equations 3.5.5 and 3.5.6 [67].

$$E_{LUMO} = -\chi \tag{3.5.5}$$

$$E_{HOMO} = -\chi - Eg \tag{3.5.6}$$

Further properties of the effective medium may be defined through characterisation, or through fitting of several characterisations together, these properties are defined in table 3.2.

| **Property** | **Symbol** | **Unit** |
|---|---|---|
| Electron mobility | $\mu_e$ | $m^2V^{-1}s^{-1}$ |
| Hole mobility | $\mu_h$ | $m^2V^{-1}s^{-1}$ |
| Effective density of free electron states (300K) | $N_c$ | $m^{-3}$ |
| Effective density of free holes states (300K) | $N_v$ | $m^{-3}$ |
| Electron trap density | $N_e$ | $m^{-3}eV^{-1}$ |
| Hole trap density | $N_h$ | $m^{-3}eV^{-1}$ |
| Electron tail slope | $E_U^e$ | $eV$ |
| Hole tail slope | $E_U^h$ | $eV$ |
| Free electron to trapped electron | $r_{ec}$ | $m^{-2}$ |
| Trapped electron to free hole | $r_{he}$ | $m^{-2}$ |
| Trapped hole to free electron | $r_{ee}$ | $m^{-2}$ |
| Free hole to trapped hole | $r_{hc}$ | $m^{-2}$ |
| Number of traps | | $bands$ |
| LUMO band edge energy | $\chi$ | $eV$ |
| Band gap | $E_g$ | $eV$ |
| Relative Permeability | $\mu_r$ | $au$ |
| Adsobrsion | $n$ | $au$ |
| Refractive Index | $k$ | |

Table 3.2: Input parameters for the photoactive layer of a PV device modelled in OghamNano.

### Poisson's Equation

With the material system defined, and boundary conditions applied, guesses of the potential, $\psi$, and carrier concentrations, $n$ and $p$ may be put forward as shown in figure 3.5. From these initial guesses, the change in potential through the active layer may be calculated using Poisson's equation. Pois-

son's equation is solved iteratively until the total change in potential is below a set tolerance, $\eta$, for the current distribution of charges. The Poisson's equation used within OghmaNano can be seen in equation 3.5.7.

$$\nabla \cdot \epsilon_0 \epsilon_r \nabla \psi = q \left( n_f + n_t - p_f - n_t \right) \tag{3.5.7}$$

Here $n_f$,$p_f$ are the density of free electrons and hole respectively, whilst $n_t$,$p_t$ are the density of trapped electrons and holes. $\epsilon_0$ is the permittivity of free space, $\epsilon_r$ is relative permittivity, and $q$ is the elementary charge.

The distribution of free charges may then be calculated either through using Fermi-Dirac statistics or the approximation of Maxwell-Boltzmann statistics, the former, as used by OghmaNano can be seen in equations 3.5.8, 3.5.9 [67].

$$n_f \left( E_f, T \right) = \int_{E_{min}}^{\infty} \rho(E) f(E, E_f, T) dE \tag{3.5.8}$$

$$p_f \left( E_f, T \right) = \int_{E_{min}}^{\infty} \rho(E) f(E, E_f, T) dE \tag{3.5.9}$$

Where

$$f(E) = \frac{1}{1 + e^{\frac{E - E_f}{kT}}} \tag{3.5.10}$$

Here $p$ is the density of states, $E$ is the energy of the carrier, $E_f$ is the fermi level, and $T$ is the temperature.

### Continuity Equation and Recombination

With Poisson's equation solved, the generation and recombination of charges may be calculated resolving carrier concentrations for the found potential distribution, through continuity equations. The continuity equation ensure that the conservation of charges is upheld as can be seen in the continuity equation for electrons 3.5.11 and holes 3.5.12.

$$\nabla J_n = q\left(R - G + \frac{\delta n}{\delta t}\right) \tag{3.5.11}$$

$$\nabla J_p = -q\left(R - G + \frac{\delta p}{\delta t}\right) \tag{3.5.12}$$

Where $R$ and $G$ are the net recombination and generation of charges, respectively. Where the generation of charges may be solved through the transfer matrix method [67], here interest is paid to the implementation of recombination. OghmaNano implements dynamic Shockley-Reed-Hall (SRH) recombination describing the rates charges are captured and escape traps, this is illustrated in figure 3.6. When combined, these processes describe the rate of change of trapped holes and electron as seen in equation 3.5.13 [67]. Whose terms are described in table 3.3.

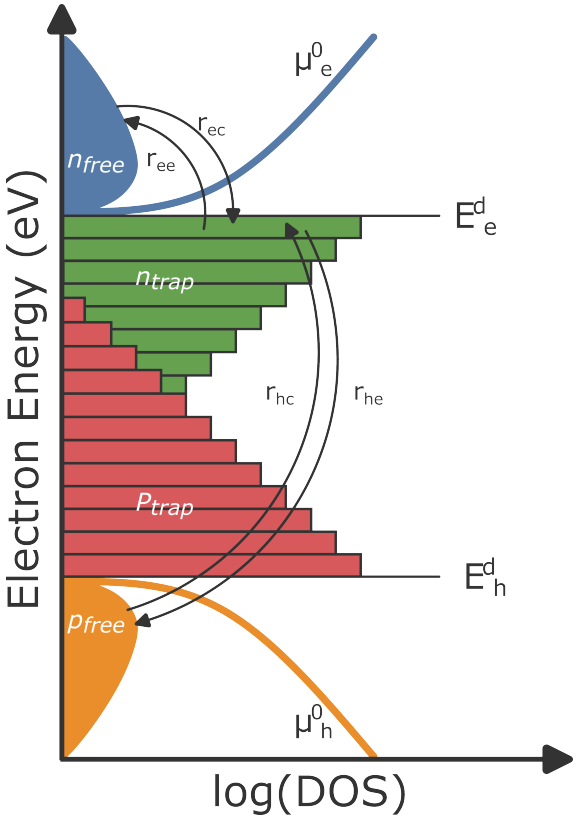


Figure 3.6: Diagram of the dynamic SRH processes [57].

$$\frac{\delta n_t}{\delta t} = r_{ec} - r_{ee} - r_{hc} + r_{he} \tag{3.5.13}$$

| Mechanism | Symbol | Description |
|---|---|---|
| Electron capture rate | $r_{ec}$ | $nv_{th}\sigma_n N_t(1-f)$ |
| Electron escape rate | $r_{ee}$ | $e_n N_t f$ |
| Hole capture rate | $r_{hc}$ | $pv_{th}\sigma_p N_t f$ |
| Hole escape rate | $r_{he}$ | $e_p N_t(1-f)$ |

Table 3.3: Dynamic SRH trap capture and emission rates [67]

In addition to the dynamic SRH implementation, bi-molecular recombination is implemented through equation 3.5.14 [68]. Where $n_0$ and $p_0$ represents the carrier concentrations through the device under equilibrium in dark conditions. The prefactor $k_r$ is defined in equation 3.5.15, where $\alpha$ and $\beta$ are Langevin reductions factors to account for phase segregation within the recombination process.

$$R_{free} = k_r \left(n_f p_f - n_0 p_0\right) \tag{3.5.14}$$

$$k_r = \frac{q\left(\alpha\mu_e(n) + \beta\mu_h(p)\right)}{2\epsilon_0\epsilon_r} \tag{3.5.15}$$

### Carrier Transport

The calculation of potential distribution and carrier concentrations are coupled until the ratio between the change in carrier concentrations and the total carrier concentrations is below a set tolerance. With both coupled equations adequately solved, the current for the electrons and holes due to both drift and diffusion may be solved as can be seen in equation 3.5.16 and 3.5.17 for electrons and holes respectively [67].

$$J_n = q\mu_e n_f \nabla E_c + qD_n \nabla n_f \tag{3.5.16}$$

$$J_p = q\mu_h p_f \nabla E_v - qD_p \nabla p_f \tag{3.5.17}$$

Where the first product represents the drift current, and the latter of diffusion current, yielding the current due to electrons, $J_n$, and $J_p$ holes respectively.

$\nabla E_c$ is the change in energy of the HOMO, and $\nabla E_v$ is the change in energy of the LUMO. Whilst $\nabla n_f$ and $\nabla p_f$ is the change in concentration of free electrons and holes respectively through the device.

Through varying the applied boundary conditions, the simulation of a device can be undertaken. This can take the form of various characterisation experiments, such as Current-Voltage (JV), External Quantum Efficency (EQE) and many transient characterisations.

### 3.5.3 Model Operation

Typical operation of OghamNano is through the user interface. However, to utilise OghmaNano within a GA for device optimisation, where millions of DD simulation are required to reach an optimal solution to the chosen problem, this is not sustainable. A python program was developed to allow for the parsing, modification and running of OghmaNano simulation files.

As the OghmaNano simulation files are archived Java Script Object Notation (JSON) files, the parsing of these files may be completed using python. With a common structure between simulation files, functions for modifying values were written and where appropriate a wrapper function was written to simplify making changes requiring multiple parameter changes, such as the change in temperature. A modified file or files may be now passed to OghamNano's solver (OghmaCore), and results may be saved to disk. This structure efficiently enables the GA to change material and device properties, as well as the operating conditions as the device is under, minimising the time needed to generate and test new devices against the chosen objective function.

This program allows for other models to easily utilise OghmaNano for their simulations, this was often used in combination with the earlier described GA in section 3.4.

## 3.6 Atmospheric Composition Model

Understanding how PV devices are affected by pollution caused by anthropogenic climate change is important to the future PV. Here, a novel diode-based model to predict the influence of the atmosphere on PV generation is described. The described model is utilised in chapter 5.

Code for this model is available at: github.com/CaiWilliams/Sefydlog

### 3.6.1 Introduction

As anthropogenic climate change further changes the climate of the earth, the most notable measure of climate change being the change in global average temperatures and despite our actions now to mitigate our impact, the global average temperature will increase [69]. This increase in temperature will likely see an increase in weather events, such as mineral dust storms [70], landscape fires [71], and a decrease in air quality due to greater stagnation [72]. In common to all these events is they will affect the incident spectrum experienced by PV devices.

Previous studies examining the impacts of weather events upon PVs have been reported [73, 74, 75]. However, these studies treat PV generation as a function dependent upon the temperature of the cell and irradiance only, ignoring the spectral change caused by these weather events.

Understanding how contemporary PV devices are affected by these modified spectra may provide insights as to how future PV devices may be affected when these weather events become more prevalent.

These modified spectra may be modelled through the combination of atmospheric composition data and radiative transfer model with a calculated spectrum. These spectra may be applied to a single diode model using EQE data. From this, the effect of these weather events on PV devices may be examined, and the design of future PV may be altered to be more tolerant of future atmospheres or weather events.

Here the operation of the radiative transfer model utilised, SMARTS, is

presented, and the development of its spectral integration with a single diode model for the first time examining large scale atmospheric events utilizing satellite data. Due to the age of SMARTS measured had to be taken to ensure compatibility with modern operating systems.

### 3.6.2 Model Operation

#### Atmospheric Composition data

The presented model relies upon observed atmospheric data. For our model, these data are gathered from Copernicus Atmosphere Modelling Serivce (CAMS) reanalysis [76] produced by European Center for Medium-Range Weather Forcasts (ECMWF). The CAMS reanalysis presents three-dimensional time consistent data for the atmosphere at 60 pressure levels from 1000 $hPa$ to 1 $hPa$ and in three hourly time steps, with each level being presented with a spatial resolution of 80km. Due to the consistent spatial resolution of the data, they may be rendered as two-dimensional images of concentration. For our complete dataset, both subsections of the CAMS reanalysis are used, the Atmospheric Composition (EAC4) [76] and Green House Gasses (EGG4) [77]. The data gathered from these subsections can be seen in table 3.4. Later, this data will be used as inputs to the radiative transfer model Simple Model of the Atmospheric Radiative Transfer of Sunshine (SMARTS) [78].
To ensure time efficient calculation, only the pressure level of 1000 $hPa$ (sea level) is utilised in SMARTS. Only utilising the sea level measurements assumes uniform concentrations of all gasses within the troposphere. This is a simplification may lead to a more absorbent atmosphere due to the higher estimated concentrations than when the concentration is calculated using each pressure level. However, as the density of air reduces with altitude so does the influence of the atmosphere upon the calculated spectra.

The gas concentrations gathered from CAMS are provided in $kg \cdot kg^{-1}$, however, for our model of the atmosphere they are required in parts per million (ppm). To achieve this conversion, concentrations are first converted

| Component Name | Short Name | Source | Unit | Molar Mass ($g \cdot mol^{-1}$) |
|---|---|---|---|---|
| Carbon Monoxide | CO | EAC4 | $kg{\cdot}kg^{-1}$ | 28.010 |
| Formaldehyde | $CH_2O$ | EAC4 | $kg{\cdot}kg^{-1}$ | 30.026 |
| Nitric Acid | $NHO_3$ | EAC4 | $kg{\cdot}kg^{-1}$ | 63.012 |
| Nitrogen Dioxide | $NO_2$ | EAC4 | $kg{\cdot}kg^{-1}$ | 46.006 |
| Ozone | $O_3$ | EAC4 | $kg{\cdot}kg^{-1}$ | 47.997 |
| Sulphur Dioxide | $SO_2$ | EAC4 | $kg{\cdot}kg^{-1}$ | 64.066 |
| Air Temperature | $T_{air}$ | EAC4 | K | $NA$ |
| Surface Pressure | $P_{Surface}$ | EAC4 | Pa | $NA$ |
| Water Vapour | $H_2O$ | EAC4 | $kg{\cdot}kg^{-1}$ | 18.015 |
| Aerosol Optical Depth | AOD | EAC4 | dimensionless | $NA$ |
| Carbon Dioxide | $CO_2$ | EGG4 | $kg{\cdot}kg^{-1}$ | 44.009 |
| Methane | $CH_4$ | EGG4 | $kg{\cdot}kg^{-1}$ | 16.043 |
| Relative Humidity | RH | EGG4 | % | $NA$ |

Table 3.4: Components used within our model from the CAMS reanalysis. Original units of the data are presented and where appropriate the molar mass of the pollutant is given.

to $mg \cdot m^{-3}$ as in equation 3.6.18

$$C(g \cdot m^{-3}) = C(kg \cdot kg^{-1}) \times (\rho_{air} \times 1) \tag{3.6.18}$$

Where $\rho_{air}$ is the density of air at sea level approximately 1.22 $kg \cdot m^{-3}$. the volumetric concentration may be converted to ppm using equation 3.6.19

$$C(ppm) = C(g \cdot m^{-3}) \times \left(\frac{R \cdot T_{air}}{M}\right) \tag{3.6.19}$$

Where R is the Universal gas constant under sea level conditions ($8.2057E^{-5}$ $m^3 \cdot atm \cdot K^{-1} \cdot mol^{-1}$), T is the air temperature at sea level, and M is the molar mass of the respective constituent.

For each component, at each time step, normalisation between the minimum and maximum value found globally is applied. Each component and time step are saved as images along with their respective minimum and maximum values. The images saved are of 8-bit greyscale images, meaning the normalised values are quantised to 256 levels from 0 to 1. 8 bits are utilised as a high degree of compression is required due to the volume of the raw data sets. To perform denormalization the respective saved minimum and maximum values be applied to each saved pixel. Compressing the data to

256 level means, resolution is lost in the respective unit of the component. However, as normalisation is applied at each time step individually, the impact of this compression is lessened compared to per annum normalisation due to the reduced spread in values.

From these images, values for single points or areas may be read by the atmospheric composition model. When reading a requested longitude and latitude, the nearest pixel is selected. Alternatively, when reading a requested rectangular area, the area is defined by its upper left and lower right corners and their respective longitude and latitude. The nearest pixels to the requested coordinates are selected, and the area read is defined by the area between these found minima and maxima. All interstitial values between the found bounds may be read, but to achieve lower resolution nearest neighbour scaling may be applied. With the pixels selected, their demoralised values may be loaded and passed to the radiative transfer model, here SMARTS was used.

### Radiative Transfer Model

SMARTS written by C. Gueymard [78] was chosen as the radiative transfer model implemented due to its use in deriving the Air Mass 1.5 Global tilt Refrence Specra (AM1.5G) standard spectrum from extraterrestrial spectra [79]. SMARTS is written in Fortran, allows for the rapid calculation of spectra across multiple cores, allowing for long periods of time at high temporal resolutions to be examined. The calculation of a spectrum can take less than half a second. However, as it was developed near the turn of the millennium it is no longer representative of the state of the art for radiative transfer models [79]. Newer models have built upon each other in all aspects in which incident irradiance may be modified by the atmosphere [80]. Despite this, its usage in the definition of AM1.5G which has yet to be updated serves as a mark of confidence in the model [79].

The effects modelled by SMARTS can be split into distinct categories of direct beam and diffuse irradiance. Each of these components of the

global irradiance, have various effects calculated for each component affecting irradiance.

Direct irradiance can be calculated thought the product of the transmittance components and the extraterrestrial spectrum, as can be seen in equation 3.6.20.

$$E_{bn\lambda} = E_{on\lambda}T_{R\lambda}T_{o\lambda}T_{n\lambda}T_{g\lambda}T_{w\lambda}T_{a\lambda} \tag{3.6.20}$$

Where $E_{no\lambda}$ is extraterrestrial spectrum, and the following extinction processes are considered: $T_{R\lambda}$ Reighley scattering, $T_{o\lambda}$ ozone absorbance, $T_{n\lambda}$ $NO_2$ absorbance, $T_{g\lambda}$ mixed gas absorbance, $T_{w\lambda}$ water vapour absorbance, $T_{a\lambda}$ aerosol absorbance [78]. With each of these absorbances calculated from the imputed atmospheric conditions, such as gas concentrations, humidity and aerosol optical depth, the direct irradiance may be found.

To calculate diffuse irradiance, a wider range of factors must be considered, from the diffuse irradiance derived from Reighley scattering ($E_{dR\lambda}$), Aerosols ($E_{da\lambda}$), and backscattering ($E_{db\lambda}$) as seen in equation 3.6.21 [78].

$$E_{d\lambda} = E_{dR\lambda} + E_{da\lambda} + E_{db\lambda} \tag{3.6.21}$$

Combining both the direct and diffuse irradiance components, the whole irradiance experienced upon a horizontal plane relative to earth, $E_\lambda$, may be calculated as in equation 3.6.22 [78]. Where $E_{bn\lambda}$ is the beam irradiance, $Z$ is the sun zenith angle and $E_d$ is the diffuse irradiance.

$$E\lambda = E_{bn\lambda}\cos Z + E_{d\lambda} \tag{3.6.22}$$

For tilted surfaces, additional complexity arises to account for reflected irradiance from the surface's surroundings, as can be seen in equation 3.6.23.

$$E_{s\lambda} = E_{bn\lambda}\cos\vartheta + R_d E_{d\lambda} + \rho'_{g\lambda}R_r E_\lambda \tag{3.6.23}$$

Where $\vartheta$ is the angle of incidence of the direct irradiance on the surface.

$R_d$ and $R_r$ are conversion factors for the diffuse and reflected irradiance, respectively, from the horizontal surface to tilted. Changing the models properties to be weighted towards the isotropic or anisotropic factors dependent upon the zenith angle, the angle of incidence, as well the angle of the tilted surface [78]. Lastly, $\rho'_{g\lambda}$ represents the local reflectance of the ground spectrally, allowing for non-Lambertian reflectance to be accounted for by wavelength [78], allowing for spectral reflectance from a surface.

From this method SMARTS may calculate the spectrally resolved irradiance on a defined plane utilising CAMS reanalysis data for atmospheric composition. This spectrally resolved irradiance may then be passed to a device model, discussed below.

### Single Diode Model

A single diode model was chosen to represent contemporary pv [81]. This choice was made due to the ease of fitting the model, compared to models such as a drift-diffusion model [68], as well as not increasing the complexity of the model as a whole. Whilst a more complicated model may provide more accurate results, this complication may raise more question about the validity of the atmospheric composition model as a whole.

The single diode model represents a PV device using an equivalent circuit, as can be seen in figure 3.7.

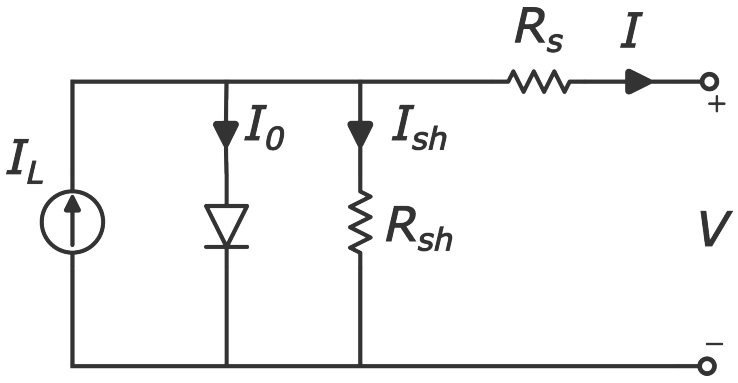


Figure 3.7: Single diode equivalent circuit of a solar cell

The presented equivalent circuit leads equations 3.6.24 and 3.6.25.Through

the Lambert W-function method, a closed-form to these equations was found [82, 83].

$$I = I_L - I_0 \left[ \exp\left( \frac{V + IR_s}{nV_{th}} \right) - 1 \right] - \frac{V + IR_s}{R_s h} \tag{3.6.24}$$

$$V_{th} = \frac{kT_c}{q} \tag{3.6.25}$$

Where $I_L$ represents the photogenerated current of the cell, $I_0$ is the reverse saturation current, $R_s$ is the series resistance and $R_{sh}$ is the shunt resistance, and $n$ is the diode ideality factor. $T_c$ is the cell temperature.

The Lambert W-function, $W(f)$ , is defined as the inverse of the function $f(w) = we^w$) Defining $z$ as seen in equation 3.6.26 allows for Lambert function to be applied in equation 3.6.27.

$$z = \frac{R_s I_0}{nV_t h \left(1 + \frac{R_s}{R_{sh}}\right)} \exp\left( \frac{R_s(I_L + I_0) + V}{nV_t h \left(1 + \frac{R_s}{R_{sh}}\right)} \right) \tag{3.6.26}$$

$$I = \frac{I_L + I_0 - \frac{V}{R_{sh}}}{1 + \frac{R_s}{R_s h}} - \frac{nV_t h}{R_s} W(z) \tag{3.6.27}$$

To solve the equation, the photogenerated current is calculated through integrating the spectrally resolved irradiance from SMARTS with the EQE of a representative device, shown in equation 3.6.28. This model may also be applied to new PV device of differing absorption. Where $S(\lambda)$ is the incident spectrum. From a representative device, the value of the saturation current and diode ideality may also be derived through a combination of both light and dark JVs through linear regression.

$$I_L = \int EQE\,(\lambda) * S\,(\lambda)\,\delta\lambda \tag{3.6.28}$$

With the parameters defined, and the device exposed to the SMARTS derived spectrum, a JV characteristic can be calculated from which the Maximum Power Point (MPP) can be extracted for each instance. The power generated, and other performance measures, may then be output for further

examination.

## 3.7 Levelised Cost of Energy

Here, the development of a LCOE model is discussed, allowing for the comparison of the commercial feasibility of energy projects and PV devices. This model, modified from the work of Nieto-Diaz et al. [35], has been further developed. Allowing for the automatic calculation of the cost of energy of utility scale solar farm projects at an hourly timescale accounting for environmental conditions. This model if later coupled with the GA in chapter 6.

Code for this model is available at: github.com/CaiWilliams/Trindod

### 3.7.1 Introduction

Due to the large scale of national global investment in photovoltaic technologies, with $ 137.4 billion invested globally in 2019 [84], the cost of energy generated by photovoltaics has declined exponentially over the past decade. The cost of utility scale solar has declined by 88% from 2010 to 2021 [85]. Future photovoltaic technologies must continue this trend of dramatically declining cost of energy if they are to be used commercially within utility scale projects.

The measure of cost of energy used within such utility scale projects is LCOE, and it is sought to be minimised. LCOE weighs the costs of a project against the energy expected to be generated by the project over time. LCOE provides a metric to analyse the feasibility of a project, or technologies, through comparison. [86, 35].

Specialised models for the calculation of LCOE for utility scale PV projects have been developed [87, 35]. These models have introduced methods to account for factors of concern for photovoltaics, such as module cost, lifetime and initial PCE.

For emerging PV devices, they may be particularly sensitive to degradation cause by exposure to atmospheric conditions and light causing photo-oxidation and/or ingress of water acting as a solvent [88]. In LCOE models, the degradation of emerging devices has been modelled linearly [89], however

this does not account for the different regimes of degradation including burn-in. The different regimes of degradation were accounted for by Nieto-Diaz et al. [35, 90], as can be seen in figure 3.8.

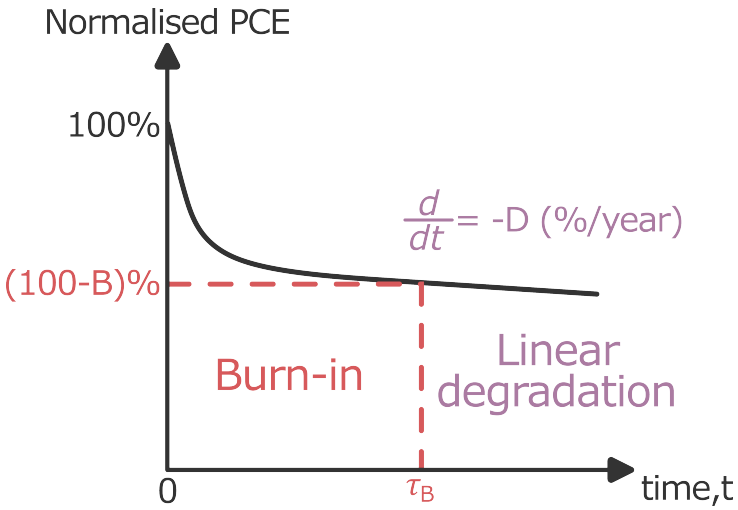


Figure 3.8: Illustration of Burn-in and Linear Degradation of a PV device over time [35].

However, the model developed by Nieto-Diaz et al. [35] does not allow for the performance of an individual PV device to vary with environmental conditions, assuming the performance of the device mirrors that of silicon, which may not be true for emerging PV devices. Through higher temporal resolution, the performance of novel PV devices can be allowed to vary with environmental conditions, namely in this work irradiance, at the dinaural scale. Higher spatial resolutions may allow for local geography to be examined for its effects on LCOE.

### 3.7.2 Model Operation

#### Levelised Cost of Energy (LCOE)

The basis for the calculation of LCOE is, Net Present Value (NPV) as shown in equation 3.7.29. NPV allows for the passage of time to be accounted for, with a progressively increasing discount rate applied to future earnings. Initially the discount rate is determined through the perceived financial risk by the location of a project, this emphasises revenue and costs earlier within

projects of higher discount rate. Therefore, in locations of higher risk shorter return of investment periods are required [91]. In equation 3.7.29, $R_t$ represents the cash outflow at time step $t$. $d$ represents the discounts rate (%) which is applied to future earnings.

$$NPV = \frac{R_t}{(1+d)^t} \tag{3.7.29}$$

On its own NPV, is a powerful tool for assessing the viability of an investment, where a positive NPV indicates an investment will result in a profit, and negative values indicate a loss [91]. However, in LCOE models, NPV is utilised to both calculate the value of the cost of the project and the sum of the energy generated over the course of the project. The equation for LCOE can be seen in equation 3.7.30.

$$LCOE = \frac{I_0 + \left|\sum_{t=1}^{l} \frac{C_t}{(1+d)^t}\right|}{\sum_{t=1}^{l} \frac{E_t}{(1+d)^t}} \tag{3.7.30}$$

Where, $I_0$ represents the installation costs of the project (€), $C_t$ is the costs occurred during time step $t$ (€), and $E_t$ is the energy generated (kWh) during time step $t$ [35]. $l$ is the length of the project in the appropriate subdivisions chosen for the calculation, this may be monthly, weekly, daily to hourly, and $d$ is the discount rate applied (%). When a predefined location is used, the discount rates applied are derived from the 2018 Grant Thornton Renewable Energy Survey Reports [92].

### Energy Generation

To calculate the energy generated by the project, various parameters are required and can be seen in table 3.5. From these parameters, the energy generated from the project over its lifetime at each time step was calculated. In order to calculate the energy generated by a PV farm at a specified latitude and longitude, additional data must be gathered. These data are gathered from PVGIS [34] via the means of a API call. From PVGIS satellite derived values for monthly Peak Sun Hours (PSH) ($PSH(t)$), the sum of monthly

| Symbol | Parameter | Unit |
|---|---|---|
| $Lon$ | Longitude | ∘ |
| $Lat$ | Latitude | ∘ |
| $Tilt$ | Tilt | ∘ |
| $F_{Cap}$ | Farm Capacity | kWh |
| $PCE_i$ | Initial PCE | % |
| $G_{FF}$ | Geometric Fill Factor | % |
| $Power_\rho$ | Power Density | $W_P \cdot m^{-2}$ |
| $B$ | Burn-in Degradation | % |
| $\tau_B$ | Burn-in Hours | Hours |
| $D$ | Degradation Rate | $\% \cdot year^{-1}$ |
| $P_{rep}$ | Panel Lifetime | Years |

Table 3.5: Parameters required for the calculation of energy generated at each time step [35].

irradiance represented as hours of under 1000 $WM^{-2}$, are gathered. Additionally, gathered for PVGIS are estimates of monthly yield ($E(t)$), the energy generated (kWh) for the installed peak capacity ($kW_p$), accounting for performance via a measured irradiance-temperature efficiency matrix as described by Huld et al. [31]. The calculations of yield were performed by PVGIS, and assumes the chosen technology performs similarly to silicon under varying environmental conditions, losing efficiency with increasing temperature and decreasing irradiance. As the values for PSH and yield gathered form PVGIS are monthly values, processing is required for them to be applied at the hourly timescale, to better resolve degradation. For this to be achieved, hourly irradiance values, $G(t)$, are gathered from PVGIS and applied to interpolating to the hourly timescale as shown in equation 3.7.31 and 3.7.32.

$$E(t) = G(t) \times \left( \frac{E(t)}{\sum_{t=M_s}^{M_e} G(t)} \right) \tag{3.7.31}$$

$$PSH(t) = G(t) \times \left( \frac{PSH(t)}{\sum_{t=M_s}^{M_e} G(t)} \right) \tag{3.7.32}$$

Here, in equations 3.7.31 and 3.7.32, $G$ is the global irradiance experience at the site and denominator is the sum of the global irradiance during the month of the respective time step, $t$ with $M_s$ and $M_e$ denoting the starting

and ending time step respectively. From hourly irradiance data, the monthly values of PSH and yield are divided in per portion with the irradiance, transforming the monthly values to hourly values allowing for dinaural effects to be preserved. The sum of both yield and PSH of the calculated hourly values for each month was ensured to be equal to that found in the original data as reported by PVGIS, ensuring no more energy is introduced through rounding errors.

From these values of yield and PSH the degradation of the panel over the course of the project lifetime is calculated. The degradation is calculated using the equations put forward by Nieto-Diaz et al. [35] These are shown in equation 3.7.33 and 3.7.34. These equations assume the degradation of the panel is solely caused by the exposure of the panel to irradiance, as previously discussed in the introduction, subsection 3.7.1, multiple factors are responsible for degradation and may occur in the presence or absence of irradiance.

$$B_F\,(\%) = a{S_c}^2 + bS_c + 100 \qquad S_c \leq \tau_B \tag{3.7.33}$$

$$D_F\,(\%) = d_L S_c + c + BS_c \qquad S_c > \tau_B \tag{3.7.34}$$

Where $S_c$ represents the cumulative PSH the panel has been exposed to, and $\tau_B$ is the time under peak irradiance needed for burn-in to end. This determines whether equation 3.7.33 or 3.7.34 is used, where $B_F$ is the Burn-in and $D_F$ is the linear degradation. $a$ and $b$ are quadratic fitting parameters and $d_L$ and $c$ represent the slope and intercept fitted from the linear degradation region. $B$ is the fraction of performance lost to burn-in. Equation 3.7.33 represents the burn-in regime of degradation, whilst equation 3.7.34 represent the linear regime, as shown in figure 3.8. Initially, equation 3.7.33 is used until the cumulative PSHs, $S_c$, is equal to that needed to reach $\tau_B$, following which equation 3.7.34 is utilised. Parameters $d_L$, $c$, $a$, and $b$ are calculated from representative panels derived from literature review performed

by Nieto-Diaz et al. [35]. From these equations, the degraded capacity of the farms can be calculated at each hourly time step through the multiplication of $B_F$ with the initial capacity and $D_F$ with the capacity at time $\tau_B$. To better represents the changing performance o9f a device with irradiance, a further equation is used, equation 3.7.35.

$$Generation(t) = E(t) \times Degraded\,Capacity(t) \tag{3.7.35}$$

### Costs

Both initial costs and recurring costs are calculated using the same methods described by in the works of Neito-Diaz et al. [35, 90]. The costs are derived from that achieved from a representative $5MW_p$ project in Fiji. However, for alternative locations recurring costs have inflation, representative to that of the chosen location, applied, as to refurbishment costs and operational and maintenance costs.

With the energy generated and initial and reoccurring costs calculated over the course of the project, the LCOE may be calculated as described in equation 3.7.30 with an appropriate discount for the arbitrary location applied.

## 3.8 Conclusion

Multiscale modelling has been shown to be applied to many problems with photovoltaics [4, 5, 9, 10]. However, they have not been used to identify how novel emerging photovoltaics devices may be integrated with wider systems. Presented within this chapter was the development of several models which may be used individually or in an interlinked multiscale nature in order to examine and identify how emerging photovoltaics may be used in future.

Here in this thesis, through utilising a multiscale approach with the developed models presented how emerging photovoltaics may be used to address challenges we face in the future is to be explored and examined. Firstly,

emerging photovoltaics devices which present opportunities to better align solar generation with demand within the UK are examined in utilising the plant dispatch model, as presented in chapter 4. Alowing for the introduction of novel photovoltaic devices to a plant dispatch model for the first time. Next, the effects of a changing climate, and atmosphere upon both silicon and organic photovoltaics are examined using the atmospheric composition model, showing how organic device may be more tolerant to changes to spectra through material selection, this can be seen in chapter 5. Modelling the spectral effects of pollution and weather upon emerging photovoltaics for the first time. Lastly, with uncertainty as to the cost of organic photovoltaic materials, a drift-diffusion model is coupled with the developed genetic algorithm and levelised cost of energy model in order to determine both the maximally acceptable commercial cost of organic materials and the effects of objective function, this work is presented in chapter 6. Coupling a drift-diffusion model with a genetic algorithm to examine the effect of active material cost for the first time. Through these chapters the possible roles of emerging photovoltaics in our future may be more clearly resolved.

# Bibliography

[1] D. A. Palacios-Gómez *et al.*, "Differing impacts of blended fullerene acceptors on the performance of ternary organic solar cells," *ACS Applied Energy Materials*, vol. 4, no. 10, pp. 10 867–10 876, 2021.

[2] B. Xiao *et al.*, "Relationship between fill factor and light intensity in solar cells based on organic disordered semiconductors: The role of tail states," *Physical Review Applied*, vol. 14, no. 2, p. 024034, 2020.

[3] O. Almora, J. Wiegand, P. López-Varo, G. J. Matt, and C. J. Brabec, "Degradation through directional self-doping and homogeneous density of recombination centers hindered by 1, 8-diiodooctane additive in non-fullerene organic solar cells," *Solar RRL*, vol. 5, no. 4, p. 2100024, 2021.

[4] L. Perdigón-Toro *et al.*, "Understanding the role of order in y-series non-fullerene solar cells to realize high open-circuit voltages," *Advanced Energy Materials*, vol. 12, no. 12, p. 2103422, 2022.

[5] J. Nelson, J. J. Kwiatkowski, J. Kirkpatrick, and J. M. Frost, "Modeling charge transport in organic photovoltaic materials," *Accounts of Chemical Research*, vol. 42, no. 11, pp. 1768–1778, 2009.

[6] I. M. Peters, C. D. R. Gallegos, S. E. Sofia, and T. Buonassisi, "The value of efficiency in photovoltaics," *Joule*, vol. 3, no. 11, pp. 2732–2747, 2019.

[7] P. H. A. Veríssimo *et al.*, "Area and lcoe considerations in utility-scale, single-axis tracking pv power plant topology optimization," *Solar Energy*, vol. 211, pp. 433–445, 2020.

[8] M. T. Patel, M. R. Khan, X. Sun, and M. A. Alam, "A worldwide cost-based design and optimization of tilted bifacial solar farms," *Applied Energy*, vol. 247, pp. 467–479, 2019.

[9] J. Kirkpatrick, V. Marcon, J. Nelson, K. Kremer, and D. Andrienko, "Charge mobility of discotic mesophases: A multiscale quantum and classical study," *Physical review letters*, vol. 98, no. 22, p. 227402, 2007.

[10] A. Pershin, S. Donets, and S. A. Baeurle, "A new multiscale modeling method for simulating the loss processes in polymer solar cell nanodevices," *The Journal of Chemical Physics*, vol. 136, no. 19, 2012.

[11] C. A. Horowitz, "Paris agreement," *International Legal Materials*, vol. 55, no. 4, pp. 740–755, 2016.

[12] IRENA, "Future of Photovoltaic," Nov. 2019. [Online]. Available: https://www.irena.org/publications/2019/Nov/Future-of-Solar-Photovoltaic

[13] "Global Energy and Climate Model Documentation," International Energy Agency, Paris, Tech. Rep., 2022.

[14] K. Mongird *et al.*, "2020 grid energy storage technology cost and performance assessment," *Energy*, vol. 2020, pp. 6–15, 2020.

[15] M. Z. Oskouei *et al.*, "A critical review on the impacts of energy storage systems and demand-side management strategies in the economic operation of renewable-based distribution network," *Sustainability*, vol. 14, no. 4, p. 2110, 2022.

[16] D. of Energy and C. Change, "DECC 2050 Calculator."

[17] T. Bulavskaya and F. Reynès, "Job creation and economic impact of renewable energy in the Netherlands," *Renewable Energy*, vol. 119, no. C, pp. 528–538, 2018, publisher: Elsevier. [Online]. Available: https://ideas.repec.org//a/eee/renene/v119y2018icp528-538.html

[18] D. Mentis *et al.*, "The benefits of geospatial planning in energy access – A case study on Ethiopia," *Applied Geography*, vol. 72, pp. 1–13, Jul. 2016. [Online]. Available: https://www.sciencedirect.com/science/article/pii/S0143622816300522

[19] M. Child, A. Nordling, and C. Breyer, "Scenarios for a sustainable energy system in the Åland Islands in 2030," *Energy Conversion and Management*, vol. 137, pp. 49–60, Apr. 2017. [Online]. Available: https://www.sciencedirect.com/science/article/pii/S019689041730047X

[20] C. Bussar *et al.*, "Large-scale integration of renewable energies and impact on storage demand in a European renewable power system of 2050—Sensitivity study," *Journal of Energy Storage*, vol. 6, pp. 1–10, May 2016. [Online]. Available: https://www.sciencedirect.com/science/article/pii/S2352152X16300135

[21] T. Boßmann and I. Staffell, "The shape of future electricity demand: Exploring load curves in 2050s Germany and Britain," *Energy*, vol. 90, pp. 1317–1333, Oct. 2015. [Online]. Available: https://www.sciencedirect.com/science/article/pii/S0360544215008385

[22] T. Burandt, B. Xiong, K. Löffler, and P.-Y. Oei, "Decarbonizing China's energy system – Modeling the transformation of the electricity, transportation, heat, and industrial sectors," *Applied Energy*, vol. 255, p. 113820, Dec. 2019. [Online]. Available: https://www.sciencedirect.com/science/article/pii/S0306261919315077

[23] A. Crossland, K. Scoles, A. Wang, C. Groves, and S. Sun, "Assessment of Electricity Decarbonization Scenarios for New Zealand and Great Britain using a Plant Dispatch and Electrical Energy Storage Modelling Framework," *Energies*, vol. 13, no. 11, p. 2799, Jan. 2020, number: 11 Publisher: Multidisciplinary Digital Publishing Institute. [Online]. Available: https://www.mdpi.com/1996-1073/13/11/2799

[24] D. of Energy Security and D. o. B. E. . I. S. Net Zero, "Digest of UK Energy Statistics (DUKES)," Aug. 2022. [Online]. Available: https://www.gov.uk/government/collections/digest-of-uk-energy-statistics-dukes

[25] "PV_live," Apr. 2023, original-date: 2018-06-04T10:45:27Z. [Online]. Available: https://github.com/SheffieldSolar/PV_Live-API

[26] "ELEXON Portal." [Online]. Available: https://www.elexonportal.co.uk/news/latest?cachebust=2l1bity9a0

[27] "ENTSO-E Transparency Platform." [Online]. Available: https://transparency.entsoe.eu/

[28] L. Hirth, J. Mühlenpfordt, and M. Bulkeley, "The ENTSO-E Transparency Platform – A review of Europe's most ambitious electricity data platform," *Applied Energy*, vol. 225, pp. 1054–1067, Sep. 2018. [Online]. Available: https://www.sciencedirect.com/science/article/pii/S0306261918306068

[29] ENTSO-E, "Detailed Data Descriptions V1.4," Tech. Rep. [Online]. Available: https://eepublicdownloads.entsoe.eu/clean-documents/pre2015/resources/Transparency/MoP%20Ref02%20-%20EMFIP-Detailed%20Data%20Descriptions%20V1R4-2014-02-24.pdf

[30] I. C. Change *et al.*, "Mitigation of climate change," *Contribution of working group III to the fifth assessment report of the intergovernmental panel on climate change*, vol. 1454, p. 147, 2014.

[31] T. Huld *et al.*, "A power-rating model for crystalline silicon pv modules," *Solar Energy Materials and Solar Cells*, vol. 95, no. 12, pp. 3359–3369, 2011.

[32] X. Rodríguez-Martínez *et al.*, "Matching electron transport layers with a non-halogenated and low synthetic complexity polymer: fullerene blend for efficient outdoor and indoor organic photovoltaics," *Journal of Materials Chemistry A*, vol. 10, no. 19, pp. 10 768–10 779, 2022.

[33] T. Du *et al.*, "Light-intensity and thickness dependent efficiency of planar perovskite solar cells: charge recombination versus extraction," *Journal of Materials Chemistry C*, vol. 8, no. 36, pp. 12 648–12 655, 2020.

[34] T. Huld, R. Müller, and A. Gambardella, "A new solar radiation database for estimating pv performance in europe and africa," *Solar Energy*, vol. 86, no. 6, pp. 1803–1815, 2012.

[35] B. A. Nieto-Díaz, A. F. Crossland, and C. Groves, "A levelized cost of energy approach to select and optimise emerging pv technologies: The relative impact of degradation, cost and initial efficiency," *Applied Energy*, vol. 299, p. 117302, 2021.

[36] A. Turing, "Intelligent machinery (1948)," *B. Jack Copeland*, p. 395, 2004.

[37] A. M. Turing, "Mind," *Mind*, vol. 59, no. 236, pp. 433–460, 1950.

[38] J. Wang, O. K. Ersoy, M. He, and F. Wang, "Multi-offspring genetic algorithm and its application to the traveling salesman problem," *Applied soft computing*, vol. 43, pp. 415–423, 2016.

[39] A. Guillaume *et al.*, "Deep space network scheduling using evolutionary computational methods," pp. 1–6, 2007.

[40] S. Jafar-Zanjani, S. Inampudi, and H. Mosallaei, "Adaptive genetic algorithm for optical metasurfaces design," *Scientific reports*, vol. 8, no. 1, p. 11040, 2018.

[41] A. Savić and Ž. Đurišić, "Optimal sizing and location of svc devices for improvement of voltage profile in distribution network with dispersed photovoltaic and wind power plants," *Applied Energy*, vol. 134, pp. 114–124, 2014.

[42] S. S. Reddy, "Optimal scheduling of thermal-wind-solar power system with storage," *Renewable energy*, vol. 101, pp. 1357–1368, 2017.

[43] B. Bala and S. A. Siddique, "Optimal design of a pv-diesel hybrid system for electrification of an isolated island—sandwip in bangladesh using genetic algorithm," *Energy for sustainable Development*, vol. 13, no. 3, pp. 137–142, 2009.

[44] S. Daraban, D. Petreus, and C. Morel, "A novel mppt (maximum power point tracking) algorithm based on a modified genetic algorithm specialized on tracking the global maximum power point in photovoltaic systems affected by partial shading," *Energy*, vol. 74, pp. 374–388, 2014.

[45] K. Yadav, B. Kumar, J. M. Guerrero, and A. Lashab, "A hybrid genetic algorithm and grey wolf optimizer technique for faster global peak detection in pv system under partial shading," *Sustainable Computing: Informatics and Systems*, vol. 35, p. 100770, 2022.

[46] L. E. de Sousa, D. A. da Silva Filho, P. de Silva, L. Ribeiro, and P. H. de Oliveira Neto, "A genetic algorithm approach to design principles for organic photovoltaic materials," *Advanced Theory and Simulations*, vol. 3, no. 8, p. 2000042, 2020.

[47] I. Y. Kanal, S. G. Owens, J. S. Bechtel, and G. R. Hutchison, "Efficient computational screening of organic polymer photovoltaics," *The journal of physical chemistry letters*, vol. 4, no. 10, pp. 1613–1623, 2013.

[48] N. Li, I. McCulloch, and C. J. Brabec, "Analyzing the efficiency, stability and cost potential for fullerene-free organic photovoltaics in one figure of merit," *Energy & Environmental Science*, vol. 11, no. 6, pp. 1355–1361, 2018.

[49] A. Gambhir, P. Sandwell, and J. Nelson, "The future costs of opv–a bottom-up model of material and manufacturing costs with uncertainty analysis," *Solar Energy Materials and Solar Cells*, vol. 156, pp. 49–58, 2016.

[50] R. L. Haupt, "Optimum population size and mutation rate for a simple real genetic algorithm that optimizes array factors," in *IEEE Antennas and Propagation Society International Symposium. Transmitting Waves of Progress to the Next Millennium. 2000 Digest. Held in conjunction with: USNC/URSI National Radio Science Meeting (C*, vol. 2. IEEE, 2000, pp. 1034–1037.

[51] W. Van Roosbroeck, "Theory of the flow of electrons and holes in germanium and other semiconductors," *The Bell System Technical Journal*, vol. 29, no. 4, pp. 560–607, 1950.

[52] D. L. Scharfetter and H. K. Gummel, "Large-signal analysis of a silicon read diode oscillator," *IEEE Transactions on electron devices*, vol. 16, no. 1, pp. 64–77, 1969.

[53] H. Bässler, "Charge transport in disordered organic photoconductors. a monte carlo simulation study," *Physica Status Solidi B (Basic Research);(Germany)*, vol. 175, no. 1, 1993.

[54] S. M. Hosseini *et al.*, "Relationship between energetic disorder and reduced recombination of free carriers in organic solar cells," *Advanced Energy Materials*, p. 2203576, 2023.

[55] W. Shockley and W. Read Jr, "Statistics of the recombinations of holes and electrons," *Physical review*, vol. 87, no. 5, p. 835, 1952.

[56] R. N. Hall, "Electron-hole recombination in germanium," *Physical review*, vol. 87, no. 2, p. 387, 1952.

[57] R. C. MacKenzie, C. G. Shuttle, M. L. Chabinyc, and J. Nelson, "Extracting microscopic device parameters from transient photocurrent measurements of p3ht: Pcbm solar cells," *Advanced Energy Materials*, vol. 2, no. 6, pp. 662–669, 2012.

[58] Y. Gao *et al.*, "Engineering ultra long charge carrier lifetimes in organic electronic devices at room temperature," *Advanced Materials Interfaces*, vol. 2, no. 4, p. 1400555, 2015.

[59] L. Sims *et al.*, "Investigation of the s-shape caused by the hole selective layer in bulk heterojunction solar cells," *Organic Electronics*, vol. 15, no. 11, pp. 2862–2867, 2014.

[60] L. Zhu *et al.*, "Single-junction organic solar cells with over 19% efficiency enabled by a refined double-fibril network morphology," *Nature Materials*, vol. 21, no. 6, pp. 656–663, 2022.

[61] S. Engmann *et al.*, "Higher order effects in organic leds with sub-bandgap turn-on," *Nature communications*, vol. 10, no. 1, p. 227, 2019.

[62] S. Ahmed *et al.*, "Simulation studies of sn-based perovskites with cu back-contact for non-toxic and non-corrosive devices," *Journal of Materials Research*, vol. 34, pp. 2789–2795, 2019.

[63] N. Majeed *et al.*, "Using deep machine learning to understand the physical performance bottlenecks in novel thin-film solar cells," *Advanced Functional Materials*, vol. 30, no. 7, p. 1907259, 2020.

[64] S. A. A. Kazmi *et al.*, "Efficient materials for thin-film cdte solar cell based on back surface field and distributed bragg reflector," *Applied Physics A*, vol. 126, pp. 1–8, 2020.

[65] X. Rodríguez-Martínez, E. Pascual-San-José, and M. Campoy-Quiles, "Accelerating organic solar cell material's discovery: high-throughput screening and big data," *Energy & Environmental Science*, vol. 14, no. 6, pp. 3301–3322, 2021.

[66] L. J. Koster, E. Smits, V. Mihailetchi, and P. W. Blom, "Device model for the operation of polymer/fullerene bulk heterojunction solar cells," *Physical Review B*, vol. 72, no. 8, p. 085205, 2005.

[67] R. C. MacKenzie, "Oghmanano user manual," 2023. [Online]. Available: https://www.oghma-nano.com/docs/man/understanding_oghma_nano.pdf

[68] R. C. MacKenzie, T. Kirchartz, G. F. Dibb, and J. Nelson, "Modeling nongeminate recombination in p3ht: Pcbm solar cells," *The Journal of Physical Chemistry C*, vol. 115, no. 19, pp. 9806–9813, 2011.

[69] M. Collins *et al.*, "Long-term Climate Change: Projections, Commitments and Irreversibility," 2018.

[70] J. F. Kok *et al.*, "Mineral dust aerosol impacts on global climate and climate change," *Nature Reviews Earth & Environment*, vol. 4, no. 2, pp. 71–86, Feb. 2023, number: 2 Publisher: Nature Publishing Group. [Online]. Available: https://www.nature.com/articles/s43017-022-00379-5

[71] U. N. Environment, "Spreading like Wildfire: The Rising Threat of Extraordinary Landscape Fires," Feb. 2022, section: publications. [Online]. Available: http://www.unep.org/resources/report/spreading-wildfire-rising-threat-extraordinary-landscape-fires

[72] D. J. Jacob and D. A. Winner, "Effect of climate change on air quality," *Atmospheric environment*, vol. 43, no. 1, pp. 51–63, 2009.

[73] S. Jerez *et al.*, "The impact of climate change on photovoltaic power generation in europe," *Nature communications*, vol. 6, no. 1, p. 10014, 2015.

[74] D. L. Donaldson, D. M. Piper, and D. Jayaweera, "Temporal solar photovoltaic generation capacity reduction from wildfire smoke," *IEEE Access*, vol. 9, pp. 79 841–79 852, 2021.

[75] A. Z. Bertoletti, T. Phan, and J. Campos do Prado, "Wildfire smoke, air quality, and renewable energy—examining the impacts of the 2020 wildfire season in washington state," *Sustainability*, vol. 14, no. 15, p. 9037, 2022.

[76] A. Inness *et al.*, "The cams reanalysis of atmospheric composition," *Atmospheric Chemistry and Physics*, vol. 19, no. 6, pp. 3515–3556, 2019.

[77] A. Agusti-Panareda *et al.*, "The cams greenhouse gas reanalysis from 2003 to 2020," *EGUsphere*, pp. 1–51, 2022.

[78] C. Gueymard, "Simple Model for the Atmospheric Radiative Transfer of Sunshine (SMARTS2) Algorithms and performance assessment," 1995.

[79] C. A. Gueymard, D. Myers, and K. Emery, "Proposed reference irradiance spectra for solar energy systems testing," *Solar energy*, vol. 73, no. 6, pp. 443–467, 2002.

[80] F. Antonanzas-Torres, R. Urraca, J. Polo, O. Perpiñán-Lamigueiro, and R. Escobar, "Clear sky solar irradiance models: A review of seventy models," *Renewable and Sustainable Energy Reviews*, vol. 107, pp. 374–387, 2019.

[81] A. M. Humada, M. Hojabri, S. Mekhilef, and H. M. Hamada, "Solar cell parameters extraction based on single and double-diode models: A review," *Renewable and Sustainable Energy Reviews*, vol. 56, pp. 494–509, 2016.

[82] A. Jain and A. Kapoor, "Exact analytical solutions of the parameters of real solar cells using lambert w-function," *Solar Energy Materials and Solar Cells*, vol. 81, no. 2, pp. 269–277, 2004.

[83] A. Jain and A. Kapoor, "A new method to determine the diode ideality factor of real solar cell using lambert w-function," *Solar energy materials and solar cells*, vol. 85, no. 3, pp. 391–396, 2005.

[84] IRENA, "Global landscape of renewable energy finance 2023," 2023.

[85] IRENA, "Renewable power generation costs in 2021," 2022.

[86] E. I. C. Zebra, H. J. van der Windt, G. Nhumaio, and A. P. Faaij, "A review of hybrid renewable energy systems in mini-grids for off-grid electrification in developing countries," *Renewable and Sustainable Energy Reviews*, vol. 144, p. 111036, 2021.

[87] M. H. Kang and A. Rohatgi, "Quantitative analysis of the levelized cost of electricity of commercial scale photovoltaics systems in the us," *Solar Energy Materials and Solar Cells*, vol. 154, pp. 71–77, 2016.

[88] Q. Zhang, Y. Chen, X. Liu, and M. Fahlman, "In situ near-ambient pressure x-ray photoelectron spectroscopy reveals the effects of water, oxygen and light on the stability of pm6: Y6 photoactive layers," *Journal of Materials Chemistry C*, vol. 11, no. 8, pp. 3112–3118, 2023.

[89] W. R. Mateker and M. D. McGehee, "Progress in understanding degradation mechanisms and improving stability in organic photovoltaics," *Advanced materials*, vol. 29, no. 10, p. 1603940, 2017.

[90] B. A. Nieto-Díaz, A. F. Crossland, and C. Groves, "How does location determine the economic competitiveness of grid-scale emerging photovoltaics?" *Energy Technology*, vol. 10, no. 5, p. 2101012, 2022.

[91] A. Gallo, "A refresher on net present value," *Harvard Business Review*, vol. 19, pp. 1–6, 2014.

[92] G. Thorton, "Renewable energy discount rate survey results-2018," 2019. [Online]. Available: https://www.grantthornton.co.uk/globalassets/1.-member-firms/united-kingdom/pdf/documents/renewable-energy-discount-rate-survey-results-2018.pdf

# Chapter 4

# Decarbonising Electrical Grids using Photovoltaics with Enhanced Capacity Factors

## 4.1 Summary

In this chapter, the plant dispatch model developed in section 3.3 is used to examine how Photovoltaic (PV) devices with enhanced capacity factors may perform when introduced to a Wide Area Synchronous Grid (WASG). The benefits of these devices in both energy and commercial terms are examined. Many scenarios for Net Zero anticipate substantial growth of Solar PV generation to satisfy 30% of our electricity needs. However, this scale of deployment introduces challenges as supply may not meet demand, thereby necessitating energy storage and demand-side management [1, 2]. Here we demonstrate a different, complementary approach to resolving this challenge in which Solar PV generation can be made intrinsically less variable than commercial PV. Dye-sensetized PVs for which the power conversion efficiency increases as light intensity reduces are demonstrated. Modelling of the UK mainland energy network predicts that these devices are more effective at displacing high carbon generation from Coal and Gas than commercial PV. The capacity factor of these PV devices are controlled by their design, and capacity factors >60% greater than silicon are predicted based on experimental data. These data demonstrate a new approach to designing PV in which minimising variability in generation is the goal. This approach is predicted to be more effective at delivering carbon reductions for a given energy network than commercial PV. The work of this chapter was published in The Royal Society of Chemistry's Journal Energy and Environmental Science [3].

## 4.2 Introduction

Silicon PV is currently the most deployed PV technology [4, 5], and due to its maturity and continued development it has become the cheapest form of renewable energy [5], with silicon PVs cost per watt peak decreasing exponentially over the last decade [6]. Due to silicon PVs low cost, predictions for how our energy needs will be met under Net Zero see PV generation increasing from 3% of our global electricity generation to more than 20%

by 2050 [7, 8, 9]. However, providing a large proportion of global energy needs with intermittent renewable energy generation comes with its own set of challenges.

The intermittent and diurnal nature of PV generation causes challenges for Electricity Systems Operators (ESOs), who must balance demand and generation to ensure power is constantly available while maintaining both voltage and frequency. Due to PVs diurnal nature, generation of PVs does not match demand, which necessitates the use of dispatchable, often non-renewable, generation to ensure generation is balanced to demand. Within some WASGs ESOs, such as California Independent Systems Operator (CAISO), PV generation causes difficult around sunset, where the rapid reduction in PV generation requires an equally rapid increase in generation from dispatchable sources [10]. These issues are also present within low voltage PV installations, where during sunny periods, reverse power flow leads to overvoltage [11, 12].

Additionally, financial challenges are present as the revenue from PV generation is expected to reduce with increased penetration [13, 14, 15]. This has led to further calls for reducing the cost of silicon PV [15], to ensure the profitability of silicon PV generation. Both the financial and power related challenges of furthering PV penetration, has its roots within the relative lack of control as to when PV generation occurs. To facilitate the transition to Net Zero, where PV is expected to represent a large proportion of generation, demand-side management [2] and grid-level energy storage [1] is expected to be required. However, the progress of these technologies is outpaced by the deployment of PV generation. Might the intermittent and diurnal nature of PV generation within future PV devices be minimised?

Capacity Factor (CF), As discussed in chapter 2, may serve as a proxy for the variability of a renewable power source. Comparing the CFs of deployed PV generation, which may vary from 10% in the UK up to 25% in California dependent upon the local climate [16, 17], to other energy generation sources within the United Kingdom in 2021 such as Biomass 64%, Nuclear 59 %, and offshore wind 38%, show the high variability of PV generation [16].

Within the wind power sector, the optimisation of the generator to maximise capacity factor [18] is a recognised approach to address the challenges of high variability generation [19]. Contrastingly, optimising a solar cell to maximise CF has not been considered. Instead to optimise PV CF external solutions such as tracking mounts [20, 21] or East/West panel azimuths are considered [22, 23].

In this chapter, a class of PV devices that have intrinsically higher capacity factor than conventional PV technology is demonstrated. Their devices are termed High Capacity Factor Photovoltaicss (CFPVs), which possess a Power Conversion Efficiency (PCE) which increases as irradiance reduces, thereby increasing generation at times of low irradiance. The consequence of this behaviour is that they energy yield decrease due to a reduced irradiance is less than the linear decrease that may be expected, due to the deviced increased PCE. Minimising the variability in power output, and maximising the energy yield for a specified capacity of grid connection. This behaviour is explored using a plant dispatch model, as discussed in section 3.3, using data from the UK's mainland WASG. Generation from the CFPVs are shown to match the demand of the UK's mainland WASG to a higher degree than an equal capacity of conventional PV, leading to several benefits proportional to capacity factor: i) higher potential for reducing Carbon Dioxide Equivilent ($CO_2e$) emissions, and ii) Increased revenue from participation in wholesale markets. Collaborators in Newcastle have shown through modification to their architectures Dye Sensetised Solar Cells (DSSCs) are shown to exhibit design variable capacity factor. This newly found control over the generation profile of PV may reduce the need for energy storage and demand side management through the deployment of future PV tailored for the local climate and WASG.

## 4.3 Modelling CFPV generation at the national scale

To demonstrate the potential benefits of CFPVs, models for both the CFPV devices themselves and the WASG are required. With consideration for the model of the CFPV device, several PV device types have been demonstrated to possess increasing PCE with reducing incident irradiance, which may see increased CF. This behaviour has been demonstrated in, organic PVs [24, 25, 26, 27, 28], perovskite PVs [29, 30, 31, 32] and DSSCs [33, 34]. Of these papers, the device reported by Bristow and Kettle [34] as shown in figure 4.1 is of particular interest as it is an outdoor test of a commercial large area DSSC module. Slow ion transportation within the electrolyte leads to insufficient mass transport under high irradiance conditions, lowering the achieved PCE. This loss in PCE is reduced by lowering irradiance such that the mass transport is sufficient and no longer limiting PCE. The Bristow and Kettle device is of additional interest due to the outdoors testing of the devices, meeting much of the conditions set about the ISOS consensus statement [35], providing a realistic test of CFPV concept. The opportunities this raises for future CFPV technologies will be discussed in the context of the results later in the chapter.

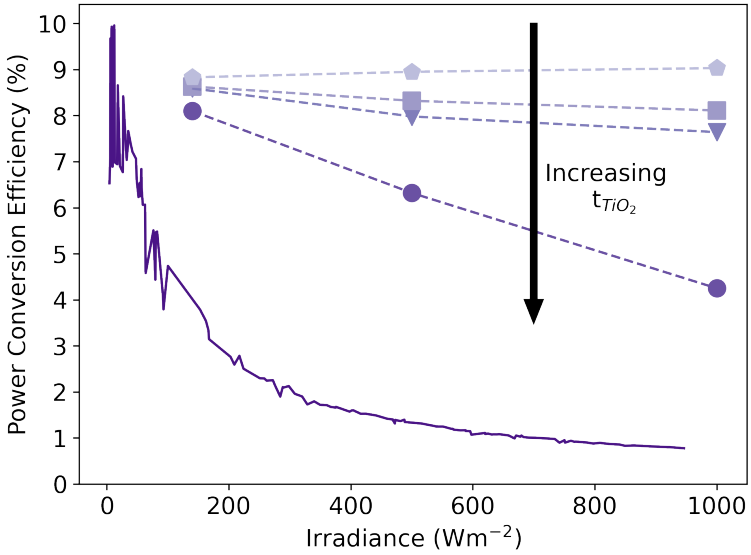


Figure 4.1: PCE irradiance characteristics of CFPV devices as reported by [34] (line), and those devices reported here (symbols) with $t_{TiO_2} = 12$ (pentagons), 18 (squares), 24 (triangles) and 48 $\mu$m (circles).

To quantify the behaviour and impact of the Bristow and Kettle device shown in figure 4.1 on a WASG in terms of generation and carbon emissions, the plant dispatch model discussed in section 3.3 was applied to the mainland UK electrical network. The UK was selected as the location for the analysis in part due to the availability of generation data, which was accessed as was described in section 3.3. Secondly, the UK's mismatch between irradiance and electricity demand with peaks at midday and in the afternoon respectively, is reported in various WASGs, such as in Brazil, California, Chile, India, Iran, Spain, and South Africa [36, 37, 38]. However, increasing capacity factor of PV in all locations, including sunny locations, is beneficial. Within the US, 85% of the deployed utility scale solar PV capacity in 2021 incorporated at least single-axis tracking [39]. These tracking systems were installed across the US, regardless of irradiance, therefore there is an economic benefit to increasing capacity factor invariant of location.

With the location, and devices to test selected, the relevant details may be fed into the developed plant dispatch model as is described in detail in section 3.3. The year 2016 was chosen to be examined, the assets reported, the capacity and assigned dispatch class can be seen in table 4.1.

| Dispatch Class | Generation Type | Installed Capacity (MW) [40] | Carbon Intensity ($gCO_2eq/kWh$) [30] |
|---|---|---|---|
| 1 | Nuclear | 8,981 | 12 |
| 2 | Solar | 11,970* [41] | 48 |
| 2 | Wind Onshore | 8,562 | 11 |
| 2 | Wind Offshore | 5,011 | 12 |
| 2 | Hydro Run-of-River and Poundage | 1,540 | 24 |
| 3 | Hydro Pumped Storage | 2,744 | 24 |
| 4 | Fossil Gas | 25,702 | 490 |
| 4 | Fossil Hard Coal | 14,889 | 820 |

Table 4.1: The Installed capacity and carbon intensity of each generation types. *Due the balancing mechanism reporting service not counting assets less than 50 MW towards the installed capacity (which artificially reduces the actual installed capacity), the installed capacity reported by PVLive [41] at the end of the year is used.

It is important to remember that data on the UK energy mix will be reported in terms of energy dispatched, not energy generated. Generated energy may be immediately dispatched, and in this case, energy generated and energy dispatched are equivalent. However, excess energy may also be used to charge storages assets and later dispatched to satisfy demand, in which case generation would be assigned to storage rather than solar assets. This enables the examination of the introduced CFPV interaction with the storage assets.

During 2016, 11,970 $MW_P$ of PV assets were installed upon the UKs WASG, with much of this capacity being silicon, and additional capacity of silicon PV ($C_{Si}$) and CFPV ($C_{CF}$) may be introduced. $C$ here represents the fraction of the historic PV capacity added to the grid through the plant

dispatch model. For example, a $C = 0.5$ assumes the introduction of 50 % of the historic capacity regardless of technology, be it silicon ($C_{Si}$) or CFPV ($C_{CF}$). The discussion is framed through value of installed capacity, $C$, as the capacity of the assets significantly affects the requirements needed to attach the asset to the WASG, as well as the procedure, duration, and cost of the grid connection [42]. The introduced assets must fit within the bounds set by the capacity of the local connections of the grid, as failure to ensure the assets does so can lead to issues of safety, reduced power quality and reduced network protection [42].

## 4.4 Benefits of CFPV behaviour on national Carbon emissions

The plant dispatch model is now used to examine the impact of CFPV behaviour seen in figure 4.1. Initially, the discussion concentrates upon a comparison of commercialised silicon devices, and the CFPV device reported by Bristow and Kettle [34]. The effect of introducing both devices can be seen in figure 4.2 where all the figures presented are in terms of the additional introduced capacity, $C_{CF}$ and $C_S$ for CFPV and silicon PV respectively. Figures 4.2a and 4.2c show predictions for the annual UK mix of dispatched energy as a function of $C_S$ and $C_{CF}$ respectively, figures 4.2d and 4.2f both show the respective change in the annual dispatched energy mix. From figures 4.2d and 4.2f it can be seen that the additional generation form the introduced PV capacity reduces the need the need for high carbon intensity generation irrespective of PV type, such as from coal and gas. Less clearly seen from the figures presented is the increase in utilisation of hydro pumped storage, but CFPV is more effective at reducing high carbon generation than the equivalent capacity of silicon. Where under C=2 a increase of 0.12% and 6.48% is seen from silicon PV and CFPV respectively, this increases in dispatch from the storage assets is due to greater periods of excess generation. Additionally, as shown by figures 4.2g and 4.2i the change in the annual energy mix results

in 11.05 Mt and 29.47 Mt of $CO_2e$ emissions saved when C=2, showing per unit capacity the CFPV device is more effective at reducing $CO_2e$ emissions. As shown from figures 4.2g and 4.2i as the additional installed capacity of either silicon PV or CFPV the $CO_2e$ emissions savings increase, with the CFPV device saving 2.67 times more than the silicon device when C=2. However, it is of note that in both cases the increase in emissions savings is non-linear, as in both cases of increasing capacity it becomes increasingly difficult to meet demand unaligned with irradiance with PVs. With the CFPV device been shown to be more effective at decarbonising the annual energy mix for an equal capacity, and examining the predicted installed capacity of PV and subsequent penetration in order to achieve Net Zero [7, 8, 9], a strong case may be made for CFPV to be included in the energy generation mix in order to reach demand.

The greater potential for decarbonisation of the CFPV as compared to silicon PV is a function of its PCE-Irradiance characteristic as presented in figure 4.1, enabling the CFPV to achieve higher yields when irradiance is below 1000 $Wm^{-2}$. Comparing the CFPV PCE-Irradiance characteristic to a histogram of irradiance values during the month of July shown in figure 4.3, in this distribution due to diurnal variation and weather sees a mean daytime irradiance 259 $Wm^{-2}$, it can be seen that the CFPV device of Bristow and Kettle [34] would achieve an enhancement of 2.94 compared to its performance under standard testing conditions. Therfore, the CFPV device provides an output power closer to the rated capacity over a the range of experienced irradiance than the installed silicon PVs.

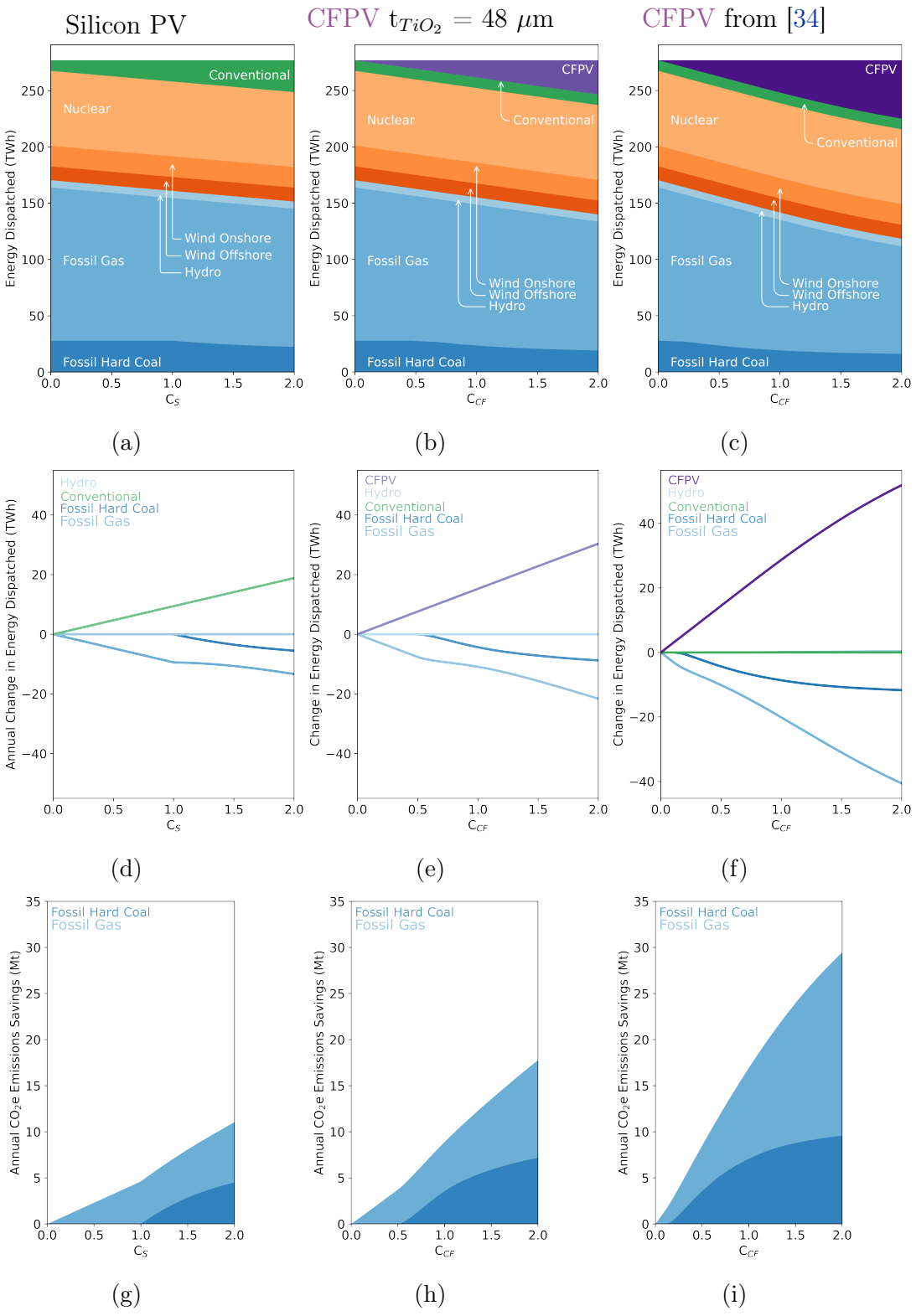


Figure 4.2: Annual generation profiles of the UK (a,b,c), change in generation (d,e,f) and carbon savings (g,h,i) as a function of additional silicon PV (a,d,g), and CFPV for $t_{TiO_2}$ = 48 $\mu$m devices shown in Fig. 1 (b,e,h), and CFPV device [34] (c,f,i). Change in generation (d,e,f) figures show change in generation against 2016 historical data. Carbon savings (g,h,i) figures show the source of carbon savings from reduction in Gas (Light Blue) and Coal (Dark Blue) emissions.

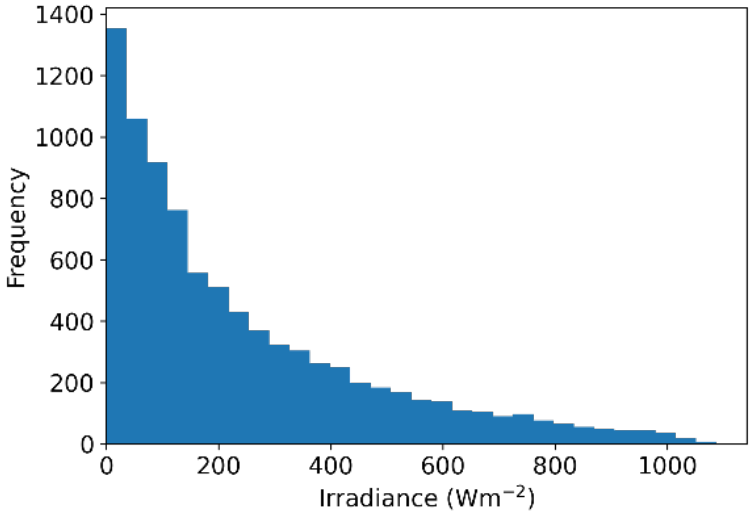


Figure 4.3: Histogram of irradiance in the UK during July as an example of data used in calculations.

| Device | PCE at 1000Wm$^{-2}$ (%) | PCE (140Wm$^{-2}$)/ PCE (1000Wm$^{S}$−2) | Annual $CO_2$e savings when C = 1 (Mt) | Predicted UK Capacity Factor (%) | Predicted wholesale revenue for 5MW$_P$ farm sited in UK (k€) | Predicted module costs (€/W$_P$) |
|---|---|---|---|---|---|---|
| Conventional Si PV | 20 | 0.9 | 4.70 | 8.89 | 194 | 0.245 |
| CFPV, tTiO2 = 12$\mu$m | 9.0 | 1.00 | 4.61 | 8.87 | 191 | 0.355 |
| CFPV, tTiO2 = 18$\mu$m | 8.1 | 1.06 | 5.00 | 9.36 | 201 | 0.395 |
| CFPV, tTiO2 = 24$\mu$m | 7.6 | 1.10 | 5.28 | 9.67 | 209 | 0.420 |
| CFPV, tTiO2 = 48$\mu$m | 4.3 | 1.90 | 9.00 | 14.50 | 315 | 0.740 |
| SolarPrint CFPV reported in 29 | 0.8 | 5.20 | 17.00 | 27.40 | 610 | 4.000 |

Table 4.2: Experimental data related to CFPV devices as well as predicted $CO_2$e savings for C = 1, capacity factor, and wholesale earnings and costs for a 5 MW$_P$ solar farm.

## 4.5 Enhanced Capacity Factors for PV

The behaviour of the CFPV devices, can be quantified using capacity factor, which is comparing the theoretical maximum energy dispatched to that predicted by the plant dispatch model over the same period. The predictions by the plant dispatch model of capacity factor can be seen in table 4.2. Typical PV capacity factors ranging from 10 to 25 % depending on local conditions [43], and conventional PV achieving capacity factors of approximately

10% in the UK due to the UKs northerly latitude and temperate climate [16]. The developed plant dispatch model predicts a capacity factor of 8.89% for silicon PV, and therefore is in line with the reported values. Contrastingly, the model predicts the Bristow and Kettle CFPV device achieves a capacity factor of 27.4 % in the UK, more than 3 times larger than that predicted for silicon PV by the model.

## 4.6 Benefits of CFPV behaviour on income generation on wholesale markets

Not only does the continual balance between energy supply and demand determine the carbon emissions generated, it is also critical in determining revenues from PV generation assets. If the whole of PV assets generate over the same period, e.g. due to similar climates at the locations of the assets such as in California, this synchronised generation diminishes the wholesale price of energy during this period. An effect that becomes more pronounced as the fraction of generation capacity increases particularly if the fraction of capacity is greater than 10% [13, 14, 15]. In contrast, if supply is unable to balance demand with the use of renewable generation the wholesale price of energy increases, representing an unbalanced demand that may be balanced through high carbon intensity generation. In order to demonstrate how the use of CFPVs effect revenue from energy generation, the annual income from a 5 $MW_P$ solar farm is estimated for both CFPVs and silicon PV. A 5 $MW_P$ farm was chosen as this would be large enough for the farm to participate in wholesale energy markets, but not large enough to significantly effect the market price of energy [14]. Revenues were calculated calculate for the 5MWp solar farm by multiplying the energy produced in each half-hourly settlement period by the marginal cost of energy in the same period, and accrued over the course of the year. It is assumed that no penalties for under- and over- generation are accrued [44]. It is important to remember that the CFPV device do not represent a probable commercial device, but serve as a

demonstrator as to possessing their irradiance dependant efficiency.

In this hypothetical senarion the silicon PV farm was estimated to return a revenue of €194,000 over the course of the year, whilst the Bristow and Kettle CFPV device yields a revenue of €611,000 for the same period, 3 times more revenue. This increase can mostly be explained through the increase in generation under low incident irradiance conditions. As shown in figure 4.3. Additionally this increase generation under low irradiance conditions enables the CFPV to provide more generation in periods where the wholesale price of energy is increased due to unbalanced demand, such as in early morning and late afternoon as can be seen in figure 4.4.

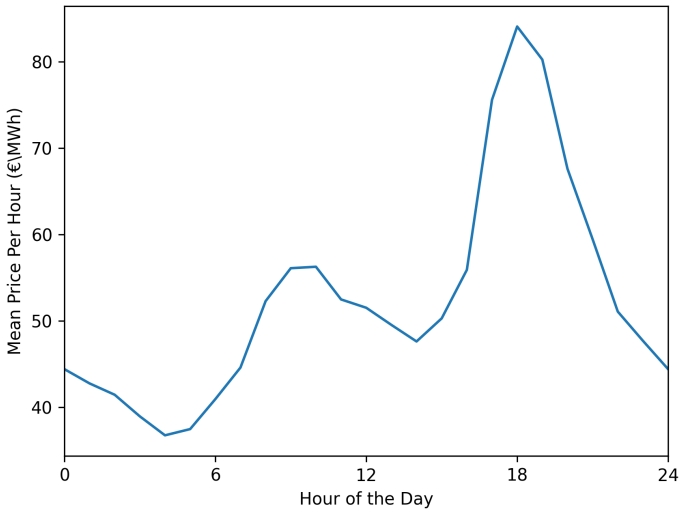


Figure 4.4: The mean price of each settlement period in 2016

Despite the greater revenue generated by the CFPV device the lower efficiency under standard testing conditions (PCE = 0.8% under Air Mass 1.5 Global tilt Refrence Specra (AM1.5G)) would typically lead to high module costs, mostly deriving from the Transparent Conducting Oxide (TCO) [45], and land cost to enable the same generating capacity. In order to quantify the trade-off, estimations of the cost of commercially produced DSSC CFPVs as described by Bristow and Kettle [34] are required. These estimations were produced by Dr. Jeff Kettle of Glasgow University, thorough examining the presented device and applying a bottom-up cost model in alignment with An-

derson [46], in which individual cost elements are identified. Manufacturing costs are based upon the manufacture of 30 MW/year. Through this method a estimated cost of 28.54 €m$^{-2}$ is predicted, and is converted to module cost per unit capacity (€/W$_P$) as shown in table 4.2. The module costs are estimated to increase as PCE under standard testing conditions reduces, with CFPV devices from [34] costing approximately 16 times that of the silicon PV devices. Additionally, land rent is also seen to increase as PCE under standard testing conditions reduces, as can be seen in table 4.3, though this is smaller than the cost of the modules needed for the 5MW$_P$ solar farm.

| **Device** | **Land Rent per Annum (k€)** |
|---|---|
| Conventional Si PV | 20.1 |
| DS PV (Fig 1), $t_{TiO_2} = 12\mu$m | 43.2 |
| DS PV (Fig 1), $t_{TiO_2} = 18\mu$m | 48.0 |
| DS PV (Fig 1), $t_{TiO_2} = 24\mu$m | 51.2 |
| DS PV (Fig 1), $t_{TiO_2} = 48\mu$m | 90.5 |
| SolarPrint DS PV (Fig.1) | 486.4 |

Table 4.3: First year land rental costs of a 5MW$_P$ Solar farm in the UK for each respective device

For the presented characteristics of the CFPV device reported by Bristow and Kettle [34], has been demonstrated to possess an intrinsically high capacity factor and more efficient utilisation of its grid connection. Though, due to the low PCE under standard test conditions leans to substantial module and land costs. Following, the possibility of designing device to posses the CFPV behaviour is explored.

## 4.7 Device fabrication and measurements

Through collaboration with Dr Marina Freitag, and her then PhD student Hannes Michaels, of Newcastle University, DSSCs based upon the architec-

ture as shown in figure 4.5 were fabricated as potential CFPVs and two methods of control over the CFPV behaviour were trialled. These DSSCs were chosen due to their high efficiencies in low light conditions [47]. The basic design of the present CFPVs followed that of Saygili et al., namely comprising the organic Y123 dye and the copper(II/I) bis(4,4',6,6'-tetramethyl-2,2'-bipyridine) bis(trifluoromethanesulfonyl)imide (known as $Cu(tmby)_2$) electrolyte [48]. The counter electrode of the cells was made from poly(3,4-ethylenedioxythiophene) (known as PEDOT), this allows the photoanode to be in direct contact with the cathode [49]. The photoanode comprised of a two-layer design, a photoactive layer of 30nm nanoparticles of an initial thickness of 12$\mu$m, and capped with a 6$\mu$m scattering layer of 400nm $TiO_2$ nanoparticles as a back reflector. Two methods of control over the CFPV behaviour which were trialled are I) Varying the thickness of the photoactive layer, II) Varying the concentration of Copper(II) within the electrolyte.

Firstly, four thicknesses of the photoactive layer were chosen, 12, 18, 24, and 48 $\mu$m. Under low illumination, as the counter electrode attaches directly to the photoanode, the effective diffusion length of ions within the electrolyte can be assumed to be the total thickness of the photoanode. Therefore, through varying the thickness of $t_{TiO_2}$, as denoted in figure 4.5, the diffusion length of ions within the electrolyte may be controlled. Secondly, with a fixed photoactive layer thickness of 12$\mu$m, several concentrations of copper(II) were tested. The following concentrations of copper(II) within the electrolyte were tested 0, 0.01, 0.02, and 0.06M, the concentration of copper(I) was kept constant at 0.2M. Varying the concentration of copper(II) will vary the number of available ions to transport charges under strong illumination. Under weak illumination, as the concentration of copper(II) is reduced the there exists less recombination sights and more electrons may be collected at the anode.

Figure 4.6 shows the PCE as a function of irradiance for CFPV devices with varying copper(II) concentrations. Similar performance is achieved approaching 0$Wm^{-2}$, compared to their performance under 1000$Wm^{-2}$. However, a

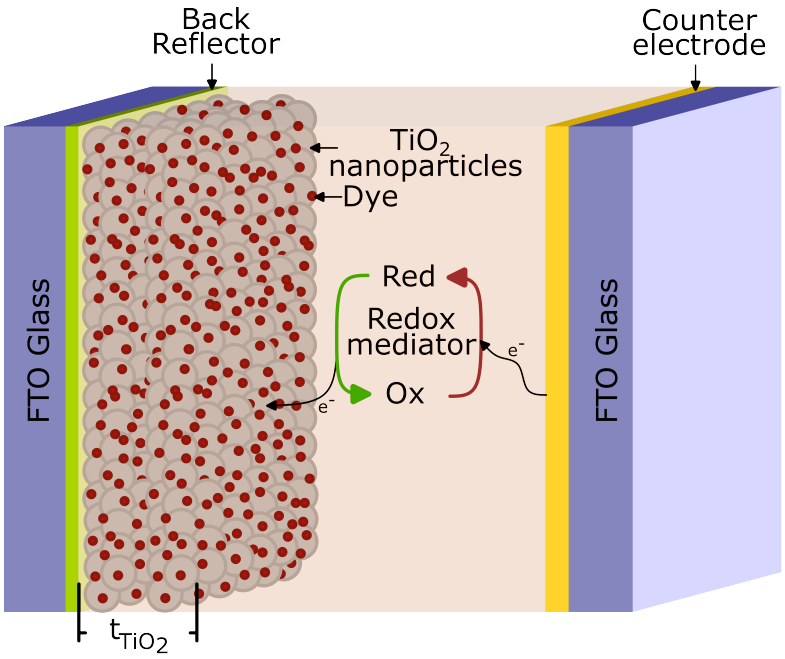


Figure 4.5: Schematic for present devices in which $TiO_2$ thickness was varied over the range $t_{TiO_2}$ = 12, 18, 24, 48 $\mu$m.

consistent change might be expected to be observed, this is not seen, the 0.06M device (red) performs inversely to the other devices of lower concentration. Whilst this has demonstrated that CFPV may be achieved through varying electrolyte species concentrations, the effect does not appear to be consistent. Unlike, that presented when the photoanode thickness is increased.

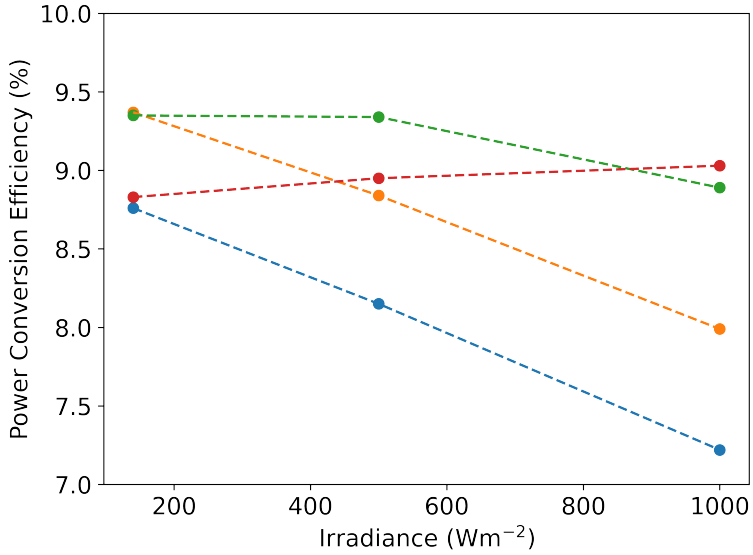


Figure 4.6: PCE irradiance characteristics of CFPV devices through modification of electrolyte $Cu^{2+}$ concentration with $Cu^{2+}_{M}$ = 0 M (blue), 0.01 M (orange), 0.02 M (Green) and 0.06 M (red). The concentration of $Cu^{1+}$ was kept constant between all devices at 0.2 M.

Figure 4.1 show the PCE-irradiance characteristics of the CFPV devices with varying photoanode thickness ($t_{TiO_2}$). With the initial device, with $t_{TiO_2}$ of 12$\mu$m, the characteristics appear constant with irradiance, a behaviour like that of commercial silicon PV [50]. However, the achieved PCE under 1000Wm$^{-2}$ is significantly below that achieved by silicon PV. With thicknesses beyond 12$\mu$m, the PCE-irradiance characteristics slope is seen to increase with lower PCEs achieved for devices with thicker photoanodes under 1000Wm$^{-2}$. The reduction in photocurrent with thicker photoanodes may be explained as DSSC are limited by the diffusion of ions, mass transport, under strong illumination [51]. Therefore, by varying the effective diffusion length we may limit the rate of mass transport, as the incident irradiance reduces the rate of mass transport needed reduces and PCE rises. Here, it has been shown that the PCE-irradiance characteristics of these DSSC may be influenced by their architecture themselves. For this reason, only the varying photoanode thickness devices are considered further within the chapter.

# 4.8 Energy systems modelling utilising designed CFPV devices

The PCE - irradiance characteristics of the devices of varying photoanode thickness, $t_{TiO_2}$, are shown in figure 4.1 form a series with the Bristow and Kettle device [34]. The Bristow and Kettle device [34] representing an extreme case of the thickest $t_{TiO_2}$ devices ($t_{TiO_2} = 48$ $\mu$m) with the lowest efficiency under 1000Wm$^{-2}$. As the $t_{TiO_2}$ is reduced from 48 $\mu$m to 12 $\mu$m, the PCE under standard testing conditions is increased, whereas the PCE under low illumination stays largely constant.

The predictions by the model for the designed CFPV are shown in table 4.2. Devices of photoanode thickness of 12 $\mu$m, 18 $\mu$m and 24 $\mu$m, whose effect upon the grid, are shown in figures 4.7 and 4.8, Their limited increase in PCE as incident irradiance reduced ($E(140\text{Wm}^{-2}) \leq 1.1$) leads to limited improvement to revenue, decarbonisation and capacity factor.

CFPV $t_{TiO_2} = 12$ $\mu$m

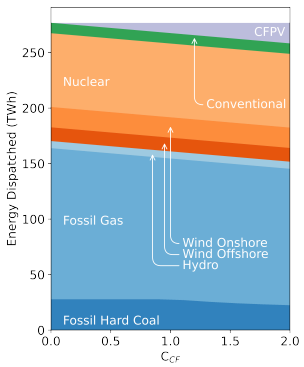


(a)

CFPV $t_{TiO_2} = 18$ $\mu$m

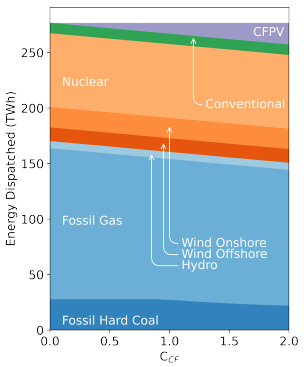


(b)

CFPV $t_{TiO_2} = 24$ $\mu$m

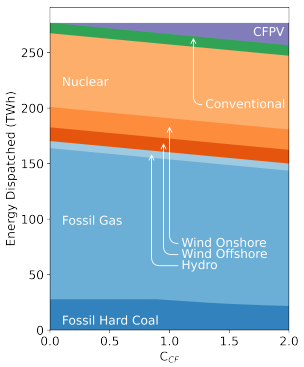


(c)

Figure 4.7: Annual energy dispatched as a function of additional CPFV capacity. Figures (a,b,c) show the annual generation mix with devices of increasing photoanode thickness.

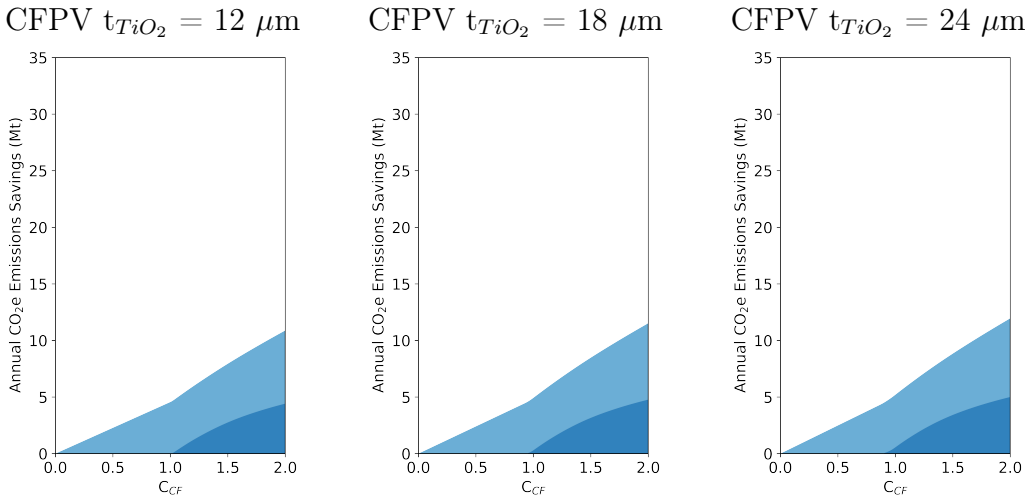


Figure 4.8: Annual carbon savings as a function of additional CPFV capacity. Figures (a,b,c) show the source of carbon savings from reduction in Gas (Light Blue) and Coal (Dark Blue) emissions.

In contrast to the $t_{TiO_2} = 48\mu$m device, where PCE increases by $E(140\text{Wm}^{-2})$ = 1.9 which lead to both substantial changes in generation and carbon emissions, the 12 $\mu$m, 18 $\mu$m and 24 $\mu$m devices see a much reduced change.

Concentrating upon capacity factor, the $t_{TiO_2}$ = 12 $\mu$m devices has a predicted capacity factor of 8.87% as compared to the 14.5% predicted for the $t_{TiO_2}$ = 48 $\mu$m, more than 60% greater. This increase in capacity factor is greater than that achieved through the implementation of single-axis (∼10-35%) and dual-axis (∼30-45%) tracking systems [52, 53], without the additional mechanical complexity. Additionally, examining the change in $CO_2$e emissions, we see an up to 60% decrease in $CO_2$e emissions for enhancement of $E(140\text{Wm}^{-2})$=1.9. These data emphasise that *the benefits associated with CFPV are due to an increase in PCE with reducing light intensity, and not the absolute value of PCE at low irradiance.*

Unlike the effect upon, capacity factor and $CO_2$e emissions, the costs associated with the designed CFPV devices is determined by the PCE of the device under standard testing conditions, as this determined the rated power of the solar installation. Therefore, higher achieved PCE under standard test conditions will lead to reduced costs. Due to this, the designed CFPV devices

are predicted to have a much lower module cost than the Bristow and Kettle device [34]. Comparing costs to the silicon PV device, the $t_{TiO_2} = 48\mu$m is 3 times higher, whilst the Bristow and Kettle [34] CFPV device is 16 times higher. This has shown that varying the photoanode thickness offers control over both the CFPV benefits, increasing both capacity factor and $CO_2$e emissions savings, as well as module cost. However, control over these factors was achieved by controlling efficiency under standard testing conditions, creating a trade-off between costs (controlled by PCE under AM1.5G) and the enhanced capacity factor (controlled by PCE increasing with reducing light intensity).

Due to this trade off, varying the photoanode thickness may not realise low costs and enhanced capacity factors within the same device. Despite this, it is important to remember that ESOs must ensure the reliable power is supplied to balance demand, especially so with higher penetrations of variable renewable generation. Examples of which within the UK may be Dinorwig power station, fast providing short term generation, or Nuclear which provides much of the UK's base load due to it highly reliable nature despite a high Levelised Cost of Energy (LCOE) [54]. Thus, introducing variety into variable solar generation may present value from a ESOs perspective.

The cost of the designed CFPV devices, raises the question as to how both benefits of low cost and enhanced capacity factor within the same device. Here two methods are shown to give high CFPV PV, modification of electrolyte concentrations and photoanode thickness, but both give similar results under standard test conditions. Despite this, module cost may be reduced through increased PCE under AM1.5G, with the current record efficiency for a DSSC at 13.5% [55], higher than the most efficient presented device.

Greater opportunity may be in the creation of CFPV devices with organic [24, 25, 26, 27, 28] and perovskite [29, 30, 31, 32] absorber layers, as higher PCEs under standard test conditions may ensure module costs remain low whilst achieving the benefits of increasing PCE with reducing light intensity.

To show this opportunity, the plant dispatch analysis was repeated on two promising devices displaying CFPV behaviour. A quaternary organic PV device as reported by Nam et. al [24], and a MAPI perovskite PV device reported by Du et. al [29].

The predicted capacity factor for these devices as a function of enhancement factor (l = 140 $Wm^{-2}$) with all other devices considered in this chapter is shown in figure 4.9. Due to the generality of the approach, it is seen that capacity factor varies approximately linearly with enhancement factor. Candidate PVs devices for CFPV applications can be easily accessed through lab experiments, PCE determination with solar simulator under varying light intensities. A more in-depth assessment of a device may require measurement of the PCE - irradiance characteristic and plant dispatch analysis.

The predicted capacity factors for the organic and perovskite PV devices are lower compared to the DSSC presented in this chapter, however these devices were not explicitly developed for CFPV devices.

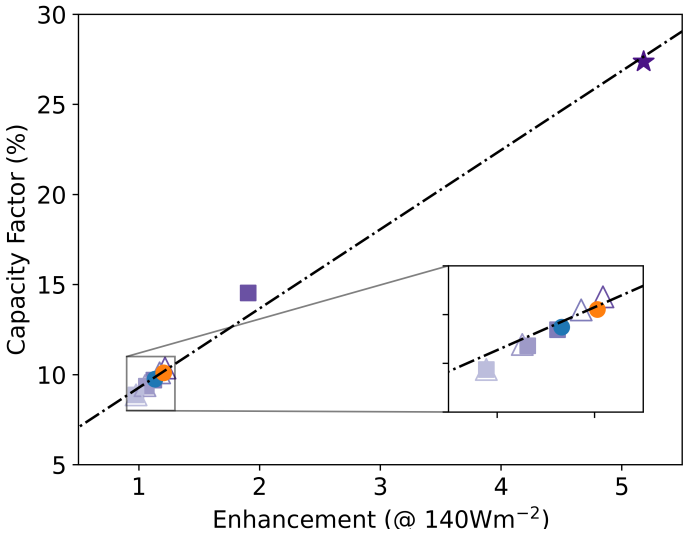


Figure 4.9: Predicted UK capacity factor for PV devices considered in this study as a function of enhancement factor at 140 $Wm^{-2}$. Purple closed squares: Dye-Cell CFPV with $t_{TiO_2}$ from 12 $\mu$m (light) to 48 $\mu$m (dark, purple) - Table 1; Purple open triangles: Dye-Cell CFPV with $Cu_M^{2+}$ from 0 M (light) to 0.06 M (dark) - Supporting Information Fig S6; Purple closed star - Bristow and Kettle Dye-Cell PV [34]; Blue filled circle - Du *et al* Perovskite PV [29]; Orange filled circle - Nam *et al* Organic PV [24]

## 4.9 Conclusions

In this chapter, the concept of high capacity factor PV was introduced, where the through engineering the PCE to increase as irradiance decreases, reducing the variation in output power. Modelling the UKs WASG and the introduction of CFPVs demonstrates these devices are more effective at reducing $CO_2e$ emissions than an equal capacity of silicon PV, by reducing the need for carbon intensive generation, as well as generating greater revenue by better meeting demand. Experimental data for DSSC exhibiting CFPV behaviour has been shown, where the PCE - irradiance characteristic has been tuned, allowing control over the capacity factor, carbon abatement and capacity factor offered by the technology. This approach presents an alternative to the sole reliance upon energy storage and demand side management in order to account for the variability associated with renewable generation, by inherently reducing the variability within the PV device itself. This concept was also shown not to be limited to DSSC, with reports suggesting both organic and perovskite devices may be developed further to exhibit CFPV behaviour, presenting a new avenue for emerging PV technologies

# Bibliography

[1] IRENA, "Electricity storage and renewables: Costs and markets to 2030," International Renewable Energy Agency, Report, 2017.

[2] IRENA, "Demand side flexibility for power sector transformation: Analytical brief," International Renewable Energy Agency, Report, 2019.

[3] C. Williams *et al.*, "Decarbonising electrical grids using photovoltaics with enhanced capacity factors," *Energy and Environmental Science*, 2023.

[4] IEA, "Renewable energy market update," Report, 2020.

[5] U. E. I. Administration, "Levelised costs of new generation resources," Report, 2022.

[6] IRENA, "Renewable power generation costs in 2021," Report, 2021.

[7] IEA, "Net zero by 2050: A roadmap for the global energy sector," Report, 2021.

[8] IRENA, "Future of solar photovoltaic: Deployment, investment, technology, grid integration and socio-economic aspects," Report, 2019.

[9] Shell, "Sky: Meeting to goals of the paris agreement," 2018.

[10] C. ISO, "What the duck curve tells us about managing a green grid," Report, 2016.

[11] A. Kharrazi, V. Sreeram, and Y. Mishra, "Assessment techniques of the impact of grid-tied rooftop photovoltaic generation on the power quality of low voltage distribution network - a review," *Renewable and Sustainable Energy Reviews*, vol. 120, p. 109643, 2020.

[12] M. Karimi, H. Mokhlis, K. Naidu, S. Uddin, and A. H. A. Bakar, "Photovoltaic penetration issues and impacts in distribution network – a re-

view," *Renewable and Sustainable Energy Reviews*, vol. 53, pp. 594–605, 2016.

[13] D. Millstein *et al.*, "Solar and wind grid system value in the united states: The effect of transmission congestion, generation profiles, and curtailment," *Joule*, vol. 5, no. 7, pp. 1749–1775, 2021.

[14] J. Chase, "View from the solar industry: We don't need cop26 to shine, but what should we worry about?" *Joule*, 2022.

[15] V. Sivaram and S. Kann, "Solar power needs a more ambitious cost target," *Nature Energy*, vol. 1, no. 4, p. 16036, 2016.

[16] "National statistics digest of uk energy statistics (dukes)," 2022.

[17] U. E. I. Administration, "Annual electric generator inventory," Report, 2019.

[18] E. J. Lantz, A. D. Riva, J. Hethey, and A. Vitina, "Iea wind tcp task 26: Impacts of wind turbine technology on the system value of wind in europe," Report, 2017.

[19] R. Wiser, D. Millstein, M. Bolinger, S. Jeong, and A. Mills, "The hidden value of large-rotor, tall-tower wind turbines in the united states," *Wind Engineering*, vol. 45, no. 4, pp. 857–871, 2021.

[20] S. Abdallah, "The effect of using sun tracking systems on the voltage–current characteristics and power generation of flat plate photovoltaics," *Energy Conversion and Management*, vol. 45, no. 11, pp. 1671–1679, 2004.

[21] M. Bolinger and J. Seel, "Utility scale solar: Empirical trends in project technology, cost, performance and ppa pricing in the united states 2018," Laurence Berkeley National Laboratory, Report, 2018.

[22] H. Wirth and K. Schneider, "Recent facts about photovoltaics in germany," *Fraunhofer Ise*, vol. 92, 2015.

[23] D. Peper, S. Lange, and C. Kost, "Photovoltaikzubau in deutschland in zahlen," *Fraunhofer ISE*, 2019.

[24] M. Nam *et al.*, "Semi-transparent quaternary organic blends for advanced photovoltaic applications," *Nano Energy*, vol. 58, pp. 652–659, 2019.

[25] Y. Kwon, C. Lee, M. Nam, and D.-H. Ko, "Revealing conflicting effects of solvent additives on morphology and performance of non-fullerene organic photovoltaics under different illuminance conditions," *Dyes and Pigments*, vol. 207, p. 110754, 2022.

[26] R. Munir *et al.*, "Air-processed organic photovoltaics for outdoor and indoor use based upon a tin oxide-perylene diimide electron transporting bilayer," *Advanced Materials Interfaces*, vol. 9, no. 3, p. 2101918, 2022.

[27] X. Rodríguez-Martínez *et al.*, "Matching electron transport layers with a non-halogenated and low synthetic complexity polymer: fullerene blend for efficient outdoor and indoor organic photovoltaics," *Journal of Materials Chemistry A*, vol. 10, no. 19, pp. 10 768–10 779, 2022.

[28] R. Steim *et al.*, "Organic photovoltaics for low light applications," *Solar Energy Materials and Solar Cells*, vol. 95, no. 12, pp. 3256–3261, 2011.

[29] T. Du *et al.*, "Light-intensity and thickness dependent efficiency of planar perovskite solar cells: charge recombination versus extraction," *Journal of Materials Chemistry C*, vol. 8, no. 36, pp. 12 648–12 655, 2020.

[30] Y. Reyna *et al.*, "Performance and stability of mixed fapbi3 (0.85) mapbbr3 (0.15) halide perovskite solar cells under outdoor conditions and the effect of low light irradiation," *Nano Energy*, vol. 30, pp. 570–579, 2016.

[31] V. Stoichkov *et al.*, "Outdoor performance monitoring of perovskite solar cell mini-modules: diurnal performance, observance of reversible degra-

dation and variation with climatic performance," *Solar Energy*, vol. 170, pp. 549–556, 2018.

[32] J. Dagar, S. Castro-Hermosa, G. Lucarelli, F. Cacialli, and T. M. Brown, "Highly efficient perovskite solar cells for light harvesting under indoor illumination via solution processed sno2/mgo composite electron transport layers," *Nano Energy*, vol. 49, pp. 290–299, 2018.

[33] E. Tanaka, H. Michaels, M. Freitag, and N. Robertson, "Synergy of co-sensitizers in a copper bipyridyl redox system for efficient and cost-effective dye-sensitized solar cells in solar and ambient light," *Journal of Materials Chemistry A*, vol. 8, no. 3, pp. 1279–1287, 2020.

[34] N. Bristow and J. Kettle, "Outdoor organic photovoltaic module characteristics: Benchmarking against other pv technologies for performance, calculation of ross coefficient and outdoor stability monitoring," *Solar Energy Materials and Solar Cells*, vol. 175, pp. 52–59, 2018.

[35] M. O. Reese *et al.*, "Consensus stability testing protocols for organic photovoltaic materials and devices," *Solar Energy Materials and Solar Cells*, vol. 95, no. 5, pp. 1253–1267, 2011.

[36] IEA, "Real-time electricity tracker," 2023. [Online]. Available: https://www.iea.org/data-and-statistics/data-tools/real-time-electricity-tracker

[37] C. ISO, "Caiso," 2023. [Online]. Available: https://www.caiso.com

[38] R. Electrica, "Demanda de energÍa elÉctrica en tiempo real," 2023. [Online]. Available: https://demanda.ree.es/visiona/home

[39] M. Bolinger, J. Seel, C. Warner, and D. Robson, "Utility-scale solar, 2022 edition," Report, 2022.

[40] Elexon, "Balancing mechanism reporting service (bmrs)," 2022. [Online]. Available: https://www.bmreports.com

[41] "PV_live – Sheffield Solar." [Online]. Available: https://www.solar.sheffield.ac.uk/pvlive/

[42] Ricardo-AEA, "Wales energy energy toolkit: Grid connection module," 2015.

[43] J. Chase, "View from the solar industry: We don't need cop26 to shine, but what should we worry about?" *Joule*, vol. 6, no. 3, pp. 495–497, 2022.

[44] "Imbalance pricing - bsc guidance notes - elexon bsc."

[45] G. Hashmi *et al.*, "Review of materials and manufacturing options for large area flexible dye solar cells," *Renewable and Sustainable Energy Reviews*, vol. 15, no. 8, pp. 3717–3732, 2011.

[46] J. Anderson, "Determining manufacturing costs," *CEP*, pp. 27–31, 2009.

[47] A. B. Muñoz-García *et al.*, "Dye-sensitized solar cells strike back," *Chemical Society Reviews*, vol. 50, no. 22, pp. 12 450–12 550, 2021.

[48] Y. Saygili *et al.*, "Copper bipyridyl redox mediators for dye-sensitized solar cells with high photovoltage," *J. Am. Chem. Soc.*, p. 10, 2016.

[49] Y. Cao, Y. Liu, S. M. Zakeeruddin, A. Hagfeldt, and M. Grätzel, "Direct contact of selective charge extraction layers enables high-efficiency molecular photovoltaics," *Joule*, vol. 2, no. 6, pp. 1108–1117, 2018.

[50] "Product Specification - REC Twinpeak 4 Black Series." [Online]. Available: https://www.recgroup.com/sites/default/files/documents/ds_rec_twinpeak_4_black_series_en.pdf?t=1663844604

[51] R. García-Rodríguez, R. Jiang, E. J. Canto-Aguilar, G. Oskam, and G. Boschloo, "Improving the mass transport of copper-complex redox mediators in dye-sensitized solar cells by reducing the inter-electrode distance," *Physical Chemistry Chemical Physics*, vol. 19, no. 47, pp. 32 132–32 142, 2017.

[52] A. F. Almarshoud, "Performance of solar resources in saudi arabia," *Renewable and Sustainable Energy Reviews*, vol. 66, pp. 694–701, 2016.

[53] E. Drury, A. Lopez, P. Denholm, and R. Margolis, "Relative performance of tracking versus fixed tilt photovoltaic systems in the usa," *Progress in Photovoltaics: Research and Applications*, vol. 22, no. 12, pp. 1302–1315, 2014.

[54] N. A. Office, "Nuclear power in the uk," National Audit Office, Report, 2016.

[55] D. Zhang *et al.*, "A molecular photosensitizer achieves a voc of 1.24 v enabling highly efficient and stable dye-sensitized solar cells with copper(ii/i)-based electrolyte," *Nature Communications*, vol. 12, no. 1, p. 1777, 2021.

# Chapter 5

# Forecasting the Effect of Wildfires, Dust Storms and Pollution on Future PV Energy Production

## 5.1 Overview

In this chapter, the atmospheric composition model developed, in section 3.6, is used to explore the impacts of changes in composition of the atmosphere upon future Photovoltaic (PV) generation. First, the model is validated through examining PV output during Californian wildfires in 2020. The impact of changes in the composition of the atmosphere upon national PV generation is further examined by consideration of wildfires in Australia. Transcontinental dust ejection in the form of Saharan mineral dust storms of 2008 and 2020 is also examined. The impact of policy changes related to air quality, and how it affects PV generation, is shown using the case study of Beijing. Lastly, the effect device design may impact PV response to changes to the composition of the atmosphere, namely the choice of active layer materials within Organic Photovoltaics (OPVs) is explored, showing how future PVs may be designed to be tolerant to a changing atmosphere.

## 5.2 Introduction

As the concentration of Carbon Dioxide Equivilent ($CO_2e$) gasses continue to increase, alongside global average temperatures, efforts must be taken to reduce $CO_2e$ emissions to a net-zero by 2050. To enable this net-zero, low carbon renewable generation, such as PV, must replace high carbon generation sources. The impacts the incident spectrum has upon the efficiency of a PV device has long been established [1], as well as the influence of the local atmosphere upon this incident spectrum [2]. Despite our best efforts, global average temperatures will rise [3] resulting in an increase in events which may cause changes to the local composition of the atmosphere, such as wildfires [4] and dust storms [5]. Due to the increase in the prevalence of such events, and the increasing penetration of PV, the impact of these events on future PV generation will grow [6]. Therefore, as PV penetration increases, understanding the interaction between power generation from PV and changes to the local atmosphere composition is of great importance.

Knowledge of the incident spectrum allows for better material selection to be undertaken and device architecture optimisation. This industry standard benchmark is the AM1.5 spectrum [7], although work considering indoor photovoltaics may utilise other spectra [8]. The AM1.5 spectrum was derived through an atmospheric model, "Simple Model of the Atmospheric Radiative Transfer of Sunshine" (SMARTS) written by C. Gueymard [9]. However, the AM1.5 spectrum does not describe irradiance with changes to the local composition of the atmosphere in mind.

In this chapter the following will be discussed. Firstly, the selection of a representative photovoltaic devices for the studies are selected. Following the selection of the devices, the measure of electrical power loss due to the atmosphere, $W_{loss}$, is introduced. From this the model is sought to be validated, predicting, and examining the effect of Californian wildfires in 2020. With validation demonstrated, the continent scale wildfires of Australia, and their effects upon their electrical grids is examined. Moving from locally derived changes to the atmospheric composition, the effects of the dust storms of the Sahara are examined in both Europe and the Americas. As not all changes to the atmosphere must be for the worst, how the introduction of air quality policy in Beijing, China, has changed the atmosphere and improved solar generation over more than a decade is examined. Lastly, how photovoltaics, particularly, organic photovoltaics may be designed in order to reduce the effects of a changing atmosphere upon their generation is explored. Showing how the previous losses may be mitigated.

## 5.3 Photovoltaic Devices

To examine the effects of changes to the atmospheric composition on PV generation, a model PV device must be selected. Here silicon [10] was chosen due to its dominance in commercial applications. Passivated Emitter and Rear Contact (PERC) devices were chosen due to their commercial success.

To enable this, light and dark Current-Voltages (JVs) as well as External

Quantum Efficency (EQE) characteristics are required for use within a single diode model as described in section 3.6. However, these data have not been reported for a single device. Hence, data for two similar PERC devices were used: light and dark JVs from Oh et al. [11], and EQE characteristics from Zhang et al. [12]. Both devices are of similar p-type monocrystalline architectures, although the scale of the Oh et al. device in 10 times smaller than that presented by Zhang et al., as EQE should be invariant with device size no issues are expected from this disparity.

## 5.4 Predicted Photovoltaic Generation and Losses

Using the atmospheric composition model, predictions may be made for the PV generation under measured atmospheric conditions, as was described in section 3.6. To model the effect of changes in composition, e.g. due to wildfires, pollution and mineral dust storms, the electrical power loss due to these changes is defined as $W_{loss}$ derived from comparing the difference between predictions of electrical generation under measured atmospheric conditions $W_{measured}$ and electrical generation predicted under a pristine "pre-industrial" atmosphere, prior to anthropogenic pollution $W_{pristine}$ as can be seen in equation 5.4.1. Values of $W_{loss}$ are all negative, as more power is generated under the pristine atmosphere than that measured. Thus, the more negative $W_{loss}$ shows more energy has been lost due to the changes to the composition of the atmosphere. In the case of the presented work, temperature, humidity, and pressure levels of the measured atmospheric conditions were applied to the pristine scenario. $W_{loss}$ is presented in units of $Wm^{-2}$ throughout the chapter.

$$W_{loss} = W_{measured} - W_{pristine} \tag{5.4.1}$$

## 5.5 Validation and Examination of Model Utilising Californian Wildfires of 2020

Applying the atmospheric composition model, as discussed in section 3.6, the impacts of a changing atmospheric composition on PV generation can be examined. California was selected as a test case due to the availability of PV generation data from the California Independent Systems Operator (CAISO), the Californian Wide Area Synchronous Grid (WASG). The model is validated by examination of wildfires in 2020 within California. Californian wildfires were selected as a test case, as the model's predictions may be compared to that reported by the Californian WASG.

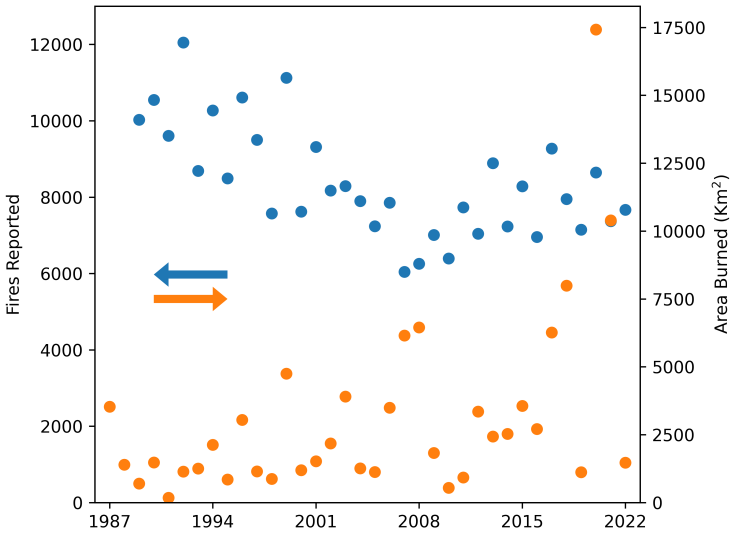


Figure 5.1: Evolution of wildfires from 1987 till 2022 within California. Blue represents the number of fires reported, and orange represent the total area burned by those fires. These values are an aggregation of reports through the California Department of Forestry and Fire Protection, Federal Firefighting Agencies, and Local Government. [13]

California has long suffered from wildfires [14], however in recent years (as seen in figure 5.1) the number of fires reported has plateaued, yet the area these fires burn is still increasing. 2020 was the worst wildfire season on record, with 8,648 individual fires burning a combined 4 million hectares of land [15], 4% of the total land area of California. However, this wildfire

impacted a greater area than that burned. Figure 5.2a show the worst fire of the 2020 wildfire season, the August complex [16], which burnt from the $16^{\text{th}}$ of August till the $12^{\text{th}}$ of November. The fire can be seen to increase in intensity, reaching a peak electrical power loss, $W_{loss}$, of -102.44 $\text{Wm}^{-2}$, 10% of full sun, before reducing in intensity.

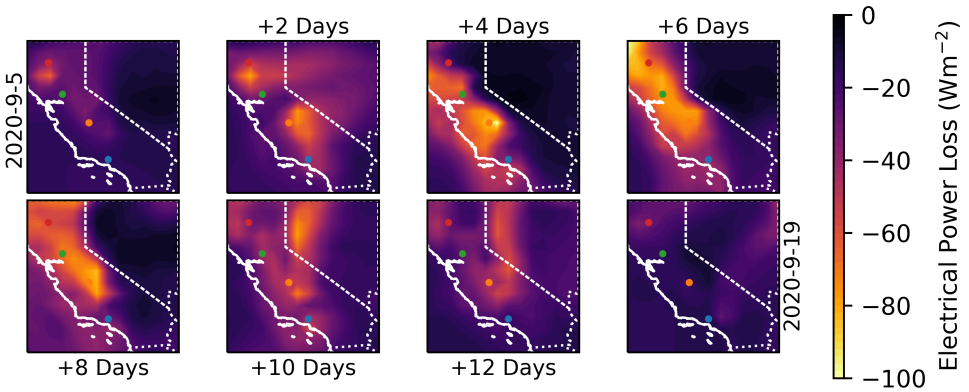


(a)

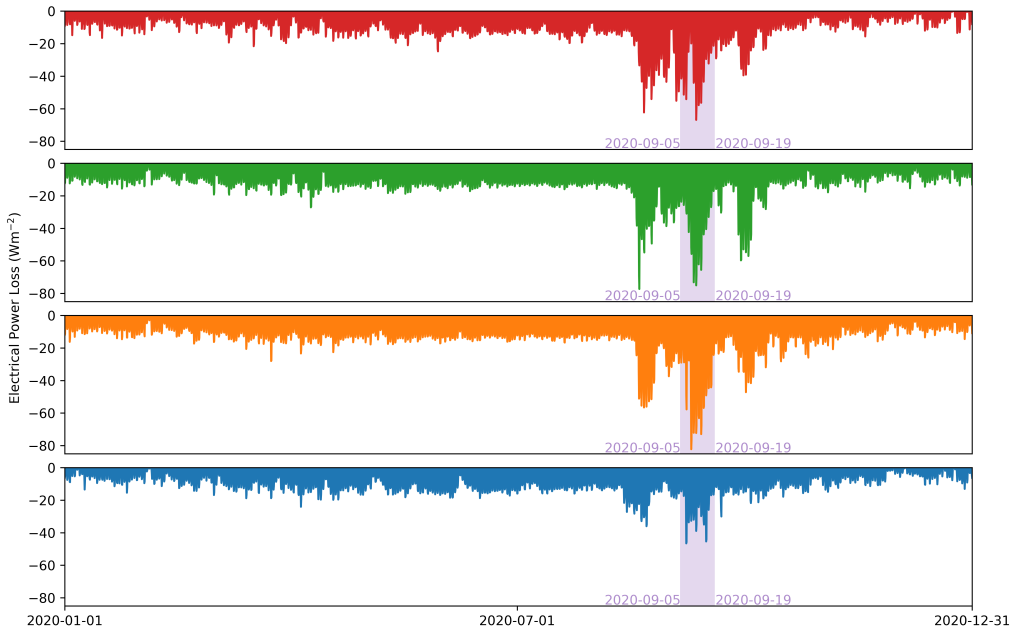


(b)

Figure 5.2: (a) Electrical Power Losses due to atmospheric conditions from a Silicon Solar Cells in California at 12:00PM from the 5-19th of September 2020 in 48hr increments. Coloured Dots indicate three locations to be further examined, Blue: Santa Clarita, Orange: Fresno, Green: Sacramento, Red: Redding. (b) Daily Mean Electrical Power Losses due to atmospheric conditions at the indicated locations (Santa Clarita, Fresno, Sacramento, Redding) over the course of 2020.

Whilst figures 5.2a may show the geographical scale of the influence of fires on PV generation, it does not convey electrical power loss in context of the year.

The electrical power loss experienced in a selection of locations is shown in as in figure 5.2b for all 2020. These locations being Santa Clarita in blue, Fresno in orange, Sacramento in green, and Redding in red. The worst effected location, Fresno, is shown to lose a peak of -82.25 $Wm^{-2}$. Over the course of the August Complex, the average $W_{loss}$ was found to be -9.48 $Wm^{-2}$. By contrast over the same date range in the least effected area, Santa Clarita, the average $W_{loss}$ is found to be -5.93 $Wm^{-2}$. It is of note that the measured electrical power loss, $W_{loss}$ in all locations does not exceed 0, this is expected as more changes have occurred to the atmosphere than wildfires alone, such as changes caused by anthropogenic climate change. From the discussed figures it can be seen, whilst limited in duration, wildfires are predicted to significantly affect the generation capability of PV.

### Benchmarking Predicted Generation

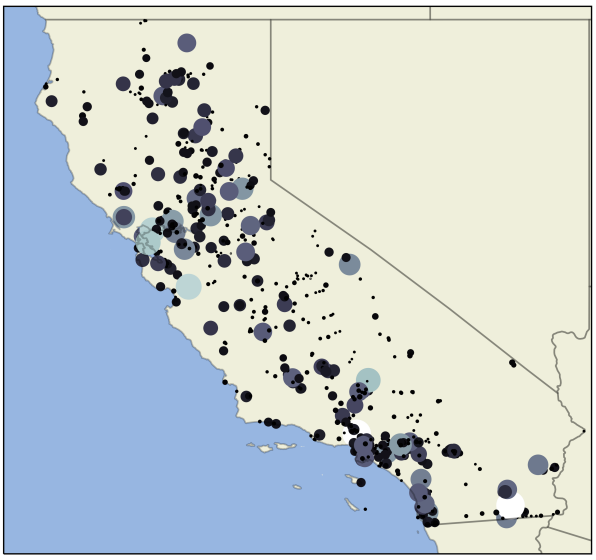

Figure 5.3: Locations of commercial solar installations within California, the size and colour are indicative of the relative size of the installations [17]

Utilising the locations and capacity of commercial solar installations within California [17] shown in figure 5.3, a geographic and capacity weighted measure of PV generation in California may be calculated. The CAISO WASG offers the opportunity to validate the predicted PV energy generation against

actual PV generation reported by CAISO and calculate a representative $W_{loss}$ for California, as can be seen in figure 5.4.

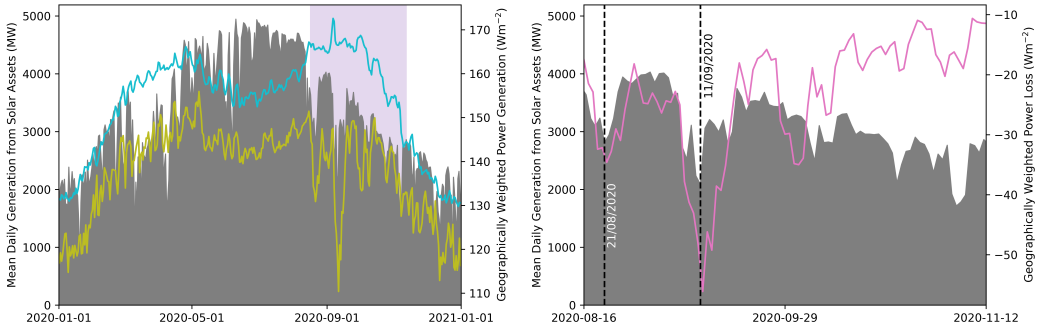


(a) (b)

Figure 5.4: (a) show a map of California with the capacity and location of each solar farm indicated by their respective dot. (b) The gray shows the sum of the dispatched energy from solar assets by California Independent System Operator (CAISO). The green and blue line indicate the geographically weighted power generation per meter squared over the course of a year within a pristine and polluted atmosphere, respectively.

Figure 5.4a shows the reported daily mean PV generation from CAISO in grey, and the predictions of PV generation under the measured and pristine atmosphere are shown by the green and blue lines respectively. As seen in all data presented, we see the seasonal variation in generation, both as reported by CAISO and predicted by the model. The peak in generation reported by CAISO is seen over the middle of the year, but due to the panel tilt in the model being fixed at the midpoint between that ideal for summer and winter, two peaks are seen in spring and autumn. The effects of single or dual axis tracking upon PV electrical power loss has yet to be seen in literature.

From figure 5.4a, first it can be seen that the predicted generation from the measured atmosphere is always lower than that predicted for the pristine atmosphere, with an average difference over the year of -15.51 $\mathrm{Wm}^{-2}$. The difference between the generation seen in the measured and pristine atmosphere reaches its maximum during the period of the August complex, a maximum of -56.12 $\mathrm{Wm}^{-2}$, the period indicated in purple in figure 5.4a.

The maximum loss is also reflected in the PV generation reported by

CAISO, where local minima can be seen on the 21/08/2020 and 11/09/2020. These can be seen in more detail in figure 5.4b. Examining both the PV generation reported by CAISO and that predicted by the model, comparing the minima of the troughs with the mean of the week proceeding shows a reduction in generation. The first minima on the 21/08/2020 shows a 19% and 10% reduction reported by CAISO and predicted by the model respectively. while secondary minima, on the 11/09/2020, shows a 55% and 22% reduction respectively.

Throughout the generation reported by CAISO, troughs are present which are not predicted by the model. These missing troughs may be explained by the differences between the data reported by CAISO and that considered by the model. Firstly, it is important to remember that the atmospheric composition model is a clear sky model, as no cloud cover is present the maximum irradiance for the time of day is always incident upon the device modelled. Therefore, some missing troughs within the predicted generation may be attributed to the absence of cloud cover. Additionally, the atmospheric composition model does not account for other factors which may effect the predicted generation such as wind cooling upon the simulated PV devices [18]. Further, the generation reported by CAISO, it is energy dispatched rather than the generation potential available to CAISO for dispatch, i.e. the generation reported may be curtailed. Which cannot be replicated by the atmospheric composition model. Curtailment is shown to be responsible for the reduced energy dispatched from PV generation in April, as reported by CAISO [19], this was found to be due to a combination of factors. PV generation increasing throughout the month, mild temperatures reducing demand due to lower heat management requirements, and the COVID-19 lockdown at this time. In combination these reasons saw PV generation curtailed for economic reasons, resulting in 318,500 MWh being curtailed over the month of April.

Due to the number of factors not considered in the presented model which effect PV generation, a strong correlation may not be expected between the energy dispatched and that predicted. Despite this, an $r^2$ of 0.71 is achieved.

However, we do note that the good alignment between the troughs of reduced energy dispatched from PV and that predicted when the effects of the wildfires is at its strongest.

### Per Atmospheric Component

By identifying the atmospheric components which change in concentration during the wildfires may allow for action to be taken to lessen their effect upon generation, or at least understand. Wildfires can generate many gaseous compounds and additionally aerosols, these may include carbon dioxide ($CO_2$), carbon monoxide ($CO$), nitrogen oxides ($NO_x$), sulphur dioxide ($SO_2$), and Particulate Matter (PM) [20]. Other compounds may be generated by wildfires but are not included within the atmospheric composition model [20]. Through substituting the concentration of components in the measured atmosphere with those found in the pristine atmosphere, a single component at a time, and calculating the difference in generation between the measured atmosphere and that substituted, will show the energy absorbed by the substituted component. From performing this analysis, the three most energy absorbing components in order are, PM, $NO_2$, and $O_3$, can be seen in figure 5.5 at the locations of, Santa Clarita (blue), Fresno (orange), Sacramento (green), Redding (red).

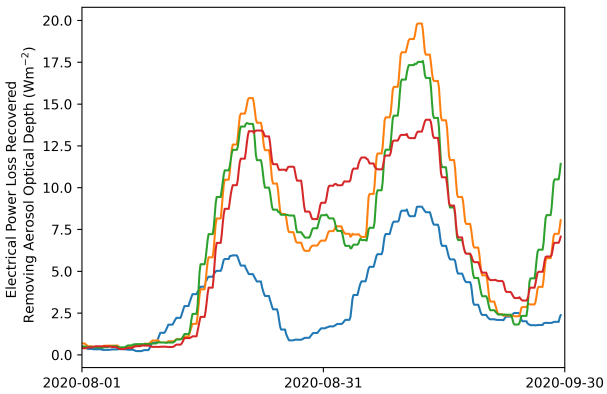


(a)

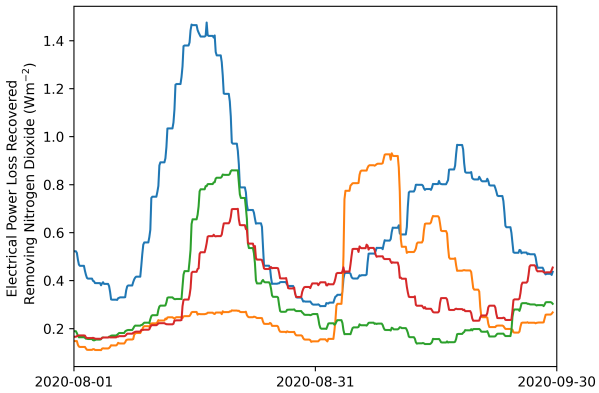


(b)

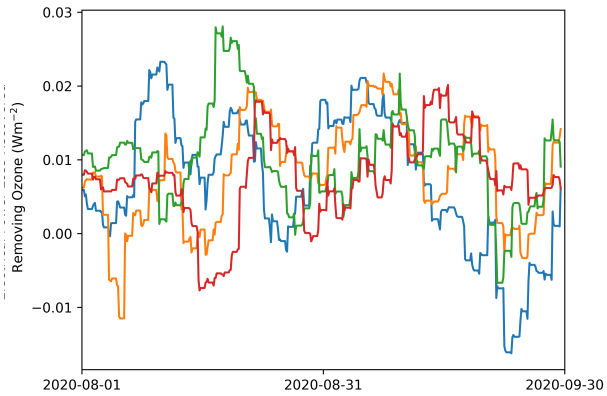


(c)

Figure 5.5: Energy recovered by removing (a) Particulate Matter, (b) Nitrous dioxide, (c) Ozone in the locations Blue: Santa Clarita, Orange: Fresno, Green: Sacramento, Red: Redding. During the period of 01/08/2020 to 30/09/2020.

Of the components presented in figure 5.5 it can be seen that the greatest absorber of energy is found to be PM which is predicted to absorb, at most, 19.81 $Wm^{-2}$ in Fresno. Much less absorbing is nitrogen dioxide with 1.48 $Wm^{-2}$ absorbed, but this is still great compared to the third most absorbing component, ozone, with 0.028 $Wm^{-2}$. Examining figure 5.5 further, it can be seen that both PM and nitrogen dioxide are well aligned with the August complex. Their peak absorption is broadly aligned to the local minima in both reported and predicted PV generation, on the 21/08/2020 and 11/09/2020 as seen in figure 5.4a. Due to this, these components may be attributed to the August complex. Within America, California possesses the strictest laws controlling air quality, including PM [21]. Outside the period of the August complex, PM concentrations are found to be one sixth of those experienced during the wildfires. Therefore, PM could be said to be largely derived from the August complex. Whilst similarly aligned to the August complex, nitrogen dioxide may not be wholly attributed to the wildfires. As a significant source of nitrogen dioxide is found to be the burning of fuels with internal combustion engines [22], but if the temperature of a wildfire is high enough, nitrogen dioxide may be generated. Contrastingly, ozone does not demonstrate such alignment with the August complex. A possible source of ozone near sea level may be the decomposition of nitrogen dioxide to ozone as it is exposed to ultraviolet radiation [23]. However, a great deal of noise is seen in figure 5.5c, this is likely due to the low concentrations of ozone that were found at sea level. The small sum of energy absorbed by both nitrogen dioxide and ozone during the period of the August complex, shows that studies which concentrate upon PM may still accurately resolve the effects of wildfires on PV generation [24].

The impacts of wildfires upon California are likely to persist in future, as demand for electricity grows, and is moved towards a renewable powered WASG, the impacts upon energy generation may grow. By 2050, across all scenarios considered by California, grid connected PV are predicted to grow to a capacity of 101 to 161 $GW_p$ resulting in a penetration of 18 to 22 % [25].

Assuming these future PVs possess a mean efficiency of 20%, the installed area would range from 505 to 805 km$^2$. If the events of the August complex were to reoccur in 2050, this would result in losses of approximately 10.1 to 16.1 GWh. These losses are limited due to PVs the inherently intermittent nature, limiting the maximum supportable installed penetration. However, with increasing temperatures the potential for a repeat of a wildfire of the scale of the August complex grows, adding to the intermittency of future PV.

## 5.6 Impacts of Wildfires on Australian Photovoltaic Generation

Australia, much the same as California, has long since suffered from wildfires, however due to the vast land area of Australia there is greater potential for these wildfires to become uncontrolled [26]. The 2019–2020 wildfires in Australia burnt more than 10 million hectares [27], further, indicating the anthropogenic impact upon climate change and consequently wildfires [28]. Here, the atmospheric composition model is applied to the wildfires in Australia in late 2019 to early 2020. Figure 5.6 shows the geographic impact of a wildfire in early 2020 in terms of electrical power loss, $W_{loss}$.

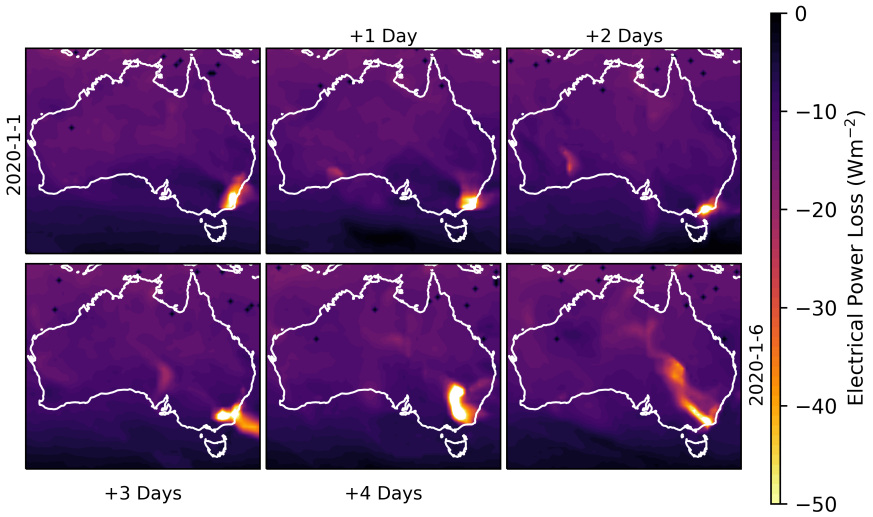


Figure 5.6: Electrical Power Losses due to atmospheric conditions from a Silicon Solar Cells in Australia at 12:00PM from the 1-6th of January 2020 in 24hr increments.

From figure 5.6 the wildfire be seen to cause losses in a large area through the smoke emitted. On the 6th of January, the area effected by the smoke from the wildfires is found to be 538,160 km$^2$, this is more than 25 times the size of Wales or 1.2 times the area of California. Due to the vast area effected, a much greater installed capacity of PV may be effected, potentially leading to large impacts for Australian WASGs.

The impacts of the wildfires upon PV generation seen by Australian WASGs, can be seen though applying a geographic and capacity weighted mean, similarly to California. However, due to the large percentage of rooftop PV installations, with 30% of detached homes possessing such an installation [29], both commercial and residential PV installations on a per-postcode basis were considered [30]. Using the weighted mean, the atmospheric composition model was applied to both the measured atmosphere and pristine atmosphere. Predictions of the geographic and capacity weighted mean PV generation under both conditions can be seen in figure 5.7.

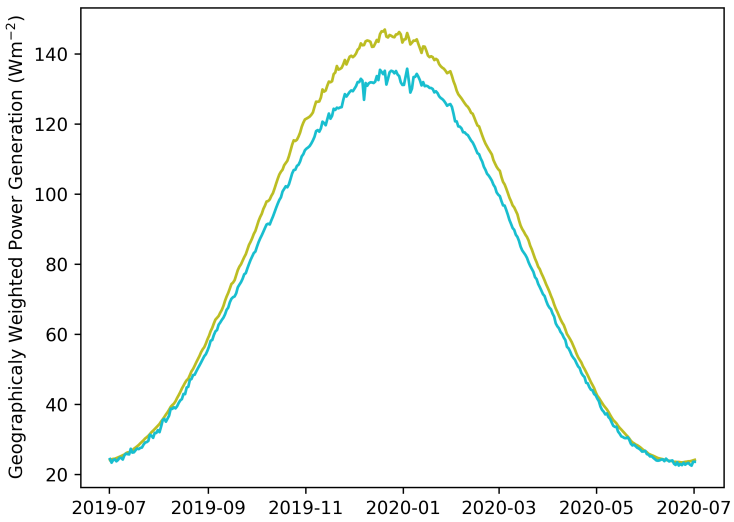


Figure 5.7: The green and blue lines indicate the geographically weighted power generation per meter squared over the course of a year within a pristine and measured atmosphere, respectively. The capacity is gathered from [30] and indicate the capacity associated with each post code.

Figure 5.7 show that over the period considered, as expected, the generation predicted from the measured atmosphere is lower than that predicted for the pristine atmosphere. From these predictions, it was found that the average electrical power loss, $W_{loss}$, was of 5.28 Wm$^{-2}$. Considering the Australian wildfires season in question, from November 2019 to March 2020, over this period the average electrical power loss was found to be 9.68 Wm$^{-2}$. Therefore, the wildfires of this season did cause a measurable impact upon PV generation.

However, unlike California, no large troughs in PV generation are predicted for the measured atmosphere during the wildfires. The lack of troughs seen in this period may be explained through the intersection of the distribution of the PV assets and areas effected by wildfires. The distribution of PV assets may be seen in figure 5.8a, and the distribution of fire risk throughout Australia can be seen in figure 5.8b. Examining these figures, most PV assets are installed in areas of lower fire risk. Further, the lack of troughs in this case indicated that the wildfires were not well aligned to PV assets,

showing the importance of examining changes to the local composition of the atmosphere spatially, as well as the distribution of PV assets within the effected area.

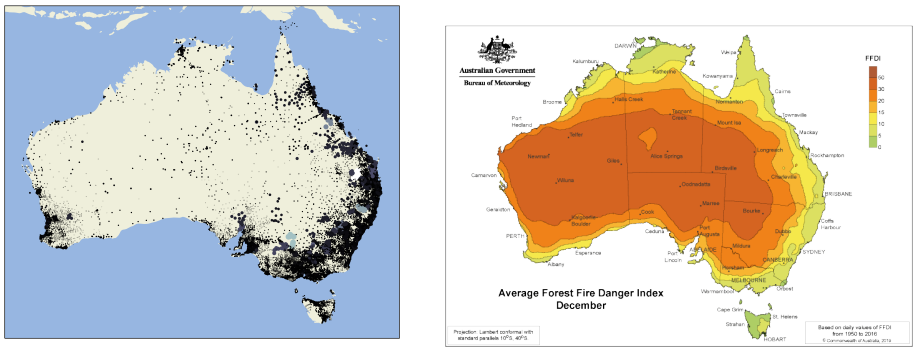


(a) (b)

Figure 5.8: (A) shows the capacity of PV generation installed at each post-code, which are gathered from [30] the size and colour of the dots denote the postcodes relative capacity. (B) Shows a map of Australia with Forest Fire Danger Index (FFDI) displayed [31].

Due to the vast land area of Australia, not one contiguous WASG covers the entire country [32], therefore electrical grids in areas with closer proximity to the wildfires may experience greater intermittency from PV assets. From examining figure 5.6 the wildfire, and electrical power losses, can be seen to be largely contained to New South Wales (NSW), Victoria (VIC), and Southern Australia (SA) as can be seen in figure 5.9. Unlike figure 5.7 here in figure 5.9 only the capacity within each respective state is considered as to reflect that Australia does not possess one contiguous WASG.

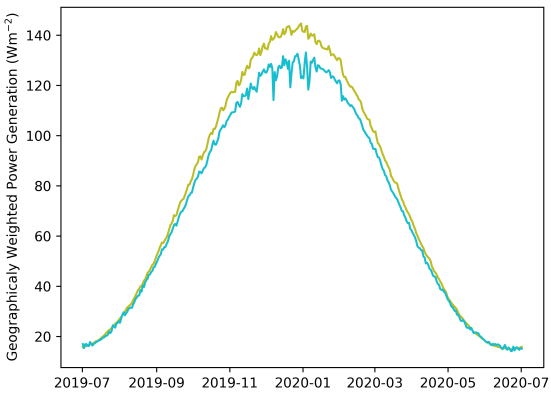


(a)

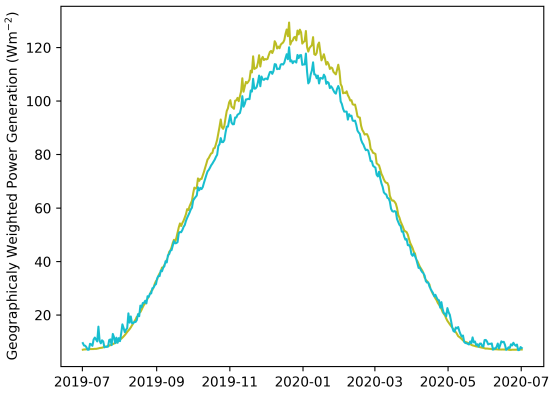


(b)

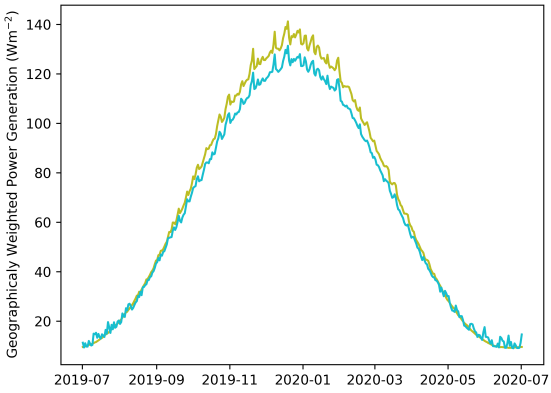


(c)

Figure 5.9: The green and blue lines indicate the geographically weighted power generation per meter squared over the course of a year within a pristine and measured atmosphere, respectively. The capacity is gathered from [30] and indicate the capacity associated with each post code. (a) Represents post codes within NSW. (b) Represents post codes within VIC. (c) Represents post codes within SA.

In these states, the percentage loss for the entire year is 6.81 %, 4.69 %, and 5.38 % respectively, whilst the percentage loss for the whole of Australia was found to be 6.39 % meaning only NSW reports losses greater than the mean loss found across Australia. Further, highlighting the need to consider the spatial distribution of PV assets as well as local atmospheric composition, as overlap between these two determine percentage loss. This presents a use case of the model in predicting how a growing or moving PV capacity may affect the sensitivity of a WASG to polluting events. Trade-offs between high fire risk and high solar potential may be explored, and by their distribution's tolerance for wildfires may be engineered into PV generation, ensuring more clean energy can be used more often.

## 5.7 Wide Impacts of Saharan Durst Storms on Photovoltaic Generation

Wildfires are not the only source of increased PM concentrations sandstorms, or mineral dust storms, increase the concentration of PM in the atmosphere, therefore increasing the observed aerosol optical depth [33]. Whilst dust storms are known to occur in many deserts, here the dust storms of the Sahara are examined due to their long-range transports [34] in both northerly and westerly directions. 2020 saw a dust storm with the highest, aerosol optical depth values on record [35]. In the popular press, this dust storm was dubbed "Godzilla" [36] as it reached across the Atlantic to the Caribbean and The Gulf of Mexico. An example of Northerly transport occurred in 2008 where much of Europe was coved by Saharan dust [37]. The impacts of these two storms on PV generation in the Caribbean and Gulf of Mexico, and Europe will be examined respectively.

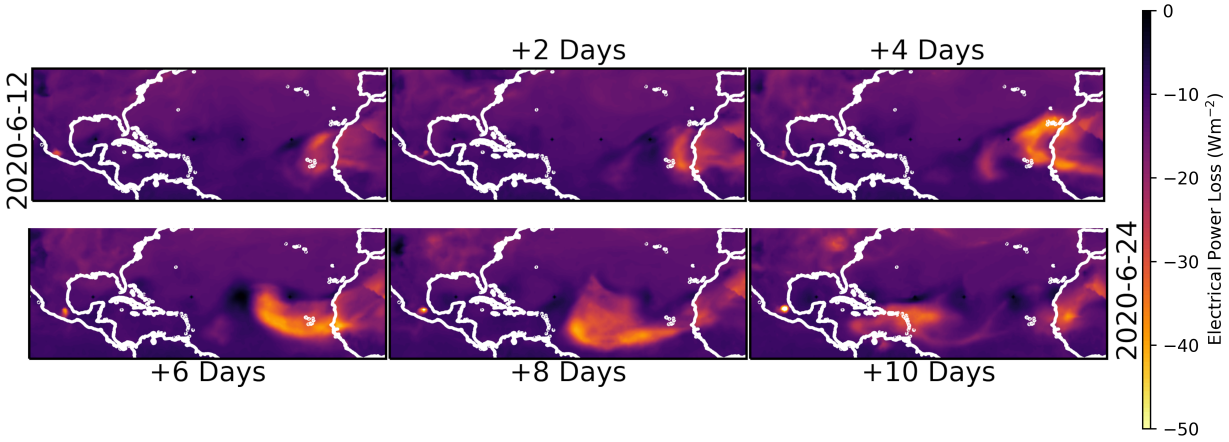


Figure 5.10: Electrical Power Losses due to atmospheric conditions from a Silicon Solar Cells over the Gulf of Mexico at 12:00PM from the 12-24$^{th}$ of June 2020 in 48hr increments.

In figure 5.10 the electrical power loss over the span of the Atlantic during the storm of 2020 which demonstrate the impact of the emission of 7.9 Tg of mineral dust into the atmosphere can be observed [38]. Figure 5.10 shows us that significant impacts to the power generation of photovoltaics can be as of the result of Saharan dust, and this can be seen across the Atlantic in the Caribbean. With the storm making landfall in Puerto Rico, PV generation is predicted to have lost a maximum of -35.97 Wm$^{-2}$. The impacts are somewhat lessened over the Gulf of Mexico, Tampico, on the coast of Mexico experiencing a maximum energy loss of -18.05 Wm$^{-2}$.

As previously discussed, dust storms from the Sahara also proceed northerly, as in 2008 [37] and more recently in 2022 [39]. The propagation of the losses with latitude can be seen in figure 5.11.

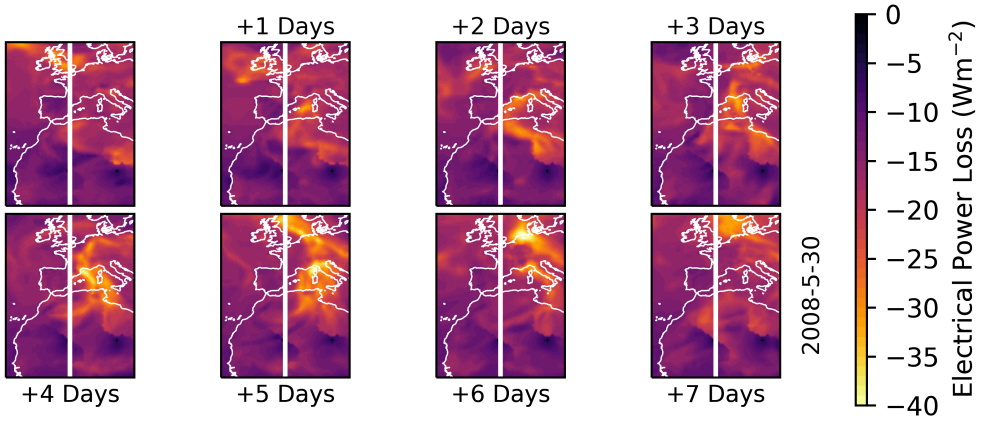


Figure 5.11: Mean electrical power loss between longitude -20 to 20 and 25 per longitude point from the 23rd of May till 2nd June 2008. The white line denotes the prime meridian.

Examining the dust plume travelling northerly presented in figure 5.11, it that can be seen that a large area of Europe is effected, from the Mediterranean to Scandinavia. It is noted that there is a lack of dissipation of losses with latitude, with losses of greater than -30 Wm$^{-2}$ at all latitudes above the most northerly point of Africa. The consistent losses with latitude, may be explained due to the formation of atmospheric rivers, carrying, and concentrating great quantities of mineral dust to higher latitudes [39].

It is important to remember the presented model only captures the first order losses cause by changes to the composition of the atmosphere, and second order losses cause by factors such as soiling of the cells [40] and surface abrasion due to cleaning [41] are not included. Soiling has been shown to result in a power loss of 4% over the course of a year, but this loss increases to 20% during prolonged periods without rain. [42].

## 5.8 Impacts of Policy on PV Generation around Beijing

Whilst both wildfires and dust storms may temporarily increase the local PM concentration, pollution from industry may present a chronic problem. Which has led to a concerted effort on improving the atmosphere have been

undertaken to lessen the atmospheres effects on human health. Many of these efforts concentrate upon the reducing the concentration of nitrogen dioxide ($NO_2$) and PM as they have respectively been found to be a respiratory irritant [43] and a probable cause of cancer [44]. A prominent example of where the local atmosphere has been improved is in China, more specifically Beijing [45]. In Beijing, much of these efforts were placed on reducing $PM_{2.5}$ concentrations, these being airborne particles with diameter of less than 2.5 $\mu m$. Since 2014 China has reduced the levels of $PM_{2.5}$ to 58 $\mu g m^{-3}$, a reduction of 35 % from 2014 to 2017 [46]. For comparison, the global average $PM_{2.5}$ concentration for urban environments was 38 $\mu g m^{-3}$ [47]. Whilst the motivation for these efforts was not improving PV generation, as changes to the local atmosphere have occurred there is an effect upon PV generation. Here, the effects of the improving atmosphere, due to policy changes in Beijing, China, are explored.

The effects of these policy changes upon PV generation have previously been investigated and have found they have been beneficial [45], reporting these policies are responsible for a 3.5% average increase in incident irradiance from 2006 to 2018 across China. However, [45] does not account for how a device may react to changes to the incident spectrum caused by the summation of the absorbance of the individual atmospheric components.

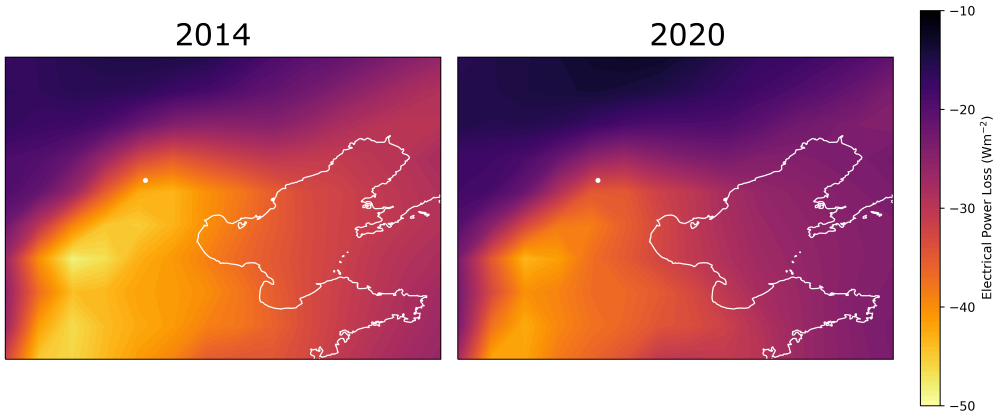


Figure 5.12: Spatial average electrical power loss at 12:00pm in Beijing, denoted by white dot, in the years 2014 and 2020 respectively. Latitude; 42.75 to 36.00. Longitude 113.25 to 123.00

Examining the area around Beijing as seen in figure 5.12, the mean midday losses for the respective years were calculated. From 2014 to 2020 there has been a slight reduction in the average peak losses, with the average over all reducing from -31 $Wm^{-2}$ to -25 $Wm^{-2}$ a reduction of just 6 $Wm^{-2}$. However, examining the change in electrical power losses from their mean does not give a whole picture for how things have improved.

The differences in distributions from 2014 to 2020 can be seen in figure 5.13. First, the reduction in the average losses is driven by reduction in losses between -30$Wm^{-2}$ and -100$Wm^{-2}$. These data suggest the effect of the change in policy can be seen through the reduction in occurrences of high levels of pollution, rather than a general improvement to air quality.

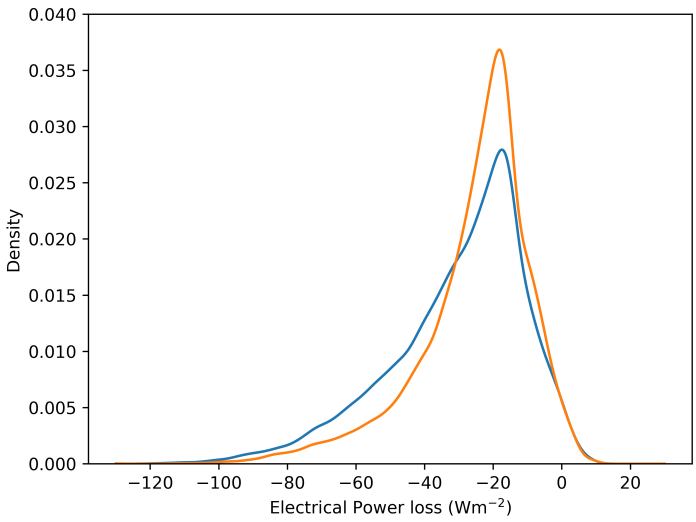


Figure 5.13: Gaussian kernel density estimation for the electrical power losses which occurred in 2014 (blue) and 2020 (orange) respectively for the geographic area as shown in figure 5.12.

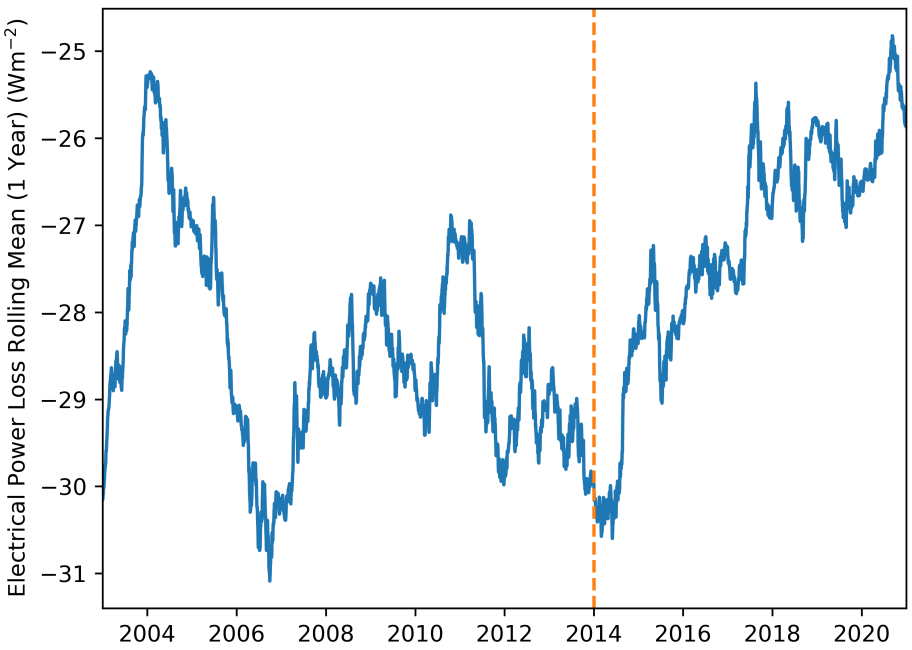


Figure 5.14: Rolling mean of the period of 1 year of the electrical power losses about Beijing from 2003 to 2020. The orange dashed line denotes the beginning of air quality legislation in 2014.

By applying a rolling mean with a window of a greater period than a year, it is possible to examine effects which are not due to the annual patterns of the climate and irradiance but are instead due to effects where their minimum period must be greater than a year. This allows for the examination of such factors such as economic growth and changes to policy, in this case related to air quality. This can be seen in figure 5.14.

As the air quality legislation came into effect in 2014 the electrical power loss can be seen to steadily reduce as we approach 2020. If a PV farm was installed in Beijing in 2014, due to the reduction in electrical power loss this solar farm may in some locations produce 15.7% more power in 2020. This of course assumes that the chosen PV devices suffer from no degradation, and that the levels of isolation have not changed from year to year. This stated increase in performance may be assumed to be largely from changes in policy.

Prior to the introduction of the legislation of interest in 2014, large variation in the electrical power loss can be seen. From 2003 losses initially reduce to almost -25 $Wm^{-2}$ before increasing rapidly to approximately -31 $Wm^{-2}$ by 2007. Post 2007 the electrical power losses, in large, level off until 2014. in the period prior to 2014 it is difficult to determine the cause of the variations of the electrical power loss due to a combination of factors, Beijing in this period saw an increase in population leading to an increased urbanisation, and the introduction of numerous small pieces of legislation which may have influenced the composition of the local atmosphere [48, 49].

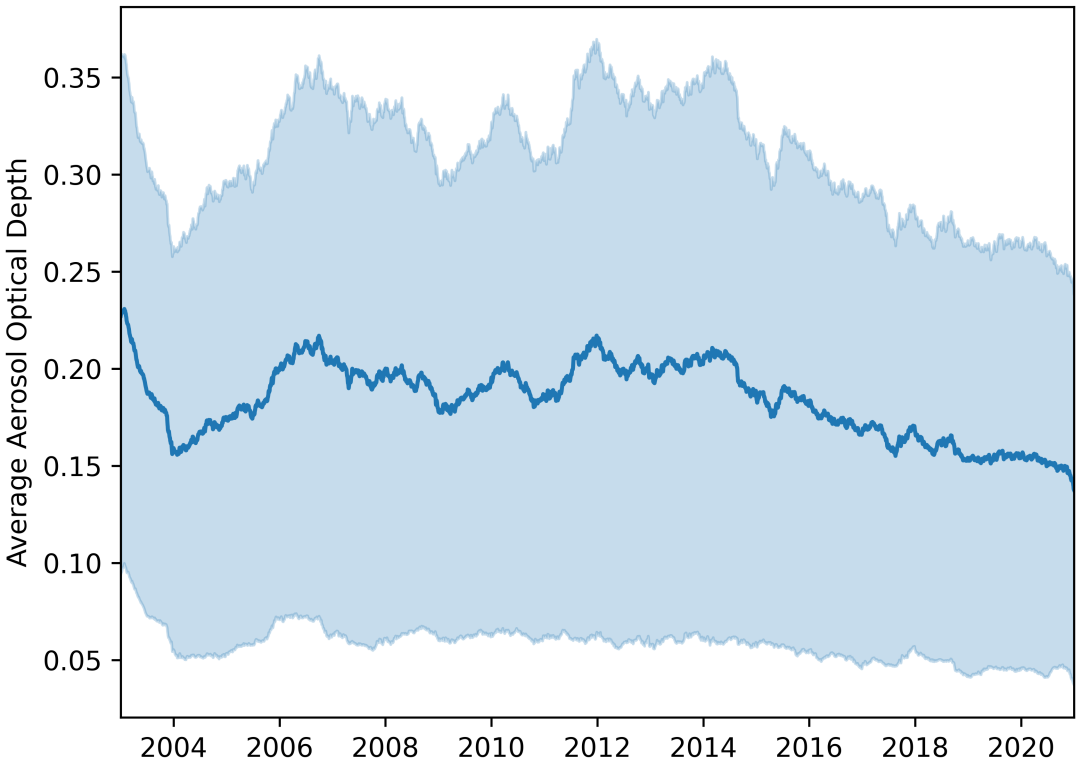


Figure 5.15: Rolling mean (1 year) of aerosol optical depth in the region of Beijing as denoted by the blue line as the standard deviation of the data as the light blue areas.

The legislation introduced in 2014 specifically targeted $PM_{2.5}$ pollution and introduced several methods to reduce the concentrations of $PM_{2.5}$. It may therefore be expected that the reduction in electrical power loss may largely

be caused by changes in the $PM_{2.5}$ concentration, as tracked in our dataset by Aerosol Optical Depth (AOD) at 550nm. AOD is tracked at 550nm as only one measure of AOD can be applied at any one time within SMARTS. From figure 5.15 it can be seen that the measured AOD reduced by 39.2% from 0.2265 to 0.1376 from 2014 to 2020. This figure shows that the atmosphere can still be significantly improved toward the pristine "pre-industrial" atmosphere, despite the decades of pollution added to the atmosphere.

## 5.9 Impacts of Material Properties on Photovoltaic Generation

In this chapter, it has been demonstrated that changes to the composition of the atmosphere can have devastating effects upon solar generation. Due to the temporary effects of wildfires and dust storms, and the chronic effects of industrial pollution. In this section, the ability for photovoltaics to be tolerant to changes to the composition of the atmosphere is examined. So far within this chapter, the impact of changes to the composition of the atmosphere upon a PERC device has been explored. However, several other technologies are approaching wide commercialisation, and of these technologies OPV are of particular interest. OPV are of interest due to the number of donor and acceptor pairs which may be utilised, allowing for the absorption characteristics to be chosen [50]. Further, both donor and acceptor molecules may be modified, allowing for further control over their absorption characteristics [51, 52]. Here, a comparison of the effects of changes to the composition of the atmosphere upon two OPVs and a PERC device is presented. To compare the devices, the single diode model, discussed in section 3.6 was fitted to device characteristics, and applied to the atmospheric composition model as explained in section 3.6. The devices were then simulated under the atmosphere experienced in California over 2020 and geographically weighted power generation was calculated, as in section 5.5.

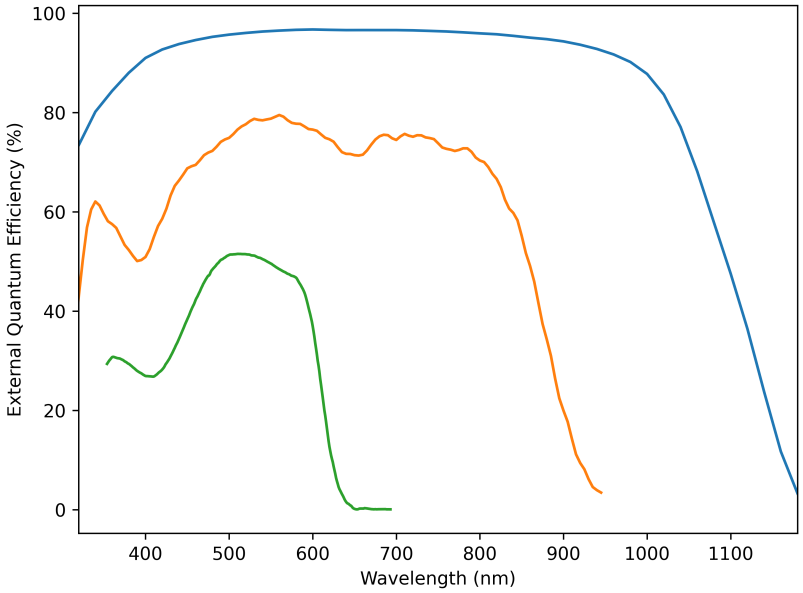


Figure 5.16: EQE of the PV devices chosen. PERC (blue), PM6:Y6 (orange), D18:PMI-FF-PMI (green).

The OPV devices chosen were a device base upon a model system, PM6:Y6 [53], and a novel device based upon D18:PMI-FF-PMI [54]. PM6:Y6 was chosen due to its wide application as a model system to further and compare the performance of OPVs. D18:PMI-FF-PMI was chosen due to the narrow nature of its absorption as seen in its EQE, alongside that of the PM6:Y6 and PERC device, in figure 5.16. These devices were then modelled in California over 2020. This test case was chosen due to the large losses which were seen in the PERC device during the period of the August complex. Seen in figure 5.17 is the geographically weighted power generation of each device.

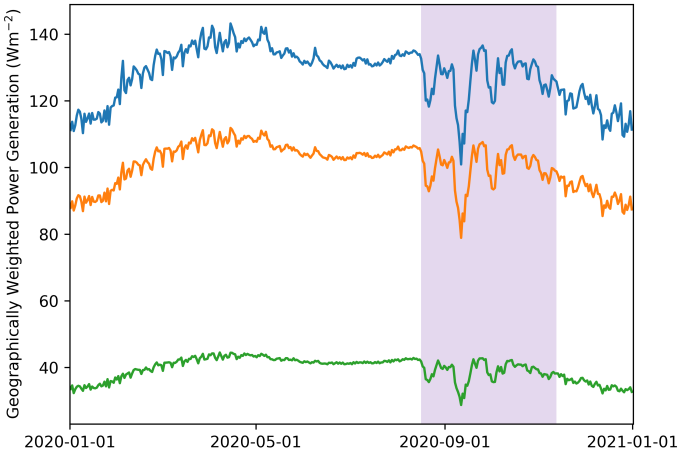


Figure 5.17: Here can be seen the geographically and capacity weighted power generation per meter squared over the course of 2020 in California under noon conditions. The purple area denotes the period of the August complex. PERC (blue), PM6:Y6 (orange), D18:PMI-FF-PMI (green).

Figure 5.17, shows the difference in the performance of the chosen devices. The mean power generation of the PERC device in California was the highest of the devices chosen, reflecting the highest EQE, with a mean generation at midday of 128.13 $Wm^{-2}$. This is followed by the PM6:Y6 device at 100.79 $Wm^{-2}$. Lastly, and significantly lower, is the D18:PMI-FF-PMI device at 39.54 $Wm^{-2}$, the device with the lowest EQE. Comparing the generation of the devices outside the period of the August complex, we can see that the magnitude of the variation in generation from the D18:PMI-FF-PMI device is less than that seen in the PM6:Y6 and PERC devices, but all devices appear to be significantly effected by the wildfires of the August complex. Comparing the generation under the measured atmosphere to the pristine "pre-industrial" atmosphere, the strength of the effect of changes to the composition of the atmosphere on the device may be quantified. The results of this comparison, in terms of percent of pristine generation achieved under the measured atmosphere, can be seen in figure 5.18.

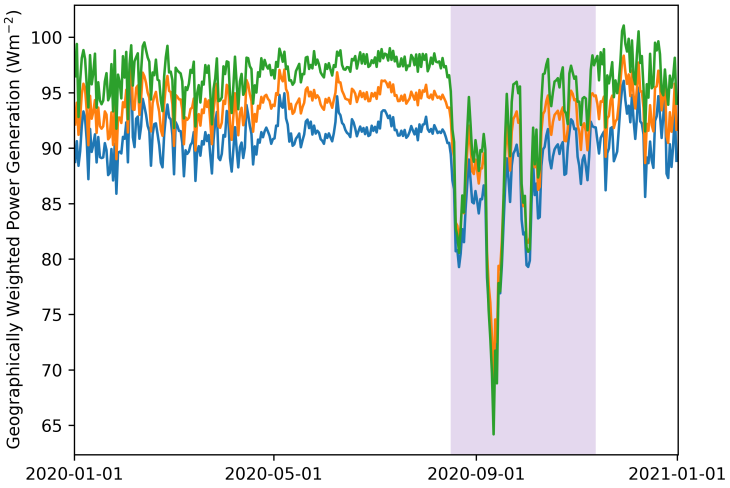


Figure 5.18: Here can be seen the geographically and capacity weighted power generation under the historic atmosphere as a percentage of that achieved under the pristine atmosphere. The purple area denotes the period of the August complex. PERC (blue), PM6:Y6 (orange), D18:PMI-FF-PMI (green)

As can be seen from figure 5.18 the D18:PMI-FF-PMI device is the least effected by changes to the atmosphere outside the period of the August complex, followed by PM6:Y6, and lastly the PERC device. Specifically, in the period prior to the August complex, the D18:PMI-FF-PMI device achieves a mean of 96.89% of that achieved under a pristine atmosphere with 94.08% and 91.16% achieved by the PM6:Y6 device and PERC device respectively. This is because of the narrowing spectra of light, which is utilised by the devices, lessening the number of atmospheric components the devices are sensitive to, as can be seen in figure 5.16.

However, during the period of the August Complex all devices are significantly effected, achieving approximately 70% of the generation under a pristine atmosphere. To enable a clearer comparison in effect of the wildfires, the difference in percent achieved from the organic devices to the PERC device is calculated and presented in figure 5.19.

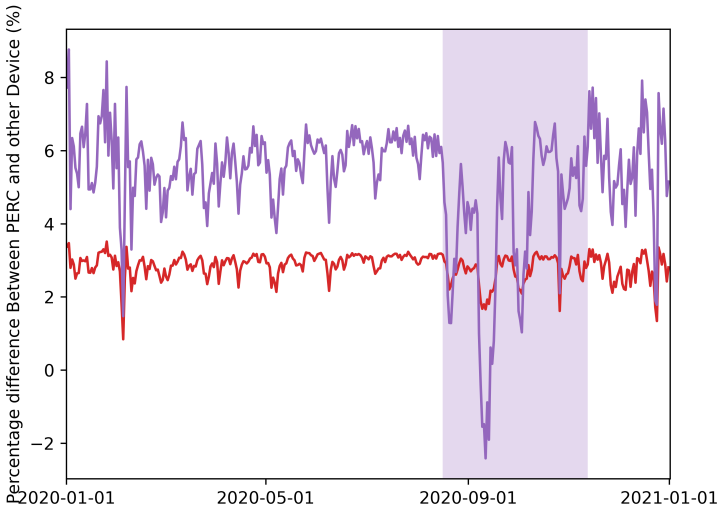


Figure 5.19: Here can be seen the difference in percentage of performance of the PM6:Y6 device (red) and D18:PMI-FF-PMI device (purple) respectively, from the performance of the PERC devices.

The most significant difference between the atmosphere within and outside the August complex is the concentration of PM. Within the period of the August complex, the dominant absorbing pollutant is PM, as measured by AOD, the absorption of PM is broadly absorbing within the model, increasingly so at shorter wavelengths [55]. Outside the period of the August complex, the concentration of PM is much lower, meaning that the incident spectrum may be effected by the other gasses modelled. These gasses rather than being broadly absorbing may absorb about specific wavelengths, each individual to each gas. Meaning, different parts of the spectrum may be absorbed as compared to PM. These effects may explain the peaks and troughs in power generation seen outside the period of the August complex. The lower variation seen in OPVs as compared to Si photovoltaics may be their narrower absorption, meaning less gasses are able to effect their performance. By examining the EQEs in figure 5.16 we may state that due to it narrower absorption within shorter wavelengths D18:PMI-FF-PMI is the least effected device over a typical period. However, due to this narrow absorption within sorter wavelengths, it is also the most susceptible to the effects of increased PM concentrations.

## 5.10 Conclusions

Understanding how changes to the composition of the atmosphere effects PV generation may be critical for future PV devices as events such as, wildfires, and dust storms become more common with higher global average temperatures. This chapter demonstrates how current PV devices are effected by changes to the composition of the atmosphere and how future PV may be effected.

The wildfires of California of 2020 were examined. Where the wildfires generate significant portions of PM, $NO_2$, and $O_3$, which can effect the performance of PV devices, with PM effecting the performance the most. Validation of the atmospheric composition model was achieved by comparing the predictions of the model to PV generation data reported by CAISO. With more confidence in the model, other polluting events were examined.

The Wildfires in Australia, in late 2019 and early 2020 were examined. These data highlighted the importance of the spatial modelling of both the wildfires and the distribution of PV assets. Thus, the impact of wildfires was shown to depend on upon the overlap of fire risk, prevailing wind conditions and PV capacity distribution. By this measure NSW, was shown to be the worst effected by wildfires.

However, not all sources of pollution are local, as demonstrated through examining the Sahara and its dust storms, shown to cause significant losses at large distances such as in Puerto Rico, reporting electrical losses of -35.97$Wm^{-2}$.

Despite the negative outlook for the future of the climate, the atmosphere and in turn pollution, the atmosphere may yet still be influenced, and the PV devices deployed chosen. Our influence upon the atmosphere was demonstrated by examining Beijing from 2003 to 2020. here with the introduction of legislature, a targeting reduction of $PM_{2.5}$ was achieved from 2014 to 2020, resulting in a predicted 15.7% increase in PV generation.

Lastly, the effects of changes to the atmosphere upon differing devices were compared. It was shown that organic PVs with narrower absorbances

were less effected by long term atmospheric change than a PERC device due to their narrower absorbance, but due to the absorbance of PM, performed 2% worse than the PERC device during periods of wildfires, or short term atmospheric change.

The model has demonstrated how further changes to the composition of the atmosphere may increase the intermittence of PV generation. For its impacts upon future PV generation to be lessened, future PV devices must account for this effect in their performance. This model presents an avenue for future PV device to be engineered through material choice, and there EQE, to be tolerant to their environment becoming tolerant to changes of spectra due to changes in atmospheric composition.

# Bibliography

[1] R. Eke, T. R. Betts, and R. Gottschalg, "Spectral irradiance effects on the outdoor performance of photovoltaic modules," *Renewable and Sustainable Energy Reviews*, vol. 69, pp. 429–434, Mar. 2017. [Online]. Available: https://www.sciencedirect.com/science/article/pii/S1364032116307079

[2] R. Gottschalg, T. R. Betts, D. G. Infield, and M. J. Kearney, "On the importance of considering the incident spectrum when measuring the outdoor performance of amorphous silicon photovoltaic devices," *Measurement Science and Technology*, vol. 15, no. 2, p. 460, Jan. 2004. [Online]. Available: https://dx.doi.org/10.1088/0957-0233/15/2/021

[3] M. Collins *et al.*, "Long-term Climate Change: Projections, Commitments and Irreversibility."

[4] U. N. Environment, "Spreading like Wildfire: The Rising Threat of Extraordinary Landscape Fires," Feb. 2022, section: publications. [Online]. Available: http://www.unep.org/resources/report/spreading-wildfire-rising-threat-extraordinary-landscape-fires

[5] J. F. Kok *et al.*, "Mineral dust aerosol impacts on global climate and climate change," *Nature Reviews Earth & Environment*, vol. 4, no. 2, pp. 71–86, Feb. 2023, number: 2 Publisher: Nature Publishing Group. [Online]. Available: https://www.nature.com/articles/s43017-022-00379-5

[6] "Future of Photovoltaic," Nov. 2019. [Online]. Available: https://www.irena.org/publications/2019/Nov/Future-of-Solar-Photovoltaic

[7] "Standard Tables for Reference Solar Spectral Irradiances: Direct Normal and Hemispherical on 37° Tilted Surface." [Online]. Available: https://www.astm.org/g0173-03r20.html

[8] L. Xie *et al.*, "Recent progress of organic photovoltaics for indoor energy harvesting," *Nano Energy*, vol. 82, p. 105770, Apr. 2021. [Online]. Available: https://linkinghub.elsevier.com/retrieve/pii/S2211285521000288

[9] C. Gueymard, "Simple Model for the Atmospheric Radiative Transfer of Sunshine (SMARTS2) Algorithms and performance assessment."

[10] D. S. Philipps, F. Ise, W. Warmuth, and P. P. GmbH, "Photovoltaics Report."

[11] K.-s. Oh, S. Bae, K.-j. Lee, D. Kim, and S.-i. Chan, "Mitigation of potential-induced degradation (pid) based on anti-reflection coating (arc) structures of perc solar cells," *Microelectronics Reliability*, vol. 100, p. 113462, 2019.

[12] S. Zhang *et al.*, "335-w world-record p-type monocrystalline module with 20.6% efficient perc solar cells," *IEEE Journal of Photovoltaics*, vol. 6, no. 1, pp. 145–152, 2015.

[13] C. FIRE, "California wildfires and acres for all jurisdictions. california department of forestry and fire protection," 2019.

[14] J. E. Keeley and A. D. Syphard, "Large california wildfires: 2020 fires in historical context," *Fire Ecology*, vol. 17, no. 1, pp. 1–11, 2021.

[15] T. W. Porter, W. Crowfoot, and G. Newsom, "Wildfire activity statistics," *California Department of Forestry and Fire Protection: Sacramento, CA, USA*, p. 46, 2019.

[16] National Interacency Coordination Center, "National Interagency Coordination Center Wildland Fire Summary and Statistics Annual Report 2020." [Online]. Available: https://www.predictiveservices.nifc.gov/intelligence/2020_statssumm/annual_report_2020.pdf

[17] "API Dashboard - U.S. Energy Information Administration (EIA)." [Online]. Available: https://www.eia.gov/opendata/browser/index.php

[18] R. Ross Jr, "Interface design considerations for terrestrial solar cell modules," in *12th Photovoltaic specialists conference*, 1976, pp. 801–806.

[19] Department of Market Monitoring, "Q2 2020 Report on Market Issues and Performance," California Independent Systems Operator, Tech. Rep., Oct. 2020.

[20] Q. Jin *et al.*, "Dynamics of pollutant emissions from wildfires in mainland china," *Journal of Environmental Management*, vol. 318, p. 115499, 2022.

[21] California Air Resources Board, "Ambient Air Quality Standards," Tech. Rep., May 2016. [Online]. Available: https://ww2.arb.ca.gov/sites/default/files/2020-07/aaqs2.pdf

[22] P. Eyzat and J.-C. Guibet, "A new look at nitrogen oxides formation in internal combustion engines," *SAE Transactions*, pp. 481–500, 1968.

[23] N. A. Ghazali *et al.*, "Transformation of nitrogen dioxide into ozone and prediction of ozone concentrations using multiple linear regression techniques," *Environmental monitoring and assessment*, vol. 165, pp. 475–489, 2010.

[24] D. L. Donaldson, D. M. Piper, and D. Jayaweera, "Temporal solar photovoltaic generation capacity reduction from wildfire smoke," *IEEE Access*, vol. 9, pp. 79 841–79 852, 2021.

[25] M. Wei, S. V. Raghavan, P. Hidalgo-Gonzalez, and L. B. N. Laboratory, *Building a Healthier and More Robust Future: 2050 Low-carbon Energy Scenarios for California: Final Project Report*. California Energy Commission, 2019.

[26] D. Bowman *et al.*, "Wildfires: Australia needs national monitoring agency," *Nature*, vol. 584, no. 7820, pp. 188–191, 2020.

[27] H. I. Jager and C. C. Coutant, "Knitting while australia burns," *Nature Climate Change*, vol. 10, no. 3, pp. 170–170, 2020.

[28] J. G. Canadell *et al.*, "Multi-decadal increase of forest burned area in australia is linked to climate change," *Nature communications*, vol. 12, no. 1, p. 6921, 2021.

[29] A. E. M. Operator, "2022 integrated system plan for the national electricity market," 2022.

[30] "Australian PV Institute (APVI) Solar Map, funded by the Australian Renewable Energy Agency." [Online]. Available: https://pv-map.apvi.org.au

[31] s. A. c. G.-B. o. Meteorology, "Bushfire Forest Fire Danger Index – climate averages maps, Bureau of Meteorology," archive Location: Australia Publisher: scheme=AGLSTERMS.AglsAgent; corporateName=Australian Government - Bureau of Meteorology. [Online]. Available: http://www.bom.gov.au/climate/maps/averages/ffdi/

[32] Energy Networks Australia, "Guide to Australia's Energy Networks," Tech. Rep. [Online]. Available: https://www.energynetworks.com.au/resources/fact-sheets/guide-to-australias-energy-networks/

[33] D. Kaskaoutis, H. Kambezidis, P. Nastos, and P. Kosmopoulos, "Study on an intense dust storm over greece," *Atmospheric Environment*, vol. 42, no. 29, pp. 6884–6896, 2008.

[34] N. Middleton and A. Goudie, "Saharan dust: sources and trajectories," *Transactions of the Institute of British Geographers*, vol. 26, no. 2, pp. 165–181, 2001.

[35] D. Francis *et al.*, "The atmospheric drivers of the major saharan dust storm in june 2020," *Geophysical Research Letters*, vol. 47, no. 24, p. e2020GL090102, 2020.

[36] "'Godzilla dust cloud' from Sahara blankets Caribbean on its way to US | Caribbean | The Guardian." [On-

line]. Available: https://www.theguardian.com/world/2020/jun/23/godzilla-dust-cloud-from-sahara-blankets-caribbean-on-its-way-to-us

[37] M. Wiegner, S. Groß, V. Freudenthaler, F. Schnell, and J. Gasteiger, "The may/june 2008 saharan dust event over munich: Intensive aerosol parameters from lidar measurements," *Journal of Geophysical Research: Atmospheres*, vol. 116, no. D23, 2011.

[38] D. Francis *et al.*, "The dust load and radiative impact associated with the june 2020 historical saharan dust storm," *Atmospheric Environment*, vol. 268, p. 118808, 2022.

[39] D. Francis *et al.*, "Atmospheric rivers drive exceptional saharan dust transport towards europe," *Atmospheric Research*, vol. 266, p. 105959, 2022.

[40] R. Conceicao *et al.*, "Saharan dust transport to europe and its impact on photovoltaic performance: A case study of soiling in portugal," *Solar Energy*, vol. 160, pp. 94–102, 2018.

[41] S. Toth *et al.*, "Soiling and cleaning: Initial observations from 5-year photovoltaic glass coating durability study," *Solar Energy Materials and Solar Cells*, vol. 185, pp. 375–384, 2018.

[42] J. Zorrilla-Casanova *et al.*, "Losses produced by soiling in the incoming radiation to photovoltaic modules," *Progress in photovoltaics: Research and applications*, vol. 21, no. 4, pp. 790–796, 2013.

[43] J. Gillespie-Bennett *et al.*, "The respiratory health effects of nitrogen dioxide in children with asthma," *European Respiratory Journal*, vol. 38, no. 2, pp. 303–309, 2011.

[44] J. D. Sacks *et al.*, "Particulate matter–induced health effects: who is susceptible?" *Environmental health perspectives*, vol. 119, no. 4, pp. 446–454, 2011.

[45] M. Labordena, D. Neubauer, D. Folini, A. Patt, and J. Lilliestam, "Blue skies over china: The effect of pollution-control on solar power generation and revenues," *PloS one*, vol. 13, no. 11, p. e0207028, 2018.

[46] "Beijing's battle to clean up its air." [Online]. Available: https://www.unenvironment.org/interactive/beat-air-pollution/

[47] V. A. Southerland *et al.*, "Global urban temporal trends in fine particulate matter (pm2· 5) and attributable health burdens: estimates from global datasets," *The Lancet Planetary Health*, vol. 6, no. 2, pp. e139–e146, 2022.

[48] P. Zhao, "Too complex to be managed? new trends in peri-urbanisation and its planning in beijing," *Cities*, vol. 30, pp. 68–76, 2013.

[49] K. He *et al.*, "A review of 20 years' air pollution control in beijing," 2019.

[50] C. Xu *et al.*, "Recent progress in all-small-molecule organic photovoltaics," *Journal of Materials Chemistry A*, vol. 10, no. 12, pp. 6291–6329, 2022.

[51] Y. Xu *et al.*, "Design of ultranarrow-bandgap acceptors for efficient organic photovoltaic cells and highly sensitive organic photodetectors," *Journal of Energy Chemistry*, vol. 72, pp. 388–394, 2022.

[52] T. Chen *et al.*, "Fluorination of terminal groups promoting electron transfer in small molecular acceptors of bulk heterojunction films," *Molecules*, vol. 27, no. 24, p. 9037, 2022.

[53] W. Tang *et al.*, "17.25% high efficiency ternary solar cells with increased open-circuit voltage using a high homo level small molecule guest donor in a pm6: Y6 blend," *Journal of Materials Chemistry A*, vol. 9, no. 36, pp. 20 493–20 501, 2021.

[54] J. Hofinger *et al.*, "Wide-bandgap organic solar cells with a novel perylene-based non-fullerene acceptor enabling open-circuit voltages be-

yond 1.4 v," *Journal of Materials Chemistry A*, vol. 10, no. 6, pp. 2888–2906, 2022.

[55] E. P. Shettle and R. W. Fenn, *Models for the aerosols of the lower atmosphere and the effects of humidity variations on their optical properties*. Air Force Geophysics Laboratory, Air Force Systems Command, United States ..., 1979, vol. 79, no. 214.

# Chapter 6

# Optimising Organic Photovoltaics Utilising Genetic Algorithms



## 6.1 Overview

This chapter presents the utilisation of Genetic Algorithums (GAs) for the optimisation of Organic Photovoltaics (OPVs). Future Photovoltaics (PVs), particularly OPVs, have suffered from uncertainty as to the cost of the active layer materials, due to the current small scale synthesis utilised. To this end, the cost of these materials is considered as a variable when both optimising devices for their optimal ratio of Power Conversion Efficiency (PCE) to cost, and Levelised Cost of Energy (LCOE). Through the presented results, we show that for current and future PVs the determined objective function can significantly affect the resultant optimal device.

## 6.2 Introduction

For future PVs to be competitive within commercial solar farm applications, they must be able to compete on cost basis with silicon PV. Over the past decade, this has become increasingly challenging as the cost of silicon PV has reduced near exponentially from 2.51 $\$W_p^{-1}$ to 0.38 $\$ W_p^{-1}$ [1]. This dramatic reduction in cost has seen the installed capacity of PV globally increase from 104,313 $MW_p$ to 854,795 $MW_p$ from 2012 to 2021 [2]. Despite this positive effect upon installed capacity, the decrease in cost has inevitably raised the barrier for commercialisation for future PV technologies such as OPVs. Optimising the structure of the device additionally adds to this barrier of entry. Optimising the structure of OPVs devices has been demonstrated to be an extremely labour-intensive process [3]. GA optimisation offers a route to shorten this process. Here a drift-diffusion/optical model that has been fitted to experimental data to simulate the process of device optimisation with the material systems of P3HT:PCBM, and PM6:Y6 for chosen objective functions.

GAs have been shown to successfully optimise several systems, such as antennas [4] for space flight applications, as was discussed in section 3.4. However, the optimisation of these systems will only be as good as the model which interacts with the GA. In the case discussed within this chapter, the drift-diffusion/optical model used is OghmaNano as developed by Roderick Mackenzie [5]. This model is discussed further in section 3.5. It is recognised that many, possible, uncontrolled factors will affect the performance of a device. For active layers, the conditions of casting, such as method [6], annealing, such as temperature [7], effect the properties of the Bulk Heterojunction (BHJ). Beyond the active layer, layers dedicated to carrier transport, such as ITO where grain size and uniformity, vary with thickness [8]. The use of a one dimensional Drift-Diffusion (DD) model inherently has its weaknesses, as it assumes material properties are invariable with thickness, and all films of a material possess identical morphology. However, this chapter will endeavour to demonstrate the utility of GAs for reaching an optimal design,

by comparing to real optimised devices, allowing a view of GAs utility where possible.

For GAs utility to be demonstrated, a common device structure must be put in place to allow for comparison with real optimised devices. The four layer structure used throughout this chapter can be seen in figure 6.1. Within this chapter, two active material blends are used, P3HT:PCBM as fabricated by Mackenzie et al. [5], and PM6:Y6 as was fabricated by Wöpke et al. [9]. The electrodes and charge transport layer are derived from the work of Mackenzie et al., when the active layer of PM6:Y6 is used it is only the characterisation of this layer by Wöpke et al.is used. The devices to which the model has been fitted are referred to as the experimental P3HT:PCBM device, and the experimental PM6:Y6 device.

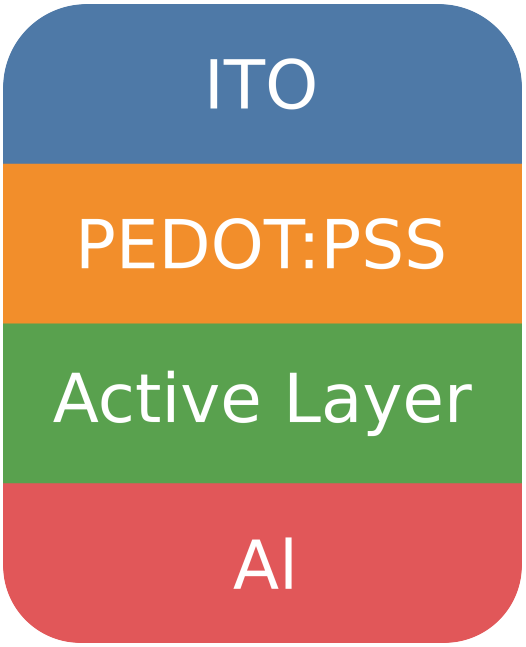


Figure 6.1: Device architecture optimised for both P3HT:PCBM and PM6:Y6 respectively where they take the place of the active layer.

Experimental device optimisation is typically limited to the objective functions which can be considered quickly, in part due to the labour-intensive fabrication process where simple measures of success are preferred, limiting additional labour. The most prevalent of these is, PCE with numerous studies reporting the effect of device structure and processing techniques

on PCE [6, 7, 10]. Additionally, the progress of PCE has been tracked by National Renewable Energy Laboratory (NREL) and M. A. Green et al. [11, 12] for decades. Other than PCE, efforts have been made to establish common protocols for the measurement of device lifetime [13]. The number studies performing lifetime measurements are limited in comparison to PCE due to their labour-intensive nature, potentially taking months to complete. Whilst estimations for the cost of experimental devices can be found [14], how changes to material selection, or material cost, change the most cost-effective device cannot be found. Through utilising a GA the cost of devices may be considered alongside PCE, either as PCE per unit cost, or further through estimation of LCOE. Optimising for this joint objective function may result in a device which is able to overcome the cost/performance barrier put in place by silicon PV.

Here in this chapter, initially both active layer materials will be optimised for PCE without strict limits upon the algorithm, examining the optimised devices against those found in literature. Where necessary, limits will be introduced to the algorithm to avoid great deviation of material properties from that fitted, and in comparison, to literature. Following this, the joint objective functions will be considered. With the cost of the active layer material becoming a variable, how the optimal device changes with active material cost for the objective functions of PCE per unit cost and LCOE will be considered.

## 6.3 Optimising for Power Conversion Efficiency

### 6.3.1 Optimising All Layers

In this section, the developed GA discussed in section 3.4 is coupled with OghmaNano, which was discussed in section 3.5 and set to optimise all layers of the standard device to achieve the maximum PCE. For these optimisations presented in this section, an upper layer thickness limit of 500nm was set, and no lower limit within the GA was set. The PCE of the devices generated,

are tested under the Air Mass 1.5 Global tilt Refrence Specra (AM1.5G), otherwise known as the standard test spectrum, within OghmaNano. The optimisation was determined to be completed when there was no improvement in PCE of the best device over ten generations. The optimisation was repeated ten times, and the presented data is the mean of these optimisations, with the final generation of each optimisation repeated until all optimisations are completed.

### P3HT:PCBM

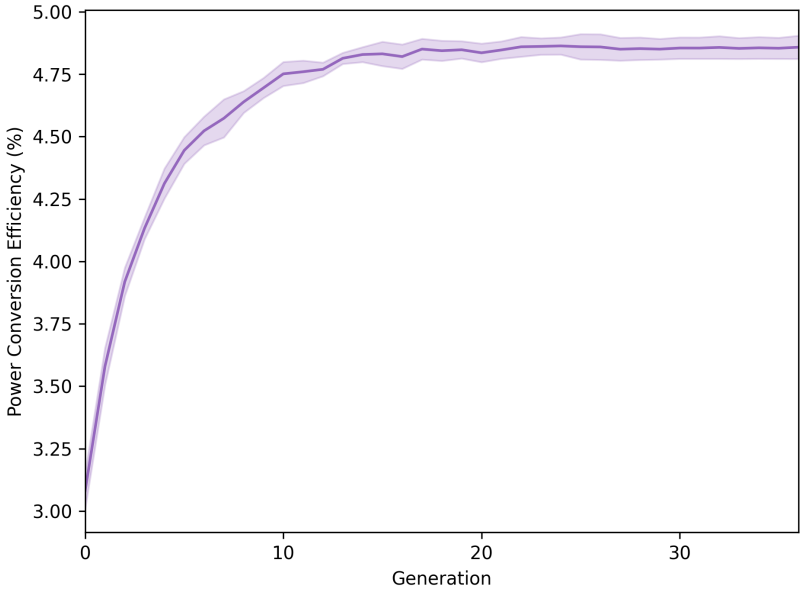


Figure 6.2: The optimisation of a P3HT:PCBM device for PCE, as show in figure 6.1 from initialisation, at generation 0, to termination. The solid purple line denotes the mean PCE each generation and the dotted lines and coloured areas denote the standard deviation of the generation.

Here, in figure 6.2, the results of optimising the standard device utilising a P3TH:PCBM active layer for maximum PCE are shown. Figure 6.2 shows the mean of each generation with the solid line, and the standard deviation is shown by the shaded area. The mean PCE of the devices is shown to increase from 3.08% to 4.85% in 36 generations. Comparing the optimisations final device to the experimental P3HT:PCBM device, where a PCE of 4.48% was achieved [5], lower than that achieved by the optimisation. The efficiency

of the characterised device is comparable to many other, state of the art, P3HT:PCBM devices [15, 16, 17, 18, 19]. The experimental P3HT:PCBM device is utilised, rather than a champion device from literature, due to the experimental device being the original used to fit the DD model. The difference between the device found through the optimisation, the optimised device, and the experimental device may be explored further through examining the differences in their architectures. The individual mean thickness of each layer, as well as their standard deviation, can be seen in figure 6.3

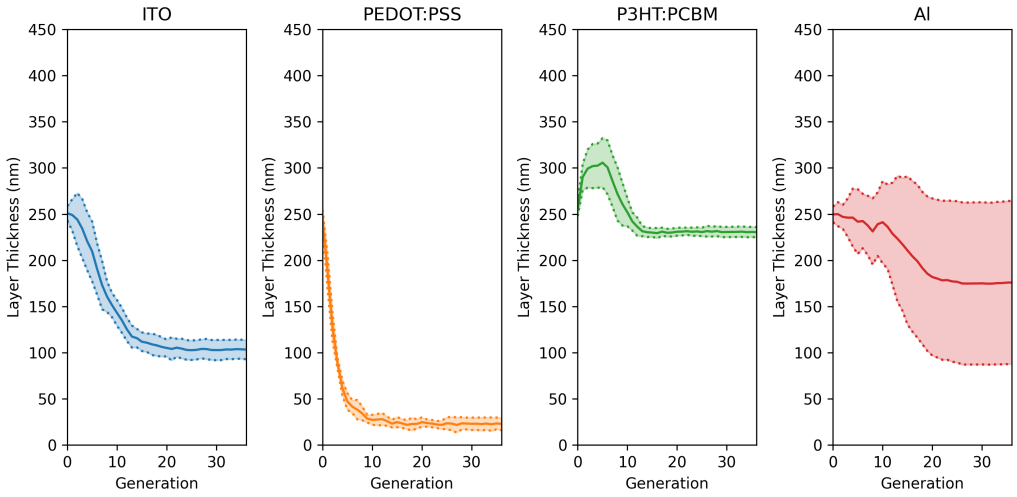


Figure 6.3: The individual layer thicknesses of the optimisation presented in figure 6.2. The solid line the mean of reach respective layer and the shaded area bound by two dotted lines denotes the standard deviation of the layer. The layers from right to left are ITO (blue), PEDOT:PSS (orange), P3HT:PCBM (green), and Aluminium (red)

Figure 6.3 shows the optimisation of each individual layer of the device, which resulted in the achieved PCE presented in figure 6.2. The mean value of each layer is presented by the solid line, and the standard deviation of the generation is shown by the shaded area. From left to right, first the optimisation of ITO is presented from an initial mean of 250±8nm, reducing over the first 20 generations towards a final value of 103±10nm. The optimisation of ITO is a balance between the optical and electrical properties of the film, with thicker films benefiting from lower sheet resistance, and thinner films possessing higher mean transmittance, as can be seen in figure 6.4. There-

fore, the optimisation must find the balance between generating additional charges through higher mean transmittance or extracting these charges efficiently from the device with lower series resistance. With the thickness of the ITO layer trending towards thinner films, generating additional charges may be said to be more important than improving the efficiency of extraction in the case of a P3HT:PCBM active layer device. Comparing the optimal device to the experimental P3HT:PCBM device, it can be seen that the ITO layer is approximately equal in thickness, at 100nm [5]. Additionally, the ITO thickness for the optimal device and the sample devices found in the literature, indicating that the ITO characterised [5] is representative of the wider pool of available commercial materials, such as those shown in figure 6.4.

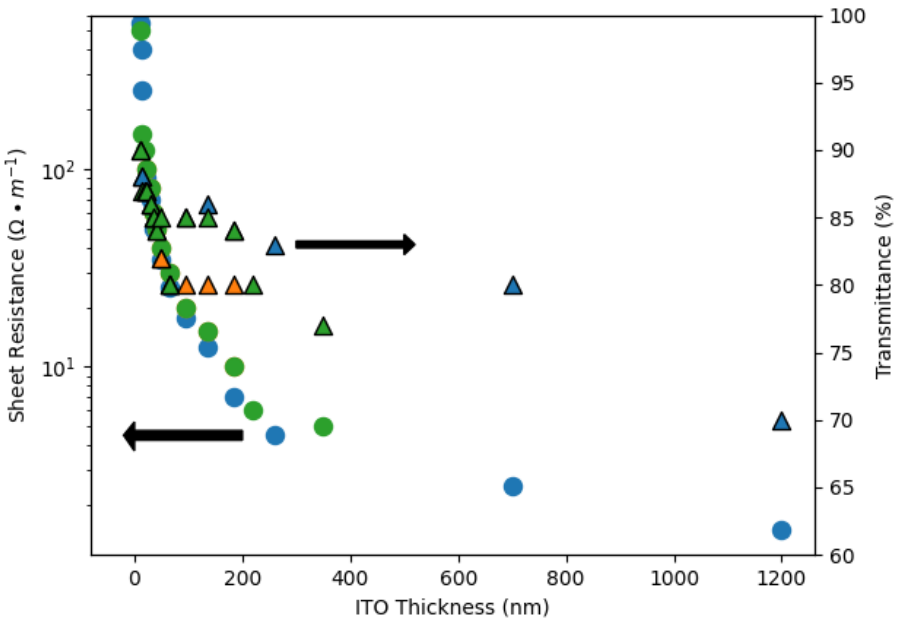


Figure 6.4: The figures show both the sheet resistance and transmittance of commercially available ITO films. The circles are sheet resistance values on the indicated axis, and the triangle are transmittance values on their respective axis. The colours indicate differing suppliers of films [20, 21, 22].

Second, the optimisation of PEDOT:PSS is presented in figure 6.3. The initial mean value of 244±10nm reducing significantly to a mean of 22±6nm by the final generation. The thickness achieved by the optimisation is thinner

than the layer with the experimental P3HT:PCBM device, at 100nm [5]. The variation between the optimised PEDOT:PSS layer thickness and the experimental film maybe explained by the anisotropic nature of conductivity within PEDOT:PSS films [23]. The anisotropic nature of conductivity is derived from the differing distance within the $\pi$ and lamellar stacking of polymer chains, leading to worse charge transport through the film than across it [24]. As the DD model is one dimensional it is unable to accurately replicate the anisotropic properties of PEDOT:PSS. The properties of the optimised layer are likely to be unattainable with the original characterised material and fabrication techniques. However, the lower thickness of the film may indicate that again generating more charges within the active layer is more beneficial than ensuring the efficient transport of the charges.

Third in figure 6.3 is the active layer, P3HT:PCBM, as shown in green. The active layer thickness from an initial mean of 255±7nm increases initially to 305±26nm by generation 5, before reducing to 230±6nm at the final generation. This initial increase of the active layer thickness may be to increase the number of bound electron hole pairs generated due to the initially thicker than ideal ITO and PEDOT:PSS layers resulting in less light reaching the active layer due to greater attenuation. As the ITO and PEDOT:PSS layer reduce, and attenuation reduces, a more typical thickness of 230±60nm is achieved, with the thickness of the experimental film being 220nm.

Lastly, shown in red is the aluminium layer in figure 6.3. The layer moves from an initial mean of 250±8nm reducing to 175±88nm, but of note is the increasing standard deviation. The increase in the standard deviation of the aluminium layer may be due to the relatively low resistivity of aluminium compared to ITO, of $1\times10^{-4}$ and $2.65\times10^{-8}$ [25, 26]. These orders of magnitude difference of resistivity mean the aluminium layer has relatively little control over the series resistance of the cell, leading to a greater standard deviation. The layer thickness for aluminium achieved is approximately in line with literature, and that used in the experimental device, with values from 100nm to 130nm found [16, 17, 19, 5].

Overall, the optimisation in its current state achieves a marginally higher efficiency than devices found in literature [15, 16, 17, 18, 19, 5]. However, due to the anisotropic properties of PEDOT:PSS and the 1D nature of the DD model, the PEDOT:PSS layer gives unphysical results within the PEDOT:PSS layer exclusively. The optimisation of the PEDOT:PSS layer may therefore be removed from the overall optimisation, as its properties at different layer thicknesses cannot be replicated by the DD model.

### PM6:Y6

Here the optimisation of the standard device with a PM6:Y6 active layer for maximum PCE is presented. PM6:Y6 devices, and its derivatives, have now reached efficiencies of 19% [27, 28]. However, the experimental PM6:Y6 device was shown to achieve an PCE of 10% [9]. Shown in figure 6.5 are the mean of 10 optimisations for maximum PCE. From these optimisations the PCE increases from an initial distribution of 4.40±0.04% raising to 7.83±0.03% by the 20th generation.

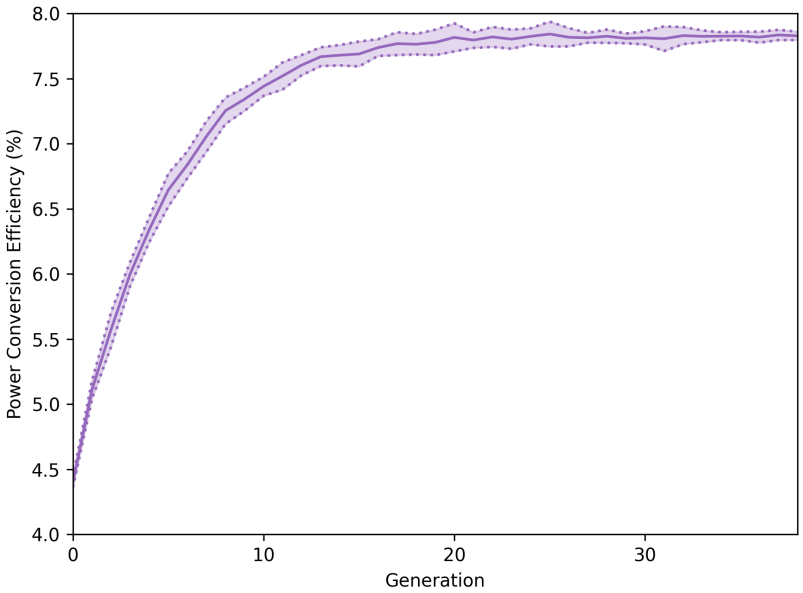


Figure 6.5: The optimisation of a PM6:Y6 device for PCE, as show in figure 6.1 from initialisation, at generation 0, to termination. The solid purple line denotes the mean PCE of each generation, and the dotted lines and coloured areas denote the standard deviation of the generation.

The achieved PCE from the presented optimisation is lower than the experimental PM6:Y6 device by 2.17%. Several reasons may explain the deviation between the device achieved in the model, the experimental device, and champion devices. Firstly, the architectures of these devices vary, not only in the materials used to fabricate the devices, but also in the number of layers. Particularly, the deviation in architecture is concentrated upon electron and hole extraction layers. The experimental PM6:Y6 device replaces PEDOT:PSS with a zinc oxide (ZnO), and the Aluminium electrode with gold, as well as introduces an interlayer of Molybdenum Oxide (MoO) [9]. The simplified architecture of the optimised device may limit the charge extraction seen, comparing the Short Circuit Current ($J_{SC}$) of the experimental device and optimised device of $1.64{\times}10^2\ A \cdot m^{-2}$ and $2.01{\times}10^2\ A \cdot m^{-2}$ respectively, it can be seen that the $J_{SC}$ becomes limited due to the simplified architecture.

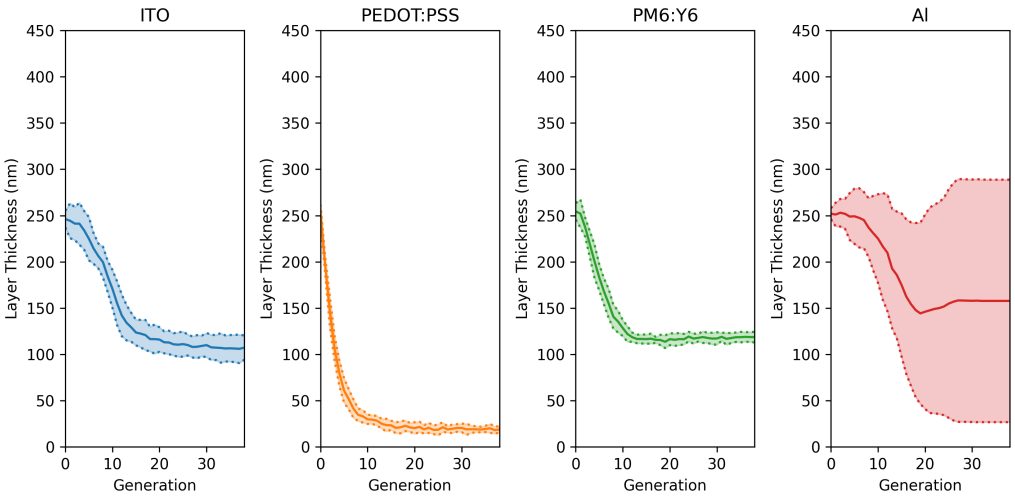


Figure 6.6: The individual layer thicknesses of the optimisation presented in figure 6.5. The solid line the mean of reach respective layer and the shaded area bound by two dotted lines denotes the standard deviation of the layer. The layers from right to left are ITO (blue), PEDOT:PSS (orange), PM6:Y6 (green), and Aluminium (red)

Figure 6.6 shows the optimisation of all the individual layers needed to achieve the PCE shown in figure 6.5. From left to right as shown in figure 6.6 first is the ITO layer thickness. The initial mean thickness of ITO

is shown to be 246±9nm, which reduces to approximately the final value of 107±13nm within 38 generations. Again, this shows the importance of generating charges is greater than their extraction despite the greater absorbing properties of PM6:Y6 compared to P3HT:PCBM as can be seen by examining their respective External Quantum Efficiencies (EQEs) [10, 29]. The optimised device layer thicknesses are like those found in the experimental device. Shown in orange in figure 6.6 is PEDOT:PSS thickness, whose optimisation will suffer from inaccuracy from its anisotropic nature as discussed previously. The PEDOT:PSS thickness moves from an initial distribution of 253±9nm to mean value of 19±3nm by the final generation. The active layer, PM6:Y6, shown in green, does not optimise similarly to P3HT:PCBM whose thickness initially increased, instead PM6:Y6 is seen to reduce from the initial thickness of 254±9nm to a final value of 119±6nm. The optimised layer thickness of PM6:Y6 is found to be approximately half of that found in the experimental device at 200nm [9]. Lastly, aluminium is shown in red, similarly to that shown in figure 6.3, the mean value is seen to reduce, but the standard deviation of the distribution is shown to increase dramatically, from an initial value of 252±6nm to a final value of 157±131nm due to its low influence on series resistance and the device as a whole. The optimisation of PM6:Y6 device appears to be further from that described in literature than the P3HT:PCBM device, which may additionally contribute to the low achieved PCE through optimisation.

Through carrying out these optimisations upon both P3HT:PCBM and PM6:Y6 inaccuracies have been identified. Namely, the anisotropic properties of PEDOT:PSS causing the properties of the optimised film to be far from those that would be found in literature and that was originally characterised. These inaccuracies must be controlled, or the results of further optimisations will also be inaccurate.

Here, a calibrated device model has not replicated the optimisation process of both P3HT:PCBM and PM6:Y6 experimental devices. In the next section we will see to place appropriate bounds to enable a replication of the

optimisation process of the experimental device to occur.

### Improving Optimisation Accuracy

To improve the accuracy of our optimisations, controls upon found inaccurate behaviours of individual layers must be introduced. Shown here are the controls which were introduced for following optimisations and were not previously discussed the reasoning for doing so is presented.

### Transparent Conducting Oxide

As previously discussed, the optimisation of the Transparent Conducting Oxide (TCO) is to balance the electrical and optical losses. As demonstrated in figures 6.3 and 6.6 the GA has been shown capable of finding this balance. The layer thicknesses found by the optimisations within these figures were found like champion devices found within literature [27, 28, 5] and from commercial suppliers [20, 21, 22]. However, seen in figure 6.4, the sheet resistance of the film does not scale linearly with film thickness. Calculating the resistivity of these films from their sheet resistance, as can be seen in figure 6.7, the resistivity is seen to increases with reducing film thickness.

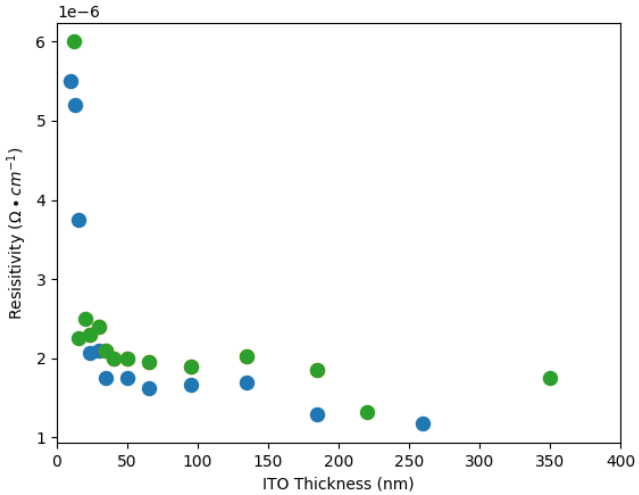


Figure 6.7: Resistivity of various commercially available Indium Tin Oxide (ITO) films, calculated from sheet resistances presented in figure 6.4.

This increasing resistivity that can be significantly seen below 25nm is due

to the discontinuous nature of the films below 25nm [8]. Initially deposited ITO will form islands that with further deposition will become interconnected, eventually forming a continuous layer. This in essence shows that two regimes of films exist, one in which the film is discontinuous, and the second where the film is continuous where film properties are seen to stabilise, leading to variation in film properties when characterised. As the characterised ITO film has a thickness of 100nm [5], it will exist in the continuous regime, therefore a lower limit of 25nm is set largely removing the discontinuous regime from the optimisation.

#### Electron transport Layer

As previously discussed, due to the various carrier transport mechanisms dependent upon the morphology of PEDOT:PSS, the conductivity of PEDOT:PSS is largely anisotropic [23]. As the used drift-diffusion model is one dimensional, it is unable to account for anisotropic material properties. Due to this, the thickness of the PEDOT:PSS layer cannot be accurately optimised. Therefore, the thickness of the PEDOT:PSS layer within all devices, hence forth, is fixed at 100nm, the thickness of layer from the experimental P3HT:PCBM device [5].

### 6.3.2 Improved accuracy

Applying the discussed limits to improve the accuracy of the optimisation with experimental works, the optimisation of the standard device utilising both a P3HT:PCBM and PM6:Y6 active layer for maximum PCE is presented. Noting if the implemented limits have improved the accuracy to the respective characterised devices.

### P3HT:PCBM

Seen in figure 6.8 is the optimisation of the P3HT:PCBM active layer from an initial efficiency of 3.74±0.03% to 4.43±0.01% within 36 generations. Comparing this to the previous optimisation, a lower PCE is achieved by 8.7%, thus moving the optimisation result closer to the device originally characterised [5].

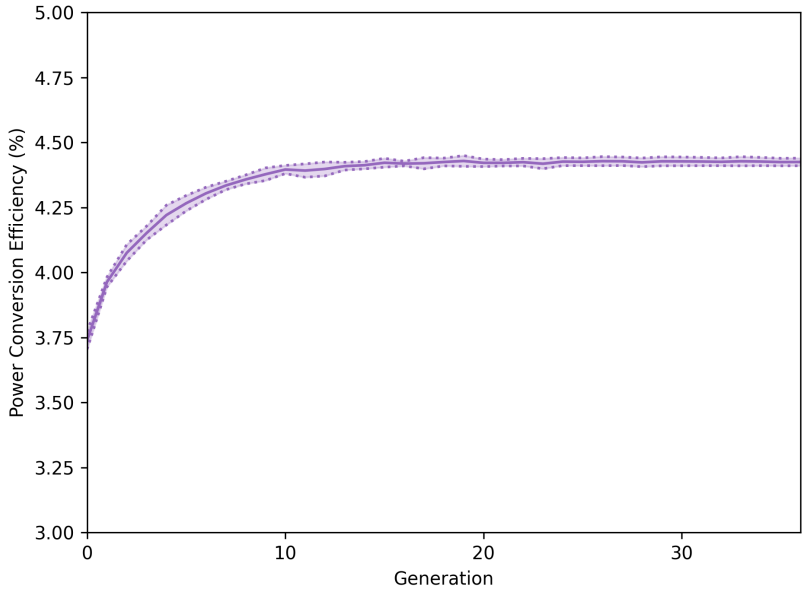


Figure 6.8: The optimisation of a P3HT:PCBM device for PCE with discussed limits implemented, from initialisation, at generation 0, to termination. The solid purple line denotes the mean PCE each generation and the dotted lines and coloured areas denote the standard deviation of the generation.

Whilst introducing these limits to the optimisation may have resulted in a lower achieved PCE, they are closer to the originally characterised device. Additionally, through examining figure 6.9 it can examine how the structure of the optimised device has changed.

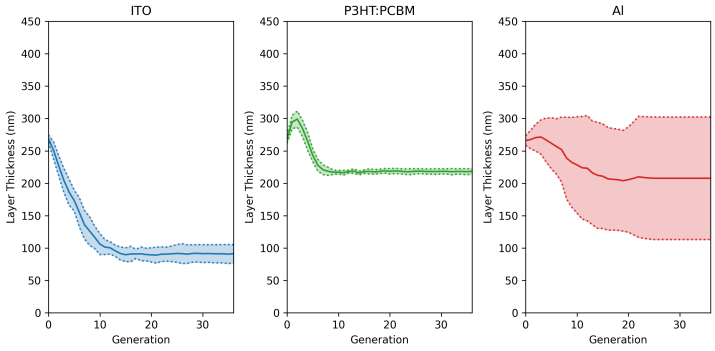


Figure 6.9: The individual layer thicknesses of the optimisation presented in figure 6.8. The solid line the mean of reach respective layer and the shaded area bound by two dotted lines denotes the standard deviation of the layer. The layers from right to left are ITO (blue), P3HT:PCBM (green), and Aluminium (red)

From figure 6.9, first in blue is the ITO layer. From an initial thickness of 269±6nm to a thickness of 91±13nm by generation 36. Approximately equal to that found in the previous optimisation, 103±10nm, and to that found in the originally characterised device. However, it is of note that the standard deviation of the final thickness has increased. This increase in uncertainty is likely due to the more limited nature of the optimisation, as PEDOT:PSS has been effectively removed from the optimisation.

Secondly, the P3HT:PCBM film is presented in green. Much like the previous optimisation, from an initial thickness of 268±6nm the mean thickness initially increases to a peak of 299±13nm, before reducing to a thickness of 218±4nm by the final generation. This initial increase, much as in the previous optimisation, due to the initially thicker ITO film. The final thickness is marginally lower than that achieved by the previous optimisation, 230±6nm, the thinner active layer may be caused by the substantially thicker PEDOT:PSS layer from 23±7nm to 100nm. The active layer thickness is now closer to that originally characterised, 220nm [5]. Lastly, the aluminium electrode is presented from an initial thickness of 266±7nm it is optimised towards 208±94nm by the final generation. It influences over the final performance of the device is still largely insignificant.

### PM6:Y6

Figure 6.10, shows the results of the optimisation of the PM6:Y6 active layer for PCE with the discussed limits introduced. From an initial efficiency of 5.45±0.07% the efficiency is optimised to 6.86±0.05% within 24 generations. In comparison to the previous optimisation, the achieved PCE is lower by 12.39% and is therefore 31.40% lower than the experimental PM6:Y6 device. The cause of these differences may be identical to that put forward for the now limited optimisation of P3HT:PCBM, but the inaccurate optimisation of the PEDOT:PSS layer is no longer counteracting the differences in materials and architecture.

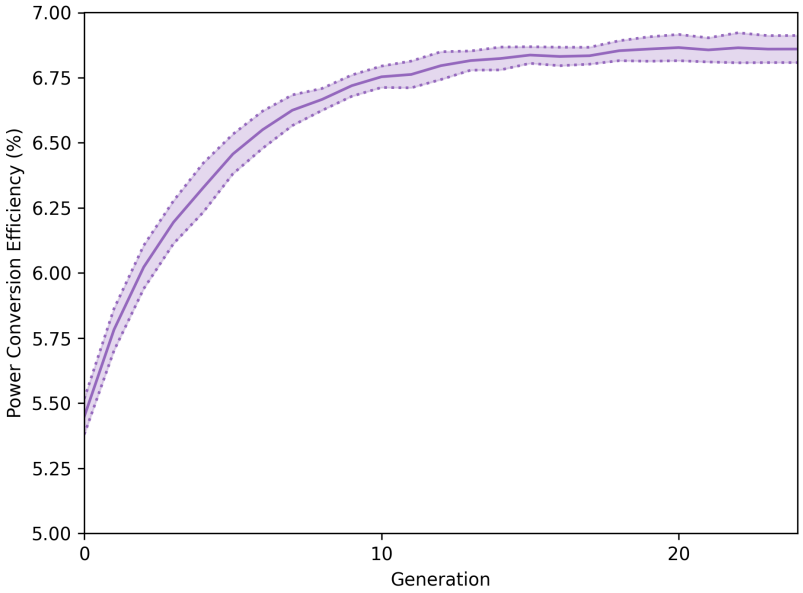


Figure 6.10: The optimisation of a PM6:Y6 device for PCE with discussed limits implemented, from initialisation, at generation 0, to termination. The solid purple line denotes the mean PCE each generation and the dotted lines and coloured areas denote the standard deviation of the generation.

From figure 6.11 the initial and optimised device structure can be seen which achieves the optimisation seen in figure 6.10. Firstly, the ITO film reduces in thickness from an initial thickness of 260±8nm to 104±18nm. This thickness is comparable to that achieved by the previous optimisation and the experimental PM6:Y6 device [5]. Much like with the P3HT:PCBM active layer, the standard deviation in the ITO layer is seen to grow, the increased uncertainty

is likely also due to the removal of PEDOT:PSS from the optimisation.

The active layer, PM6:Y6, can be seen reducing in thickness from an initial distribution of 261±9nm to 106±5nm by the final generation. This film is marginally thinner than that presented in the previous optimisation, and further than that of the experimental PM6:Y6 device [9].

Lastly, the optimisation of the aluminium layer is presented the thickness reduces from an initial thickness of 262±10nm to the final of 202±105nm. Again, the wide standard deviation indicates the lack of influence of this layer on the performance of the device.

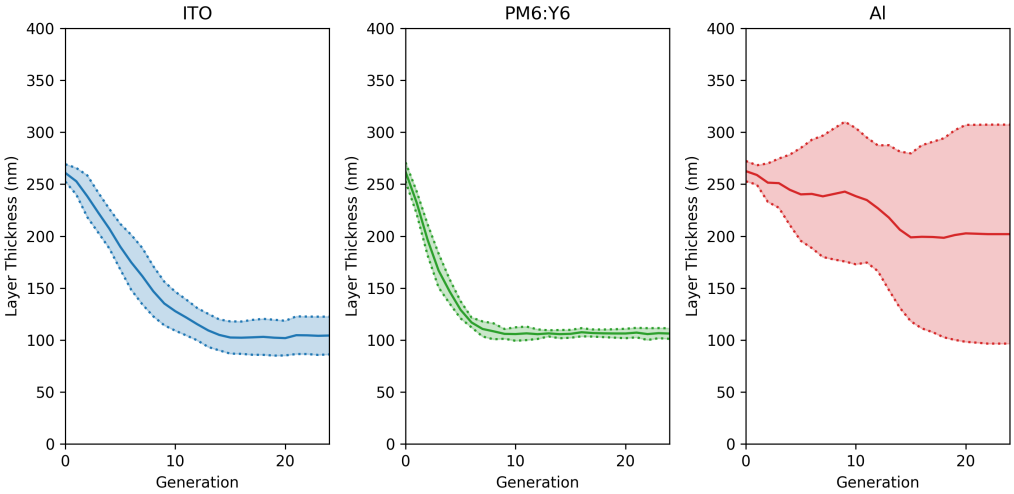


Figure 6.11: The individual layer thicknesses of the optimisation presented in figure 6.10. The solid line the mean of reach respective layer and the shaded area bound by two dotted lines denotes the standard deviation of the layer. The layers from right to left are ITO (blue), PM6:Y6 (green), and Aluminium (red)

Whilst efforts to improve the accuracy of the optimisation by introducing limits to the optimisation, this does appear to have the improved the accuracy of the individual layer thicknesses or achievable PCE. However, the previous PCEs were only achievable due to the unphysical properties of layers optimised, namely, PEDOT:PSS. Introducing these limits has appeared to have marginally improved the closeness of the optimised P3HT:PCBM device to its respective experimental device, but the same is not found for PM6:Y6. With the presented optimisation, the utility of a GA coupled with

drift-diffusion/optical model appears to be limited for the objective function of PCE. However, more utility may be found in the consideration of alternative objective functions.

The different in performance seen in the optimised PM6:Y6 device, and the experimental PM6:Y6 device [9] is likely due to only the active layer from the experimental PM6:Y6 devices is used in the optimisation, whilst the charge transport layers seen in figure 6.1. OgmahNano was utilised within [9] to study the experimental PM6:Y6 device, and good fits of device characteristics are presented.

To summarise optimising for PCE, it has been shown that GAs are capable of optimising a OPV for PCE when coupled with a drift-diffusion model. However, it has also been demonstrated that care must be taken when choosing which materials are optimised due to the dimensionality of the drift-diffusion model. The optimisation has been demonstrated for two material systems P3HT:PCBM, and PM6:Y6, resulting in PCEs and layer thicknesses comparable to the originally characterised devices. With the utility of the GA shown, we may consider further objective functions.

## 6.4 Optimising for Power Conversion Efficiency per unit cost

Within laboratory environments when fabricating novel devices, the cost of manufacture and materials are often not considered. Most work upon future PV technologies consider how to better the efficiency of the device by new fabrication techniques or materials, leaving the cost of the device far outside the scope of the work. Allowing for the consideration of cost within novel device fabrication may better allow researchers to develop devices that are cost-effective and may aid in the commercialisation of these future PV technologies. Here, the optimisation of the previously considered standard device is considered again with the active layers of P3HT:PCBM and PM6:Y6, but with rather than simply optimising for the maximum PCE the optimal max-

imal ratio between PCE and the material cost of the device is sought. In the presented case, the ratio is sought to be maximised, achieving the maximum PCE for the minimal material cost.

### 6.4.1 Calculating Cost

Estimating the true cost of a novel PV device has many considerations, which often leads to a high degree of complexity to achieve an accurate estimation. These complexities are often derived from the novel nature of devices, such as novel materials and fabrication techniques [30, 31, 32, 33]. Due to the combination of these factors, any such estimation of the cost of the device will lead to uncertainties in the answers. However, concentrating on the cost of the materials may allow for a cost which may be applied comparatively.

To calculate the material cost of the device, the volume of each respective layer is calculated and along with the density of the material, the mass is calculated. A table of the densities used for each material can be seen in table 6.1.

| Material | Density ($g \cdot cm^{-3}$) |
|---|---|
| ITO | 7.14 [34] |
| PEDOT:PSS | 1.01 [35] |
| P3HT | 1.15 [36] |
| PCBM | 1.15 [37] |
| P3HT:PCBM | 1.15 [38] |
| PM6 | 1.02 [39] |
| Y6 | 0.50 [40] |
| PM6:Y6 | 0.61 [41] |
| Al | 2.7 |

Table 6.1: Table of material densities used within the optimisation. For the presented densities of the active layers, the ideal material blend ratios were used to calculate their mean combined density as found from the respective references.

From the calculated mass of each respective layer, the cost of the layer was calculated by taking the product of its mass with the cost of the respective material per gram. The sum of the cost of these layers shows the material cost of the device optimised. The material cost per gram for each layer was derived from the examination of a specialist chemical supplier [42], from the highest quantity either volume or mass, the cost per gram was calculated. An assumption to note is the assumed totally efficient fabrication process, with all the starting material being incorporated into the device. The calculated costs per gram of these materials can be found in table 6.2. These costs were accurate at the time of optimisation, economic factors such as inflation, or failures in supply chains will affect the relative price of the materials.

| Material | Cost per Gram (£/g) |
|---|---|
| ITO | 6.66 |
| PEDOT:PSS | 7.96 |
| P3HT | 597.00 |
| PCBM | 1594.00 |
| P3HT:PCBM | 1892.00 |
| PM6 | 5880.00 |
| Y6 | 6190.00 |
| PM6:Y6 | 6654.00 |
| Al | 0.24 |

Table 6.2: Table of material costs found from the described method, all costs were derived from Merck and were accurate at time of access [42]. The ideal ratios of P3HT to PCBM and PM6 to Y6 were found from [38] and [41] respectively.

Despite the found cost for the active layer materials, there is much speculation on how these costs may change if the demand grows significantly [14, 43]. For this reason, here, the cost of the active materials is also considered a variable. How the optimal devices for both P3HT:PCBM and PM6:Y6 change with active layer cost will be examined, the active material cost was varied from £0.01 to £10,000 per gram in decade steps. This optimisation may

reveal the balance between the performance a device achieves and the cost of this performance as a function of active material cost. In the ideal case, the cost of a device should not be a factor in its optimisation, leading to the most efficient devices. The active material cost at which device cost is considered by the algorithm denotes an upper bound for the cost of the active material within commercial applications. This assumes that commercial devices must be optimised for maximum efficiency.

### 6.4.2 P3HT:PCBM

Presented here are the optimisations of the standard device with a P3HT:PCBM active layer for the maximal ratio of PCE to cost. Where the cost per gram of the active layer has been varied from £0.01 to £10,000 per gram in decade steps. Figure 6.12 shows the results of these optimisations as well as the achieved PCE and material cost of the device.

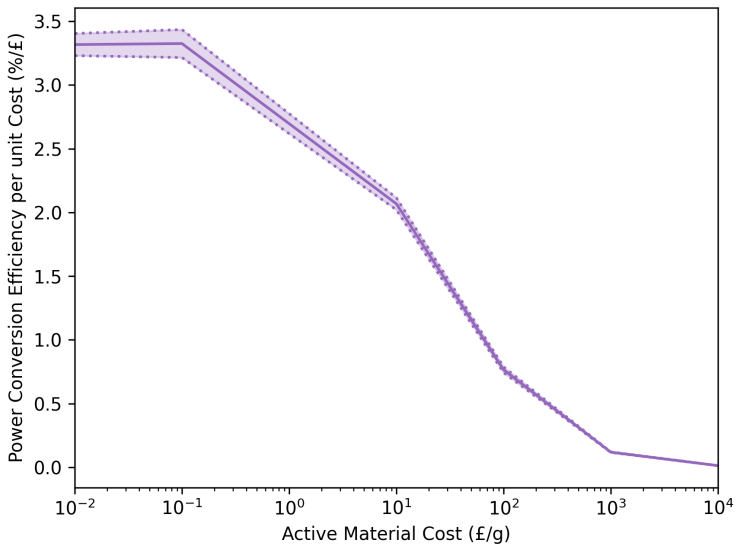


(a)

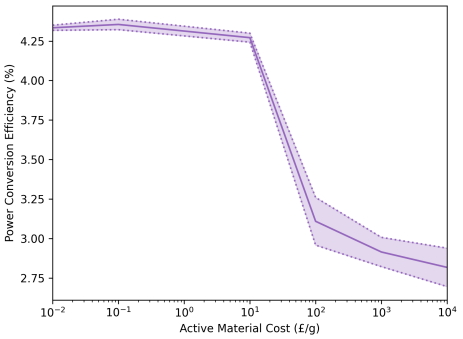


(b)

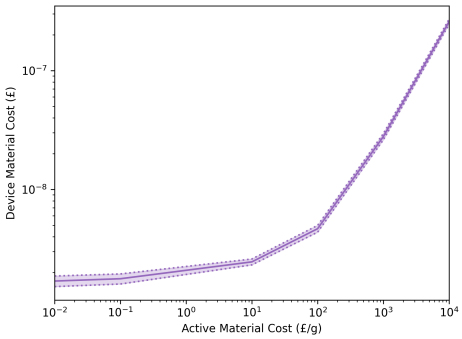


(c)

Figure 6.12: The optimised P3HT:PCBM device for PCE per unit cost (%/£) with discussed limits implemented. The solid purple line denotes the mean PCE each active layer material cost and the dotted lines and coloured areas denote the standard deviation of the optimised device. Figure 6.12a, (a), shows the PCE per unit cost (%/£). Figure 6.12b, (b), and Figure 6.12c, (c), show both the PCE and Cost of the devices respectively, the component parts of the objective function.

From Figure 6.12a the optimal ratio of PCE to cost is seen to reduce from its initial value of 3.32 to near zero as the active material cost increases. Examining both figures 6.12b and 6.12c the cause of this reduction can be determined. Whilst the cost can be seen in figure 6.12c to rise exponentially with the logarithmic rises in active material cost, as might be expected, PCE shown in figure 6.12b is not consistent across the entire range of active layer

material costs. At the lowest active material cost of £0.01 per gram, a PCE of approximately 4.3% is sustained until an active material cost of £10 per gram, following this a large drop is seen over the next decade to a PCE of 3.1% gradually reducing further to 2.8% by £10,000 per gram. From both components parts it is clear the optimal device over the range of active layer material costs must be changing with two regimes of PCE and the rise in device cost. Figure 6.13 shows the thickness of each individual layer over the active layer material cost range specified, and may show the reasons for the collapse of PCE.

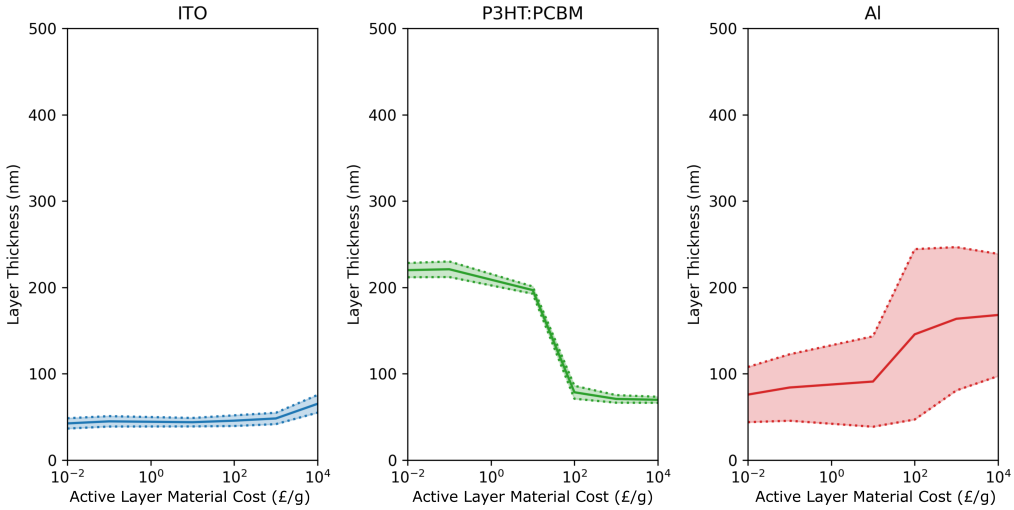


Figure 6.13: The individual layer thicknesses of the optimisation presented in figure 6.8. The solid line the mean of reach respective layer and the shaded area bound by two dotted lines denotes the standard deviation of the layer. The layers from right to left are ITO (blue), P3HT:PCBM (green), and Aluminium (red)

From left to right in figure 6.13 is ITO in blue, P3HT:PCBM in green and lastly Al in red. The optimal thickness of ITO does not appear to change dramatically over the range of active layer material costs increased from 43±6nm to 65±10nm over the range examined. Thinner than the film found when only optimising form PCE at 91±14nm. P3HT:PCBM thickness at the minimum active layer material cost is near that of the experimental P3HT:PCBM device with a thickness of 220±8nm, this thickness is somewhat stable until £10 per gram where a substantial decrease is seen reducing to

69±3nm for the remainder of the range of active layer material costs. Lastly, Al thickness is initially seen to gradually increase up to £10 per gram from a thickness of 75±32nm, at £10 per gram a jump in thickness is seen flowed by a gradual increase in thickness to a maximum of 168±71nm at £10,000 per gram.

Examining this data, the thickness of the active layer is critical for determining the PCE and therefore PCE to cost ratio. At low active layer material costs from £0.01 to £10 per gram the optimisation is dominated by PCE, above £10 per gram however the ratio is dominated by cost. The cost of the P3HT:PCBM per gram becomes too great to justify its PCE and action must be taken to reduce the cost of the device, and as this is achieved through reducing the thickness of the P3HT:PCBM layer and the subsequent reduction in PCE is seen. The increases in thickness seen by ITO and Al may be because of the reducing thickness of P3HT:PCBM, causing a reduction in the number of charges generated, and therefore more efficient charge extraction is needed. From this, one may conclude that the maximum upper limit for cost per gram for P3HT:PCBM lies at £10 per gram, as after this cost becomes the dominating factor in optimisation, comparing this to the cost found through chemical suppliers a P3HT:PCBM device manufactured today would be in the cost dominated regime, and therefore it is likely unsuitable for a commercial device.

### 6.4.3 PM6:Y6

Here are presented the optimisation of the standard device with a PM6:Y6 active layer, where active layer material costs were varied from £0.01 to £10,000 per gram in decade steps. Figure 6.14 shows the results of these optimisations as well as the achieved PCE and material cost of the device.

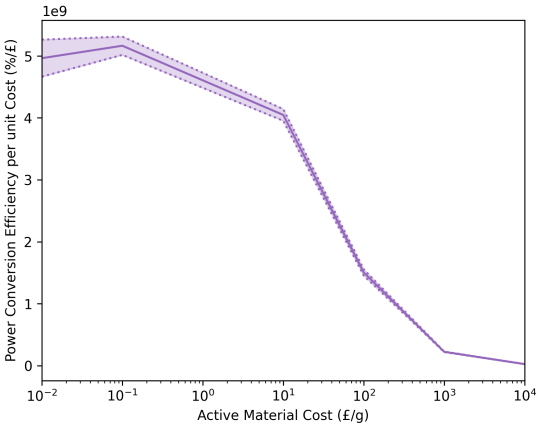


(a)

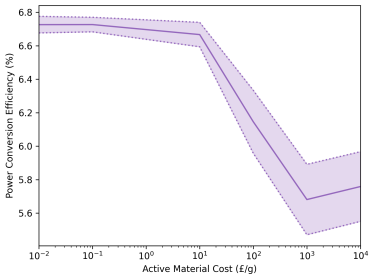


(b)

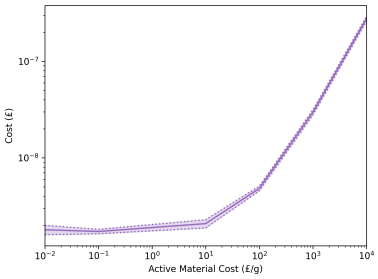


(c)

Figure 6.14: The optimised of a PM6:Y6 device for PCE per unit cost (%/£) with discussed limits implemented. The solid purple line denotes the mean PCE each active layer material cost and the dotted lines and coloured areas denote the standard deviation of the optimised device. Figure 6.14a, (a), shows the PCE per unit cost (%/£). Figure 6.14b, (b), and Figure 6.14c, (c), show both the PCE and Cost of the devices respectively, the component parts of the objective function.

Figure 6.14a shows the optimal ratio between PCE and device material cost, as shown by figures 6.14b and 6.14c respectively over the active layer material cost range. The optimal PCE to cost ratio at the lowest active layer cost initially increases slightly to $5.16 \pm 0.15 \times 10^9$ at £0.1 per gram before reducing by several orders of magnitude to $2.42 \pm 0.03 \times 10^7$ at £10,000 per gram. The PCE achieved across the range of active layer material costs, as can be seen in figure 6.14b. Across the range of active layer material costs, initially the PCE remains stable at 6.7% until £10 per gram where a reduction is seen to 5.7% at £1000 per gram, before increasing slightly to 5.8% at £10,000 per gram. Figure 6.14c again it is seen that the cost of the devices rises

exponentially as the cost of the active layer material rises logarithmically, as was show to occur in P3HT:PCBM in figure 6.12c, but unlike in figure 6.12c the cost of the optimal PM6:Y6 devices remains constant between £0.01 and £10 per gram. Examining the two components of the ratio, may determine that the increase seen at £0.1 per gram is caused by the stability of devices cost. As the cost is largely stable in the range of £0.01 to £10 per gram, changes to the device architecture must occur, presented in figure 6.15 is the layer thicknesses over the range of presented active layer material costs.

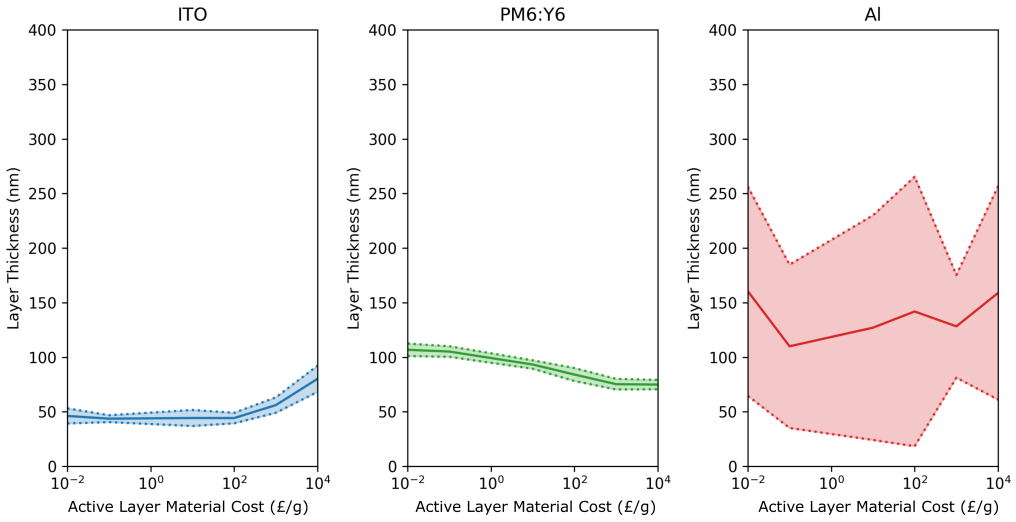


Figure 6.15: The individual layer thicknesses of the optimisation presented in figure 6.10. The solid line the mean of reach respective layer and the shaded area bound by two dotted lines denotes the standard deviation of the layer. The layers from right to left are ITO (blue), PM6:Y6 (green), and Aluminium (red)

From figure 6.15 firstly, in blue, the optimal thickness of ITO for the range of active layer material costs can be seen. As found for the P3HT:PCBM device, the thickness of ITO found in these optimisations for PM6:Y6 are lower than the minimum found when optimising for maximum PCE, stable from £0.01 to £100 per gram at 44±5nm before increasing to the maximum thickness of 80±12nm at £10,000 per gram. Examining the active layer thickness, green, across the range of active material cost may explain the increase in ITO thickness. At £0.01 per gram a comparable thickness to that seen when PM6:Y6 was optimised of PCE, with a thickness of 107±6nm, followed by a

| Active Material Cost (£) | PCE Per Unit Cost (%/£) | PCE (%) | Cost (£) | ITO Thickness (nm) | PM6:Y6 Thickness (nm) | Al Thickness (nm) |
|---|---|---|---|---|---|---|
| 10,000 | $4.96\text{x}10^{9}$ | 6.7 | $1.80\text{x}10^{-9}$ | 46 | 107 | 160 |
| 1000 | $5.19\text{x}10^{9}$ | 6.7 | $1.73\text{x}10^{-9}$ | 43 | 105 | 110 |
| 100 | $4.05\text{x}10^{9}$ | 6.7 | $2.08\text{x}10^{-9}$ | 44 | 93 | 127 |
| 1 | $1.50\text{x}10^{9}$ | 6.1 | $4.82\text{x}10^{-9}$ | 44 | 84 | 142 |
| 0.1 | $2.23\text{x}10^{8}$ | 5.7 | $2.96\text{x}10^{-8}$ | 56 | 75 | 127 |
| 0.01 | $2.42\text{x}10^{7}$ | 5.8 | $2.77\text{x}10^{-7}$ | 80 | 75 | 159 |

Table 6.3: Table of mean values presented in figures 6.14 and 6.15

gradual decrease to 74±4nm. Unlike P3HT:PCBM there is no rapid decline in the thickness of PM6:Y6, this may be due to PM6:Y6 being a stronger absorber leading to its thickness to already be minimised even at low active layer material costs [10, 29]. Lastly, Al in red. The thickness of Al remains relatively consistent over the range and presents a wide standard deviation. This wide standard deviation, of at time more than 100nm, indicates the Al electrode does not influence the behaviour of the device significantly in comparison to ITO and PM6:Y6. To enable better comparison the mean values presented in figures 6.14 and 6.15 are presented in table 6.3.

Examining the optimisation of the PM6:Y6 device for PCE per unit cost, shows the effect of improvement in charge generation from the P3HT:PCBM device. While both the PM6:Y6 and P3HT:PCBM devices show that with increased active layer material cost, performance on a PCE per-unit cost basis will decrease, in PM6:Y6 an absolute collapse in performance due to increased active layer material cost does not appear, and cost does not become a dominating factor in the optimisation. Meaning with our assumption that for commercial applications require cost not be a factor in the determination of the optimal devices, PM6:Y6 is nearer to a commercially applicable OPV active layer blend than P3HT:PCBM. Device material cost only appears to become a great factor within the optimisation above £100 per gram, where the active layer thickness has been reduced, and subsequently PCE, such that action must be taken to reduce the series resistance experienced by the cell. Therefore, it could be said that if the cost per gram of a PM6:Y6 was below £100 per gram, it could begin to be commercially approachable. How-

ever, with the current costs seen from chemical suppliers, seen in table 6.2, PM6:Y6 is not commercially approachable.

## 6.5 Optimising for Levelised Cost of Energy

Whilst optimising for a maximum PCE to device material cost ratio may allow the consideration of some degree of cost it does not fully account for the operating environment of commercial solar cells. An alternative objective function which may accurately depict the operating environment the cell experiences over its deployment is LCOE. Here, the diurnal and seasonal variation in irradiance and temperature are accounted for by calculating the yield of a solar farm at a specific location. As described in section 3.7. The material cost of the device may be calculated and scaled and used as device cost, and brining in land use as this is an important factor not considered before, from these factors LCOE for the specified device and environment may be calculated and optimised for. Here, the optimisation of the described standard device, with a P3HT:PCBM and PM6:Y6 active layer, for minimum LCOE is presented where active layer material cost is again varied from £0.01 to £10,000 per gram in decade steps.

### 6.5.1 Calculating LCOE

LCOE may be calculated using the discussed LCOE model in section 3.7. Here, the imputed cost and yield of the cells will be calculated first, and then passed to the model as inputs. The costs of the cells may be calculated through the same method as presented in section 6.4.1, however as here their generation in a commercial setting is also considered as the costs will be scaled to reflect real operation. Scaling the costs is simply achieved by scaling the costs by the difference in active area. Yield was calculated through the method presented by Huld et al. [44] utilising equation 6.5.1 yielding coefficients $k_{1-6}$.

$$\mathrm{P}\left(G',T'\right) = G'\left(P_{STC} + k_1 ln\left(G'\right) + K_2 ln\left(G'\right)^2 + k_3 T' ln\left(G'\right) + k_5 T' ln\left(G'\right)^2 + k_6 T'^2\right) \tag{6.5.1}$$

Where $P_{STC}$ is the device module efficiency under standard test conditions. $G'$ and $T'$ is the normalized in-plane irradiance and module temperature, which are given by equations 6.5.2 and 6.5.3 respectively.

$$G' \equiv G/G_{STC} \tag{6.5.2}$$

$$T' \equiv T_{mod} - T_{STC} \tag{6.5.3}$$

From the virtual Current-Voltage (JV) characterisations the efficiency of the device may be calculated at each point shown in table 6.4, forming a table of efficiencies. These efficiencies under know irradiance and temperatures may be used to fit the coefficients found in equation 6.5.1. These fitted coefficients may then be applied to historical irradiance and temperature data, estimating the power output of the panel at the chosen location. This is the method utilised by Photovoltaic Geographical Information Systems (PVGIS), and irradiance and temperature data were gathered from PVGIS [45]. With estimations for both yield and device cost, the candidate devices may be imputed into the LCOE model and an estimation of LCOE may be calculated. It is of note, due to both the estimated yield and device cost, the LCOE values achieved may likely only be used comparatively against other devices within this optimisation.

| Irradiance | Temperature ($°C$) | | | |
|---|---|---|---|---|
| ($Wm^{-2}$) | 15 | 25 | 50 | 75 |
| 100 | X | X | | |
| 200 | X | X | | |
| 400 | X | X | X | |
| 600 | X | X | X | X |
| 800 | X | X | X | X |
| 1000 | X | X | X | X |
| 1100 | | X | X | X |

Table 6.4: Temperature and Irradiance conditions the devices under optimisation are tested under. $X$ marks one test point.

Farm are set to a fixed peak energy generation capacity of 5MW$_p$, and the area and number of panels deployed are scaled to achieve this peak capacity, with projects set to last 20 years, simulated at hourly time steps. The location of Portsmouth on the south coast of England was chosen due to the south coast of England possessing the highest solar resource within the UK.

### 6.5.2 P3HT:PCBM

Presented here is the optimisation of the previously defined standard device with a P3HT:PCBM active layer for the minimal LCOE where the active layer material cost is varied from £0.01 to £10,000 per gram. The estimations for yield were calculated for performance in Portsmouth, UK, along the south coast of England. Figure 6.16 shows the achieved LCOE over the range of the active layer material costs, as well as the achieved yield and device costs.

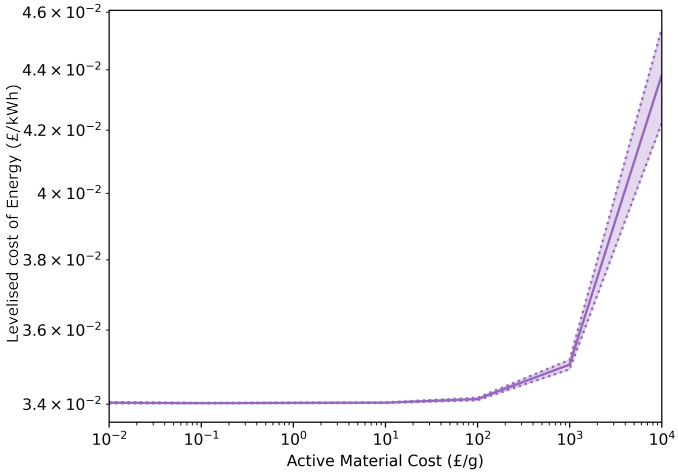


(a)

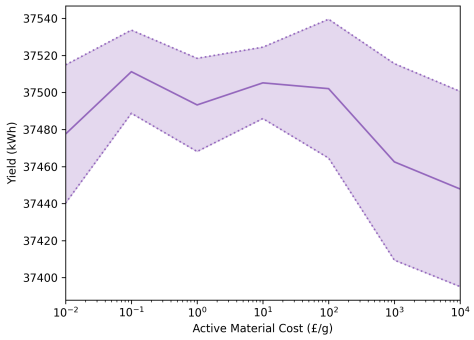


(b)

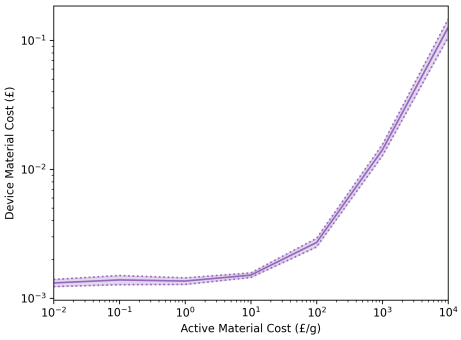


(c)

Figure 6.16: The optimisation of a P3HT:PCBM device for LCOE (£/kWh) with discussed limits implemented, from initialisation. The solid purple line denotes the mean PCE each active layer material cost and the dotted lines and coloured areas denote the standard deviation of the optimised device. Figure 6.16a, (a), shows the LCOE (%/£). Figure 6.16b, (b), and Figure 6.16c, (c), show both the yield and cost of the devices respectively, the component parts of the objective function.

Shown in figure 6.16a the achieved LCOE remains constant until £100 per gram, where in which the LCOE increases from $3.41\times10^{-2}$ $£\cdot KWh^{-1}$ up to $4.38\times10^{-2}$ $£\cdot KWh^{-1}$ at £10,000 per gram. The behaviour is also reflected in figure 6.16c, where a significant rise in devices cost is seen. As a constant peak capacity of $5\text{MW}_p$ is maintained, it may be expected that no change in yield occurs as the same historical data is used. However, figure 6.16b that small variation does occur in the yield, meaning the optimised devices' architecture

must vary as well as their performance under the historical irradiance and temperatures. The change in the optimal device architecture can be seen through examining figure 6.17.

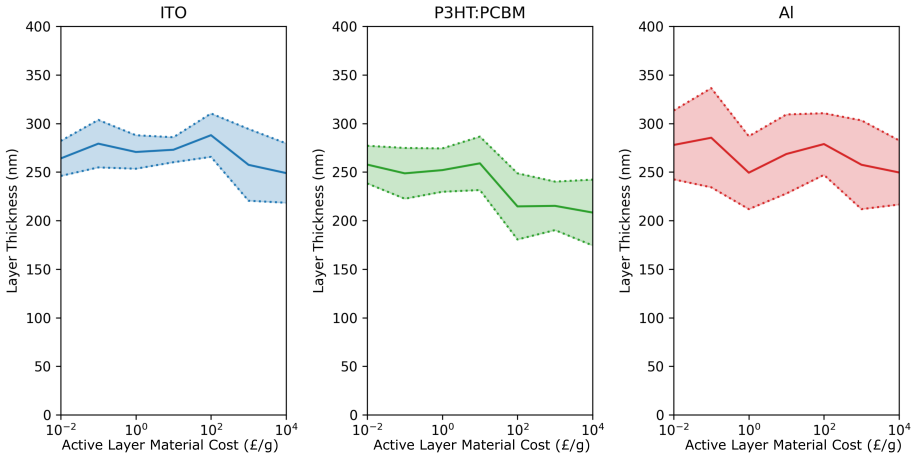


Figure 6.17: The individual layer thicknesses of the optimisation presented in figure 6.16. The solid line the mean of reach respective layer and the shaded area bound by two dotted lines denotes the standard deviation of the layer. The layers from right to left are ITO (blue), P3HT:PCBM (green), and Aluminium (red)

Firstly, both ITO, blue, and Al red are largely invariant over the course of the active layer material costs with both maintaining a thickness of approximately 250nm. The thickness of the active layer, P3HT;PCBM in green, exhibits two distinct regimes as seen in figures 6.8 and 6.13. With approximate thicknesses of 260nm until £10 per gram and 210nm thereafter.

Of note from the optimisations presented in figure 6.16 is the lack of change in the architecture of the device. Here, the active layer thickness is seen to change by 50nm across the cost range, this is 33% of that seen when optimising for PCE per unit cost. This may be due to mechanisms within the LCOE model requiring high PCE devices. When PCE is reduced, a greater number of panels are required, additionally increasing land rent and operational costs. The cost of a low PCE only grow with increased active layer material costs, further increasing the cost of additional devices. Therefore, the sharp rise in LCOE is not a failure in optimisation, but a result of the increasing active layer material costs with the soft requirement

for high PCE devices. Counterintuitively, ever layer within the devices is thicker than that seen in optimisations for PCE per unit cost and PCE. The mean thickness of the devices from the LCOE optimisation was found to be 872nm, whilst for PCE per unit cost and PCE both 413nm and 617nm were found respectively. This increase in thickness may be due to the lower average irradiance and temperature that was experienced by the devices as compared to the standard test conditions used in previous optimisations.

### 6.5.3 PM6:Y6

Here the optimisation of the standard device with a PM6:Y6 active layer for minimum LCOE is presented, where the cost of the active layer material is varied from £0.01 to £10,000 per gram. The results of this optimisation can be seen in figure 6.18.

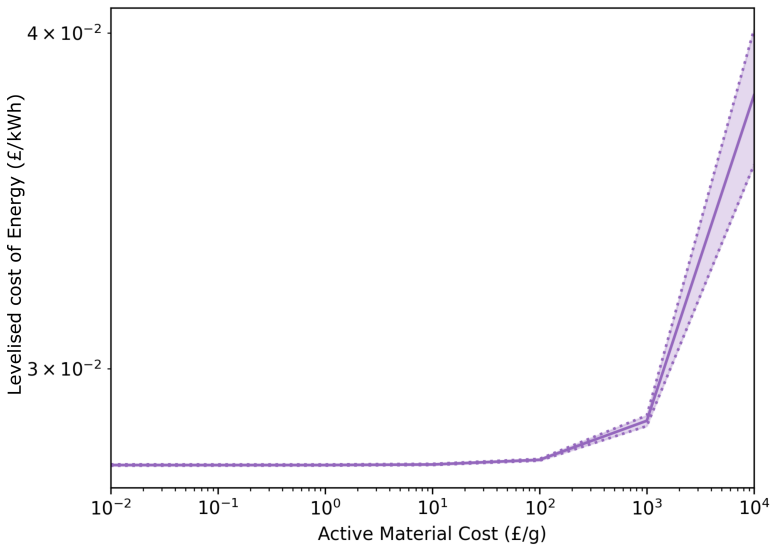


(a)

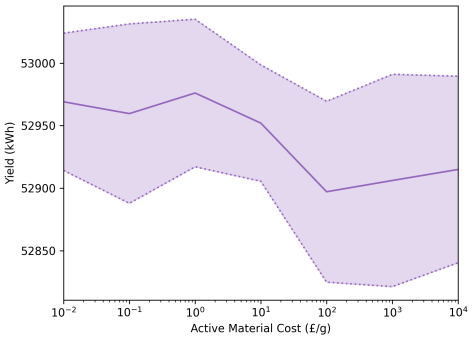


(b)

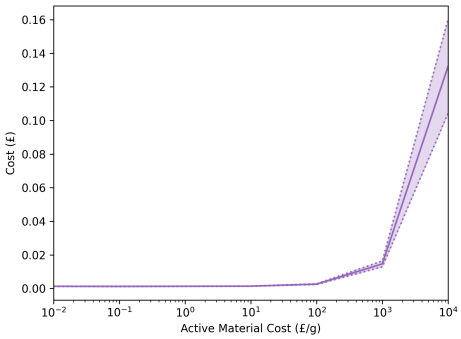


(c)

Figure 6.18: The optimisation of a PM6:Y6 device for LCOE (£/kWh) with discussed limits implemented. The solid purple line denotes the mean LCOE at each active layer material cost and the dotted lines and coloured areas denote the standard deviation of the optimised device. Figure 6.18a shows the LCOE (£/kWh). Figure 6.18b and Figure 6.18c show both the yield and Cost of the devices respectively, the component parts of the objective function.

Much like that presented in figure 6.16a for the P3HT:PCBM device, as similar trend is seen in with PM6:Y6 in figure 6.18a. Where an exponential rise in both LCOE and device cost is seen as well a near constant, but importantly not constant yield value is achieved over the farms lifetimes. The cause of the variation in the yield may be examined in figure 6.19.

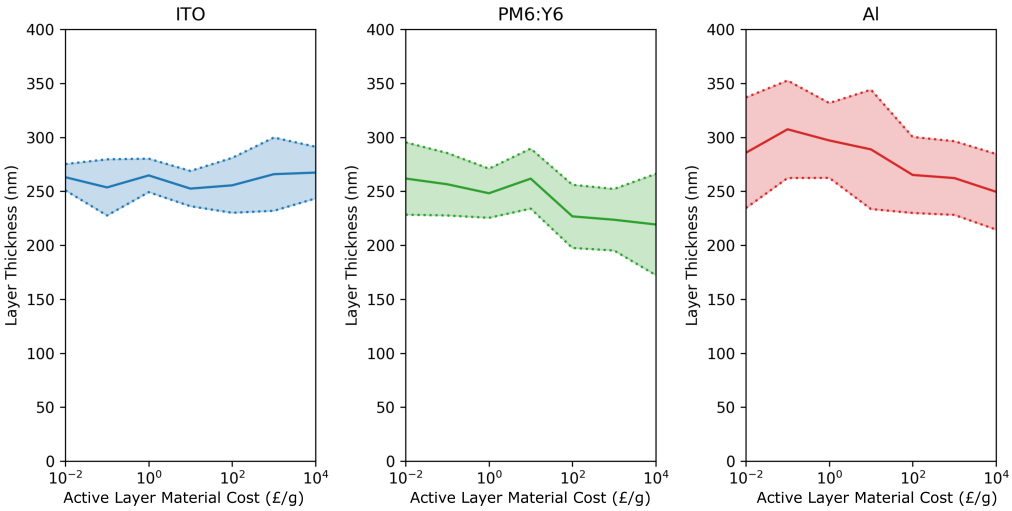


Figure 6.19: The individual layer thicknesses of the optimisation presented in figure 6.18. The solid line the mean of reach respective layer and the shaded area bound by two dotted lines denotes the standard deviation of the layer. The layers from right to left are ITO (blue), PM6:Y6 (green), and Aluminium (red)

Figure 6.19 shows the found mean layer thicknesses for ITO in blue, PM6:Y6 in green, and Aluminium in red. Examining the layers as a whole, it can be seen that all the layer are significantly thicker at all active layer material costs in the range considered, when optimised for PCE per unit cost.

The layer of most interest, the PM6:Y6 active layer, at the lowest cost per gram it is 2.4 times thicker than that found during the optimisation of PCE per unit cost. The thickness of the active layer is seen to generally reduce with active layer material cost from 262±34nm to 219±49nm from £0.01 to £10,000 per gram. The range of this thickness is comparable to that seen when optimising for PCE per unit cost, with a range of 30nm, and the optimisation for LCOE yields a range of 42nm.

This increase in thickness in dramatic compared to that seen by the P3HT:PCBM active layer, which from PCE per unit cost to LCOE only saw an increase of 50nm. The cause of this increase may be the same as that proposed previously, due to the lower irradiance and temperature experienced by the devices. Upon examination the average irradiance, ignoring nighttime, is found to be 248 $Wm^{-2}$, and the average temperature is found

to be $11°C$, both lower than the 1000 $Wm^{-2}$ and $25°C$ used under standard testing conditions. A hypothesis for the difference in increase seen between the P3HT:PCBM and PM6:Y6 active layer, is that due to the strong absorbing properties of PM6:Y6. A greater PCE is able to be achieved under the seen conditions by increasing the active layer thickness, whist adding additional cost per device, but avoids the more costly addition of devices, as experienced by the P3HT:PCBM device. The P3HT:PCBM devices still undergoes the same process of optimisation for the seen conditions, but the performance achieved does not sufficiently outweigh the need from additional devices. The balance between the cost of additional thickness, optimisation for the seen conditions, and additional devices is likely responsible for the variation in yield seen.

From the presented optimisations of both P3HT:PCBM and PM6:Y6, the much more complex optimisation problem of LCOE leads to significantly different results than that seen when only directly considering PCE and device costs.

## 6.6 Conclusions

Within this chapter, the optimisation of OPVs looking at the role of objective functions has been demonstrated for a series of different optimisation problems. From optimisation for maximum PCE, and the consideration of the impact of active layer material cost when considering device performance against cost with both PCE per-unit cost and lastly LCOE.

Initially, all layers of the devices were modifiable by the GA and optimisations were carried out for the maximum PCE. The optimised P3HT:PCBM device achieved a PCE of 4.86%, higher than the experimental device at 4.48% [5]. However, this closeness to literature was not repeated with the optimised PM6:Y6 devices with a PCE of 7.83% when the experimental device was shown to achieve PCE of 10% [9]. The difference between the PCE of PM6:Y6 device and that found in the literature may be due to the differences

in materials and fabrication techniques between those in the experimental device and those found in the standard device. Examining both devices, a significant difference in the optimised structure, particularly the thickness of the PEDOT:PSS layer, where due to the 1D nature of the DD model utilised, the highly anisotropic material properties of PEDOT:PSS could not be accounted for leading to inaccurate optimisation [24]. To counter this inaccuracy, the thickness of the PEDOT:PSS layer was fixed to that originally characterised. Additionally, through investigation, limits were placed upon the minimum thickness of ITO due to varying material properties as the film is initially deposited [8]. With appropriate bound for layers set the optimisation was repeated and yielded similar, yet lower, PCEs than previously reported.

From this, the optimisation of both active layer materials was trailed for PCE per unit cost of the device. As difficulty was found in determining accurate estimates for the cost of both active layer material blends, the active layer cost was set as a variable. Optimisation were therefore taken with active layer material cost from £0.01 to £10,000 per gram in decade steps. Examining the optimisation of the P3HT:PCBM device for all material costs, it was found that up until £10 per gram the optimisation was dominated by PCE, and after £10 per gram was dominated by cost. This is reflected in the structure of the devices, where the active layer thickness drastically reduces to reduce the material cost of the device. Such distinct regimes were not seen in the PM6:Y6 device, which displayed rather a more gradual decrease in active layer thickness is seen as the cost raises. This comparative lack of movement in the layer thicknesses in the PM6:Y6 device may be caused by its comparatively strong absorption compared to P3HT:PCBM meaning the device performance becomes less dependent upon its thickness even at low active material costs. The optimisations for PCE per unit cost have in essence revealed the range of active material cost where these materials may be considered viable, £10 per gram for P3HT:PCBM, and £100 for PM6:Y6 above which considerations for cost must be made to improve the objective

function of PCE per unit cost.

Lastly, the GA was applied to the minimisation of LCOE for both active layer materials. For both, P3HT:PCBM and PM6:Y6, the LCOE achievable was found to be dependent upon the active layer material cost. Due to the balance of the cost of panels and other costs, such as land rent, reducing PCE to reduce the cost of the project is no longer a powerful way of optimising the problem at high active layer material costs. This would see a larger area needed from the same peak capacity. Due to this, changes in the change in devices over the range of active layer material costs is limited compared to those seen in previous optimisations. Additionally, the devices produced by the optimisation for LCOE were significantly thicker than those even the thickest device found in previous optimisations. The increase in the thickness and the degree to which this occurs, is hypothesised to be due to a balance of costs, where in which the device may be optimised for the seen conditions through thicker layers, alternatively additional devices may be introduced. The material used and its properties effect this balance.

In conclusion, this chapter has shown the limitations of utilising GA coupled with a 1D DD model. Highlighting the optimisation can only consider factors considered in the chosen model, otherwise these factors must be controlled. However, it has also shown the low cost of active layer materials needed for consideration for commercial use and its importance in determining the achievable LCOE.

# Bibliography

[1] D. Feldman, V. Ramasamy, and R. Margolis, "Us solar photovoltaic bess system cost benchmark q1 2020 report," National Renewable Energy Laboratory-Data (NREL-DATA), Golden, CO (United . . . , Tech. Rep., 2021.

[2] R. E. S. IRENA, "International renewable energy agency," *Abu Dhabi*, vol. 2022, 2022.

[3] J. Wagner *et al.*, "The evolution of materials acceleration platforms: toward the laboratory of the future with amanda," *Journal of Materials Science*, vol. 56, pp. 16 422–16 446, 2021.

[4] Z. Cai, S. Zeng, Y. Yang, and L. Kang, "Automated antenna design using normalized steady state genetic algorithm," in *2008 NASA/ESA Conference on Adaptive Hardware and Systems*. IEEE, 2008, pp. 125–132.

[5] R. C. MacKenzie, C. G. Shuttle, M. L. Chabinyc, and J. Nelson, "Extracting microscopic device parameters from transient photocurrent measurements of p3ht: Pcbm solar cells," *Advanced Energy Materials*, vol. 2, no. 6, pp. 662–669, 2012.

[6] Y. Li *et al.*, "Additive and high-temperature processing boost the photovoltaic performance of nonfullerene organic solar cells fabricated with blade coating and nonhalogenated solvents," *ACS Applied Materials & Interfaces*, vol. 13, no. 8, pp. 10 239–10 248, 2021.

[7] Y. Qin, Y. Xu, Z. Peng, J. Hou, and H. Ade, "Low temperature aggregation transitions in n3 and y6 acceptors enable double-annealing method that yields hierarchical morphology and superior efficiency in nonfullerene organic solar cells," *Advanced Functional Materials*, vol. 30, no. 46, p. 2005011, 2020.

[8] H. Kim *et al.*, "Effect of film thickness on the properties of indium tin oxide thin films," *Journal of applied physics*, vol. 88, no. 10, pp. 6021–6025, 2000.

[9] C. Wöpke *et al.*, "Traps and transport resistance are the next frontiers for stable non-fullerene acceptor solar cells," *Nature communications*, vol. 13, no. 1, p. 3786, 2022.

[10] Y. Zeng *et al.*, "Enhanced charge transport and broad absorption enabling record 18.13% efficiency of pm6: Y6 based ternary organic photovoltaics with a high fill factor over 80%," *Advanced Functional Materials*, vol. 32, no. 13, p. 2110743, 2022.

[11] NREL, "Best research-cell efficiency chart," 2023. [Online]. Available: https://www.nrel.gov/pv/cell-efficiency.html

[12] M. Green *et al.*, "Solar cell efficiency tables (version 62)," *Progress in photovoltaics: research and applications*, vol. 31, no. 7, pp. 651–663, 2023.

[13] M. O. Reese *et al.*, "Consensus stability testing protocols for organic photovoltaic materials and devices," *Solar Energy Materials and Solar Cells*, vol. 95, no. 5, pp. 1253–1267, 2011.

[14] A. Gambhir, P. Sandwell, and J. Nelson, "The future costs of opv–a bottom-up model of material and manufacturing costs with uncertainty analysis," *Solar Energy Materials and Solar Cells*, vol. 156, pp. 49–58, 2016.

[15] L. K. Jagadamma *et al.*, "Efficient inverted bulk-heterojunction solar cells from low-temperature processing of amorphous zno buffer layers," *Journal of Materials Chemistry A*, vol. 2, no. 33, pp. 13 321–13 331, 2014.

[16] Y.-J. Cheng, F.-Y. Cao, W.-C. Lin, C.-H. Chen, and C.-H. Hsieh, "Self-assembled and cross-linked fullerene interlayer on titanium oxide for

highly efficient inverted polymer solar cells," *Chemistry of Materials*, vol. 23, no. 6, pp. 1512–1518, 2011.

[17] J. A. Mikroyannidis, A. N. Kabanakis, S. Sharma, and G. D. Sharma, "A simple and effective modification of pcbm for use as an electron acceptor in efficient bulk heterojunction solar cells," *Advanced Functional Materials*, vol. 21, no. 4, pp. 746–755, 2011.

[18] C.-H. Hsieh *et al.*, "Highly efficient and stable inverted polymer solar cells integrated with a cross-linked fullerene material as an interlayer," *Journal of the American Chemical Society*, vol. 132, no. 13, pp. 4887–4893, 2010.

[19] M. D. Irwin, D. B. Buchholz, A. W. Hains, R. P. Chang, and T. J. Marks, "p-type semiconducting nickel oxide as an efficiency-enhancing anode interfacial layer in polymer bulk-heterojunction solar cells," *Proceedings of the National Academy of Sciences*, vol. 105, no. 8, pp. 2783–2787, 2008.

[20] "ITO Conductive Glass - Product Detail - Latech - Singapore Leading Lab Consumable Supplier." [Online]. Available: http://www.latech.com.sg/product/1423715396-ITO+Conductive+Glass.html

[21] "ITO Glass Substrates | MSE Supplies." [Online]. Available: https://www.msesupplies.com/collections/ito-indium-tin-oxide-glass-substrates

[22] "ITO coated glass substrate For sale, supplier | Wafer price." [Online]. Available: http://www.crystal-material.com/Substrate-Materials/ITO-coated-glass-conductive.html

[23] A. M. Nardes *et al.*, "Microscopic understanding of the anisotropic conductivity of pedot: Pss thin films," *Advanced Materials*, vol. 19, no. 9, pp. 1196–1200, 2007.

[24] H. Shi, C. Liu, Q. Jiang, and J. Xu, "Effective approaches to improve the electrical conductivity of pedot: Pss: a review," *Advanced Electronic Materials*, vol. 1, no. 4, p. 1500017, 2015.

[25] J. Sambles, K. Elsom, and G. Sharp-Dent, "The effect of sample thickness on the resistivity of aluminium," *Journal of Physics F: Metal Physics*, vol. 11, no. 5, p. 1075, 1981.

[26] G. Mei-Zhen, R. Job, X. De-Sheng, and W. Fahrner, "Thickness dependence of resistivity and optical reflectance of ito films," *Chinese Physics Letters*, vol. 25, no. 4, p. 1380, 2008.

[27] L. Zhu *et al.*, "Single-junction organic solar cells with over 19% efficiency enabled by a refined double-fibril network morphology," *Nature Materials*, vol. 21, no. 6, pp. 656–663, 2022.

[28] Y. Cui *et al.*, "Single-junction organic photovoltaic cell with 19% efficiency," *Advanced Materials*, vol. 33, no. 41, p. 2102420, 2021.

[29] T. J. Brenner *et al.*, "White-light bias external quantum efficiency measurements of standard and inverted p3ht: Pcbm photovoltaic cells," *Journal of Physics D: Applied Physics*, vol. 45, no. 41, p. 415101, 2012.

[30] P. Bi *et al.*, "A high-performance nonfused wide-bandgap acceptor for versatile photovoltaic applications," *Advanced Materials*, vol. 34, no. 5, p. 2108090, 2022.

[31] Y. Lin *et al.*, "18.4% organic solar cells using a high ionization energy self-assembled monolayer as hole-extraction interlayer," *ChemSusChem*, vol. 14, no. 17, pp. 3569–3578, 2021.

[32] J. Wang *et al.*, "A new polymer donor enables binary all-polymer organic photovoltaic cells with 18% efficiency and excellent mechanical robustness," *Advanced Materials*, vol. 34, no. 35, p. 2205009, 2022.

[33] P. Bi *et al.*, "Reduced non-radiative charge recombination enables organic photovoltaic cell approaching 19% efficiency," *Joule*, vol. 5, no. 9, pp. 2408–2419, 2021.

[34] "Kurt J. Lesker Company." [Online]. Available: https://de.lesker.com/newweb/deposition_materials/depositionmaterials_sputtertargets_1.cfm?pgid=in3

[35] "PEDOT:PSS Poly(3,4-ethylenedioxythiophene)-poly(styrenesulfonate) 2.2-2.6 in H2O, (high-conductivity grade)." [Online]. Available: http://www.sigmaaldrich.com/

[36] Albree Rae Weisen, "Density of P3HT," May 2019. [Online]. Available: https://scholarsphere.psu.edu/resources/1f0cd735-6a0d-4c6d-aaea-17369594db0c

[37] J. W. Kiel, B. J. Kirby, C. F. Majkrzak, B. B. Maranville, and M. E. Mackay, "Nanoparticle concentration profile in polymer-based solar cells," *Soft Matter*, vol. 6, no. 3, pp. 641–646, 2010.

[38] B. A. Collins, J. R. Tumbleston, and H. Ade, "Miscibility, crystallinity, and phase development in p3ht/pcbm solar cells: toward an enlightened understanding of device morphology and stability," *The Journal of Physical Chemistry Letters*, vol. 2, no. 24, pp. 3135–3145, 2011.

[39] J. Xu *et al.*, "The molecular ordering and double-channel carrier generation of nonfullerene photovoltaics within multi-length-scale morphology," *Advanced Materials*, vol. 34, no. 16, p. 2108317, 2022.

[40] H.-R. Bai *et al.*, "A random terpolymer donor with similar monomers enables 18.28% efficiency binary organic solar cells with well polymer batch reproducibility," *ACS Energy Letters*, vol. 7, no. 9, pp. 3045–3057, 2022.

[41] L. Perdigón-Toro *et al.*, "Barrierless free charge generation in the high-performance pm6: Y6 bulk heterojunction non-fullerene solar cell," *Advanced Materials*, vol. 32, no. 9, p. 1906763, 2020.

[42] "Merck | United Kingdom | Life Science Products & Service Solutions." [Online]. Available: https://www.sigmaaldrich.com/GB/en

[43] B. Lee, L. Lahann, Y. Li, and S. R. Forrest, "Cost estimates of production scale semitransparent organic photovoltaic modules for building integrated photovoltaics," *Sustainable Energy & Fuels*, vol. 4, no. 11, pp. 5765–5772, 2020.

[44] T. Huld *et al.*, "A power-rating model for crystalline silicon pv modules," *Solar Energy Materials and Solar Cells*, vol. 95, no. 12, pp. 3359–3369, 2011.

[45] T. Huld, R. Müller, and A. Gambardella, "A new solar radiation database for estimating pv performance in europe and africa," *Solar energy*, vol. 86, no. 6, pp. 1803–1815, 2012.

# Chapter 7

# Conclusions and Further Work



## 7.1 Chapter Overview

Emerging photovoltaics promise high efficiencies at low costs; however, these promises have not reached fruition. Within this thesis, multiscale modelling of emerging photovoltaics is used to explore new methodologies for device design and application discovery. Namely, attention was paid to the development of photovoltaics which better decarbonise energy networks; the assessment of photovoltaics' tolerance to our variable climate, and the commercial viability of optimised photovoltaics.

This chapter summarises the contributions made by each result chapter. Lastly, recommendations for work furthering the aims of this thesis are made.

## 7.2 Chapters and Contributions Summary

### 7.2.1 Chapter 4

The first results chapter examines the ability of emerging photovoltaics to be developed to better meet our energy demands, by utilising a plant dispatch model which simulates the wide area synchronous grid of the United Kingdom. Photovoltaics with increasing power conversion efficiency with reducing irradiance are proposed and their generation in a grid context simulated. These devices are shown to possess enhanced capacity factors are compared to silicon photovoltaics and are hence named Capacity Factor Photovoltaics (CFPV). CFPVs were demonstrated to be more effective at reducing carbon equivalent emissions, and generating additional revenue, as there is better alignment of generation with electricity demand, leading to the reduction of carbon intensive generation.

From this, control was demonstrated over CFPV behaviour, through architectural design of dye-sensitised solar cells (DSSCs). Further, CFPV behaviour has been found within both organic and perovskite photovoltaics, and the potential from these devices is also demonstrated.

This approach has demonstrated that emerging photovoltaics may be developed to better meet our energy demands within themselves by reducing their variable generation, providing an alternative to a reliance upon energy storage and demand side management.

### 7.2.2 Chapter 5

As our climate becomes more variable both in the short and long term, photovoltaics is likely to experience changes to the spectrum of irradiance they experience due to changes to the composition of the atmosphere. Tolerance to these changes in spectrum would further reduce the variability of generation from photovoltaics. In this chapter, the tolerance of both silicon and organic photovoltaics due to changes in spectrum were explored utilising the atmospheric composition model. Importantly, the atmospheric composition

model was validated through examining both the predicted generation and that reported by California's independent system operator over the course of 2020 including periods of wildfires. Further analysis of wildfires in Australia, showed the importance of the spatial resolution and the relative distribution of photovoltaics. Further, the impacts of mineral dust storms of the Sahara were examined, showing predicted losses as far away as Puerto Rico and Scandinavia. However, not all change in the atmosphere must be negative, as examining the air quality change in Beijing from 2014 to 2020 showed that a reduction in particulate matter due to legislation led to 15% increase in generation in some cases.

Lastly, the tolerance of both silicon and organic photovoltaics are compared during the wildfires of California in 2020. This showed that the organic device, PM6:Y6, were less effected than by the pollution due to its narrow but strong absorption. With the chemical modification to adapt adsorption, organic photovoltaics could be developed with yet increased tolerance to pollution.

### 7.2.3 Chapter 6

The last results chapter sought to both explore the utility of genetic algorithms coupled to a drift-diffusion model for the optimisation of organic photovoltaics and explore the learnings which may be derived from these optimisations. First, devices were optimised for power conversion efficiency (PCE), showing the importance of understanding the limitations of the effective medium models and how these relate to practical fabrication of devices. With these factors controlled, architectures derived through optimisation were found to be near those found in literature.

Beyond PCE, devices were optimised for PCE per unit cost, for a range of active material costs reflecting current uncertainty in the manufacturing process. Devices with active layers of P3HT:PCBM and PM6:Y6 were shown to require materials costs below £10 and £100 per gram respectively for PCE to be near its maximal value. The difference in the cost of these material

systems is attributed to differences in their optical and electrical performance. This shows the impact materials properties have on optimal manufacturing processes.

Lastly, the devices are optimised for levelised cost of energy with varying active material cost. Where in which devices were simulated under operation of a solar farm and the levelised cost of energy was calculated, accounting for not only the cost of the devices themselves, but the cost of the farm. The devices found were largely unsensitive across the cost range, as compared to PCE per unit cost. as low PCEs are unsustainable as they result in further land and operational costs, imposing a requirement for high PCE devices. The little variation seen in device architecture across the cost range is due to the change in the balance of costs from optimising the device for the seen conditions and the addition of additional devices to meet the required capacity.

Therefore, this chapter has shown that to be commercially viable PCE must be maximised, but it has also shown that the current price of the material systems tested are not commercially viable as they require cost to be accounted for in their optimisation.

## 7.3 Thesis Conclusion

In summary, the development and interlinking of several models, multiscale modelling, has expanded our understanding of how emerging photovoltaics could be developed for the future.

In particular, the work has shown that emerging photovoltaics developed to better meet our energy needs, through the introduction of capacity factor photovoltaics, inherently reducing the variability of their generation. Additionally, it has been shown that emerging photovoltaics may be engineered to be tolerant to changes to their incident spectrum caused by pollution, Lastly, the maximally acceptable commercial price for organic photovoltaic active layer materials has been found, further systems may be tested, and the gap to commerciality identified.

## 7.4 Further Work

In this thesis, using multiscale modelling, emerging photovoltaics' path to fulfilling their promise of high efficiencies at low costs has been explored, though further work towards this aim is needed. Here, suggestions for works furthering this aim are made.

### 7.4.1 Extending Presented Work

#### Decarbonising Electrical Grids using Photovoltaics with Enhanced Capacity Factors

Within this work, a single location of UK generation capacity was assumed to estimate the enhancement in generation that would be seen within the introduced Capacity Factor Photovoltaics (CFPVs). Whilst this was shown to result in a slight underestimate of generation, compared to randomly selected locations, both do not represent where and how much photovoltaics is installed. Whilst not all the locations of solar assets within the mainland UK can be found, the Departments for Energy Security and Net Zero's renewable planning database [1] shows not only the existing sites of large scale ($\geq$1MW) solar installations, but it shows the location and proposed capacity of solar assets where planning permission has been applied for.

Further, the yield calculation assumed the same temperature and irradiance dependence as silicon. Ideally, this would be measured for CFPVs and allow for the applications of yield models such as that presented by Huld et al. [2, 3].

Through the combination of proposed solar farm locations and the estimation of yield at each proposed location, more accurate calculations of CFPV solar farms within the UK can be made.

#### Forecasting the Effect of Wildfires, Dust Storms, and Pollution on Future PV Energy Production

Through this presented work, it is assumed the atmosphere is under clear sky conditions, due to the underpinning assumption used in the used radiative transfer model (SMARTS) [4]. However, as discussed within the background, the degree to which clear sky conditions are applicable varies with location. To account for cloud cover a new radiative transfer model is needed, explicitly developed to allow for cloud cover, and several options are available [5, 6, 7]. The inclusion of cloud cover within the atmospheric composition model may allow for greater context for the losses experienced, with comparison against varying degrees of cloud cover.

#### Optimising Organic Photovoltaics Utilising Genetic Algorithms

In this work, upper and lower bounds of thickness for layers were introduced to avoid unphysical behaviour. Rather than the introduction of these limitations upon the genetic algorithm, the fitting of curves to empirical data for varying properties with layer thickness may avoid the need for strict limits, as these may be found naturally by the algorithm as it increases or decreases layer thickness. To achieve these fittings, further experimental work would be required to inform the parameters used in the model. For isotropic properties this may be easily accomplished, however for anisotropic properties this may be more complicated, such as the conductivity of PEDOT:PSS, as the dominance of the charge transport pathways within the material may change with the aspect ratio of the layer measured and later simulated [8].

### 7.4.2 Organic Photovoltaics

As demonstrated in chapter 4 and suggested by chapter 5 organic photovoltaics may be optimised for the electrical demand present and may also be developed for their incident irradiance at that location. Both concepts may be combined to create organic photovoltaics for a specific geography

and electrical demands using multiscale modelling and optimisation.

This would be a new concept, as photovoltaics are today deployed as a one size fits all solution. Yet, through their localisation, environments or grids with unusual demands may be catered for. This would further differentiate organic photovoltaics from their silicon counterparts and may aid in their commercialisation.

An example of an interesting case which may be examined, the development of organic photovoltaics for California. California already has a high penetration of solar assets, at times leading to negative energy prices as supply exceeds demand [9]. Additionally, as examined in chapter 5, California is susceptible to wildfires, leading to a significant loss of solar generation from silicon photovoltaics due to particulate matter pollution. Therefore, an organic photovoltaic device which is tolerant to the effects of particulate matter, and whose generation profile differs for silicon may be well positioned. Through the combination of a plant dispatch model, atmospheric composition model, drift diffusion model and optimisation techniques this challenge may be addressed.

### 7.4.3 Commercial Viability Assessment of Organic Photovoltaic Active Material Systems

As organic molecules used within state-of-the-art devices have become increasingly complex, questions have been raised as to whether these molecules may ever be commercially viable [10].

Shown within chapter 6, when optimising a device for power conversion efficiency per unit cost across a range of active material costs, two regimes within the optimisation are shown, one where power conversion efficiency dominates the optimisation and another where cost dominates. To be applied commercially, a balance between the cost and power conversion efficiency must be found, this may be defined as the inflection point between these two regimes.

So far only two active material blends have been considered by this means,

to develop a greater picture of how these costs vary between organic material blends a wide survey of active material blends must be characterised, fitted to a drift-diffusion model, and optimised for power conversion efficiency per unit cost. Revealing the inflection price in several blends.

Not only would this show the range of cost which may be required for commercial organic photovoltaics, due to extensive characterisation required for fitting to a drift-diffusion model, an examination of the sensitivity of this inflection point to factors, such as both electronic and optical losses, may be examined. Additionally, active material blends which do not fit the general trend seen may be identified, offering a lower priced inflection point for higher-than-expected performance, and these systems may be further studied.

# Bibliography

[1] "Renewable Energy Planning Database: quarterly extract," Nov. 2023. [Online]. Available: https://www.gov.uk/government/publications/renewable-energy-planning-database-monthly-extract

[2] T. Huld *et al.*, "A power-rating model for crystalline silicon pv modules," *Solar Energy Materials and Solar Cells*, vol. 95, no. 12, pp. 3359–3369, 2011.

[3] T. Huld, R. Müller, and A. Gambardella, "A new solar radiation database for estimating pv performance in europe and africa," *Solar energy*, vol. 86, no. 6, pp. 1803–1815, 2012.

[4] C. Gueymard, "Simple Model for the Atmospheric Radiative Transfer of Sunshine (SMARTS2) Algorithms and performance assessment."

[5] C. Emde *et al.*, "The libradtran software package for radiative transfer calculations (version 2.0. 1)," *Geoscientific Model Development*, vol. 9, no. 5, pp. 1647–1672, 2016.

[6] R. Mueller, C. Matsoukas, A. Gratzki, H. Behr, and R. Hollmann, "The cm-saf operational scheme for the satellite based retrieval of solar surface irradiance—a lut based eigenvector hybrid approach," *Remote Sensing of Environment*, vol. 113, no. 5, pp. 1012–1024, 2009.

[7] Z. Qu *et al.*, "Fast radiative transfer parameterisation for assessing the surface solar irradiance: The heliosat-4 method," *Meteorologische Zeitschrift*, vol. 26, no. 1, pp. 33–57, 2017.

[8] A. M. Nardes *et al.*, "Microscopic understanding of the anisotropic conductivity of pedot: Pss thin films," *Advanced Materials*, vol. 19, no. 9, pp. 1196–1200, 2007.

[9] J. Seel, D. Millstein, A. Mills, M. Bolinger, and R. Wiser, "Plentiful electricity turns wholesale prices negative," *Advances in Applied Energy*, vol. 4, p. 100073, 2021.

[10] M. Moser, A. Wadsworth, N. Gasparini, and I. McCulloch, "Challenges to the success of commercial organic photovoltaic products," *Advanced Energy Materials*, vol. 11, no. 18, p. 2100056, 2021.